Seasonal variability of sea surface carbonate chemistry and temperature

by

John Brian Robin Matthews
B.Sc. (Hons), University of East Anglia, 2009

A Dissertation Submitted in Partial Fulfillment of the
Requirements for the Degree of

DOCTOR OF PHILOSOPHY

in the School of Earth and Ocean Sciences

Seasonal variability of sea surface carbonate chemistry and temperature

by

John Brian Robin Matthews
B.Sc. (Hons), University of East Anglia, 2009

Supervisory Committee

Dr. A. J. Weaver, Supervisor
(School of Earth and Ocean Sciences)

Dr. J. R. Christian, Departmental Member
(School of Earth and Ocean Sciences)

Dr. K. L. Denman, Departmental Member
(School of Earth and Ocean Sciences)

Dr. K. Zickfeld, Outside Member
(Department of Geography, Simon Fraser University)

Supervisory Committee

Dr. A. J. Weaver, Supervisor
(School of Earth and Ocean Sciences)

Dr. J. R. Christian, Departmental Member
(School of Earth and Ocean Sciences)

Dr. K. L. Denman, Departmental Member
(School of Earth and Ocean Sciences)

Dr. K. Zickfeld, Outside Member
(Department of Geography, Simon Fraser University)

ABSTRACT

Ocean uptake of anthropogenic CO_2 causes ocean acidification, a secular, global-scale decline in the pH of seawater. In order to better understand the implications of contemporary acidification for marine organisms and ecosystems, there is a need to better characterise natural variability in carbonate chemistry. In this thesis, climatological seasonal variability of sea surface pH and aragonite saturation state (Ω_A) in the open ocean is indirectly derived from other parameters of the marine CO_2 system, namely total alkalinity (TA) and seawater pCO_2/fCO_2 (pCO_{2sw}/fCO_{2sw}). New monthly sea surface TA, fCO_{2sw} and temperature climatologies are developed for this purpose, utilising newly-released observational synthesis products (PACIFICA for TA and SOCAT v2 for fCO_{2sw}).

Two versions of the new SST climatology are developed, referred to as upper and lower SST (USST and LSST), to test sensitivity to the depth range of the input observations. Annual ranges are generally found to be larger for the USST climatology, derived using observations from the upper 2 m, compared to LSST (which is based on

deeper observations). Further, a seasonal cycle is found in the monthly average of the differences between these climatologies north of 30°N, perhaps partly due to seasonal variation in near-surface stratification. The USST seasonal ranges are also found to be generally larger than in two previous SST climatologies, however, difference in the depth distribution of the input measurements is unlikely the main cause.

The new monthly sea surface TA climatology extends coverage into the Nordic seas, excluded from previous climatologies. TA seasonality is found to be small outside of regions with large seasonal ranges in salinity. Large seasonal ranges in salinity and TA are found beneath the Intertropical Convergence Zone, in the Antarctic seasonal sea ice zone and in the western Greenland Sea. Non-salinity driven TA seasonality is found to be large in the Gulf of Alaska, eastern equatorial Pacific and western Greenland Sea. Compared to the Lee et al. (2006) TA climatology, substantially lower annual means and seasonal ranges are found for the subarctic Pacific, a region with greatly improved coverage courtesy of PACIFICA.

The pH/Ω_A climatologies derived in the final chapter suggest pH seasonality is predominantly temperature driven in the subtropics and mainly driven by variation in salinity normalised dissolved inorganic carbon (sDIC) in the subpolar north Atlantic, western subarctic Pacific and Southern Ocean. Salinity variation is found to only exert a strong influence on pH seasonality in the western Greenland Sea. Climatological seasonal pH ranges are found to be mostly small in the tropics ($<$0.05), moderate in the subtropics (0.05-0.10) but very large ($>$0.1) in parts of the Ross, Weddell, Irminger and Iceland Seas and western subarctic Pacific gyre. Ω_A seasonality is found to be predominantly sDIC-driven everywhere except in the western Greenland Sea, with temperature variation generally being of modest influence. Seasonal cycles of pH and Ω_A are found to be in anti-phase where pH is mainly thermally driven and in-phase where pH is mainly sDIC-forced (both pH and Ω_A vary inversely with DIC).

Comparison is made between the primary new pH/Ω_A climatology and various open ocean carbonate chemistry time-series. The climatology captures the general form of the climatological seasonal cycles of pH and Ω_A from the time-series, although with some differences in phasing and seasonal range. Analysing the time-series for long-term trends, I find that inter-decadal anthropogenic CO_2 uptake-driven pH and Ω_A declines can be modulated by trends in temperature, salinity or sTA.

Investigation is also conducted into how the amplitude of pH and Ω_A seasonal cycles might change by 2100 for a subpolar and subtropical time-series. Under a high CO_2 emissions scenario, the seasonal range of pH is found to be strongly enhanced

for the subpolar time-series and moderately reduced for the subtropical time-series, with both being due to changes in seawater buffer capacity.

Contents

List of Tables

List of Figures

ACKNOWLEDGEMENTS

Firstly, I am much indebted to my supervisor, Prof Andrew Weaver MLA, for assistance in getting 'er done. Thanks for always being jolly, for keeping my thesis on track and for helping me see the forest for the trees. I particularly appreciate your encouragement and support in developing my interest in Science outreach.

I also acknowledge my long-suffering committee members, Jim Christian, Ken Denman and Kirsten Zickfeld for their guidance over the years. A special thanks to Jim for providing insight into the mysterious world of carbonate chemistry. My thanks also go to Holger Brix for graciously agreeing to be my external examiner.

I owe a debt of gratitude to my father, Dr Brian Matthews, for teaching me how to think outside the box and giving me the confidence to challenge conventional wisdom. I am also grateful to my mother, Nina, for sound, motherly advice and my sister, Holly, for her love and support. I also pay homage to Tim Lenton and James Lovelock for the inspiration to become a scientist.

My thanks to numerous members of the Climate Lab, past and present, for making my graduate experience such a memorable one. A special mention for the legendary 'old guard': Chris Avis, Laura Bianucci, Katie Brennan, Aaron Culver, Jeremy Fyke, Dianna Porter, Udo Skielka, Stephen Sobie, Neil Swart and Rita Wania. My gratitude also goes to our lab support crew (Mike Eby, Ed Wiebe and Wanda Lewis) for always being on-hand to solve problems of a technical or administrative nature. And my thanks also to our personable departmental secretary, Allison Rose for helping me navigate degree admin. A special mention for a staff member all-too-often overlooked in thesis acknowledgements, our cheerful floor cleaner, Charlene Forsyth. Conversations with you always brightened my day.

To my good friends and confidants, Grace Kuei, Jean Paul Zacharias, Mouhannad Oweis, Stephanie Hsu, Patrick Szetey and Jeff Thompson, I raise a glass for reminding me of the importance of having a life outside of UVic and Science. My gratitude also to SEOS undergrad Fei Luo for keeping up my morale with her kind gestures.

I thank Nick Bates for provision of Hydrostation S carbonate chemistry data and Kim Currie for provision of Station Munida data. Thanks also to Ken Masarie for supplying some of the GLOBALVIEW atmospheric pCO_2 data and to John Kennedy for provision of hard-to-find papers on measurement of sea surface temperature.

For crucial financial support, I thank the Natural Sciences and Engineering Research Council of Canada (NSERC) Collaborative Research and Training Experience

Program (CREATE) in Interdisciplinary Climate Science at the University of Victoria and the Isle of Man Government.

And last but certainly not least; thanks to my electronic drum kit. Many an important thesis insight came to me whilst drumming away upon you.

DEDICATION

To my father for showing me the rewards of a scientific life.

To the enduring memory of Amanda Rachel Thornley (1989-2010).
You are sorely missed.

"Life is a struggle, not against sin,
not against the Money Power,
not against malicious animal magnetism,
but against hydrogen ions."
Henry Louis Mencken (1880-1956)

Chapter 1

Introduction

Since the pre-industrial, anthropogenic CO_2 emissions have caused the concentration of CO_2 in the troposphere to rise by ∼120 parts per million by volume (ppmv), from ∼280 to 400 ppmv. One-third of humanity's aggregate CO_2 emissions since 1800 are estimated to have been absorbed by the ocean (Sabine et al., 2004; Khatiwala et al., 2013). The ocean presently takes up about a quarter of our annual CO_2 emissions (Le Quéré et al., 2013), an amount equivalent to about a hopper's-worth of coal every second. Ocean uptake of CO_2 alters seawater chemistry, simultaneously perturbing several parameters of the marine CO_2 system. Notably, it acts to increase the concentration of dissolved inorganic carbon (DIC), reduce the concentration of carbonate ions (CO_3^{2-}) and lower the pH (a measure of hydrogen ion activity). Global-mean sea surface pH is estimated to have declined from ∼8.2 to 8.1 since the pre-industrial (Royal Society, 2005; Cao and Caldeira, 2008). This rate of pH decline and projected future rates of decline under 'business-as-usual' CO_2 emissions scenarios appear unparalleled within the past 300 million years (Hönisch et al., 2012). A further decline of 0.1-0.4 units in global-mean sea surface pH is projected by the end of this century under the Representative Concentration Pathway scenarios (Bopp et al., 2013). Such a general worldwide increase in ocean acidity is referred to as ocean acidification. There is widespread concern that contemporary ocean acidification will have substantial detrimental impacts on the structure and function of marine ecosystems. Particularly worrisome is that these ecosystems are likely to be affected not only by acidification, but by multiple anthropogenic stressors including other climate change-related impacts (e.g. upper ocean warming, subsurface deoxygenation) and overfishing.

Surprisingly, the potential ecological significance of ocean acidification has only

been widely recognised within about the last 15 years (Kleypas et al., 1999; Caldeira and Wickett, 2003; Royal Society, 2005; Doney et al., 2009). Early acidification research focused on potential impacts for calcifying organisms, a group likely to be particularly susceptible given the lower thermodynamic favorability for forming and maintaining calcium carbonate shells and skeletons in more acidic seawater. Calcifiers include corals, echinoderms, bivalves and certain zooplankton (e.g. pteropods, foraminifera) and phytoplankton (e.g. coccolithophores). Ocean acidification could disrupt other processes besides calcification and other organisms besides calcifiers through perturbing intracellular pH. Although acid-base regulation is likely a universal feature of all life on Earth (Raven, 2013), as stressed by Henry Louis Mencken in his quote at the start of this thesis, the ability of marine organisms to regulate their internal pH varies widely between species. Research into potential impacts on organisms besides calcifiers remains in its infancy.

The principal method used to examine the influence of acidification on marine organisms has been to conduct lab experiments. These generally involve exposing a particular species to pre-industrial, present-day and/or projected future pH levels for several days, weeks or months (e.g. Ries et al., 2009). In part due to difficulties measuring and controlling seawater carbonate chemistry in real-time to high precision, the partial pressure of CO_2 (pCO_2) of each seawater treatment has usually been held fixed in such experiments, often at a value equal to some global atmospheric mean. Any deviation of the real-world environment inhabited by the test organisms from these conditions (e.g. due to diel or seasonal variability) is thus neglected. Indeed, the carbonate chemistry conditions used for present-day experiments have often not even been representative of annual mean conditions in the organisms' habitat (McElhany and Busch, 2013).

The need to consider natural variability in lab exposure experiments is increasingly being recognised, in part driven by the first high-frequency pH observations from autonomous in situ sensors (Hofmann et al., 2011). These have revealed that there is considerable variability in pH on sub-diurnal to diel timescales in coastal environments, with diel fluctuations on some coral reefs found to exceed 0.2 units (Price et al., 2012; Shaw et al., 2012). While diel variations are likely much smaller in the open ocean, modelled seasonal variability has been found to be sizeable relative to secular acidification trends (Cooley et al., 2009, 2012; Friedrich et al., 2012). Moreover, autonomous pH sensors on moored buoys have revealed seasonal cycles of 0.04 unit range at Ocean Station Papa in the Gulf of Alaska (Emerson et al., 2011)

and 0.1 units offshore in the California Current (Hofmann et al., 2011).

With aquarium systems that enable dynamic control of carbonate chemistry to high precision now becoming available, there is a need for improved characterisation of natural variability of ocean CO_2 parameters so that this can be incorporated into lab experiments. That simulation of natural variability can have an influence on the response of test organisms to acidification has already been demonstrated, with Alenius and Munguia (2012) finding different responses between stable and fluctuating low pH waters for an intertidal isopod.

This PhD thesis is dedicated towards improving quantification of the present-day seasonal variability of carbonate chemistry parameters at the sea surface in the open ocean, focusing on pH and aragonite saturation state (Ω_A). In the subsequent chapters, new gridded monthly climatologies are developed for sea surface temperature (SST), total alkalinity (TA), seawater fugacity of CO_2 (fCO_{2sw}) and pH/Ω_A. The pH/Ω_A climatologies are derived using climatologies for pCO_{2sw}/fCO_{2sw}, TA, temperature, salinity, phosphate and silicate. While there are pre-existing climatologies for pCO_{2sw} and TA, they are based on much more limited data than is now available. Thus the purpose of developing new climatologies for these parameters is to make use of additional data to improve the accuracy of the resulting climatologies, to extend coverage into new regions and to better characterise uncertainties. A slightly different method was used for the new fCO_{2sw} climatology so that the influence of methodological uncertainties can be assessed. For TA, a similar method was used as for the previous climatology, e-nabling further testing of this method with additional data. New climatologies were derived for SST to investigate the spatial and seasonal prevalence of vertical near-surface temperature gradients. Evidence of strong near-surface temperature gradients in the central tropical Pacific is presented in Chapter 3. pH is sensitive to temperature ($\frac{\partial pH}{\partial T} \approx$ -0.015 °C^{-1}) and so may exhibit sizeable vertical gradients across the near-surface due to temperature variation.

The SST and TA climatologies are separately covered in Chapters 4 and 5, while the fCO_{2sw} and pH/Ω_A climatologies are discussed together in the final chapter. In the penultimate chapter (Chapter 6), a collection of open ocean carbonate chemistry time-series is presented and compared against the primary new pH/Ω_A climatology. Each time-series is subjected to a suite of standardised analyses to assess the magnitude and cause of seasonal variability and long-term trends.

It is intended that the pH/Ω_A and TA climatologies be used to evaluate the ability of models (e.g. Earth System Models, regional ocean models) to simulate present-day

seasonal variability of carbonate chemistry parameters. It is important that these models can accurately simulate this natural variability, and do so for the correct mechanistic reasons, since they provide the principle means for characterising the progression of future acidification. pH and Ω_A levels below the present-day envelope of natural variability will likely first occur at seasonal minima. Indeed, McNeil and Matear (2008), studying the Southern Ocean, found a lag of several decades between a pH threshold being crossed at the seasonal minimum and the same threshold being breached on the annual mean.

The next chapter introduces the carbonate chemistry system. Parameters of the system are defined, processes influencing them discussed and their annual mean distributions presented.

Chapter 2

The carbonate chemistry system

The carbonate chemistry system comprises the species aqueous CO_2 ($CO_2\,(aq)$), carbonic acid (H_2CO_3), bicarbonate (HCO_3^-), carbonate (CO_3^{2-}), the CO_2 solubility constant (K_0) and the apparent dissociation constants of carbonic acid (K_1', K_2'). Formation and consumption of carbonate chemistry species is modelled by chemical equilibrium reactions.

2.1 System components

2.1.1 Chemical equilibria

When CO_2 dissolves in seawater, carbonic acid (H_2CO_3) is produced (CO_2 hydration), which dissociates to release a hydrogen ion or proton (H^+). Around 19 out of every 20 protons released react with a carbonate ion (CO_3^{2-}) to form bicarbonate (HCO_3^-) (Sarmiento and Gruber, 2006), with a net release of H^+. The end result is an increase in the concentration of aqueous CO_2 ($CO_2\,(aq)$) and bicarbonate ions (HCO_3^-) and decline in $[CO_3^{2-}]$. The main reactions are described by the following series of chemical equilibria:

$$CO_2\,(aq) + H_2O \rightleftharpoons H_2CO_3 \tag{2.1}$$

$$H_2CO_3 \rightleftharpoons H^+ + HCO_3^- \tag{2.2}$$

$$HCO_3^- \rightleftharpoons H^+ + CO_3^{2-} \tag{2.3}$$

Notice that bicarbonate is an amphiprotic species, with the ability to either release or consume a proton.

Since the vast majority of CO_2 in seawater is in ionised form (>99%) but only unionised $CO_2\,(aq)$ can freely exchange with the atmosphere, equilibration of mixed layer CO_2 with the atmosphere is much slower than for unreactive gases like oxygen, taking around one year (Sarmiento and Gruber, 2006). Note, however, that the individual equilibrium reactions of the carbonate chemistry system are fast. Hydration of CO_2 (2.1) occurs in tens of seconds while the acid-base reactions (2.2 and 2.3) take microseconds (Iglesias-Rodriguez et al., 2010).

2.1.2 Dissociation constants

While called constants, the magnitude of K_0, K_1' and K_2' varies with temperature, salinity and pressure. They are called apparent or stoichiometric constants since they are written in terms of concentrations rather than activities and must be empirically determined. K_0 is commonly written in terms of CO_2^* (or equivalently $H_2CO_3^*$), which is the sum of the two unionised forms of CO_2 in seawater, $CO_2\,(aq)$ and H_2CO_3, $[H_2CO_3]$ is <0.3% of $[CO_2\,(aq)]$ (Zeebe and Wolf-Gladrow, 2001).

$$K_0 = \frac{[CO_2^*\,(aq)]}{fCO_{2sw}} \tag{2.4}$$

K_0 is in units of $\mathrm{mol\,kg^{-1}\,atm^{-1}}$, with $[CO_2^*\,(aq)]$ and fCO_{2sw} being in units of $\mathrm{mol\,kg^{-1}}$ and atmospheres (atm), respectively. CO_2 solubility is higher at lower temperature and salinity (lower K_0), while the temperature dependencies on K_1' and K_2' drive a shift towards higher $[CO_2^*\,(aq)]$ at higher temperature (Fig. 2.1; Sarmiento and Gruber, 2006). K_1' and K_2' define the ratio of the products to reactants in (2.2) and (2.3), respectively:

$$K_1' = \frac{[H^+][HCO_3^-]}{[H_2CO_3]} \tag{2.5}$$

$$K_2' = \frac{[H^+][CO_3^{2-}]}{[HCO_3^-]} \tag{2.6}$$

All quantities in these equations are in $\mathrm{mol\,kg^{-1}}$. They can be related to the thermodynamic constants K_1 and K_2 using activity coefficients (Murray, 2004). By analogy to pH, we can define $pK_1' = -log_{10}[K_1']$ and $pK_2' = -log_{10}[K_2']$.

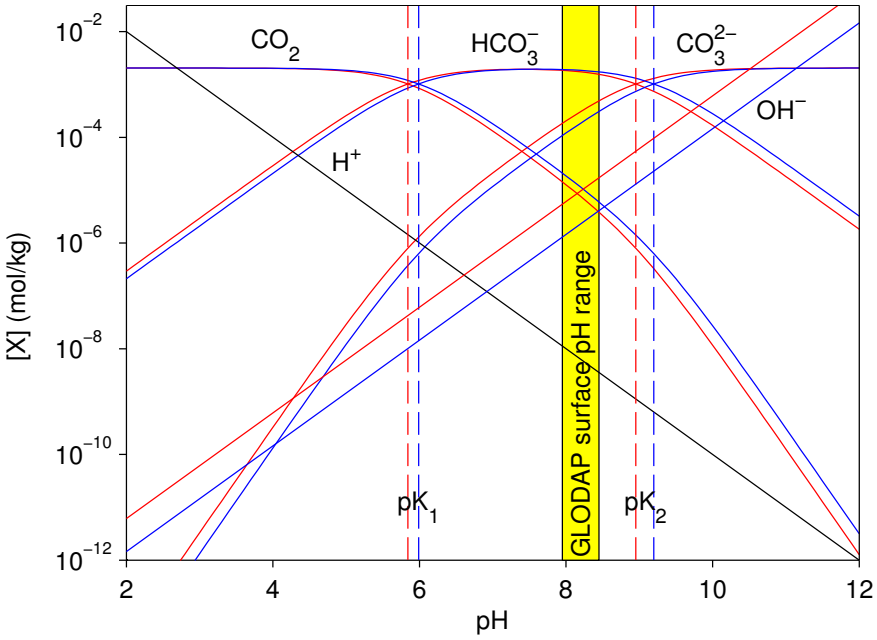

Figure 2.1: Bjerrum plot illustrating the speciation of the carbonate chemistry system as a function of pH for a dissolved inorganic carbon concentration of 2050 μmol kg^{-1} and a salinity of 36.5 psu. Speciation is plotted for two different temperatures: 25 °C (red) and 10°C (blue). The straight black line defines [H^+]. The straight red and blue lines define [OH^-] for 25 and 10°C, respectively. The plot was generated using the Seacarb routine 'bjerrum'. GLODAP refers to the GLobal Ocean Data Analysis Project.

2.1.3 System parameters

Dissolved Inorganic Carbon

Dissolved inorganic carbon (DIC) is the sum total concentration of inorganic carbon species dissolved in seawater:

$$DIC = [HCO_3^-] + [CO_3^{2-}] + [CO_2\,(aq)] + [H_2CO_3] \tag{2.7}$$

The square brackets denote total concentrations, i.e. the concentration of the species when considering both free ions (i.e. the hydrated forms of the ions) and ion pairs (e.g. CO_3^{2-} paired with $Mg^{2+}$and Ca^{2+}).

As can be seen from Fig. 2.1, in the pH range of surface seawater, most dissolved inorganic carbon is present as bicarbonate (HCO_3^-, ~90%) and carbonate ions (CO_3^{2-}, ~9%). Less than 1% of DIC is in unionised form as either $CO_2\,(aq)$ or H_2CO_3.

$CO_2\,(aq)$ is the species that exchanges with CO_2 in the air (ionised species cannot diffuse across the air-sea interface).

DIC is depleted by CO_2 uptake during photosynthesis and net CO_2 outgassing and enhanced by CO_2 release from respiration and net CO_2 ingassing. An idealised chemical reaction for CO_2 and nutrient uptake and production of organic matter by phytoplankton in photosynthesis is:

$$106\,CO_2 + 16\,HNO_3 + H_3PO_4 + 78\,H_2O \rightleftharpoons C_{106}H_{175}O_{42}N_{16}P + 150\,O_2 \qquad (2.8)$$

where HNO_3 is nitric acid, H_3PO_4 is phosphoric acid, $C_{106}H_{175}O_{42}N_{16}P$ is an idealised formula for phytoplankton particulate organic matter (POM) and O_2 is molecular oxygen. The reverse reaction describes the release of inorganic carbon and nutrients by remineralisation of POM. DIC is also influenced by calcification, which results in net release of CO_2:

$$Ca^{2+} + 2HCO_3^- \rightleftharpoons CaCO_3 + CO_2 + H_2O \qquad (2.9)$$

A major effort to sample DIC and TA was undertaken in the 1990s through the World Ocean Circulation Experiment (WOCE), Joint Global Ocean Flux Study (JGOFS) and Ocean-Atmosphere Carbon Exchange Study (OACES). These observations, together with some earlier measurements were synthesised by the GLobal Ocean Data Analysis Project (GLODAP; Key et al., 2004). DIC and TA measurements are usually reported in gravimetric units (e.g. μmol kg^{-1}), which are density-independent. DIC and TA concentrations mix conservatively when in these units.

The GLODAP gridded product indicates that DIC is high in the cold waters at high latitudes where CO_2 solubility is greater and lower at low latitudes (Fig. 2.2c).

Total Alkalinity

Total alkalinity is a measure of the amount of "excess base" (i.e. proton acceptors) in seawater available to take up protons and thus reduce the net change in hydrogen ion concentration below that which would occur in their absence. Carbonic, boric, silicic, phosphoric and some organic acids contribute to alkalinity. Bicarbonate, carbonate and borate ions comprise ~99% of TA, with the contribution of organic acids being as yet poorly quantified (Wolf-Gladrow et al., 2007). A parameter related to TA is the traditional buffer capacity of a chemical system, β_H, which quantifies the resistance

to change of the system pH to additions of strong acid or base, TOTH (Egleston et al., 2010): $\beta_H = -(\frac{\partial pH}{\partial TOTH})^{-1}$.

TA equations are derived using the principles of conservation of mass and charge (seawater cannot maintain a net charge as it has a high conductivity). The standard TA expression for oxic seawater is that of Dickson (1981), modified by Wolf-Gladrow et al. (2007) to:

$$\begin{aligned} TA =& [HCO_3^-] + 2\,[CO_3^{2-}] + [B(OH)_4^-] + [OH^-] \\ &+ [HPO_4^{2-}] + 2\,[PO_4^{3-}] + [H_3SiO_4^-] + [NH_3] + [HS^-] + ... \\ &- [H^+] - [HSO_4^-] - [HF] - [H_3PO_4] - [HNO_2] + ... \end{aligned} \tag{2.10}$$

The ellipses represent unidentified acid-base species. The equation defines TA as the number of moles of H^+ ions equivalent to the excess of proton acceptors (bases of weak acids) over proton donors (acids with $pK \leq 4.5$) in the seawater solution. Species are partitioned into proton donors and acceptors about a zero proton level (taken to be pH = 4.5). Species with a pK value above 4.5 have fewer protons than the zero level. Species that dominate a given acid-base system at the zero proton level do not appear in the TA equation (e.g. CO_2+H_2O / H_2CO_3 for carbonic acid). The coefficients in (2.10) indicate how many protons must be gained or lost from the particular species in order to reach the zero proton level species. For instance, two hydrogen ions must be gained by CO_3^{2-} to yield H_2CO_3.

Phosphate and silicate contribute to total alkalinity and need to be specified to solve the carbonate chemistry system to high accuracy. Their annual mean distributions are presented in Fig. 2.4c,d. They are in low concentration throughout the oligotrophic subtropical gyres, but in high concentration in the high nutrient, low chlorophyll Southern Ocean and subarctic Pacific. Phosphate is also high in the eastern equatorial Pacific upwelling region.

While absorption of atmospheric CO_2 changes all the concentrations in (2.10), TA does not change since CO_2+H_2O is the zero proton level species. TA is, however, influenced by uptake of nitrate (NO_3^-) and phosphate (PO_4^{3-}) in primary production, which act to raise TA (Wolf-Gladrow et al., 2007). Note that while NO_3^- does not appear in (2.10), its uptake still has an influence on TA since it causes an increase in $[OH^-]$ (obeying charge balance). Dissolution of calcium carbonate and denitrification (reduction of NO_3^- to N_2) also act to increase TA. Conversely, calcification and nitrification (oxidation of NH_4^+ to NO_3^-) deplete TA, as do remineralisation of particulate

organic matter and ammonia uptake. Atmospheric deposition of nitric and sulphuric acids can also lower TA (Doney et al., 2007).

As revealed by comparison of Figs. 2.2d and 2.4b, TA exhibits a strong relationship with salinity. High TA values are found in the high-salinity subtropical gyres of the north Atlantic and south Pacific, with low values found in the Indo-Pacific warm pool, eastern equatorial Pacific, subarctic Pacific and Southern Ocean.

The influence of precipitation and evaporation on TA can be removed by salinit normalisation. Salinity normalised TA (sTA, Fig. 2.3b) is high in the Southern Ocean, subarctic north Pacific and parts of the eastern equatorial Pacific due to upwelling of TA-rich deep waters. It is also high along the western margin of the north Atlantic where high sTA surface waters flow southward from the Greenland and Labrador Seas (Millero et al., 1998). We do not see high sTA values along the equatorial Pacific cold tongue since upwelled surface waters here are sourced from the equatorial undercurrent, which lies at relatively shallow depth compared to the dissolution length scale for calcium carbonate.

Seawater fCO_2

Seawater CO_2 fugacity (fCO_2) is a measure of the amount of unionised CO_2 in seawater, defined as:

$$fCO_{2sw} = \frac{[CO_2^*(aq)]}{K_0} \tag{2.11}$$

fCO_{2sw} is the partial pressure of seawater CO_2 (pCO_{2sw}) corrected for the non-ideal behaviour of CO_2. It can also be expressed as a mixing ratio (xCO_{2sw}). Both fCO_{2sw} and pCO_{2sw} are commonly expressed in μatm, while xCO_{2sw} is usually expressed in ppmv.

pCO_{2sw} increases with temperature, salinity and DIC and decreases with TA. Net outgassing occurs where pCO_{2sw} exceeds the overlying atmospheric pCO_2 and net ingassing in the reverse situation.

Surface waters in the subtropical gyres are close to equilibrium with atmospheric CO_2 due to their long residence time at the surface (Fig. 2.3a). Seawater pCO_2 is higher than atmospheric in the eastern/central equatorial Pacific and Atlantic where cold, upwelled waters warm and outgas CO_2. In addition to local upwelling along the Pacific and Atlantic equatorial cold tongues, there is advection of waters upwelled along the Pacific coast of South America and Atlantic coast of Africa west by the

Pacific and Atlantic south equatorial currents. pCO_{2sw} is lower than atmospheric at mid-latitudes (40-60°N and °S) due to the lower temperature and biological drawdown (Takahashi et al., 2002). Poleward-flowing waters in western boundary currents (e.g. the Kuroshio and Gulf Stream) take up atmospheric CO_2 as they cool.

pH

Devised by Søren Sørensen in 1909, the logarithmic pH scale provides a convenient means for expressing hydrogen ion activity, which can vary over several orders of magnitude in natural waters. Interestingly, what Sørensen intended the p in pH to stand for is unclear, although likely he meant some variant on power or potential of hydrogen. pH is defined as:

$$pH = -log_{10}\{H^+\} \tag{2.12}$$

where $\{H^+\}$ is in $\mathrm{mol\,kg^{-1}}$.

Rearranging, we find that $\{H^+\} = 10^{-pH}$ where $\{H^+\} = f_H[H^+]$, with f_H being the apparent total hydrogen ion activity coefficient. Like pCO_{2sw}, pH is a measure of an individual species and so is non-conservative, varying with temperature and pressure.

It is important to recognise that hydrogen ions do not exist freely in solution, but rather form complexes with water molecules and anions (e.g SO_4^{2-}, F^-). A consequence of this is that seawater pH can be defined on different scales depending on which complexes are accounted for. Presently the most widely-used scales are the seawater and total pH scales. On the total scale, 'free' hydrogen ions (i.e. hydronium or H_3O^+ ions) and those in association with sulphate (HSO_4^-) are considered. On the seawater scale, complexes with fluoride (HF^-) are also considered. I use the total pH scale throughout this thesis, as also adopted by Phase 5 of the Coupled Model Intercomparison Project (CMIP5).

pH is commonly measured at 25°C, thus conversion is required to obtain pH at in situ temperature, either using a formula (e.g. Hunter, 1998) or a carbonate chemistry routine (e.g. CO2SYS).

On an annual average, open ocean pH varies over a fairly narrow range (7.9 - 8.1), at least outside the Arctic (Fig. 2.2a). Hinga (2002) suggests that the paradigm of relative constancy in open ocean pH may have led to an apparent historical neglect of the influence of seawater pH on marine phytoplankton.

Saturation state

Saturation state is an index which characterizes the favorability of seawater for production and dissolution of calcium carbonate ($CaCO_3$). The most common bio-produced forms (polymorphs) of $CaCO_3$ are aragonite (produced by warm water corals), calcite (produced by coccolithophores and foraminifera) and high-Mg calcite ($\geq$4 mol% $MgCO_3$, produced by coralline algae). There is also a rare polymorph called vaterite produced by some coccolithophores. Aragonite is more soluble than calcite, while high Mg-calcite is more soluble than aragonite.

Saturation state is denoted by the Greek symbol Ω and defined as the ratio of the product of the measured concentration of calcium and carbonate ions to that which would exist at saturation:

$$\Omega = \frac{[Ca^{2+}][CO_3^{2-}]}{[Ca^{2+}]_{sat}[CO_3^{2-}]_{sat}} = \frac{[Ca^{2+}][CO_3^{2-}]}{K'_{sp}} \tag{2.13}$$

where K'_{sp} is the apparent solubility product in $(\mathrm{mol\,kg^{-1}})^2$ and the concentrations are in mol $\mathrm{kg^{-1}}$. Like pH, saturation state is dimensionless.

Separate saturation state parameters are defined for aragonite and calcite (Ω_A and Ω_C) by using different formulae for K'_{sp}.

Aragonite and calcite become more soluble at lower temperatures and higher pressures, the former being unusual behaviour for a salt. The latter occurs because the combined volume of one Ca^{2+} and one CO_3^{2-} ion is less than that of a single calcium carbonate molecule (with the phase occupying the least volume being favoured under increased pressure).

Annual mean sea surface Ω_A shows a similar distribution to carbonate ion, being higher in the tropics and lower at high latitudes (Fig. 2.2b). Within the spatial and temporal coverage of GLODAP, surface waters are oversaturated ($\Omega_A > 1$) everywhere, with the depth level at which $\Omega_A = 1$ (the aragonite saturation horizon) lying beneath the surface. This would appear to suggest that calcium carbonate should spontaneously precipitate from seawater. However, inorganic precipitation of $CaCO_3$ (e.g. whitings, ooids) is actually rarely observed. This is attributed to inhibition by substitution of Mg^{2+} for Ca^{2+}. Despite this, Ω_A has been found to correlate with calcification rate in warm water corals (e.g. Langdon et al., 2003) and other calcifiers (e.g. Ries et al., 2009) and so provides a useful parameter for ocean acidification monitoring. Aragonite saturation states exceeding 4 are considered optimal for calcification by warm water corals (Guinotte et al., 2003). High Ω_A values are required

to maintain net reef calcification against the destructive influence of physical and biological erosion.

Buffer factors

Buffer factors characterise the relative change in a given carbonate chemistry parameter when another parameter is perturbed. The most oft-used such factor is the Revelle buffer factor (RF), originally defined by Revelle and Suess (1957):

$$RF = \frac{\left(\frac{\Delta pCO_2}{pCO_2}\right)}{\left(\frac{\Delta [DIC]}{[DIC]}\right)} = \frac{\partial \ln(pCO_2)}{\partial \ln[DIC]} \tag{2.14}$$

RF ranges from ∼11-22 in surface waters (Fig. 2.3c), meaning that a 1% change in DIC yields an 11-22% change in pCO_{2sw}. A smaller Revelle buffer factor indicates a greater capacity to buffer pH change. Mid-to-high latitude waters are thus more weakly buffered than those at lower latitudes.

RF increases with anthropogenic CO_2 uptake, with the same fractional change in DIC resulting in a larger fractional change in pCO_{2sw}. In effect, a smaller change in DIC can counter a given undersaturation of seawater pCO_2 below the atmospheric level and so less CO_2 ingassing is required to achieve equilibrium. Thus the ability of seawater to take up atmospheric CO_2 declines with acidification.

2.2 Sea surface temperature and salinity

2.2.1 Sea surface temperature

The temperature of surface seawater (sea surface temperature, SST) has been routinely measured for around 160 years, and obtained from a variety of different platforms, instruments and depths over this period. Given that a large proportion of this thesis is devoted to comparison of SST measurement methods and development of SST climatologies (Chapters 3 and 4, Appendices B and C), a detailed review of the history of SST measurement is presented below. Appendix A provides additional details about the bucket and engine intake methods.

SST measurements were originally obtained using buckets aboard ships of opportunity. The buckets were used to capture seawater samples, the temperature of which was then measured using liquid-in-glass thermometers. It has been suggested that

the buckets used transitioned from predominantly wooden to predominantly canvas between the 1850s and 1920s (Folland and Parker, 1995; referred to as FP95). Canvas buckets are thought to have remained the dominant bucket type in use from the 1920s until their gradual replacement by rubber and other modern "insulated" meteorological buckets in the 1950s and 1960s (Kennedy et al., 2011a). Examples of the latter are described by Kent and Taylor (2006).

A new method of SST measurement evolved with the advent of steamships. To maintain engine temperatures below critical thresholds, large volumes of subsurface seawater were pumped on board for engine cooling. To monitor the efficiency with which the seawater was removing heat from the engine, ships' engineers began observing seawater temperature in engine cooling water intakes. Meteorologists recognised that intake temperature measured prior to the engine might be representative of seawater temperature at intake depth. Such engine intake temperatures (EIT) are known to have been recorded since at least the 1920s (Brooks, 1926; referred to as B26).

While buckets generally sample the upper few tens of centimetres, depths sampled by intakes are highly variable. Engine intake inlets are usually close to keel depth to ensure submergence under all sea conditions. Intake depths on modern merchant vessels are generally around 7-10 m, although they can exceed 15 m, with an intake at 26 m being reported by Kent and Taylor (2006). Actual sampling depth for intakes on container ships and bulk carriers can vary by several metres depending on ship load (Beggs et al., 2012). Large ships can have dual seawater intakes, one close to keel depth and another a few metres higher (Ecology and Environment Inc., 2007). The deep intake is used at sea and the upper when in shallow coastal waters or canals.

In recent decades the number of bucket and engine intake observations has declined, in part due to reduction in the World Meteorological Organization (WMO) Voluntary Observing Ship (VOS) fleet from a peak of over 7500 ships around 1985 to under 4000 today (Kennedy et al., 2011a). Shipboard hull contact sensors, that is temperature sensors mounted to the outside or inside of the hull (e.g. Beggs et al., 2012), have increased in prevalence over this period, providing more SST observations than buckets by the late 1990s (Kent et al., 2007). They presently contribute around a quarter of all VOS SST measurements (Kent et al., 2010). Other dedicated shipboard methods include radiation thermometers, expendable bathythermographs and trailing thermistors.

Since the early 1970s VOS SST measurements have been augmented by temperatures from ocean data acquisition systems (ODAS), principally moored and drifting

buoys. Around 70% of in situ observations were obtained by buoys in 2006 (Kennedy et al., 2011a). ICOADS contains drifting buoy measurements from 1978 onwards and moored buoy observations from 1971 (Woodruff et al., 2011). Earlier measurements from these platforms may exist but are not included in ICOADS. While drifting buoys are purported to measure sea temperature at a nominal depth of $\sim 25\,\mathrm{cm}$ (Kennedy et al., 2007), they oscillate within the surface wave field such that actual measurement depth can be anywhere within the upper 2 m (Emery et al., 2001).

Satellite retrievals of SST have been obtained since the 1960s (Krishna Rao et al., 1972), although only observations obtained following the advent of the Advanced Very High Resolution Radiometer (which measures in the infrared) are generally utilised today, typically from 1981 onwards (e.g. Reynolds et al., 2002). Since 1991, SST retrievals have also been obtained using along-track scanning radiometers, which measure over three channels in the thermal infrared (Merchant et al., 2008). Unlike earlier instruments, these are self-calibrating, providing fairly accurate retrievals without the need for calibration using in situ measurements. SST has also been measured by satellite-borne passive microwave radiometers since 1997 (Wentz et al., 2000). These have an advantage over infrared sensors in that microwaves can penetrate clouds with little attenuation.

Satellite instruments observe temperature within the sea surface skin (upper $\sim$1 mm) whereas in situ methods measure the so-called bulk temperature beneath (Donlon et al., 2002). Skin temperatures are generally a few tenths of a °C cooler than the bulk temperatures immediately below due to long-wave, latent and sensible heat loss. Differences can be as high as 1°C in regions of high heat loss (Soloviev and Klinger, 2008).

On an annual mean, the sea surface temperature distribution corresponds closely to that of insolation, being higher in the tropics and lower at mid and high latitudes (Fig. 2.4a). Some of the deviations from this pattern are due to advection of warm, tropical waters poleward and cooler waters equatorward by ocean currents (e.g. the Gulf Stream, Kuroshio and Canary Current).

2.2.2 Sea surface salinity

Salinity is a measure of the concentration of dissolved salts in seawater. The modern method of in situ measurement involves use of platinum electrodes to determine conductivity and then relation of conductivity to salinity. Ship-based sampling equipment

includes Conductivity-Temperature-Depth sensors (CTDs) and expendable CTDs, rosettes with Nansen bottles and thermosalinographs. Salinity is also measured by Argo floats and moored buoys. Within the last five years attempts have been made to measure sea surface salinity via satellite as part of the European Space Agency's Soil Moisture and Ocean Salinity (SMOS) mission and the National Aeronautics and Space Administration's Aquarius mission.

The distribution of sea surface salinity (SSS) primarily reflects net evaporation minus precipitation (E-P). SSS is high in the subtropical gyres (Fig. 2.4b) where E>P and lower at mid to high latitudes where P>E. SSS is relatively low in the tropics beneath the Intertropical Convergence Zone where there is heavy convective rainfall. Runoff from land is important in certain locations (e.g. the Bay of Bengal).

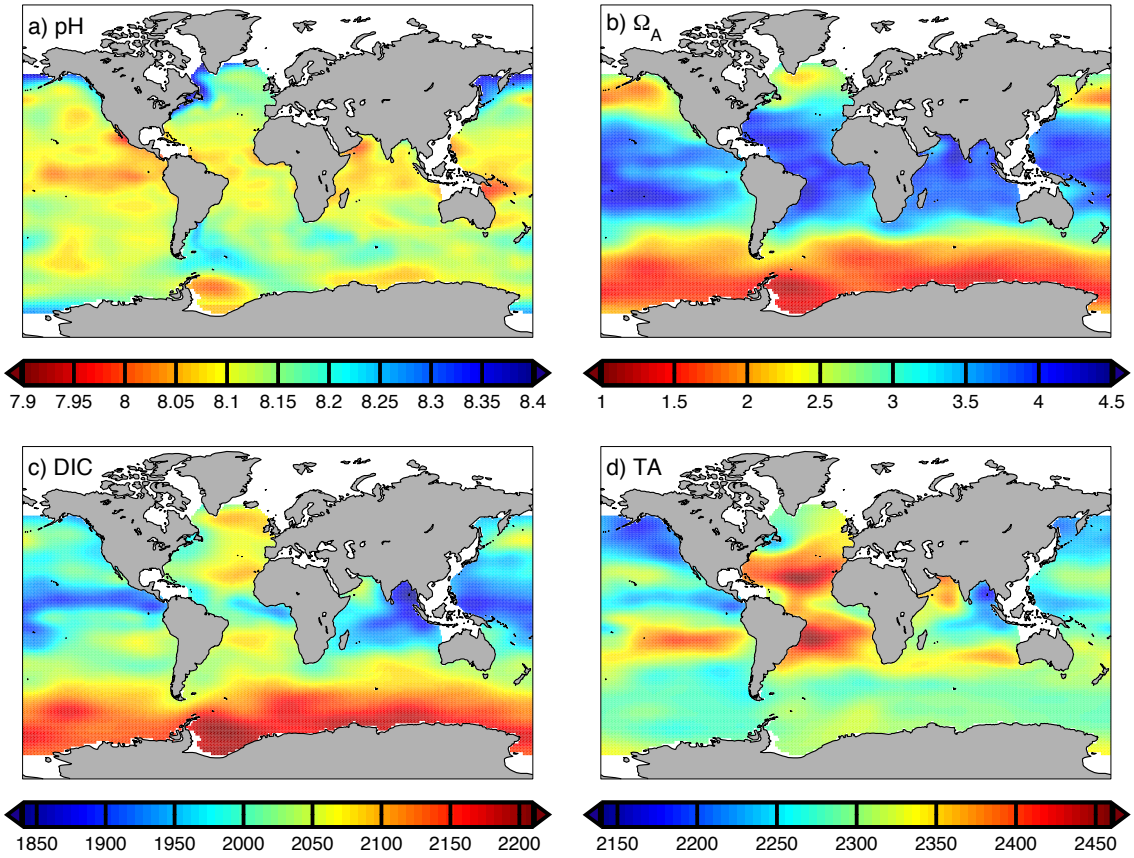

Figure 2.2: Annual mean fields for sea surface a) pH (total scale), b) aragonite saturation state Ω_A, c) dissolved inorganic carbon (DIC, μmol kg^{-1}), and d) total alkalinity (TA, μeq kg^{-1}). Fields (c) and (d) are from the GLODAP gridded product. (a) and (b) were calculated by solving the ocean CO_2 system in CO2SYS (Lewis and Wallace, 1998) from (c) and (d) using the carbonic acid dissociation constants of Mehrbach et al. (1973) as refit by Dickson and Millero (1987). Annual mean sea surface temperature, salinity, phosphate and silicate fields from World Ocean Atlas 2009 were also used as inputs.

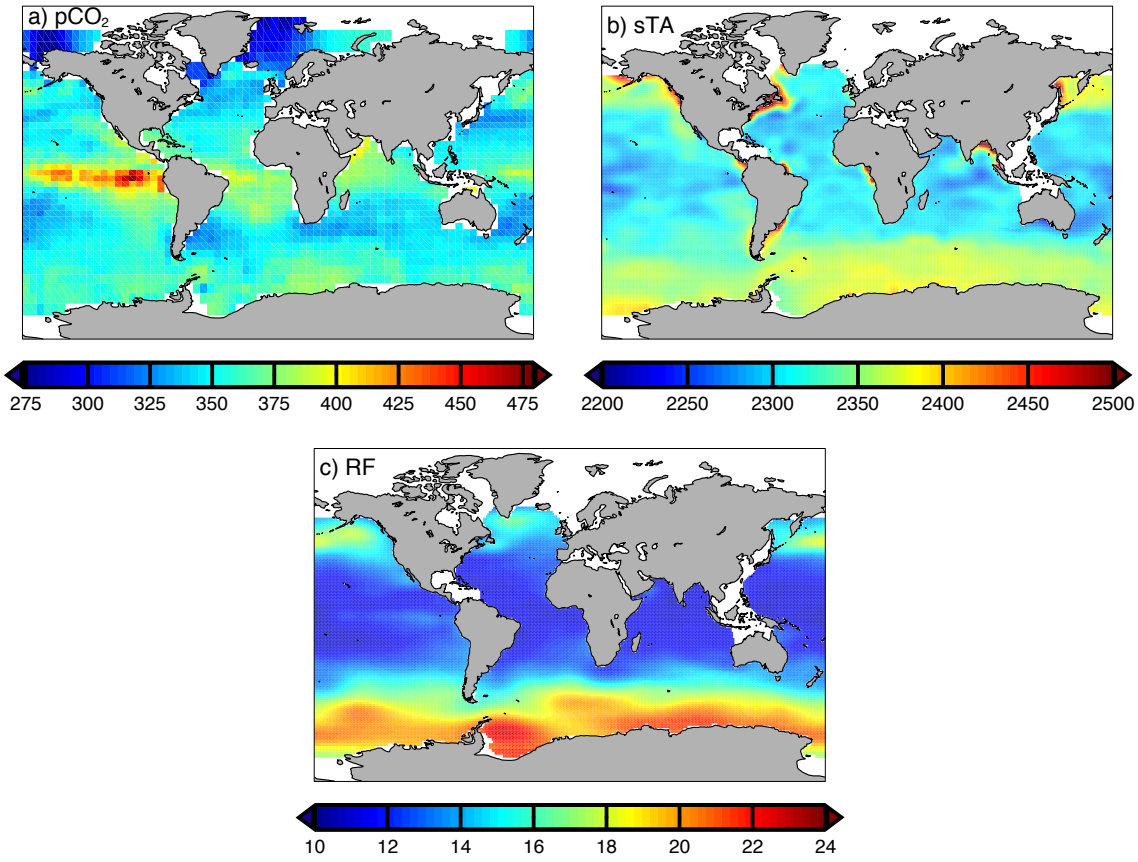

Figure 2.3: Annual mean sea surface a) pCO_{2sw} from the Takahashi et al. (2009) climatology in μatm. b) Salinity normalised TA (sTA) in μeq kg^{-1}, calculated from GLODAP TA using $sTA = \frac{TA}{S}35$, where S is salinity. c) The Revelle buffer factor (RF) calculated using the explicit formula of Egleston et al. (2010) and GLODAP DIC and TA.

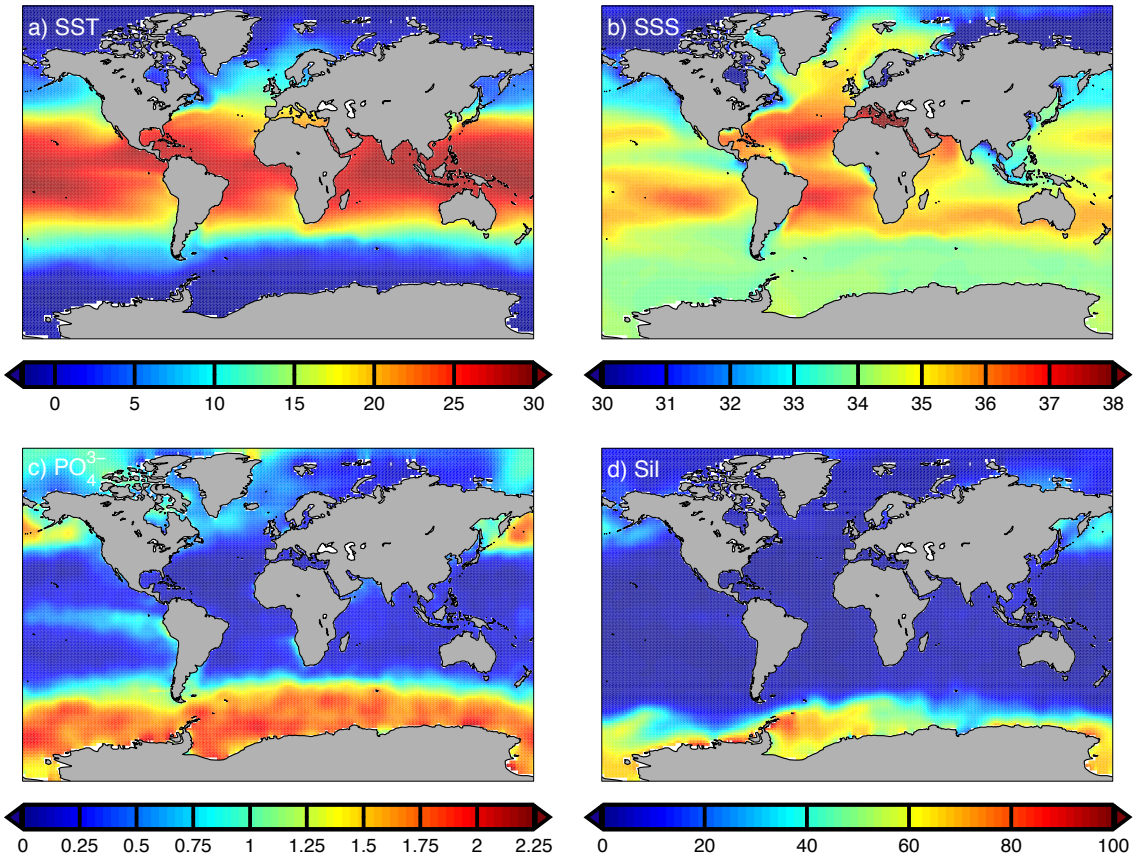

Figure 2.4: Annual mean fields for sea surface a) temperature (°C), b) salinity (psu), c) phosphate (μmol kg^{-1}) and d) silicate (μmol kg^{-1}) from World Ocean Atlas 2009.

Chapter 3

Comparison of sea surface temperature measurement methods

Here I report the results of a shipboard experiment to directly compare several sea temperature measurement methods. This field comparison is published as Matthews and Matthews (2013).

Due to supposed differences in their propensities for captured seawater to change temperature following collection, rubber buckets are known as "insulated", wooden as "partially-insulated" and canvas as "uninsulated". The walls of canvas buckets can be permeable to sample seepage, with consequent evaporation from the external bucket surface thought to lead to sample cooling. Evaporation of water absorbed into the walls or adsorbed to their outer surface during sampling can also contribute. For buckets without lids, evaporation can also occur about the exposed upper surface of the sample.

Bucket temperatures have generally been found to average a few tenths of a °C cooler than simultaneous intake temperatures in field studies (e.g. James and Fox, 1972). Field and lab experiments demonstrate that cooling of bucket samples prior to measurement provides a plausible explanation for negative average bucket-intake differences. Cooling rates of around 0.05-0.1°C min^{-1} are generally reported for small-volume canvas buckets (e.g. Ashford, 1949), although rates of 0.15°C min^{-1} or more are sometimes reported (e.g. Roll, 1951a). Positive intake-bucket differences are also attributed to warm error in EITs, which have been found to average overly-warm by

>0.5°C on some vessels (e.g. Brooks, 1928; Tauber, 1969). Separate average errors in bucket and intake temperatures cannot be directly distinguished from such relative bucket-intake differences, nor can the role of near-surface temperature gradients. A comprehensive review of field and lab experiments assessing the accuracy of historical methods of SST measurement is provided in Appendix B.

Here I compare wood, canvas and rubber bucket temperatures to 3 m seawater intake temperature along a central tropical Pacific transect conducted in May and June 2008.

3.1 Methods

Original data were collected on a 5-week research cruise from Papeete, Tahiti to Honolulu, Hawaii aboard the SSV *Robert C. Seamans* of the US Sea Education Association from May 9^{th} to June 14^{th} 2008 (Siuda, 2008; Matthews, 2009). The *Seamans* is a ∼41 m-long modern sailing vessel of draft ∼4 m, achieving an average speed of around 4.7±1.8 kt (∼2.4±0.9 m s^{-1}) under-sail and 7.2±1.7 kt (∼3.7±0.9 m s^{-1}) under-motor on our cruise. Several upper surface and near-surface temperature measurement methods were directly compared along the cruise transect (Fig. 3.1), which was conducted at the end of the 2007/8 La Niña event. The current structure encountered was unusual (Fig. 3.4), with the NECC straddling the equator rather than lying to its north, with eastward rather than the normal westward flow at the equator.

Hourly bucket temperatures were obtained from ∼17.5°S to ∼3°N using three different bucket types, with various meteorological measurements recorded near-simultaneously. Thermosalinograph temperature at a nominal depth of 3 m was measured each minute between 17.5°S and 19°N and considered analogous to accurate engine intake temperature (EIT) for the same intake depth. Daytime temperature profiles to 20 m were obtained by CTD at the locations marked in Fig. 3.1, enabling assessment of temperature variation over the typical depth range of VOS intakes.

3.1.1 Bucket temperatures

Bucket temperatures were obtained using wood, canvas and a modern rubber meteorological bucket (Zubrycki bucket) in what was apparently the first major field comparison of wood and canvas bucket temperatures. The wood and canvas buckets were of similar size (wood: 22.5–25.5 cm inner diameter by 18 cm deep, volumetric

capacity ∼8 L; canvas: 24 cm by 25.5 cm, capacity ∼11.5 L; Fig. 3.2), with the canvas bucket being a modern general-purpose ships' bucket. The wood bucket is of similar diameter but reduced height to the 19^{th} century wooden ships' bucket modelled by Folland and Parker (1995) (25 cm inner diameter by 25 cm deep, volumetric capacity ∼12 L). Whilst constructed of softwood pine rather than the hardwood oak of the Folland and Parker (1995) (referred to as FP95) wooden bucket, pine is of similar specific heat capacity to oak (2.5 kJ kg^{-1} K^{-1} compared to 1.9 kJ kg^{-1} K^{-1}). The volumetric capacity of our canvas bucket was around three times that of the canvas bucket described by Brooks (1926) (∼4 L, 13 cm diameter by 36 cm high) and that of the UK Met Office Mk II canvas meteorological bucket (∼4 L, 16 cm by 25 cm, fillable to 20 cm deep). However, it is of similar capacity to canvas buckets used by Japanese ships around the 1930s (∼12.5–28 L, 20–30 cm diameter by 40 cm high, Uwai and Komura, 1992). Unlike the Mk II, our canvas bucket did not have a wooden lid or base and could be placed on deck without collapse. The Zubrycki rubber bucket had the smallest volumetric capacity at ∼0.7 L (the sample vessel was ∼7.5 cm in inner diameter by 16.5 cm deep), far smaller than the 5 L rubber bucket used by Tabata (1978b). Temperatures from this bucket were used as a reference, with captured seawater samples assumed not to warm or cool prior to measurement.

At each bucket station the three buckets were consecutively cast overboard, filled with seawater, hauled up and placed on the wooden deck. A factory-calibrated Fisher traceable thermistor probe with 0.1°C resolution was inserted into each bucket sample and a reading recorded once the display stabilised in around 10–20 s. Stations were generally conducted within five minutes prior to the top of a given hour. The walls of the wood and canvas buckets generally remained wet from one deployment to the next. Hauling times were short given that bucket launch and retrieval was from ∼2.5 m above the waterline. The total hauling and on-deck measurement period (the "exposure time") was ∼1 min.

3.1.2 Meteorological observations

Several meteorological variables were recorded at each bucket station. Dry and wet bulb air temperatures were taken from liquid-in-glass thermometers mounted in a Stevenson screen on the poop deck (∼5 m above the waterline) and reported to 0.5 or 1°C. Beaufort wind force and cloud cover in oktas were estimated by eye and atmospheric pressure read from a barometer installed in the deckhouse.

Wind speed and direction were measured each minute by an anemometer atop the foremast at ∼33 m above the waterline. Wind speed at 33 m (U_{33}) was converted to wind speed at other heights (U_z) using the log-profile formula from the TurboWin software, as given by Thomas et al. (2005):

$$U_z = U_{33} \frac{\ln(\frac{z}{0.0016})}{\ln(\frac{33}{0.0016})} \tag{3.1}$$

Wind speed and direction from ≤5 min prior to the top of each hour were averaged for comparison to hourly measurements.

3.1.3 Subsurface measurements

Scientific seawater intake temperature was recorded at 1 min intervals by thermosalinograph (TSG) (Seabird SBE45, calibrated in February 2008, accurate to at least 0.01°C). The TSG measures seawater in the scientific flow through, sampled by a sea chest at ∼3 m depth and piped up to the TSG in the wet lab at the main external deck level. TSG temperature was averaged as per wind speed and direction for comparison to hourly measurements.

CTD casts with a Seabird SEACAT Profiler (SBE19plus, temperature accurate to at least 0.01°C) were taken hove to at 22 locations along the transect (Fig. 3.1). Mean speed over ground whilst hove to was 1.4±0.8 kt (∼0.7±0.4 m s^{-1}), with hove to periods identified from coincident changes in apparent wind direction. At each location, CTD temperature was recorded every 5 m at nominal depths between 5 and 20 m. Besides two mid-afternoon casts observed around 15:30–16:30 LT (local time, UTC-10), CTD-1 and CTD-22, all casts were taken in mid- to late morning between 9 a.m. and noon. Current velocities at ∼19 m depth were measured every 20 min using a shipboard acoustic Doppler current profiler or ADCP (RDI Ocean Surveyor 75 kHz).

3.1.4 OSTIA data

Daily foundation temperatures from the Operational Sea Surface Temperature and Sea Ice Analysis (OSTIA) were obtained for comparison to the shipboard temperatures. Foundation temperatures are near-surface temperatures of sufficient depth to be free of diel variability. OSTIA is a high-resolution (1/20°, ∼6 km) gridded dataset derived from buoy, ship and satellite (infrared and microwave) observations

Table 3.1: Average upper 3 m temperature differences and eastward 19 m velocities in various current regimes encountered along the cruise transect. The regimes exhibit distinct differences in surface current velocity and/or direction. Four currents were recognised along the transect: the South Equatorial Current (SEC), the South Equatorial Countercurrent (SECC), the North Equatorial Countercurrent (NECC) and the North Equatorial Current (NEC). Adjectives in regime names describe relative current strength in sub-branches of these currents.

Regime	**Approximate latitudinal range (°N)**	**Eastward 19m current velocity ($cm\,s^{-1}$)**	**Composite bucket SST minus 3 m temperature (°C)**		
			All	Day	Night
SEC Weak	−17.5 to −12.4	-5.5 ± 11.1	0.4 ± 0.2	0.5 ± 0.1	0.4 ± 0.1
SEC Moderate	−12.4 to −10.3	-10.6 ± 14.4	0.4 ± 0.2	0.5 ± 0.2	0.3 ± 0.1
SECC	−10.3 to −8.8	4.0 ± 9.1	0.4 ± 0.2	0.6 ± 0.3	0.3 ± 0.1
SEC Strong	−8.8 to −2.5	-19.7 ± 21.2	0.3 ± 0.1	0.4 ± 0.2	0.3 ± 0.1
Cold tongue (NECC)	−2.5 to 1.4	55.1 ± 25.6	0.3 ± 0.1	0.4 ± 0.1	0.3 ± 0.1
NECC (outside cold tongue)	1.4 to 5.7	29.8 ± 8.3	0.3 ± 0.1	0.4 ± 0.1	0.3 ± 0.1
NEC Strong	5.7 to 11.0	-23.3 ± 14.3			
NEC Weak	11.2 to 19.0	-8.3 ± 10.4			

by optimal interpolation (Donlon et al., 2012). Temperatures obtained in daytime under low wind speeds ($<6\,m\,s^{-1}$) are rejected in an attempt to exclude measurements influenced by formation of a diurnal thermocline.

The OSTIA system uses a rolling 36 h observation window centred on 12:00 UTC with a single field produced for each UTC day. OSTIA grid cells traversed by the *Seamans* on each local day were identified and the corresponding foundation temperatures extracted and averaged for the equivalent OSTIA UTC day. Difference in phasing of local and UTC days was ignored, given the long observation window.

3.2 Results and discussion

3.2.1 Bucket temperature comparison

No significant difference was found between the wood, canvas and rubber bucket temperatures across the stations, with mean differences of 0.0°C (the standard error on the mean, $\sigma M = 0.0$°C and the standard deviation, $\sigma = 0.1$°C) between all bucket types (Fig. 3.3). This was also the case when observations were separated by day and night, with daytime measurements taken to be those obtained between the local times of sunrise and sunset and vice versa for nighttime measurements. When partitioned

into the regions identified in Table 3.1 and Fig. 3.4, absolute mean inter-bucket temperature differences were all under 0.1°C, with standard deviations around ±0.1 to ±0.2°C. This was also true when observations were further separated by day and night, except for daytime measurements from the North Equatorial Countercurrent (NECC) outside the equatorial cold tongue, where sample size was <10.

The rubber bucket temperatures show a slight cool tendency relative to those from the canvas and wood buckets, with rubber-canvas and rubber-wood differences of −0.1°C found for a relatively large number of stations (26 and 30%, respectively). This might reflect susceptibility for the rubber bucket samples to cool prior to measurement due to their small volume. Even so, assumption that the rubber bucket samples remained of stable temperature pre-measurement is a reasonable approximation. Taking the bucket temperatures to be accurate to 0.1°C, I averaged over temperatures from each bucket type at each station to create a "composite" bucket temperature variable.

No correlations were found between inter-bucket temperature differences and apparent wind speed at 3 m, apparent wind direction, ship speed over ground, local time, atmospheric pressure, air minus composite bucket temperature or relative humidity. To assess correlations between inter-bucket differences and meteorological variables estimated by eye (i.e. Beaufort wind force and cloud cover), temperature differences were split into two groups from coincidence with high or low values of these meteorological variables. High Beaufort wind forces were considered those ≥4 and high cloud cover ≥5 oktas. All groupings were found to have means of 0.0°C (σM = 0.0°C, σ = 0.1°C).

The results suggest that accurate bucket temperatures can be obtained using large-volume buckets and fast-response scientific thermometers. I find no evidence for evaporative cooling of seawater samples in the wood and canvas buckets in the ∼1 min exposure period.

It is unclear whether the FP95 bucket models would also simulate negligible cooling after one minute if adapted to the buckets I used and environmental conditions experienced. Their bucket adjustments for the tropical Pacific are amongst the largest derived on an annual average, due to the strong and seasonally invariant evaporation rates simulated. Their final adjustments for June in the central tropical Pacific are around +0.1–0.3°C and +0.4–0.7°C in 1860 and 1940, respectively. The corresponding adjustments for December are around +0.1–0.2°C and +0.4–0.6°C. These values are not directly comparable to my results given the longer exposure times used (4 min

for the wooden bucket adjustments) and the different bucket sample volumes. At two-thirds full, our canvas bucket contained nearly three times the simulated filled volume of the Mk II (∼8 vs. ∼3 L, Mk II water depth: 14 cm), the larger of the two canvas buckets modelled by FP95. Conversely the sample volume in their modelled wooden bucket (water depth 20 cm) was around twice that of the wooden bucket used here at two-thirds capacity (∼10 L vs. ∼5.5 L).

An earlier document describing the FP95 models, Folland (1991), presents a plot showing simulated cooling for a canvas bucket of similar diameter to the Mk II (filled with ∼4 L) as being 0.25°C in the first minute given an air temperature of 28°C, sea temperature of 30°C, relative humidity of 75%, 10 m wind speed of 5 m s^{-1} and a ship speed of 7 m s^{-1}. Besides the ship speed, these environmental conditions are comparable to those experienced aboard the *Seamans* around the nighttime daily maximum sea–air temperature difference, for which composite bucket temperature averaged 2.1±0.5°C warmer than the air temperature. The observed relative humidity and 10 m wind speed (excludes the effect of ship motion) respectively averaged 79±6% and 4.9±1.8 m s^{-1} across bucket deployments. Apparent wind speed at 3 m (approximately the height of the bucket deployments) averaged 4.9±1.5 m s^{-1}. Under the same aforementioned model environmental conditions, but given a ship speed of 4 m s^{-1}, more comparable to that of the *Seamans* (average speed over ground of 2.4±1.1 m s^{-1} across bucket stations), simulated cooling of a wooden bucket sample of 10 L was only 0.025°C in the first minute. Simulated cooling of the canvas bucket sample after 1 min appears to have been ∼0.2°C, based on reported cooling at 4 min of 0.6°C (note that the cooling slows with time). For comparison, the rubber-canvas and rubber-wood bucket differences averaged 0.0°C (σM = 0.0°C, σ ∼0.15°C) for deployments conducted when the sea-air temperature contrast exceeded 1.5°C (n = 28).

Assuming the same heat loss from our canvas and wood bucket samples in the first minute as for the respective simulations with a 4 m s^{-1} ship speed, I would have expected average rubber-canvas and rubber-wood bucket differences of ∼0.1 and ∼0.05°C, respectively. However, given the different bucket diameter-to-height ratios of the modelled buckets to those used, it is not clear that the heat loss from our samples would have actually been similar for the same exposure conditions and sample volumes. Further, our canvas bucket did not have a lid, in contrast to that modelled by Folland (1991) and FP95. Thus I cannot directly assess the accuracy of the FP95 bucket models using my experimental results. However, the models do

make use of some poorly tested and uncertain assumptions on which it is appropriate to comment. For instance, the canvas bucket samples are assumed to be well mixed and at the same temperature as the bucket walls, implying the sample was actively stirred by the observer. Whether this was actually generally the case is not known. In the absence of stirring we would expect sample heat loss to be strongest near the walls, with a temperature gradient across them. Further, FP95 assume wooden buckets were filled to near the brim and so the water surface fairly exposed to the airflow. However, in my practical experience it is difficult to fill buckets of this type more than two-thirds full.

The results suggest that large-volume samples ($\geq$5 L) in wood and canvas buckets do not change temperature appreciably in the first minute after collection. This conclusion is of most direct relevance to wood and canvas bucket temperatures obtained underway aboard sailing vessels in the 19^{th} and early 20^{th} century, for which exposure times could have been short (1.5 min or less; e.g. 30 s hauling period, 1 min on-deck period), although this is uncertain.

3.2.2 Vertical near-surface temperature gradients

Given that our bucket temperatures appear accurate, they can be used together with subsurface temperatures from the TSG and CTD casts to reveal near-surface temperature gradients within the depth range of VOS intakes. Here I restrict discussion to vertical gradients within the coverage of the bucket measurements ($\sim$17.5°S to $\sim$3°N). Strong vertical gradients were consistently observed day and night throughout this portion of the transect (Fig. 3.5, Table 3.1), with the temperature difference between 3 and 0 m averaging -0.4 ± 0.2°C (temperature decline with depth). Temperature gradients were weaker at nighttime than in daytime, respectively averaging -0.10°C m^{-1} and -0.16°C m^{-1} across the upper 3 m, with the corresponding average 3 m–0 m differences being -0.3 ± 0.1°C and -0.5 ± 0.2°C. Evidently the near-surface thermocline did not breakdown overnight, in contrast to the observed behaviour in the western equatorial Pacific (Soloviev and Lukas, 2006). Differences across the upper 3 m were found to be strongest in early to mid-afternoon (around 12:00–15:00 LT) and weakest overnight from 19:00–07:00 LT (Fig. 3.6). This is a consequence of the diurnal temperature cycles being of larger amplitude at the surface than at 3 m. Diurnal air temperature cycles were larger still due to the lower specific heat capacity of air. Diurnal ranges in composite bucket SST were particularly large in the weak

and moderate branches of the South Equatorial Current (SEC) averaging 0.9 ± 0.3°C and somewhat reduced in its strong branch averaging 0.6 ± 0.1°C. The corresponding average diurnal ranges in 3 m TSG temperatures were 0.5 ± 0.2°C and 0.3 ± 0.1°C.

Thermoclines were found across the upper 5–15 m in all CTD casts (Fig. 3.7). Temperature differences and gradients over the upper 5m respectively averaged -0.8 ± 0.2°C and -0.15°C m^{-1} during morning casts, excluding casts 11–13 (for which the temporally-closest bucket temperatures could not be considered near-contemporaneous with the deeper measurements). Gradients between 5 and 10 m were generally weak, with temperature differences averaging -0.08 ± 0.08°C over morning casts, although several differences around -0.1 to -0.3°C were found. Temperature declines between 10 and 15 m ranged from 0.00–0.03°C across morning casts. The only afternoon cast with a corresponding composite bucket temperature, CTD-1, recorded temperatures 1.3 °C colder at 10 m than at the surface, with the coincident gradient across the upper 5 m being -0.24°C m^{-1}. The 10 m temperature difference is likely slightly overestimated by $\sim$0.1–0.2°C due to mismatch in timing of the bucket measurements and CTD cast (the CTD cast was conducted around 15:30 LT while the bucket temperatures were obtained at 14:00 LT). Temperature differences between 5 and 10 m, and 10 and 15 m were -0.11 and -0.07°C, respectively. The apparent temperature difference over the upper 3 m was -0.9°C, close to the largest observed, which was around -1°C. Strong vertical temperature gradients in the upper 10 m are thought ubiquitous under weak winds and strong insolation. Temperature contrasts of up to several °C have been found across the upper few meters in the tropical Pacific and Gulf of California (e.g Webster et al., 1996; Donlon et al., 2002).

Interestingly the near-surface thermocline persisted when 10 m wind speeds exceeded 6 m s^{-1} (Fig. 3.8a), both day and night, in contrast to conventional wisdom (Soloviev and Lukas, 2006; Donlon et al., 2012). Daytime upper 3 m temperature declines exceeding 0.7°C were, however, generally not encountered under these conditions. Note that where 10 m wind speeds exceeded 6 m s^{-1}, all remained below 10 m s^{-1} except in one case.

I find a slight negative correlation between ship speed and upper 3 m temperature difference (Fig. 3.8b), suggesting measured near-surface temperature gradients were slightly reduced at higher ship speeds. As a further test I compared average 3 m TSG temperatures for periods when the ship was hove to for scientific sampling with those for the 30 min periods immediately before and after. A mean difference of 0.0 ± 0.1°C was found suggesting ship motion did not strongly mix the near-surface.

3.2.3 Comparison with the Operational Sea Surface Temperature and Sea Ice Analysis (OSTIA)

Foundation temperatures from OSTIA are comparable to CTD temperature at 15 m (Fig. 3.5b). The $CTD_{15\,m}$-OSTIA temperature difference from all CTD casts averaged 0.0±0.2°C, smaller than the supplied OSTIA errors which ranged from ±0.3 to ±0.8°C. The OSTIA temperatures successfully capture daily average near-surface meridional gradients, although with only a limited number of CTD casts for comparison in the North Equatorial Current (NEC). A temperature dip observed in daily average composite bucket SST in the moderate branch of the South Equatorial Current is particularly pronounced in OSTIA, with temperatures dropping ∼0.8°C from the weak SEC regime. OSTIA temperatures were closest to daily average 3 m temperatures in the NECC outside the cold tongue but were still ∼0.2°C cooler. Evidently it would be inappropriate to substitute OSTIA foundation temperatures for daily average bucket SST.

3.2.4 Intake temperature errors and engine room warming

Where EIT have been found to average warmer than bucket temperatures, heating of intake seawater by warm engine room air has often been suggested as a potential cause (e.g. Saur, 1963). To test this idea I developed a physical model for warming of intake seawater by net heat transfer into the intake pipe across the pipe wall. The model is based on standard calculations from chemical engineering (McCabe et al., 2001). Fixed parameters were set so as to maximise computed warming. Pipe wall thickness was varied in tandem with outside diameter (o.d.) according to Table C.1, with the largest common wall thickness used for each standard outside diameter. Note that real engine intake pipes are of lower schedule than those modelled, with flow velocities standardised at 1–1.5 $m\,s^{-1}$. I use a lower limit flow velocity of 1 $m\,s^{-1}$ and an upper limit engine room air temperature of 50°C. The model is derived in Appendix C.

Calculated warming after a 20 m length of pipe (an upper limit for inlet-thermometer distance) with variable o.d. and inlet temperature is presented in Fig. C.3. Warming is enhanced with larger temperature contrast across the pipe wall (i.e. as inlet temperature is lowered). Calculated warming is minimal for all but the smallest o.d. pipes and largest temperature contrasts. Engine intakes on merchant vessels generally have outside diameters exceeding 20 cm (discussed in Appendix C), for which computed

warming was below 0.05°C. Thus heating of intake seawater by engine room air is unlikely a major cause of reported negative average bucket-intake temperature offsets of several tenths of a °C.

This was previously noted by James and Shank (1964) who found that given an 8-inch (∼20 cm) diameter pipe, a 2000 gallon min^{-1} (∼3.8 $\mathrm{m\,s}^{-1}$) flow rate and a 30°F (∼16.5°C) temperature contrast across the pipe wall, over 1000 ft (∼305 m) of pipe would be required for a 0.1°F (∼0.05°C) temperature rise. Modelling a standard 21.91 cm o.d. pipe with 20.63 cm inside diameter (schedule 20) and flow velocity of 3 $\mathrm{m\,s}^{-1}$ (a modern absolute maximum) with this temperature contrast, I find a 0.1°F temperature rise would require a pipe length ∼432 m. Pipe lengths necessary to achieve along-pipe warming of 0.2°C are plotted in Fig. C.4, again for a range of outside diameters and temperature contrasts. The minimum pipe length required is ∼92 m for o.d. above 20 cm and the longest ∼737 m. These are far greater than the inlet-thermometer distances reported in the literature (Table C.2). For instance, James and Fox (1972) found 73% of intake thermometers to be within 3 m of the inlet.

Other explanations for warm bias in intake temperatures include heating of thermometers by conduction along metal fittings (Saur, 1963) and gradual warming of stagnant intake seawater around pumps (Brooks, 1926) or in faucet pipes (Piip, 1974). Engine intake temperatures tend to be noisy, with random errors likely reflecting poor observing and recording practices. Poor quality is unsurprising given that these measurements were traditionally obtained by ships' engineers for engine monitoring purposes, where accuracy of 1–2°C is sufficient. Sailors are likely to report at most to the smallest graduation on the thermometer used, which appears often to have been 1°C or °F or more for intake thermometers. A preference for whole-number values was found in the dry bulb air temperatures where the thermometer was marked in 1°C increments. Further, intake thermometers have sometimes been noted as difficult to read, with unclear graduations and locations close to floor level (Brooks, 1926). They may be particularly prone to drift in the harsh engine room environment.

3.3 Conclusions and recommendations

Progress in the field of historical SST reconstruction has been hampered by neglect of near-surface dynamics, lack of comprehensive field comparisons between measurement methods, limited metadata and observations of variable quality. I find no evidence

for cold bias in wood or canvas bucket temperatures in the central tropical Pacific when measurement is rapid ($\sim$1 min) and the bucket samples of large volume ($\geq$5 L). My results suggest that susceptibility of bucket samples to heat loss or gain may be more dependent on their volume than bucket material. Thus I suggest volumetric capacity be the principal consideration in design of meteorological buckets. Additional field experiments should test whether the findings apply in other seasons and ENSO states and to historically used buckets of smaller volume and different type. Experiments should be conducted on vessels of different class and in other ocean regions. In particular, the accuracy of bucket temperatures from large modern merchant vessels should be evaluated, on which hauling times would be longer and apparent wind speeds stronger. Studies could initially target those regions and seasons where bucket cooling is predicted to be largest (e.g. the Gulf Stream in winter). Bucket experiments would benefit from continuous monitoring of the sample temperature during the measurement period. This could be achieved by attachment of a rugged digital thermometer and data logger to the bucket wall. This setup could also be used to measure the hauling time, of which there are few reports in the literature. Combined with estimates of response time for a range of fast and slow-response liquid-in-glass thermometers, the lower bound of possible exposure times could be better constrained. It could be assumed that mariners obtained a temperature reading as soon as the thermometer achieved approximate equilibration.

While the results of the bucket comparison are not directly comparable to the bucket models and adjustments of FP95, I question their derivation and use of long exposure times (4 min for wooden buckets). FP95 estimated exposure times for canvas buckets using their finding that seasonal SST cycles in the extratropics were generally of larger amplitude prior to 1942. Although not stated directly, their method effectively assumes that seasonal cycles of spatially co-located bucket and intake temperatures are the same in their 1951–1980 reference period. However, if seasonal cycles in the extratropics are, in fact, generally larger at the surface compared with, say, 5–10 m depth, then a portion of the larger amplitude cycles of pre-1942 years may be attributable to sampling being from a generally shallower depth (more bucket than intake observations). Characterisation of climatological seasonal temperature cycles at various upper surface and near-surface depths (e.g. using drifting and moored buoy data) would enable separation of such depth-related effects from other influences (e.g. bucket cooling). A complete explanation for the anomalous seasonal cycles pre-World War II (WWII) must be able to account for the spatial pattern of

the differences (e.g. the particularly enhanced amplitudes about the Gulf Stream and Kuroshio), which the bucket cooling theory can explain.

Field and lab experiments have typically found cooling rates of around 0.05–0.1°C min^{-1} for small-volume canvas buckets, although rates of 0.15°C min^{-1} or more are sometimes reported. A critical assumption in converting cooling rates to bucket adjustments is the time taken for a reading to be obtained post-sampling (i.e. the exposure time). As discussed in Appendix B, I suggest historical exposure periods for wood and canvas buckets were typically shorter than those derived by FP95 (1–2 min as opposed to 4–5) and thus that their corresponding bucket adjustments are too large (the largest in the central tropical Pacific being ∼0.7°C). However, the distribution of actual historical exposure times remains highly uncertain and so this suggestion only serves to widen the range of possible average exposure times. Even so, the long exposure times used by FP95 imply that mariners would have waited several minutes for thermometers to equilibrate before reading. I think this is unlikely, firstly since it is unclear how frequently observing instructions were actually relayed to observers and moreover, how often they were actually followed where they were. Time spent taking meteorological observations would be time away from higher priority tasks. Note that ships voluntarily obtain these observations.

While both bucket and intake temperatures can exhibit large systematic and random errors (e.g. Brooks, 1926, 1928; Roll, 1951b; Saur, 1963; Tauber, 1969; Tabata, 1978c,d; Kent and Challenor, 2006), I consider EITs a particularly unreliable measure of actual SST (as defined here) given the potential for large vertical near-surface temperature gradients. Intakes sample at variable and often unknown depth, at which the temperature may differ by a few tenths to several °C from that in the upper few centimeters. I found temperature declines of up to 1°C across the upper 3 m in the central tropical Pacific. The average upper 3 m temperature difference between 17.5°S and 3°N was −0.4±0.2°C, with differences of this order found to persist day and night, even when 10 m wind speeds exceeded 6 m s^{-1}. EIT generally cannot be corrected for such near-surface gradients, even where these are known, due to limited metadata on intake depth. While intake depths have been reported for some Voluntary Observing Ships since 1995, they remain unknown in many cases and must be assumed invariant even where they are reported (individual vessels are assigned a single intake depth whereas actual sampling depth varies with vessel loading).

The extent to which mechanical stirring by VOS ship propellers and motion acts to disturb near-surface gradients is unclear, as is its influence on measured bucket

and intake temperatures. The latter likely depends on sampling point, with the near-surface probably less disturbed away from the stern. Evidently findings of large negative average bucket-intake differences cannot reflect typical near-surface temperature gradients. Physical modelling suggests they are also not likely due to warming of intake seawater by engine room air (I estimate this to be hundredths rather than tenths of a °C). Thus we cannot assume that intake thermometers accurately measure the intake temperature and that warm bias is simply due to warming of the incoming seawater. EITs have been found to average systematically too warm on some ships by >0.5°C (e.g. Brooks, 1928; Tauber, 1969). I suggest that reliable correction of such errors is not possible since their cause is largely unknown and their general magnitude can only be indirectly estimated from signals in the data.

I propose a new, alternative approach to SST record construction in which the need for poorly field-tested adjustments is reduced through more restrictive data selection. Namely, I suggest exclusion of intake and other subsurface temperatures based on the potential for strong vertical near-surface temperature gradients. Removal of subsurface temperatures would suppress any artificial signals from variable measurement depth since the main remaining in situ methods (bucket and buoy) measure at a more consistent and historically invariant depth. It would also likely reduce the need for reliance on bucket adjustments to improve homogeneity, provided a new reference period climatology was also developed. Additional homogenisation could be achieved by identification and removal of bucket temperatures suspected to be in large error due to sample cooling (e.g. those collected using small-volume canvas buckets under strong winds and large sea-air temperature contrasts). Further field experiments would be required to determine environmental criteria for such exclusion. That bucket adjustments might still yield improvements in homogeneity in spite of the proposed approach has not been ruled out.

Note that I do not question that bucket and other adjustments can improve homogeneity in SST datasets and comparability with records derived from independent datasets, and do so with some skill (e.g. spatially). FP95 found that their bucket adjustments resolved an offset between global and hemispheric-average SST and Night Marine Air Temperature anomalies pre-WWII. Kennedy et al. (2011a) developed separate global and hemispheric SST records for 1945–2006 using bucket and intake measurements and found that adjustments improved consistency between them, particularly over 1945–1970. However, large uncertainty remains surrounding the accuracy of such adjustments. This is apparent from Gouretski et al. (2012) who com-

pared adjusted and unadjusted versions of the HadSST3 global-average SST record against a global-average record of near-surface temperature (0–20 m) derived using independent hydrographic observations. While application of bucket adjustments to HadSST3 reduced the offset between these records pre-WWII, notable discrepancies remained, the precise cause of which is unclear (the hydrographic observations were also adjusted). Post-WWII, global-average SST from HadSST3 shows similar trends to the hydrographic record with and without adjustments, suggesting the trends are robust.

Loss of spatial and temporal coverage due to exclusion of subsurface temperatures will require detailed consideration, but may not be as dramatic as it would first appear. Intake temperatures appear to have comprised only a small proportion of the SST measurements obtained pre-WWII. Post-WWII, bucket temperatures are thought to have comprised around 40–60% of global monthly SST observations until the introduction of moored and drifting buoys in the 1970s (Kennedy et al., 2011a). Note that around 2.5–15% or more of monthly observations were of unknown method during this period and that undoubtedly some portion of the measurements assumed to be by bucket will have come from intakes. Improved metadata will thus be required to more completely identify subsurface measurements for exclusion. I suggest historical meteorological data recovery initiatives (e.g. Wilkinson et al., 2011) target digitisation of bucket temperatures over intake temperatures from unknown or poorly-known depth.

Subsurface VOS temperatures can contribute to knowledge of diurnal and seasonal near-surface hydrodynamics where accurate and of known sampling depth. Thermometers used for bucket and intake measurements should ideally be calibrated before every cruise and measure to precision of at least 0.01°C. There is an urgent need to improve the general quality of VOS SST data since they are used for a wide variety of scientific purposes (not just for producing global-mean SST records, for which random errors are less critical). In addition, reprogramming of Argo floats to measure temperature and salinity every meter in the upper 20 m would improve coverage of near-surface variability, particularly beyond the shipping lanes to which VOS are largely restricted. Synthesis of near-surface hydrodynamics from existing floats measuring at least two temperatures and salinities within the upper 10 m should also be conducted. Further data could be obtained by mounting additional thermometers on moored buoys in the upper 30 m.

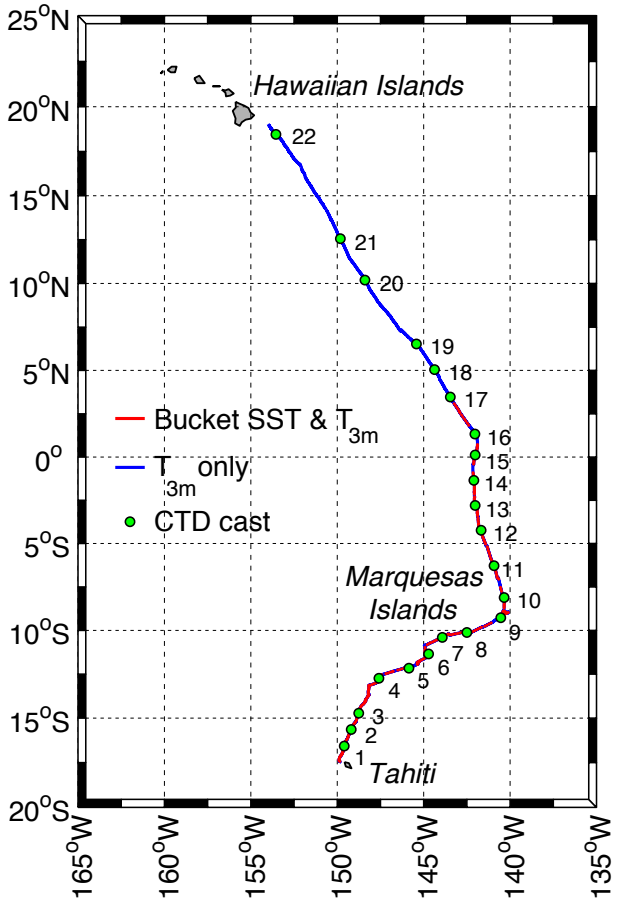

Figure 3.1: Map of the cruise transect across the central tropical Pacific. The red line denotes the portion of the transect where both bucket and 3 m thermosalinograph temperatures ($T_{3\,m}$) were observed. The blue line denotes the portion of the transect where bucket measurements were not taken. Locations of CTD casts are marked by green dots.

Figure 3.2: From left to right, the wood, canvas and rubber buckets used in the field comparison. Note that the wooden bucket was sealed with white caulk along the inner seams and reinforced around the outside by two stainless steel bands. The rubber bucket is of both plastic and rubber construction, with a black rubber protective layer around the base.

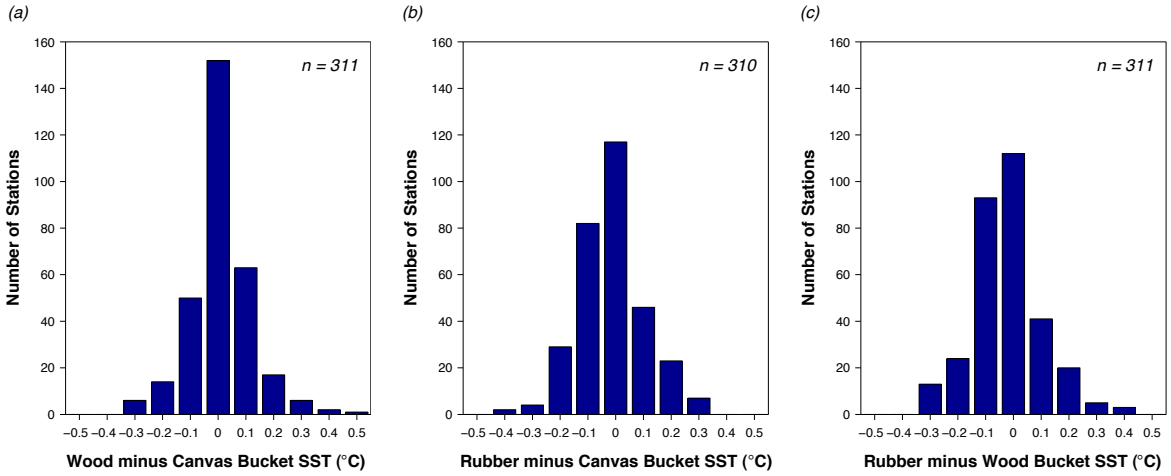

Figure 3.3: Histograms of differences between near-simultaneous sea surface temperatures obtained with **(a)** wood and canvas buckets, **(b)** rubber and canvas buckets and **(c)** rubber and wood buckets. A single value of 0.7°C is not shown in **(b)**, hence this subplot has one fewer total number of stations than **(a)** and **(c)**.

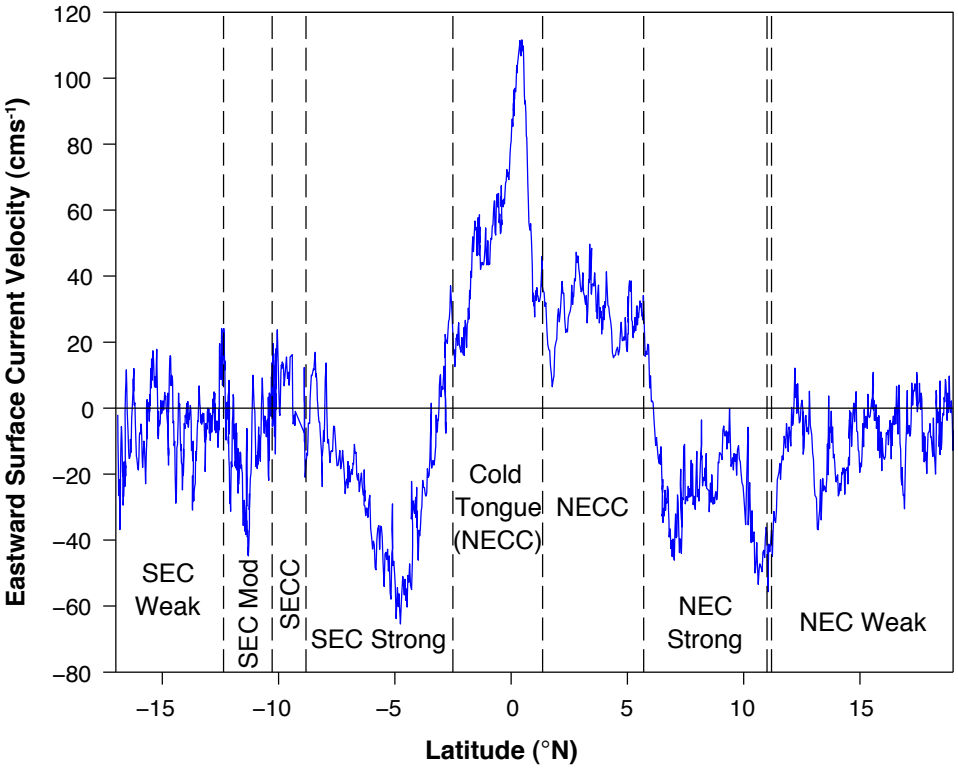

Figure 3.4: Eastward 19 m current velocity along the cruise transect between ∼17.5°S and 19°N as measured by acoustic Doppler current profiler. Dashed lines and associated text labels indicate current regimes identified in Table 3.1. "Mod" means moderate.

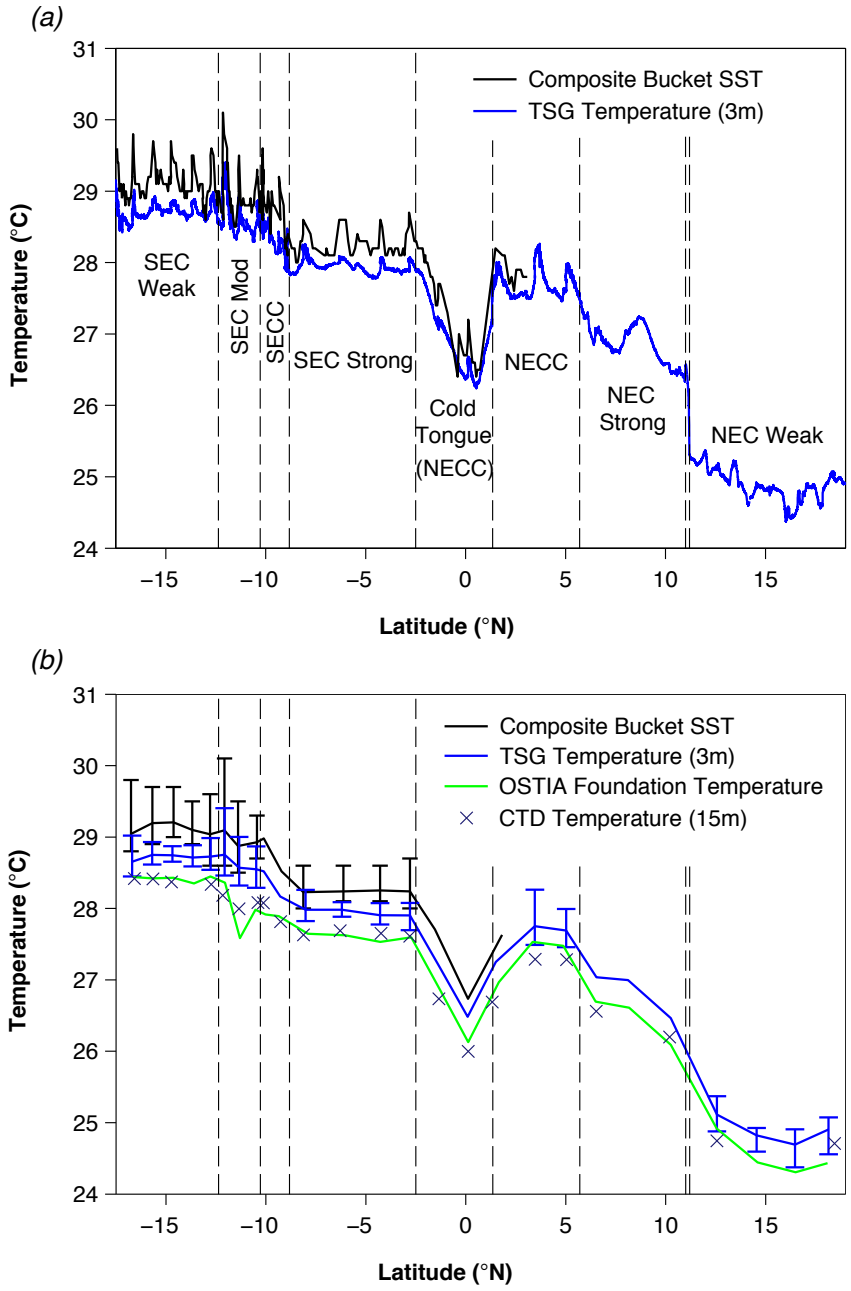

Figure 3.5: Meridional temperature structure of the upper surface and near-surface along the cruise transect: **(a)** composite bucket SST and 3 m thermosalinograph temperature, **(b)** daily average composite bucket SST, 3 m thermosalinograph temperature, OSTIA foundation temperature and 15 m CTD temperature. The maximum and minimum values of composite bucket SST and 3 m temperature on each local day are denoted by the upper and lower bars (not plotted in current regimes with strong meridional temperature gradients). Currents regimes are demarcated as in Fig. 3.4.

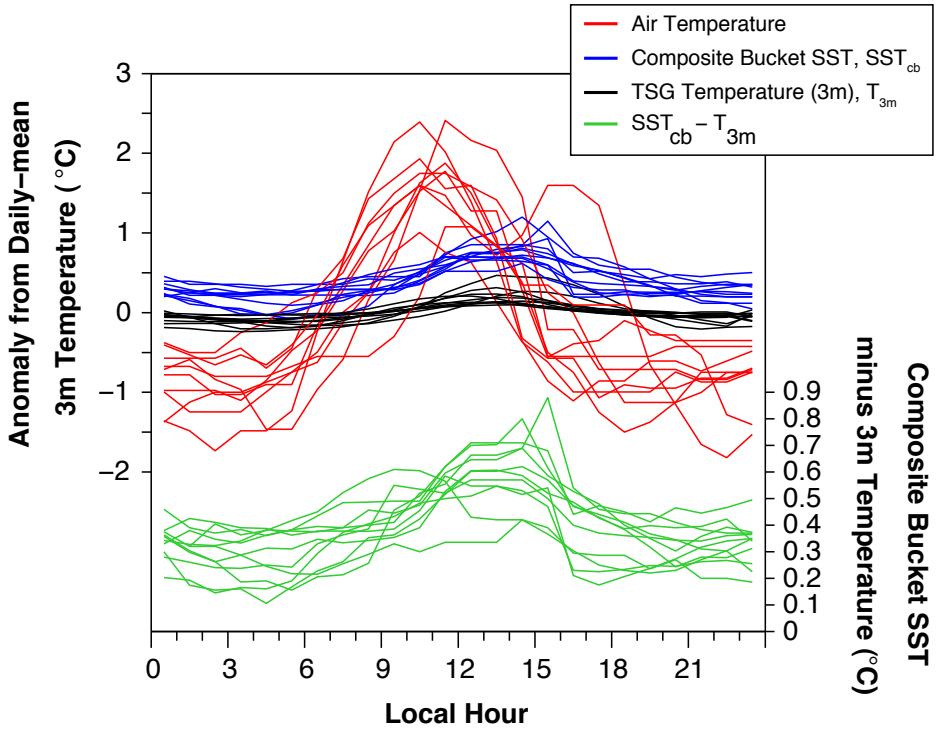

Figure 3.6: Diurnal temperature cycles within the weak, moderate and strong branches of the South Equatorial Current from three-hour moving averages. Air temperature, composite bucket SST and 3 m thermosalinograph temperature are plotted on the left-hand axis and expressed as anomalies from daily mean 3 m temperature for the respective local day. Temperature difference across the upper 3 m is plotted on the right-hand axis.

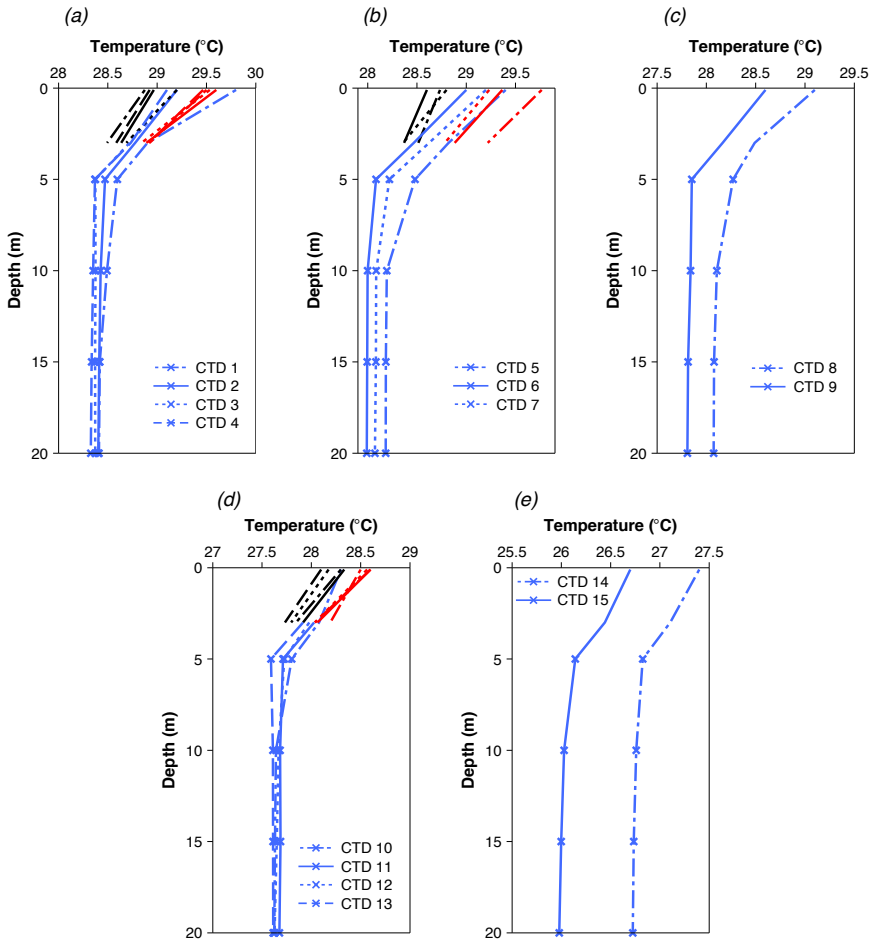

Figure 3.7: Temperature structure of the upper 20 m in various current regimes along the cruise transect: **(a)** the weak and **(b)** moderate branches of the South Equatorial Current (SEC), **(c)** the South Equatorial Countercurrent (SECC), **(d)** the strong branch of the SEC and **(e)** the equatorial cold tongue. The blue lines are temperature profiles corresponding to individual CTD casts. Temperatures at 5, 10, 15 and 20 m are from CTD (indicated by the crosses) while those at 0.1 and 3 m are from composite bucket SST and thermosalinograph, respectively. The bucket measurements were obtained within 2 h and 15 km of each respective CTD cast. Bucket temperatures are not plotted for casts 11–13 since they are unlikely to be representative of conditions at the time of the respective CTD cast (they were obtained at 12:00 or 13:00 LT whereas the CTD casts were conducted between 10:00 and 11:00 LT). The remaining bucket temperatures will be in error by ∼0.1°C or less due to such timing differences. All casts were taken between 09:00 and 12:00 LT, except CTD-1 which was taken around 15:30–16:00 LT. Cast numbers correspond to those on Fig. 3.1. The red and black lines characterise the daily extremes of the upper 3 m temperature profile on the local day of the corresponding CTD cast. They are respectively defined from maximum and minimum 3-hourly average 3 m temperatures, and corresponding 3-hourly average composite bucket temperatures. They are not plotted in the panels for the SECC and cold tongue, where diurnal cycles were masked by transit through strong meridional gradients.

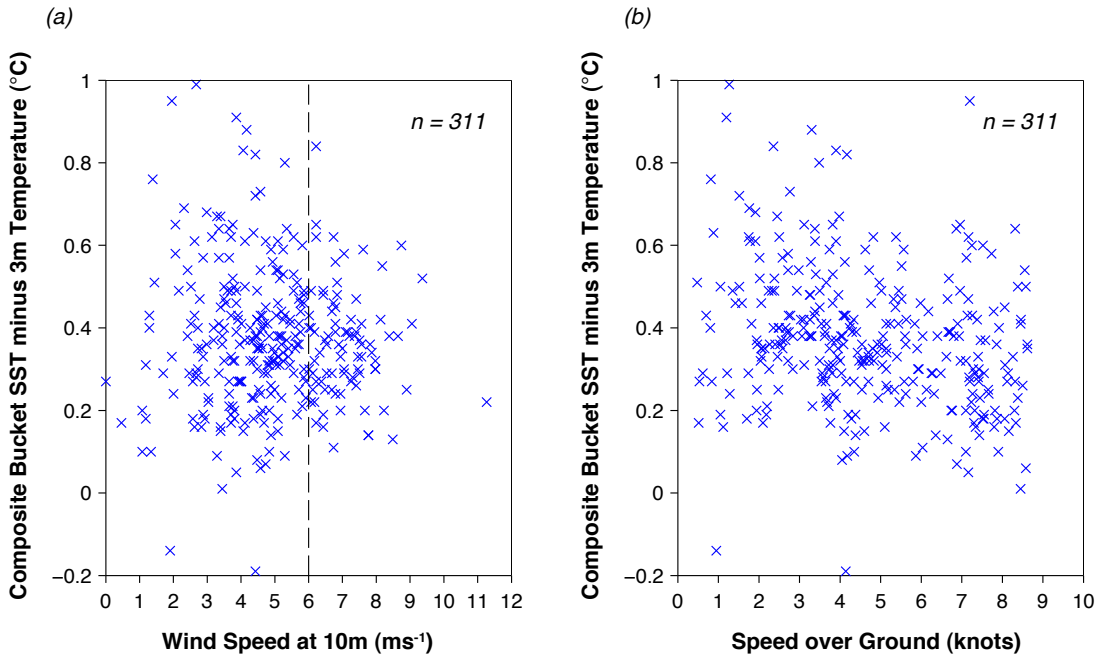

Figure 3.8: Scatter plots comparing upper 3 m temperature differences with **(a)** true wind speed at 10 m and **(b)** speed over ground of the *Seamans*. A linear least squares regression for plot **(b)** yields a sizeable negative gradient of $-0.02°\mathrm{C\,kt^{-1}}$, although with $r^2 = 0.06$ ($p < 0.05$). The vertical dashed line on **(a)** denotes a wind speed of $6\,\mathrm{m\,s^{-1}}$. General thinking holds that the near-surface should be near-isothermal at higher wind speeds.

Chapter 4

Upper and lower sea surface temperature climatologies

Sea surface temperature climatologies are used for a wide variety of purposes, including derivation of climatologies for ocean CO_2 parameters (e.g. pCO_{2sw}, TA) and as baselines for computing anomalies in historical SST records. SST climatologies differ in terms of the input data and construction methods used (e.g. gridding procedure, grid resolution). Some are derived from in situ data alone (e.g. World Ocean Atlas 2009, WOA09; Locarnini et al., 2010), while others use only satellite data (e.g. the Hamburg Ocean Atmosphere Parameters and Fluxes from Satellite Data SST) or a combination of both (e.g. the National Oceanic and Atmospheric Administration Optimum Interpolation SST v2, OISSTv2; Reynolds et al., 2002). In the previous chapter I questioned the accuracy of engine intake temperatures, which have often been found to read warmer than bucket readings (Kennedy et al., 2011a; Appendix B). I also suggested that there may be differences in the amplitude of seasonal temperature cycles between the depths sampled by buckets and those of intakes. Here I assess these ideas by generating three different SST climatologies using in situ measurements from different depth ranges. One climatology (referred to as Mixed Layer SST, MLSST) uses all observations from above 30 m (except those from moored buoys), another uses only temperatures from the upper 2 m (referred to as Upper SST, USST) and the third uses temperatures from beneath 2 m and above 30 m (referred to as Lower SST, LSST). These climatologies are compared against each other and to WOA09 SST and OISSTv2.

4.1 Method

The MLSST, USST and LSST climatologies were derived using in situ data for the 30-year period 1976-2005, obtained from release 2.5 of the International Comprehensive Ocean-Atmosphere Data Set (ICOADS R2.5; Woodruff et al., 2011). ICOADS R2.5 contains SST observations from buckets, intakes, through-hull and hull-contact sensors and trailing thermistors. The dataset also incorporates hydrographic observations from World Ocean Database 2005 (WOD05), a compilation of temperatures from reversing thermometers, mechanical and expendable bathythermographs, Conductivity-Temperature-Depth (CTD) meters, moored and drifting buoys and profiling floats (Johnson et al., 2009). An updated version of WOD05 was used to derive the WOA09 SST climatology.

ICOADS metadata were used to separate temperatures likely to be from the upper 2 m (USST measurements) from those likely to have been obtained at depths of 2–30 m (LSST measurements). Measurement method metadata from the World Meteorological Organization (WMO) Publication No. 47 that has been merged with ICOADS was used in this process. Unless the measurement depth indicated otherwise, observations identified as being from buckets, drifting buoys and trailing thermistors were assumed to be from the upper 2 m. Temperatures from moored buoys were excluded from USST since they are not assigned a measurement depth in ICOADS. Measurements listed as being from coastal or remote-sensing platforms were excluded from all climatologies (i.e. observations stated to be from the following platforms: coastal station, aircraft, satellite or other coastal/island station). Where there was disagreement between the measurement method given by the ICOADS SST method indicator field (SI) and the equivalent WMO Pub. 47 field (SIM), the temperature was assumed to be from the uppermost 2 m only if one field specified an upper SST method while the other listed the method as "unknown" or "other", or if both fields indicated an upper SST method. At this stage, temperatures not identified as USST measurements that were not from a coastal, remote-sensing platform or radiation thermometer, or noted to be from a depth >30 m were assumed to be LSST measurements. These included observations from intakes, hull-contact and through-hull sensors and moored buoys. Measurements were identified as being from a certain method where one or both of the SI and SIM fields indicated that method or one field indicated a particular method while the other listed the method as "unknown" or "other". Measurements stated to be from drifting buoys by the platform indicator were taken to be so, without

reference to SI or SIM. Moored buoy LSST measurements are included under "other subsurface" measurements in Table 4.1.

Temperatures from coastal waters (taken to be waters shallower than 200 m) were excluded, as were temperatures obtained during El Niño months (listed in Appendix D) in the equatorial Pacific (10°N-10°S) for consistency with the Takahashi et al. (2009) pCO_{2sw} climatology. Duplicate records (i.e. those assigned a 'duplication status' indicator value >2) were removed, as were those from deck 732, for which some observations are known to be incorrectly located (Kennedy et al., 2011a). Other suspect ship positions were identified using QC indicator 20 (those flagged as 2, 3, 4, 6, 7, or 9) and removed.

For the purpose of temperature measurement quality control, values falling outside $\pm 4.5\sigma$ from the mean across all values for a given latitude band were discarded, as were those >35°C and <-2°C (the freezing point of seawater is -1.8°C). In addition, for grid cells with at least 50 observations in a given month, values falling outside $\pm 4.5\sigma$ from the mean were excluded.

Only measurements likely to be of high precision were used to derive USST, while all measurements were used, regardless of precision, to generate MLSST and LSST. High precision measurements were taken to be those reportedly measured to tenths of a °C or °F or hundreths of a °C, those from hydrographic methods (hull-contact and through-hull sensors, moored and drifting buoys, reversing thermometers and trailing thermistors), and those reported to at least one decimal place.

No bias adjustments were applied to the data. Buckets in use since the 1970s have been insulated meteorological buckets, for which I assume sample cooling pre-measurement is small; although this requires field confirmation (as discussed in Chapter 3).

Observations were sorted onto the 1°x1° WOA09 grid. For grid cells containing at least 10 years of data with ≥10 observations for at least 7 months in each year, a linear trend was fit to the data and the data normalised to the year 2000 when this trend was significant ($p < 0.05$). The grid cell data were then compiled on to a composite year and monthly means calculated either by simple averaging or harmonic curve fitting. The latter was applied where the composite dataset contained ≥10 observations for 7 or more months, with no more than 2 consecutive months with <10 observations ('the 7 month condition'), and at least one of the following daily-resolved harmonic fits yielded an r^2 value of ≥0.4:

$$SST = a_0 + a_1 \sin\left(\frac{2\pi t}{365}\right) + a_2 \cos\left(\frac{2\pi t}{365}\right) \tag{4.1}$$

$$SST = a_0 + a_1 \sin\left(\frac{2\pi t}{365}\right) + a_2 \cos\left(\frac{2\pi t}{365}\right) + a_3 \sin\left(\frac{4\pi t}{365}\right) + a_4 \cos\left(\frac{4\pi t}{365}\right) \tag{4.2}$$

where t is Julian day. If so, the fit yielding the highest r^2 value was used and daily values from this fit averaged over to yield monthly means. Note that (4.2) was previously used by Lüger et al. (2004) to derive seasonal cycles from pCO_{2sw} and SST observations. Where simple averaging was instead applied, monthly means were not directly calculated for months with <10 observations. These missing means were estimated by linear interpolation where the aforementioned '7 month condition' held. Annual averages were calculated from the monthly means.

4.2 Results and discussion

4.2.1 Measurement coverage

The most noticeable consequence of using only in situ data is the lack of coverage in the Southern Ocean and Arctic (Fig. 4.1a). For USST, coverage is also poor in the equatorial Pacific, likely due to movement of drifting buoys away from the equator in association with upwelling. For LSST, coverage is particularly restricted in the southern hemisphere (Fig. 4.1c), with shipping lanes being clearly apparent in the south Pacific.

The majority of the USST observations are from drifting buoys (77.8%, Table 4.1), with most of the remainder being from buckets (21.6%). For LSST, 40.0% of the observations are from intake and 55.8% from a method listed as "other" or "unknown". For MLSST, the observations are split between drifting buoys (35.9%), "other"/"unknown" (29.4%), intakes (21.0%) and buckets (11.1%).

4.2.2 Annual mean distribution

Differences between the annual means for USST and the other climatologies are mostly within ±0.5°C (Fig. 4.2). Interestingly, the LSST temperatures are not found to be strongly warmer than those of USST, as would have been expected based on

Table 4.1: Percentage of observations from individual methods used to derive the upper, lower and mixed layer SST climatologies (USST, LSST and MLSST, respectively).

SST method	**USST**	**LSST**	**MLSST**
Bucket	21.60	0.00	11.1
Drifting buoy	77.78	0.00	35.93
Trailing thermistor	0.15	0.00	0.07
Other surface	0.44	0.00	0.24
Unknown surface	0.03	0.00	0.01
Intake	0.00	40.01	21.03
Hull contact	0.00	1.88	0.99
Through-hull	0.00	0.41	0.22
Reversing thermometer	0.00	1.90	1.00
Bathythermograph	0.00	0.03	0.01
Other subsurface	0.00	24.12	12.72
Unknown subsurface	0.00	31.64	16.67

reports of overly-warm intake readings. The mean$\pm\sigma M$ (standard error on the mean) difference between annual mean USST and LSST is -0.01$\pm$0.00°C. To investigate this further, I analysed the monthly mean USST-LSST differences for north of 30°N (Fig. 4.3). We find a seasonal cycle in the monthly mean differences, with a tendency for USST to have warmer monthly means than LSST in summer and cooler in winter. While several explanations can be envisaged for this, I suggest it is indicative of formation of near-surface thermoclines in summer against a year-round background of warm error in intake temperatures. In this case, intake warm errors only become apparent in winter once diurnal thermoclines have decayed. Annual mean USST has cooler temperatures than LSST in the Gulf Stream and warmer temperatures in the Greenland and Labrador currents (Fig. 4.2a).

Unlike for USST-LSST, a sizeable mean$\pm\sigma M$ difference is found between the annual means for USST and WOA09 (0.14$\pm$0.00°C, Fig. 4.2d). The spatial pattern of the differences is fairly complex, with the USST annual means being warmer by >0.5°C in the east and west Greenland currents and Labrador current, as well as in isolated pockets at 40-50°S in the Atlantic and Indian oceans. The average differences between annual mean USST, and MLSST and OISST are smaller at -0.06$\pm$0.00 and -0.03$\pm$0.00°C (Fig. 4.2c), respectively. From Fig. 4.2b we see that MLSST tends to be warmer by >0.3°C in the subtropical Atlantic and Kuroshio.

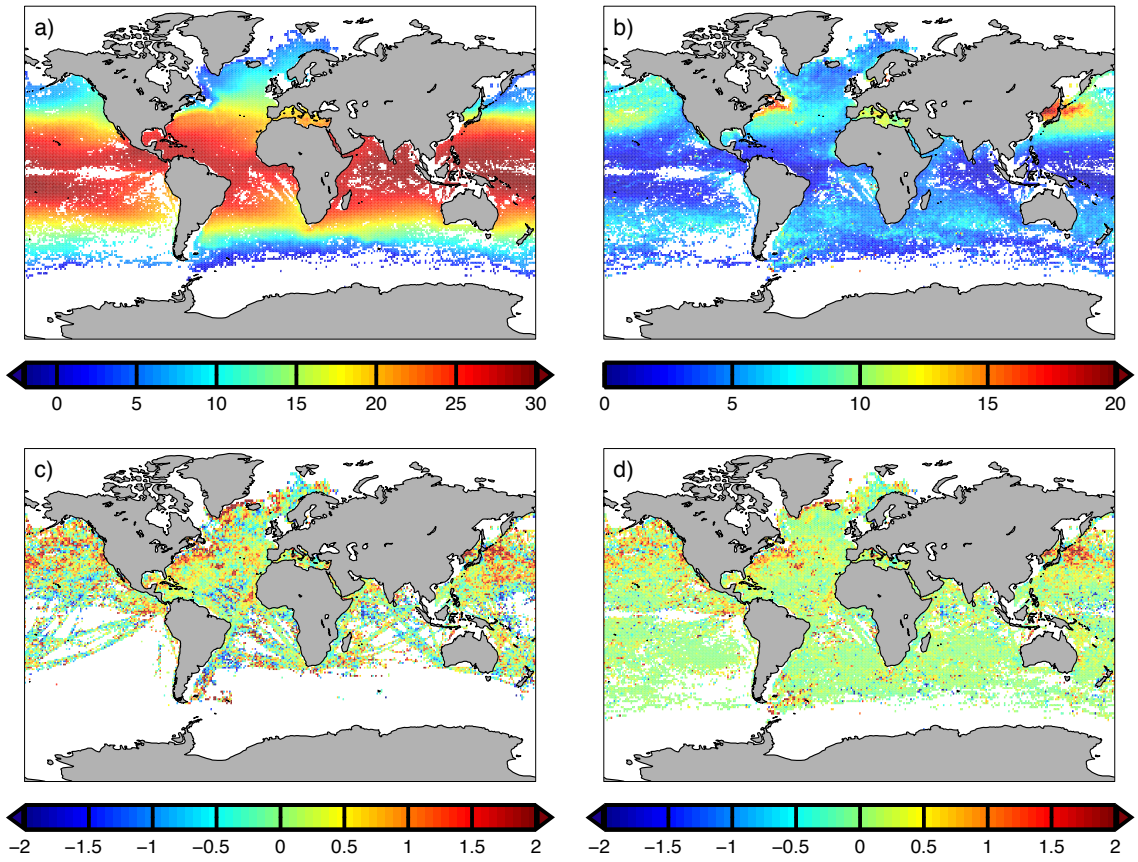

Figure 4.1: a) Annual mean USST (°C), b) USST annual range (°C), c) USST-LSST annual range difference (°C), d) USST-MLSST annual range difference (°C).

4.2.3 Seasonal range

As for previous SST climatologies, the seasonal range in USST is found to be small (<3°C) in the tropics and moderate (3-5°C) to large (>5°C) in the subtropics (Fig. 4.1b). The largest seasonal ranges are found for the Gulf Stream and Kuroshio (>10°C), where there is strong sensible and latent heat loss in winter due to interaction between warm surface waters and cold, dry continental air.

The USST climatology generally has larger SST annual ranges than LSST, OISST and WOA09 with little spatial uniformity in the differences (Figs. 4.1c and 4.4a,b). The histograms of the differences (Fig. 4.5a,c,d) have means$\pm\sigma M$ of 0.25±0.01, 0.52±0.01 and 0.48±0.01°C respectively. That the annual ranges for USST tends to be larger than those for LSST may be due to seasonal ranges tending to be larger in the upper 2 m than at greater depth. This effect may be aliased by warm error in

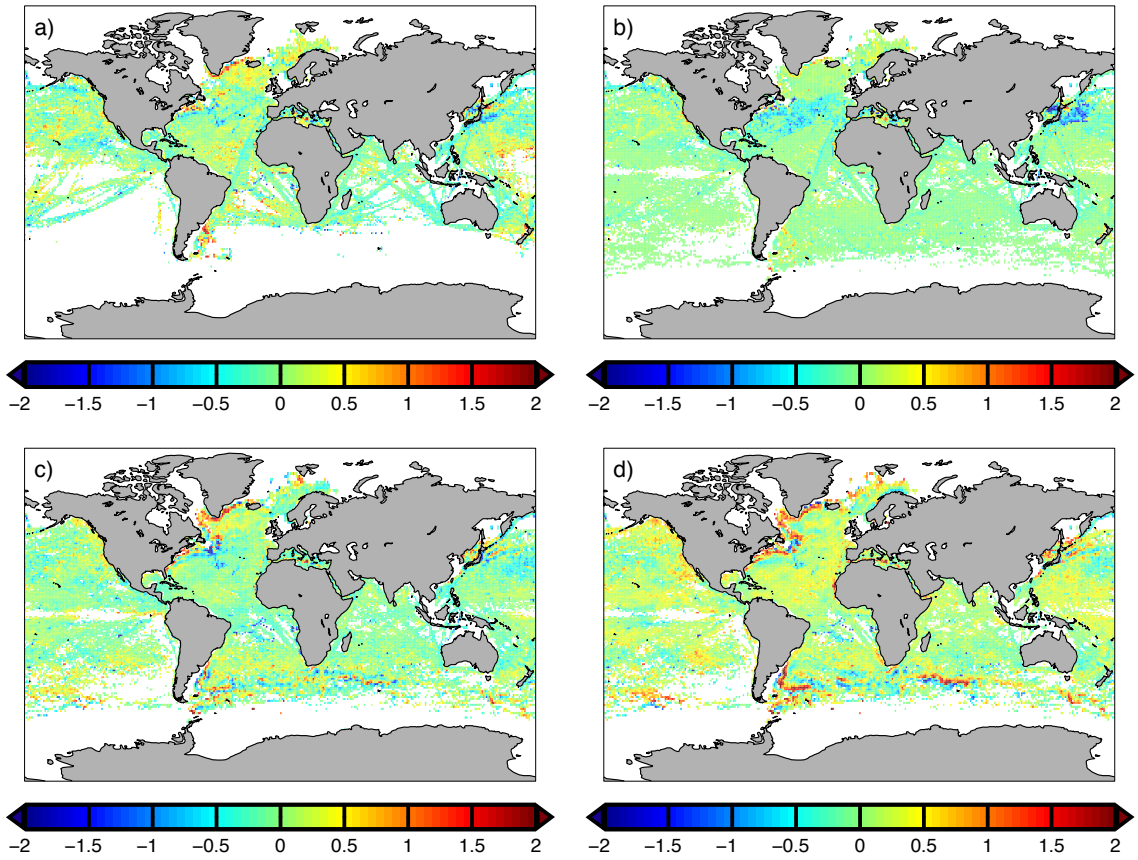

Figure 4.2: a) Annual mean differences (in °C): a) USST-LSST, b) USST-MLSST, c) USST-OISST, d) USST-WOA09.

intake temperatures, particularly if this varies seasonally. USST exhibits a stronger tendency towards larger seasonal ranges than LSST above 30°N than in the tropics (30°N to 30°S) (Fig. 4.1c), with mean seasonal range differences of 0.41±0.01 and 0.14±0.01°C, respectively.

The mean seasonal range difference is smaller between USST and MLSST than between USST and LSST, at 0.16±0.00°C (Figs. 4.1d and 4.5b), likely due to less independence between the input data (bucket and buoy measurements were used to derive both USST and MLSST, i.e. all USST input data were also used to derive MLSST). Note that the mean seasonal range differences between USST and OISST, and USST and WOA09 are much larger than that between USST and MLSST, suggesting a dominant role for dataset construction in causation of the first two differences. We would expect OISST and WOA09 to be similar to MLSST since these

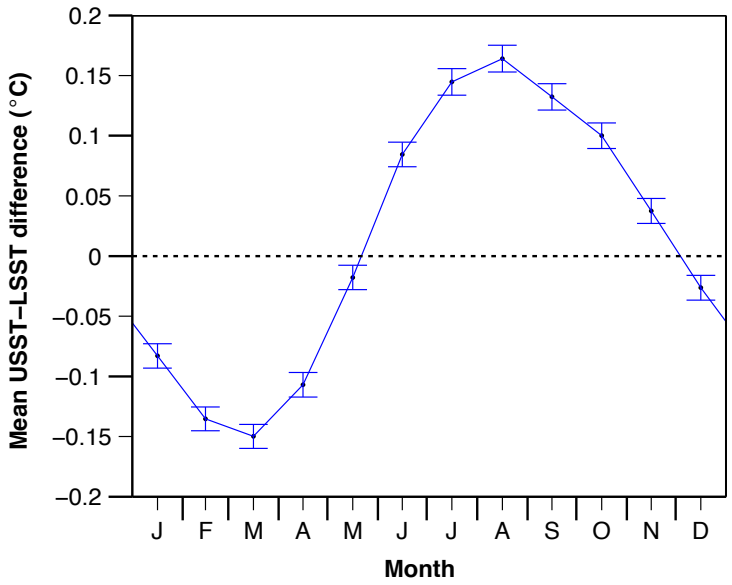

Figure 4.3: Average of the monthly differences between USST and LSST north of 30°N. The error bar is $\pm\sigma M$ (the standard error on the mean).

datasets are based on measurements from all depths, and thus that the differences from USST would be similar to the USST-MLSST difference. Interestingly, OISST and WOA09 exhibit large differences in seasonal range between each other in the Arctic (Fig. 4.4c), where there is poor in situ measurement coverage. The mean$\pm\sigma M$ OISST-WOA09 seasonal range difference is -0.17$\pm$0.00°C.

The spatial pattern of the seasonal range differences between USST, and OISST and WOA09 are similar (Fig. 4.4a,b), likely indicative of the differences between OISST and WOA09 generally being smaller than those between USST and OISST, and USST and WOA09. The seasonal range in USST tends to be larger at the northern limit of the Antarctic circumpolar current. Large range differences in percentage terms are also apparent in the central and western equatorial Pacific (Fig. 4.6c,d), although the magnitude of the ranges here are small. The percentage differences are small to moderate (within $\pm$20%) outside of these regions (Fig. 4.6).

4.3 Conclusions

Three new SST climatologies were constructed using input measurements from different depth ranges. In terms of annual means the climatology derived using measurements from the upper 2 m (USST) is not greatly warmer than the climatology

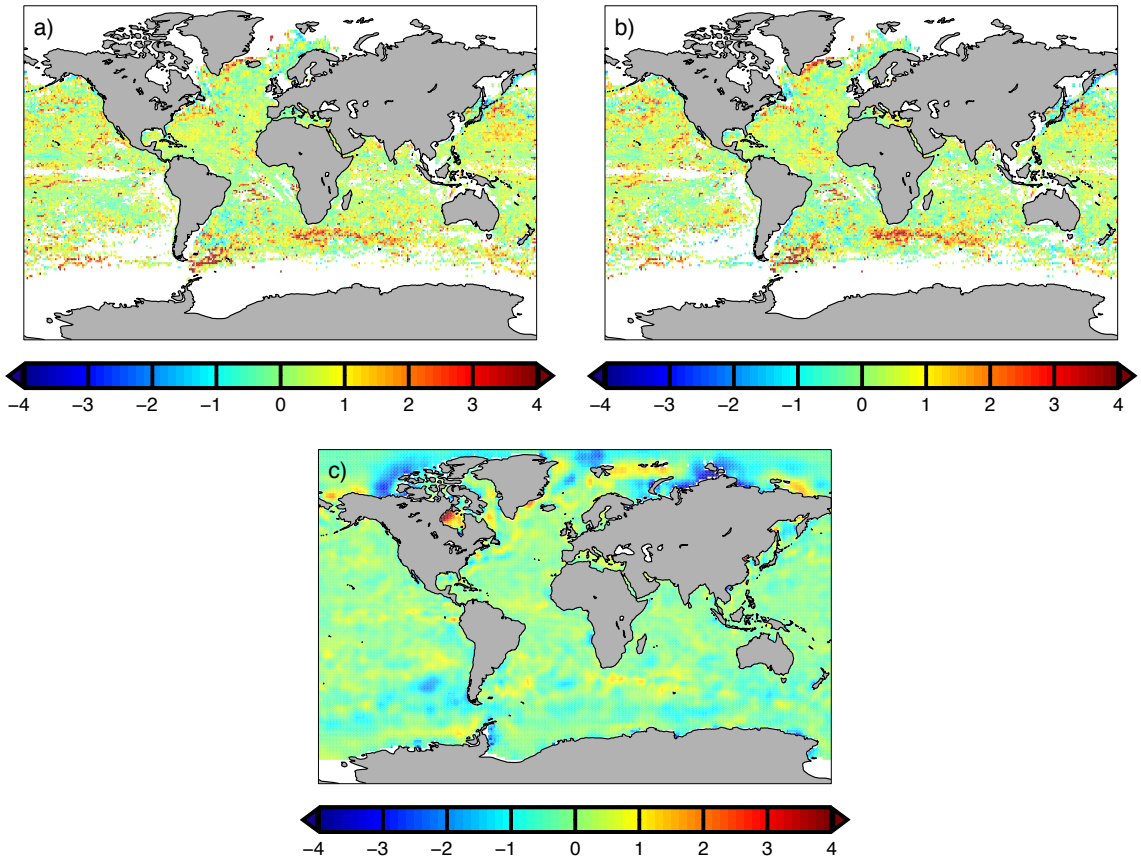

Figure 4.4: Annual range differences (in °C): a) USST-OISST, b) USST-WOA09, c) OISST-WOA09.

based on 2–30 m measurements (LSST). However, a clear seasonal cycle is apparent in the average of the USST-LSST monthly differences north of 30°N, with warmer temperatures in summer and cooler in winter. I suggest this is due to the presence of vertical near-surface temperature gradients in summer and to warm error in engine intake temperatures in winter. Future work should investigate the prevalence of near-surface thermoclines and errors in intake temperatures through new field measurements.

USST generally has larger seasonal ranges than LSST, suggesting that seasonal ranges tend to be larger in the uppermost 2 m than at greater depth. The seasonal ranges also tend to be larger than in OISST and WOA09, however, this is most likely due to differences in construction method rather than differences in the input measurements.

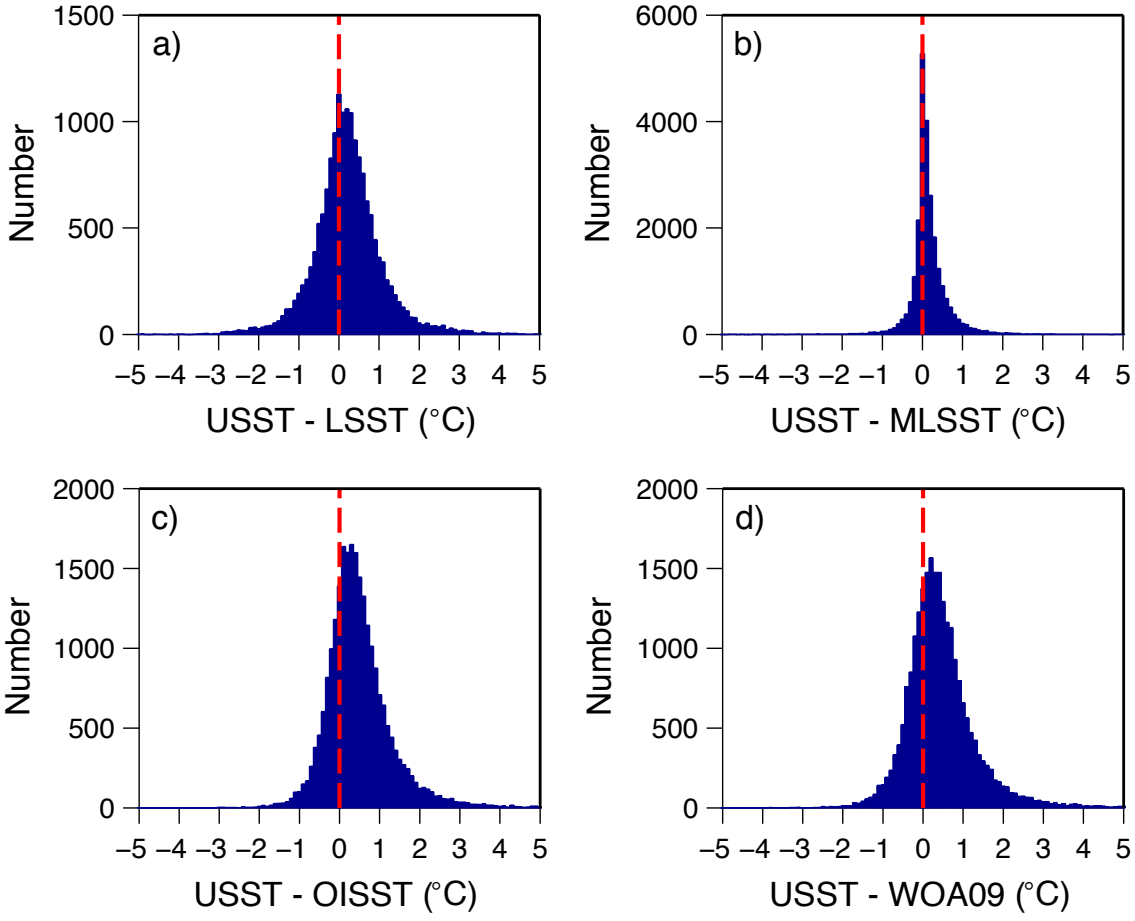

Figure 4.5: Histograms of annual range differences for USST minus: a) LSST, b) MLSST, c) OISST and d) WOA09.

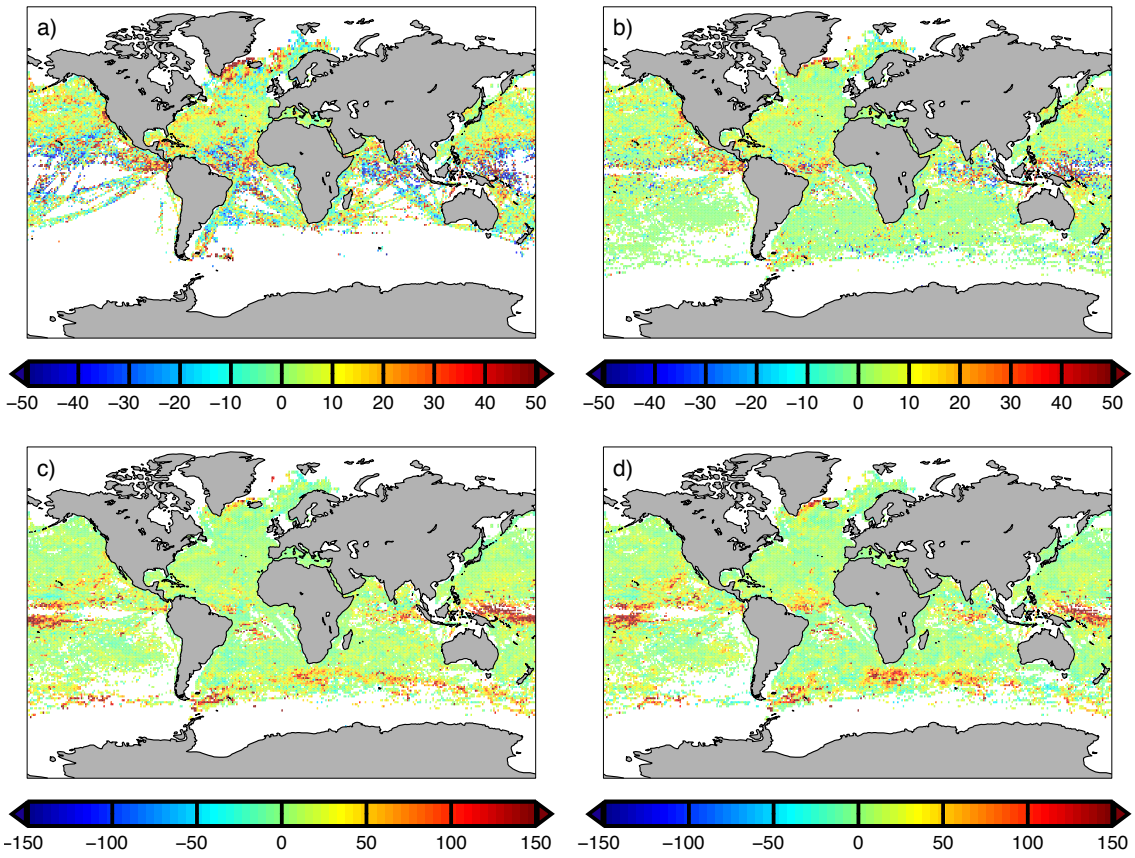

Figure 4.6: Annual range difference between USST and the other SST climatologies in percentage terms of the annual range for the comparison climatology (i.e. how much larger or smaller as a percentage is the annual range in USST compared to that in the comparison climatology): a) LSST, b) MLSST, c) OISST, d) WOA09.

Chapter 5

Total alkalinity climatology

Despite the observational synthesis efforts of GLODAP (GLobal Ocean Data Analysis Project; Key et al., 2004), CARINA (CARbon IN the Atlantic ocean; Key et al., 2010) and PACIFICA (PACIFic ocean Interior CArbon; Suzuki et al., 2013), insufficient measurements of total alkalinity are available to directly construct a global-scale seasonal climatology. Existing TA climatologies have been derived by relating better-observed parameters to TA and then deriving fields for TA from these relations. Both single and multi-parameter linear regression (e.g. Lee et al., 2006; referred to as L06) have been used, with the latter originally being suggested by Wallace (1995). Salinity is commonly used as a predictor since TA exhibits conservative behaviour, varying approximately linearly with salinity. As discussed in Chapter 2, TA is also influenced by non-conservative processes including formation and dissolution of calcium carbonate and nutrient uptake and release. Millero et al. (1998) developed separate fits for salinity normalised TA (sTA) in terms of temperature for various ocean regions and used these to produce a global-scale field for sTA, excluding the Arctic. Their salinity normalisation procedure has since been criticised as it does not allow for freshwater endmembers with non-zero TA (Friis et al., 2003; L06). L06 developed a gridded TA climatology by multilinear regression of GLODAP TA observations with temperature and salinity across five ocean regions. McNeil et al. (2007)(referred to as M07) developed TA relations in terms of salinity, nitrate and silicate for the Southern Ocean and used these to produce TA fields for four seasons. More recently, Velo et al. (2013) developed neural networks to estimate TA from other observed variables in GLODAP and CARINA, although they did not produce spatial fields for TA. Here, a new gridded monthly TA climatology is derived following the method of L06 and using data from GLODAP, CARINA and PACIFICA. It is thus referred to as the GCP TA

climatology, where GCP is not to be confused with the Global Carbon Project.

5.1 Method

5.1.1 Dataset construction

The GLODAP, CARINA and PACIFICA databases were obtained from cdiac.ornl.gov/oceans and combined into a single dataset, with replicate records identified and removed. Bottle measurements flagged as anything other than 2 or 6 (meaning "Acceptable" and "mean of replicates') and Conductivity-Temperature-Depth (CTD) measurements flagged as other than 2 were discarded. Bottle salinity was used where CTD salinity was missing.

TA was calculated from pH and DIC in CO2SYS (Lewis and Wallace, 1998) where excluded or not measured, with pH measurements first converted to in situ temperature from 25°C. Uncertainty on TA values calculated this way is at most $\sim \pm 8\,\mu\text{eq}\,\text{kg}^{-1}$. Climatological mean values from WOA09 were used in place of missing phosphate and silicate values. Where TA was not available and could not be calculated due to missing DIC and/or pH, calculated TA values from the original database were used if provided (calculation method unknown).

Only open ocean measurements from the upper 11 m were used to generate the TA climatology. Open ocean waters were taken to be those deeper than 200 m, defined using bottom depths from the NOAA 2-minute Gridded Global Relief Database (ETOPO2v2). To ensure independence for the comparison between the GCP TA climatology and climatological TA for carbonate chemistry time-series in Chapter 6, records from within 10 km of the nominal locations for ESTOC, HOT, K2, KNOT, Munida and OWSM were excluded. Observations obtained within 21 km of the BATS site were also not used.

Observations from each database were separated into unique combinations of cruise, station and cast numbers. Where there were multiple values for a given cast, these were first averaged by bottle and then averaged over the following depth ranges: $\geq$0 to <2, $\geq$2 to <4, $\geq$4 to <6, $\geq$6 to <9, and $\geq$9 to <11 m. The resulting depth layer averages were used to compute the TA relations. Data from 14 casts for cruise number 8 in CARINA (station numbers 1000000, 1000010, 1000020, 1000030, 1000040, 1000050, 1000060, 1000070, 1000080, 1000090, 1000100, 1000110, 1000120, 1000130; each station has a single cast) were found to be from inconsistent locations and times

and so were subdivided assuming they were actually from different casts.

5.1.2 Fitting procedure

The TA observations were partitioned into 9 regions and separate TA relations derived for each (Fig. 5.1a, Table 5.1). Individual tropical/subtropical regions were defined for the Atlantic, Indian and Pacific oceans (regions 1, 3 and 9), as opposed to the single tropical/subtropical region of L06. Various isohalines were used to define the poleward extents of these regions (see Fig. 5.1 caption), as opposed to use of the 20 °C isotherm by L06. The Southern Ocean is divided into a northern and southern region about the 2°C isotherm. Note that L06 derived a single regional fit for the entire Southern Ocean. The northern region is largely comprised of subantarctic and polar frontal zone waters and the southern of Antarctic zone waters. Unlike GLODAP and the Millero et al. (1998) and L06 climatologies, GCP TA incorporates the Nordic Seas, for which CARINA has enhanced observational coverage.

The TA observations were fit with relations of the following general form, following Lee et al. (2006):

$$TA = a_1 + a_2(SSS - 35) + a_3(SSS - 35)^2 + a_4(SST - 17.5) + a_5(SST - 17.5)^2 \tag{5.1}$$

An additional SSS-SST cross-term $a_6(SSS-35)(SST-17.5)$ was used for regions 2, 3, 7 and 8. Addition of a longitude term ($a_6(SST - 17.5)\,lon$, where lon is in °E) was found to be necessary to obtain a good fit for the north Pacific region (R4), as previously found by L06. The fits for all but the south Southern ocean region were forced to match constraints so as to avoid discontinuities across regional boundaries (Table 5.2). Constrained fits were derived using the fmincon function in Matlab and the unconstrained fit for R6 using the fminunc function. In both cases, the objective assigned these functions was to minimise the root mean square error (RMSE) between the observed and fit-derived TA values.

As an analysis tool, I calculate monthly anomalies in salinity normalised TA (sTA) to characterise non-salinity driven variation in TA:

$$\Delta sTA = \Delta TA - \frac{\partial TA}{\partial S}\Delta S \tag{5.2}$$

Similarly I define the anomaly parameter ΔTAs to characterise salinity-driven sea-

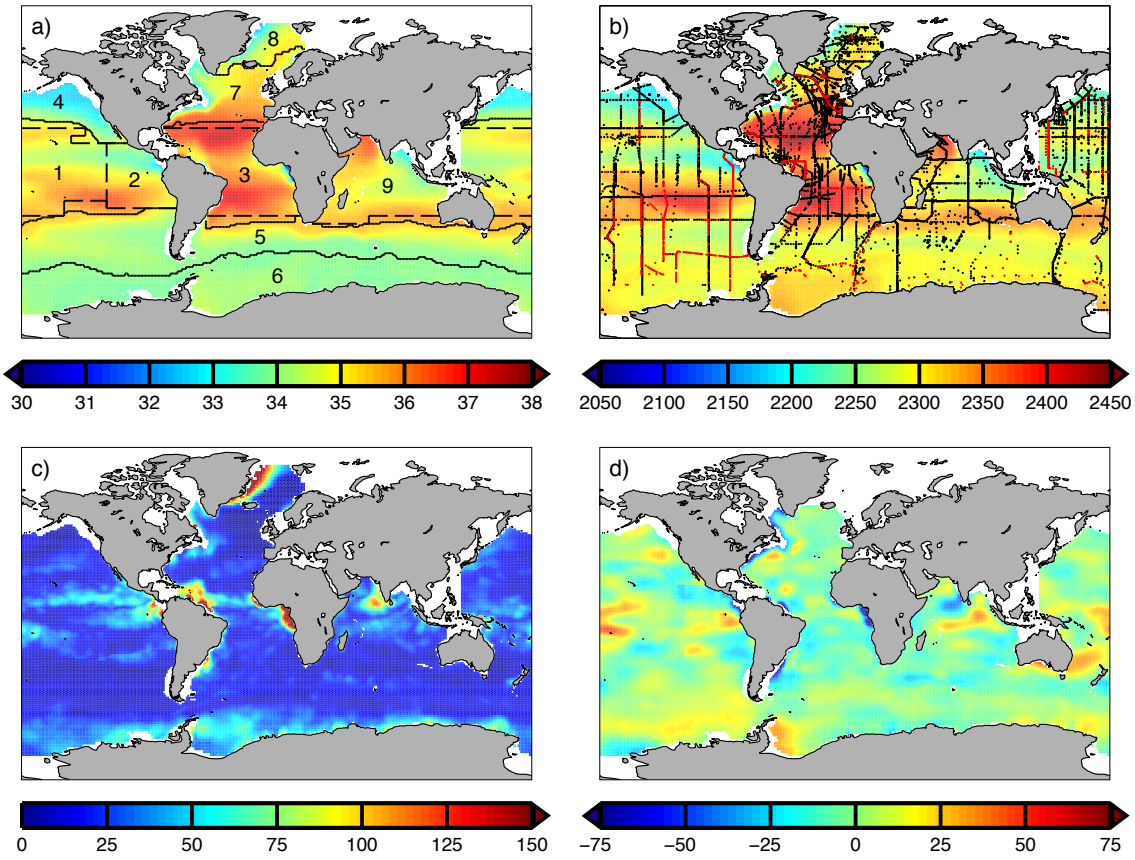

Figure 5.1: a) The nine regions with fits for the GCP TA climatology atop a background of WOA09 annual mean salinity (psu). The numbers correspond to those in Table 5.1. The regional boundaries (solid lines) are based on annual mean SST and SSS. The northern boundaries of regions 1, 3 and 5 are defined by the 34.5, 36.5 and 35.5 isohalines, respectively. The 7°C isotherm separates regions 7 and 8 and the 2°C isotherm separates regions 5 and 6. In the monthly climatology, these shift location from month-to-month as the corresponding isohalines and isotherms move. The dashed lines indicate the fixed, minimum extents of the tropical/subtropical regions. The corresponding isohalines are used to define the tropical/subtropical regional boundaries where they extend beyond the fixed boundaries. b) Locations of the input TA observations atop the annual mean GCP TA field (μeq kg^{-1}). Measured and calculated TA values are denoted by black and red dots, respectively. c) Annual range (maximum minus minimum monthly mean values) for GCP TA (μeq kg^{-1}). d) Difference between the annual mean fields for GCP and GLODAP TA (μeq kg^{-1}).

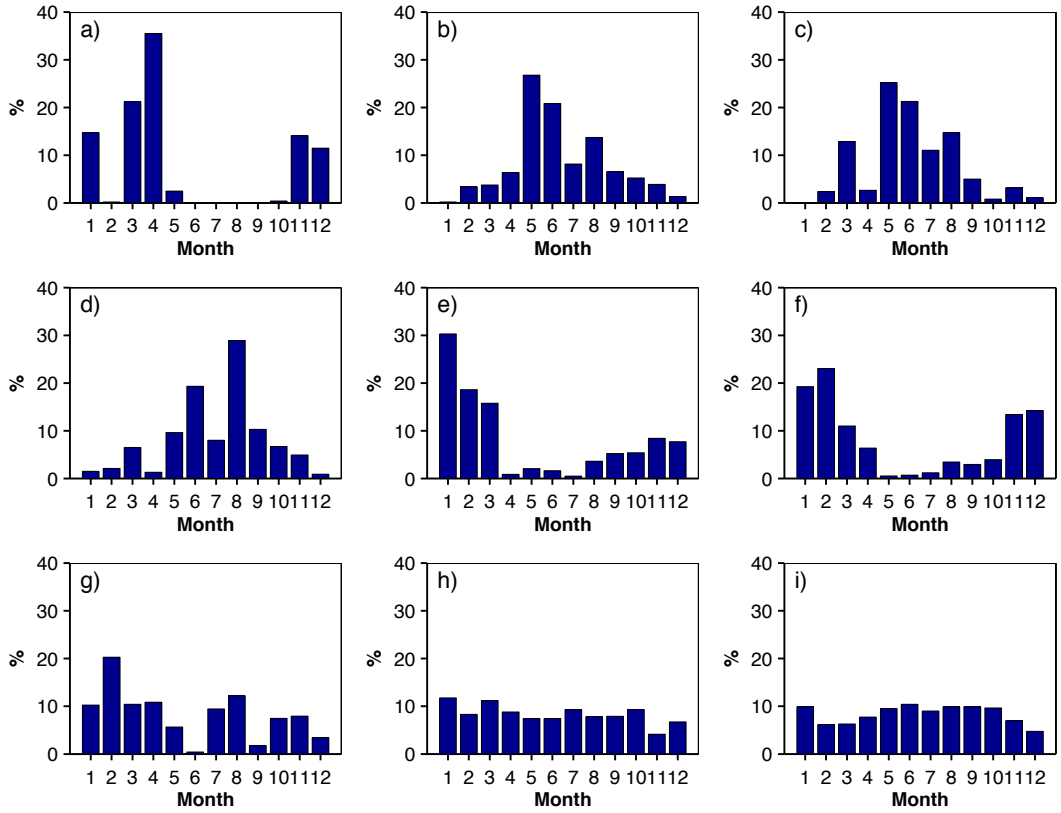

Figure 5.2: Histograms of the percentage of observations from each month for each GCP region: a) eastern equatorial Pacific, b) southern north Atlantic, c) northern north Atlantic, d) north Pacific, e) north Southern Ocean, f) south Southern Ocean, g) tropical Atlantic, h) tropical Indian, i) tropical Pacific.

sonal variability in TA, calculated as:

$$\Delta TAs = \frac{\partial TA}{\partial S}\Delta S \tag{5.3}$$

The partial derivatives $\frac{\partial TA}{\partial S}$ and $\frac{\partial TA}{\partial T}$ are calculated directly from the regional TA relations.

5.1.3 Measurement coverage

The seasonal distribution of observations varies greatly between the regions (Fig. 5.2). The tropical Indian and Pacific are fairly evenly sampled across all months, whereas there is aliasing towards austral summer and fall in the Southern Ocean regions, and

Table 5.1: TA fits for each region in terms of sea surface salinity (SSS) and temperature (SST). The valid SSS and SST ranges are given in the final two columns. RMSE is the root mean square error, n the number of observations.

Region	Location	Fit	RMSE	n	SSS range	SST range
1	tropical Pacific	$2299.0 + 67.61(SSS-35) + 0.97(SSS-35)^2 - 0.01(SST-17.5) + 0.01(SST-17.5)^2$	11.8	2190	33.4–36.7	13.5–31.0
2	eastern equatorial Pacific	$2300.9 + 75.41(SSS-35) - 0.46(SSS-35)^2 + 5.49(SST-17.5) - 0.59(SST-17.5)^2 - 1.45(SSS-35)(SST-17.5)$	8.3	524	31.5–36.6	18.0–30.5
3	tropical Atlantic	$2307.1 + 53.36(SSS-35) + 0.70(SSS-35)^2 + 0.46(SST-17.5) - 0.08(SST-17.5)^2 + 0.57(SSS-35)(SST-17.5)$	9.4	1717	26.2-37.6	16.0-29.9
4	north Pacific	$2279.8 + 28.43(SSS-35) - 0.37(SSS-35)^2 - 9.29(SST-17.5) + 0.05(SST-17.5)^2 + 0.05(SST-17.5)lon$	12.0	1000	32.3–34.5	0.5–29.5
5	north Southern Ocean	$2306.2 + 51.55(SSS-35) + 4.70(SSS-35)^2 0.23(SST-17.5) + 0.18(SST-17.5)^2$	9.6	1414	33.6–35.5	2.0–23.5
6	south Southern Ocean	$2307.4 + 104.28(SSS-35) + 16.36(SSS-35)^2 - 9.68(SST-17.5) - 0.28(SST-17.5)^2$	10.8	582	33.0–34.6	-1.9–2.0
7	southern north Atlantic	$2310.6 + 48.85(SSS-35) + 2.64(SSS-35)^2 - 0.14(SST-17.5) - 0.03(SST-17.5)^2 + 0.17(SSS-35)(SST-17.5)$	9.9	3006	32.0–36.5	-1.3–28.8
8	northern north Atlantic	$2293.7 + 102.91(SSS-35) - 5.05(SSS-35)^2 - 3.15(SST-17.5) - 0.17(SST-17.5)^2 + 4.48(SSS-35)(SST-17.5)$	10.2	381	30.1–35.2	-1.9–7.0
9	tropical Indian	$2302.3 + 58.27(SSS-35) + 2.95(SSS-35)^2 - 0.93(SST-17.5) - 0.00(SST-17.5)^2$	7.3	1012	32.2–37.0	14.3–32.2

towards boreal summer in the north Pacific. Seasonal coverage is restricted to boreal winter and spring in the eastern equatorial Pacific, while spring and summer are the best covered in the southern and northern north Atlantic.

In terms of spatial distribution, the subpolar north Atlantic, tropical/subtropical Atlantic, and western north Pacific have the densest coverage (Fig. 5.1b). Spatial coverage is particularly poor in the Indian ocean sector of the Southern Ocean and the Antarctic seasonal sea ice zone. Note that the Arctic, Indonesian and Bering Seas and Sea of Okhotsk have been excluded from the climatology.

5.1.4 The GCP TA Climatology

The TA relations for each region were used together with climatological SST and SSS fields to produce a 1°x1° gridded monthly TA climatology. The SST climatology was derived from NOAA Optimum Interpolation SST (OISST) v2 monthly means for the 30-year period from 1982-2011, with exclusion of temperatures from El Niño months in the equatorial Pacific (10°N-10°S) for consistency with the Takahashi et al. (2009) pCO_{2sw} climatology. The USST climatology was not used since this is uninterpolated

Table 5.2: Constraints for each regional fit. The constraint is the combination of SSS, SST and TA values (i.e. the equation is forced to yield the specified TA value for the respective combination of SSS and SST values). UC = unconstrained.

Region	Location	SSS	SST	TA
1	tropical Pacific	35.5	16.5	2333.1
2	eastern equatorial Pacific	35.1	27.0	2306.4
		35.5	16.5	2333.1
3	tropical Atlantic	35.5	16.5	2333.1
4	north Pacific	34.5	17.5	2265.5
5	north Southern Ocean	33.9	2.0	2295.0
6	south Southern Ocean	UC	UC	UC
7	southern north Atlantic	36.5	18.5	2389.9
8	northern north Atlantic	35.0	7.0	2308.6
9	tropical Indian	35.5	16.5	2333.1

and based solely on in situ data and thus has more limited spatial coverage that the interpolated OISST, which was derived using a combination of in situ and satellite data. Monthly climatological SSS from WOA09 was used for salinity.

Where the climatological SST and/or SSS values fell outside the specified ranges for the particular region (Table 5.1), the fit for a bounding region with valid ranges were used. A special case was for temperatures >2°C and salinities ≥33.4 psu and <35.5 psu for region 7 (R7), for which the fit for R5 was used. In addition, for salinities ≥33 and <33.6 psu and temperatures ≥-1.9 and <4°C for R5, the fit for R7 was used. In other cases, the grid cells were masked out (e.g. the low salinity waters of the northern Bay of Bengal).

5.1.5 Recreated L06 TA Climatology

The L06 climatology was reconstructed using the same SST and SSS climatologies as used to derive GCP TA. The intention was that any differences would be due to use of different fits and TA observations. Note that the original L06 climatology was constructed using the WOA09 SST climatology.

Following L06, where the monthly temperature for a grid cell was outside the regional range specified by L06, the relation for the nearest bounding region into which range fell was used. The boundaries of the L06 regions are demarcated in Fig. 5.3a.

5.2 Results and discussion

5.2.1 Annual mean distribution

The general global-scale pattern in annual mean TA is similar between GLODAP, GCP and L06 (Figs. 2.2d, 5.1b, 5.3b and 5.4a). The highest TA values are found in the Atlantic and Pacific subtropical gyres, the Arabian Sea and in a band north of the subtropical front in the Indian and Pacific. TA is relatively low in the northeast Pacific, increasing westward across the subarctic Pacific. Low values are also found in the equatorial Pacific, associated with fresher waters beneath the Intertropical Convergence Zone (ITCZ), and in the Bay of Bengal, where there is freshwater outflow from the Ganges/Brahmaputra river delta. The lowest TA values within the spatial coverage of the GCP climatology are found in the low-salinity waters of the Gulf of Guinea in the eastern equatorial Atlantic, into which the Niger river flows.

5.2.2 Comparison with previous climatologies

GLODAP

Comparison between GLODAP TA and annual mean GCP reveals a complex spatial pattern of differences, with large differences in certain locations, although most of the differences are within $\pm 15\,\mu\mathrm{eq\,kg^{-1}}$ (Fig. 5.1d). The largest discrepancies are likely due to use of different mapping procedures, with GLODAP TA being directly interpolated from TA observations by objective analysis. Sharp gradients in poorly-sampled regions are smoothed by this method. For instance, the low-salinity waters extending from the Gulf of Guinea have a more pronounced TA minimum in GCP than in GLODAP TA. Similarly, the low-salinity waters along the eastern seaboard of north and south America have lower TA by $>20\mu\mathrm{eq\,kg^{-1}}$ in GCP.

L06

The differences between annual mean GCP and L06 (Fig. 5.4a) are spatially more smoothly varying than those between GCP and GLODAP. With the exception of the subarctic Pacific and eastern tropical/subtropical Pacific, the differences are small (within $\pm 10\,\mu\mathrm{eq\,kg^{-1}}$). GCP has lower annual mean TA values by 20-45 $\mu\mathrm{eq\,kg^{-1}}$ in the subarctic Pacific, likely due to the improved data coverage for this region provided by PACIFICA. A pocket of higher annual mean values by 5-30 $\mu\mathrm{eq\,kg^{-1}}$ is apparent

to the west of Baja California; part of the north Pacific region in GCP and part of the tropical/subtropical region in L06. Observational coverage is poor in this region. The southern boundary of the eastern equatorial Pacific for L06 is also apparent from the differences. The annual means are similar within R2 for L06 (>90% of differences are within $\pm 5\,\mu\mathrm{eq\,kg^{-1}}$), but higher within the south Pacific subtropical gyre in GCP by 5-20 $\mu\mathrm{eq\,kg^{-1}}$. The eastern part of the latter region, where the largest deviations are found, is part of the eastern equatorial Pacific region in GCP, while the western section is part of the Pacific tropical/subtropical region. The whole region is part of the tropical/subtropical region in L06. This demonstrates the sensitivity of the TA relation method to the specification of regional boundaries, in spite of the use of constraints.

Compared to L06, the seasonal range for GCP is found to be smaller by 10-65 $\mu\mathrm{eq\,kg^{-1}}$ in the subarctic Pacific, outside the western subarctic gyre (Fig. 5.3d). Larger ranges by 5-25 $\mu\mathrm{eq\,kg^{-1}}$ are found in the southeast subtropical Pacific, in the Weddell Sea and along the Antarctic continental shelf. Again these discrepancies are likely due to specification of different boundaries, with the use of a separate relation for the south southern Ocean for GCP. Note that measurement coverage is poor in these regions, so additional measurements are required to determine which TA climatology is more accurate.

McNeil et al. (2007)

M07 developed TA fields for the Southern Ocean south of 40°S for four seasons (JJA, SON, DJF, MMA). The annual mean TA distributions are similar for GCP and M07, with a mean$\pm\sigma M$ (standard error on the mean) difference of $1.1\pm0.0\,\mu\mathrm{eq\,kg^{-1}}$ (Fig. 5.5a,b,e). Both climatologies suggest relatively high TA values in the Weddell Sea and to the north of the Ross Sea. The GCP climatology has higher annual means by 5-15 $\mu\mathrm{eq\,kg^{-1}}$ in a band across the Atlantic and Indian sectors of the Southern Ocean at 50-60°S. A band of lower annual means is found for GCP to the north of this at 40-50°S. The annual range is found to be larger for GCP by 10–45 $\mu\mathrm{eq\,kg^{-1}}$ in parts of the Antarctic seasonal sea ice zone (Fig. 5.5c,d,f).

5.2.3 Driving components of seasonality

In this section I separate GCP TA seasonality into salinity and non-salinity driven components, with the latter being related to temperature. The magnitude and sign of

the partial derivatives $\frac{\partial TA}{\partial S}$ and $\frac{\partial TA}{\partial T}$ are then analysed to investigate spatial patterns in the sensitivity of TA to salinity and non-salinity influences, and the direction of these influences.

Seasonal variations in TA are largely salinity-driven, with non-salinity driven seasonality being weak in most regions (Fig. 5.6a,b). For instance, TA seasonality is small to moderate within the subtropical gyres (annual range $<30\,\mu\mathrm{eq\,kg^{-1}}$, Figs. 5.1c and 5.3c), where salinity seasonality tends to be small. Large seasonal salinity-driven TA variations occur beneath the Intertropical and south Pacific convergence zones (ITCZ and SPCZ), in the western Pacific warm pool, and offshore of the Amazon/Orinoco and Congo/Niger river outflows. Salinity-driven seasonality is also large in the Arabian Sea, where there are monsoon-driven variations in rainfall and upwelling. TA is highest here during the southwest monsoon in boreal summer. At high latitudes, salinity and TA seasonality are large in the Greenland Sea, Labrador current and Antarctic seasonal sea ice zone (Fig. 5.4b).

Non-salinity driven (i.e. temperature-related) TA seasonality has a small ($<10\,\mu\mathrm{eq\,kg^{-1}}$) annual range throughout much of the open ocean. There is moderate sTA seasonality in the polar frontal zone (10-20 $\mu\mathrm{eq\,kg^{-1}}$ in annual range). The annual range in ΔsTA is also large in the Gulf of Alaska and parts of the eastern equatorial Pacific, with the latter perhaps due to seasonal variation in the strength of upwelling of TA-rich thermocline waters. Large sTA seasonality is also found in the cold, southward-flowing waters of the Oyashio current (10-35$\mu\mathrm{eq\,kg^{-1}}$ on the annual range) where there is large SST seasonality. Note that the large ΔsTA range found adjacent to Baja California is likely an artifact of seasonal changeover in the TA relation used for the region.

Interestingly, $\frac{\partial TA}{\partial T}$ is found to be positive in the Antarctic zone (Fig. 5.6d), whereas it is negative in the polar frontal zone to the north (where sTA seasonality is large). The former may reflect release of carbonate minerals (e.g. ikaite) in sea ice during spring melt (Dieckmann et al., 2008), such that a temperature increase is associated with a TA increase. However, perhaps contradicting this suggestion, $\frac{\partial TA}{\partial T}$ is negative in the western Greenland Sea. $\frac{\partial TA}{\partial T}$ is strongly positive in the eastern subarctic Pacific, where sTA seasonality is large. $\frac{\partial TA}{\partial T}$ is of small to moderate absolute magnitude in the north Atlantic and tropics outside the eastern equatorial Pacific, although of variable sign between basins.

$\frac{\partial TA}{\partial S}$ is positive everywhere but of quite variable magnitude (Fig. 5.6c). It is of moderate magnitude in the tropics and subtropics and Antarctic seasonal sea ice zone,

where the annual range in ΔTAs is high. Maxima are found in the Ross and Weddell seas. $\frac{\partial TA}{\partial S}$ is relatively small in the subarctic Pacific, north Atlantic and polar frontal zone, where salinity-driven seasonality tends to be small. Large ΔTAs seasonality occurs in the Greenland Sea and Labrador current despite low $\frac{\partial TA}{\partial S}$ values due to the large seasonal salinity variation.

5.3 Conclusions

The new TA climatology derived here suggests that TA seasonality is fairly small throughout the majority of the open ocean (annual range $<30\,\mu\mathrm{eq\,kg^{-1}}$). TA seasonality is found to be predominantly salinity driven in the tropics, outside of the eastern equatorial Pacific. Salinity-driven seasonality is large beneath the ITCZ and SPCZ and adjacent to river outflows in the equatorial Atlantic. Large annual ranges for ΔTAs are also found in the Greenland and Labrador currents and the Antarctic seasonal sea ice zone. TA seasonality has a moderate non-salinity driven component in the Gulf of Alaska and Oyashio, parts of the eastern equatorial Pacific and in the Southern Ocean polar frontal zone.

Comparison with previous climatologies revealed differences due to variable construction methods. Sharp spatial gradients were found to be smoothed in the GLODAP climatology, which can be a problem when directly interpolating from sparse measurements. Differences due to discrepancies in regional boundaries were found between annual mean GCP and L06 for the eastern equatorial Pacific. A substantially lower annual mean and seasonal range were found for the subarctic Pacific in GCP, a region with enhanced measurement coverage from PACIFICA. Larger ranges were found for the southeast subtropical Pacific, Weddell Sea and Antarctic continental shelf waters. GCP and M07 show a generally similar distribution on the annual mean in the Southern Ocean, but GCP has larger seasonal ranges in the Antarctic zone.

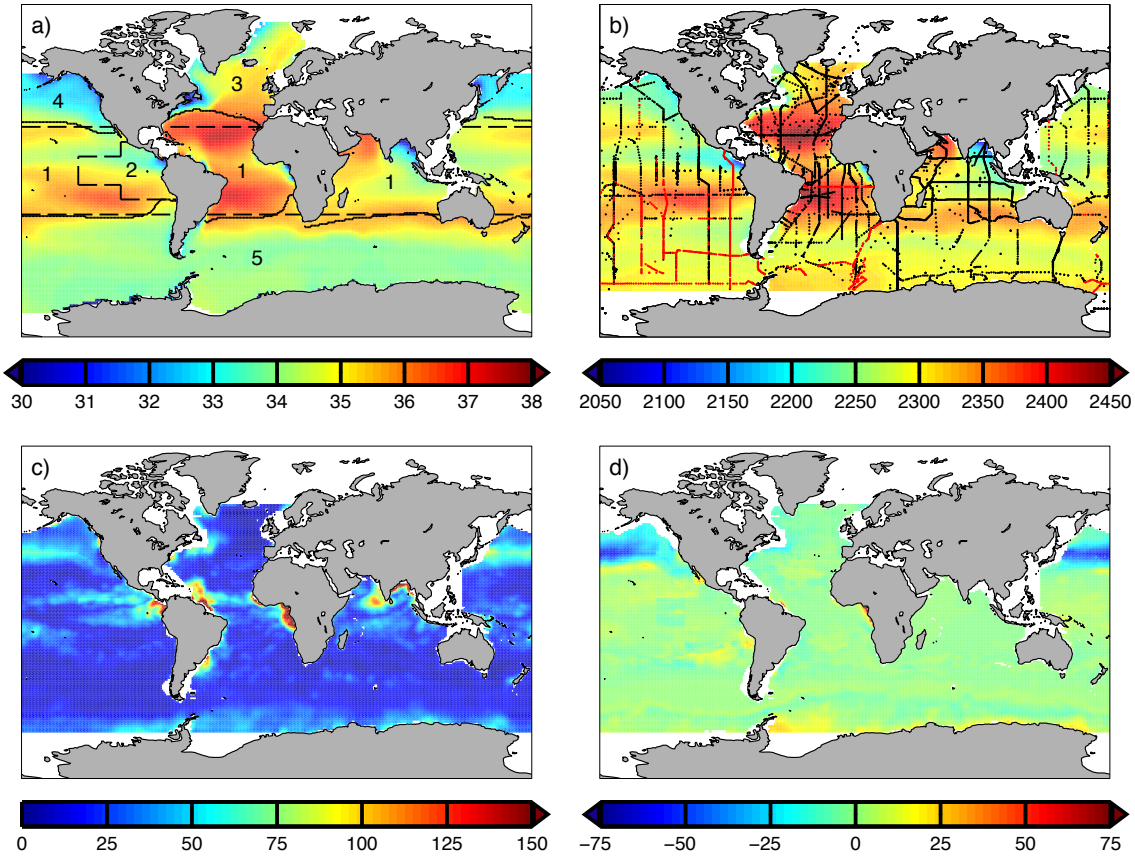

Figure 5.3: a) The regions for the reconstructed L06 TA climatology atop a background of WOA09 annual mean salinity (psu). The region numbers correspond to those used by L06. The dashed lines indicate the fixed, minimum extents of the tropical/subtropical region. The 20°C isotherm (solid lines, defined from annual mean SST here) defines the tropical/subtropical regional boundary where it extends beyond the fixed boundaries. b) Locations of the GLODAP TA observations used by L06, atop the background of the reconstructed annual mean L06 TA field (μeq kg^{-1}) Measured and calculated TA values are denoted by black and red dots, respectively. c) Seasonal range (maximum minus minimum monthly means) for reconstructed L06 (μeq kg^{-1}). d) Difference between the annual ranges for GCP TA and reconstructed L06 (μeq kg^{-1}).

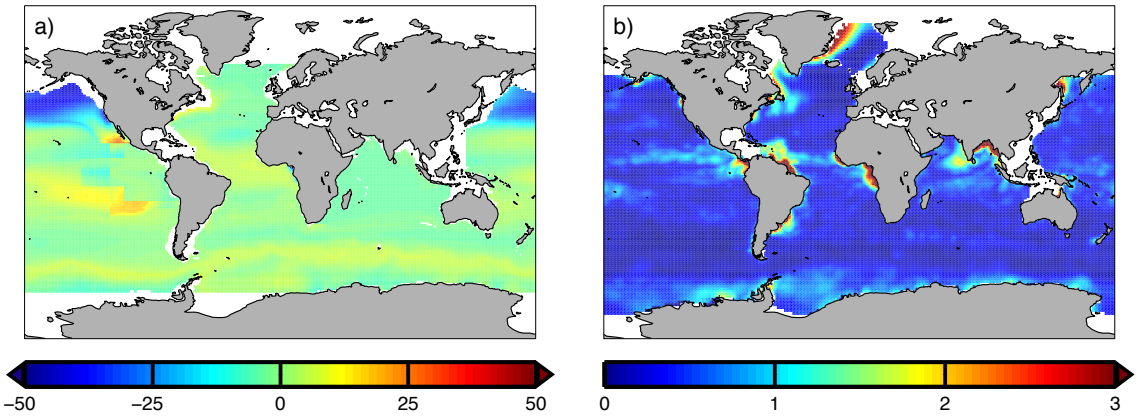

Figure 5.4: a) Difference between annual mean GCP and reconstructed L06 TA (μeq kg^{-1}). b) Annual range for salinity (psu) from WOA09.

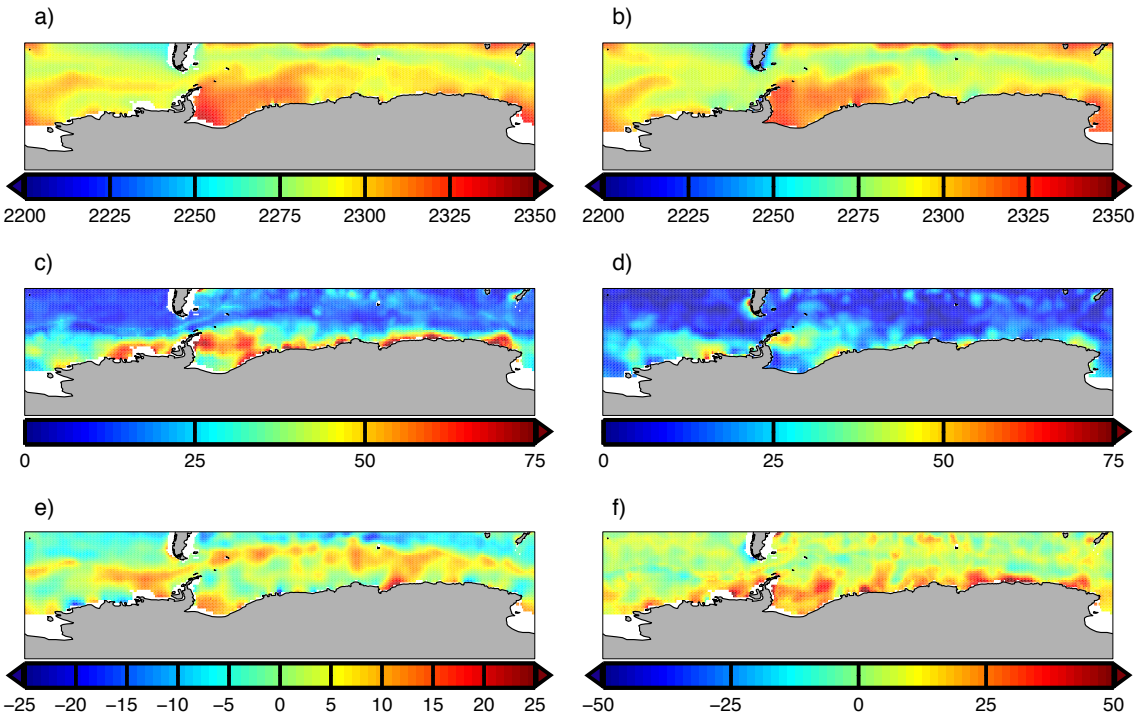

Figure 5.5: Comparison of GCP with the McNeil et al. (2007) Southern Ocean TA climatology. All quantities are in μeq kg^{-1}. a) Annual mean GCP TA. b) Annual mean M07 TA. c) Annual range for GCP TA. d) Annual range for M07 TA. e) Difference between the annual mean for GCP and M07. f) Difference between the annual TA ranges for GCP and M07.

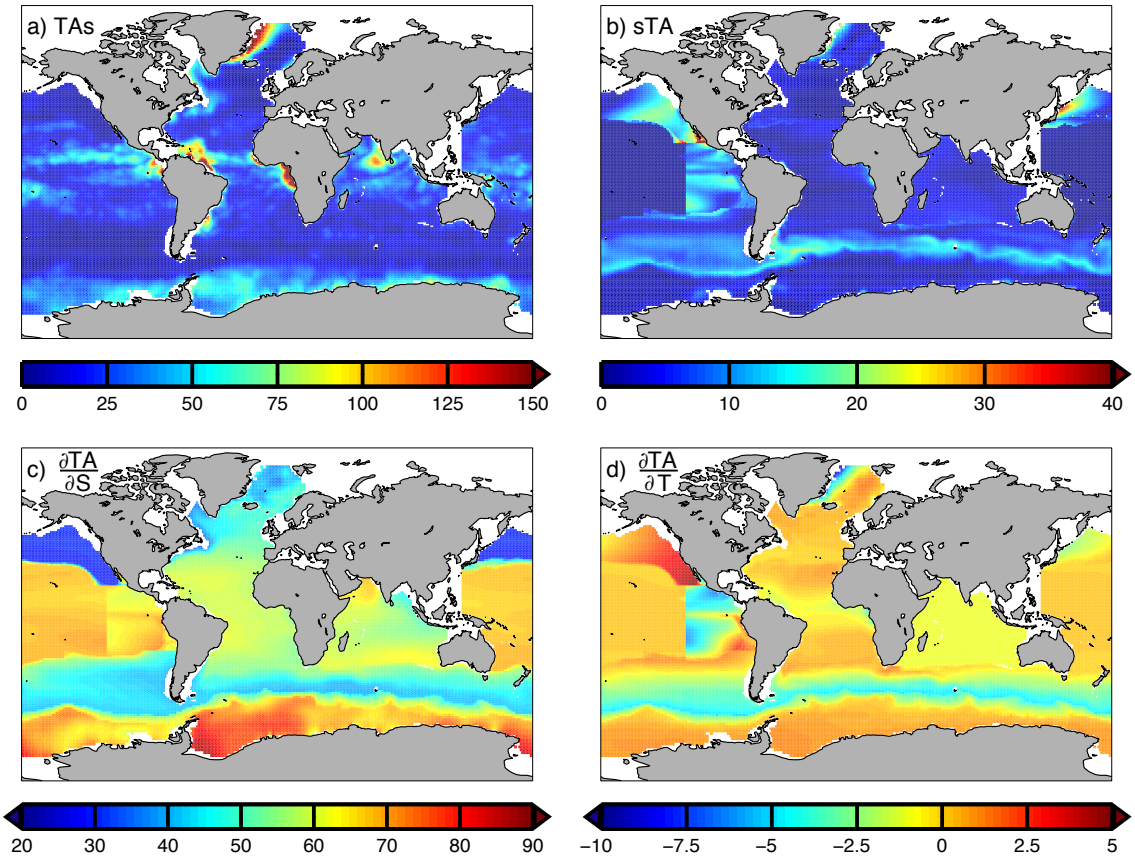

Figure 5.6: Analysis of the drivers of GCP TA seasonality. a) Annual range for ΔTA_s (μeq kg^{-1}). b) Annual range for ΔsTA (μeq kg^{-1}). c) $\frac{\partial TA}{\partial S}$ at annual mean conditions (μeq kg^{-1} psu^{-1}). d) $\frac{\partial TA}{\partial T}$ at annual mean conditions (μeq kg^{-1} $^{\circ}$C^{-1}).

Chapter 6

Open ocean carbonate chemistry time-series

Most of what we know about seasonality of pH and aragonite saturation state (Ω_A) in the open ocean comes from analysis of Eulerian time-series. These vary in terms of their sampling frequency and the carbonate chemistry parameters that are measured (some combination of pCO_{2sw}, DIC, TA and pH). For instance, autonomous pH and pCO_{2sw} sensors mounted on moored buoys make measurements every few minutes whereas sampling for ship-based time-series is typically monthly. An important consideration in time-series analysis is the timescale-dependent variability that occurs at a location relative to the sampling interval. Variability in carbonate chemistry can occur on sub-diurnal (e.g. tidal), diel, seasonal, inter-annual and multi-decadal timescales. Seasonal variability appears to generally be the largest component of natural variability in the open ocean.

Here I analyse and compare open ocean carbonate chemistry time-series that have been sampled at least four times a year for at least two carbonate chemistry parameters, over a period of five or more years. While detailed analysis of seasonal variability and long-term trends in pH and Ω_A has been conducted for some of the time-series, none have been subjected to the comprehensive range of analyses applied here. Moreover, the large assortment of time-series analysed here have never before been systematically compared using standardised analyses. Previous comparisons have mostly been restricted to the Bermuda Atlantic Time-series Study (BATS), the European Station for Time Series in the Ocean at the Canary Islands (ESTOC) and the Hawaii Ocean Time-series (HOT), all being located in subtropical gyres.

6.1 Method

The selected time-series are are all ship-based and all located in the northern hemisphere, except for Station Munida off the South Island of New Zealand (Fig. 6.1). Only observations from the upper 11 m and within 21 km (BATS) or 10 km (all other stations besides Munida) of the nominal time-series locations were used. Station Munida does not have a nominal location, rather observations are gathered across a 10 km-long linear transect.

Observations from the same cast were first averaged within the following depth ranges: 0-2 m, 2-4 m, 4-6 m, 6-9 m and 9-11 m, and then averaged across these to yield single parameter values for each cast.

6.1.1 Input measurements

pH measurements reported at 25°C ($pH_{T=25}$) from records with at least one other measured carbonate chemistry parameter were converted to in situ temperature using CO2SYS (Lewis and Wallace, 1998). $pH_{T=25}$ values from records for which this was the only measured parameter were discarded. pH measurements on the seawater scale were converted to the total scale. Potentiometric measurements on the National Bureau of Standards/National Institute of Standards and Technology (NBS/NIST) scale were not used.

Bottle salinity and reversing thermometer temperatures were used where CTD salinity and temperatures were missing. For records without phosphate and silicate, corresponding climatological monthly means from World Ocean Atlas 2009 were used.

6.1.2 Carbonate chemistry calculations

Where a carbonate chemistry parameter was not measured or could not be measured (e.g. Ω_A) but two or more ocean CO_2 parameters were, it was calculated using the combination of observed parameters that yielded the lowest uncertainty. The carbonic acid dissociation constants of Mehrbach et al. (1973) as refit by Dickson and Millero (1987) were used for SST $\geq$2°C, Millero et al. (2006) for 0$\leq$ SST <2°C and Millero et al. (2002) for SST <0°C. Uncertainty on calculated values was determined using Gaussian error propagation, following the method of Juranek et al. (2011), but also accounting for uncertainties on K_0, K_1' and K_2'. One thousand random Gaussian-distributed values were generated for each carbonate chemistry measurement, with

mean equal to the measured value and standard deviation equal to the assigned measurement uncertainty ($3\,\mu\mathrm{mol\,kg^{-1}}$ for DIC, $3\,\mu\mathrm{eq\,kg^{-1}}$ for TA, 0.005 for pH).

Randomised values were similarly generated for K_0, $K_1^{'}$, $K_2^{'}$, temperature, salinity, phosphate and silicate. The uncertainty on K_0 was taken to be 0.5% after Dickson and Riley (1978), while the 1σ uncertainties of Dickson and Millero (1987) were used for $K_1^{'}$ and $K_2^{'}$ (1.3 and 2.3%, respectively). Measurement uncertainties for temperature, salinity, phosphate and silicate were taken to be 0.01°C, 0.01 psu, 4% and 3%. The randomised values were then input to CO2SYS and the uncertainty on the computed value taken to be the standard deviation of the 1000 randomised output values from the routine. The uncertainties so derived are consistent with those calculated from a simple error propagation analysis (Appendix F). When calculated from DIC and TA, the uncertainties on pH and Ω_A are ∼0.01 and 0.1. When calculated from pCO_{2sw} and TA, the uncertainties are ∼0.007 and 0.1.

6.1.3 Long-term trends

To estimate long-term trends, the measured and calculated values were combined, averaged by Julian day and month and deseasonalised by subtraction of climatological monthly anomalies. The latter were calculated as in Chapter 4, after first normalising the data to the year 2000 by removal of long-term statistically significant ($p < 0.05$) linear trends. The final long-term trends were estimated from linear fits to the deseasonalised data, with the gradients of these taken be zero where the trends were not statistically significant.

6.1.4 Linear decomposition analysis

Changes in pH and Ω_A can be partitioned into components due to variation in DIC, TA, temperature and salinity through linear decomposition by Taylor series expansion. For a monthly pH anomaly from the annual mean (ΔpH), we have:

$$\Delta pH = \frac{\partial pH}{\partial DIC}\Delta DIC + \frac{\partial pH}{\partial TA}\Delta TA + \frac{\partial pH}{\partial T}\Delta T + \frac{\partial pH}{\partial S}\Delta S + Res. \qquad (6.1)$$

where *Res.* is the residual error comprised of second and higher order terms. We replace pH with Ω_A to obtain the equivalent equation for Ω_A.

The partial derivatives are calculated in CO2SYS by varying the value of the denominator variable (e.g. temperature) while all other input variables are held

fixed at annual mean values. The resulting pairs of values for the numerator and denominator variables are then fit with a piecewise cubic spline. The partial derivative is taken to be the first derivative of this spline curve at the climatological annual mean value of the denominator variable. To graphically illustrate the method by which the partial derivatives are derived, three-dimensional surface contour plots showing dependencies between various carbonate chemistry parameters are presented in Appendix E.

Since both DIC and TA are influenced by salinity, we can further separate the DIC and TA anomalies into salinity-driven (ΔDIC_s and ΔTA_s) and salinity normalised components ($\Delta sDIC$ and ΔsTA):

Following Hauri et al. (2013), I group the salinity driven components into a single term, ΔpH_{FW} so that (6.1) becomes:

$$\Delta pH = \frac{\partial pH}{\partial DIC}\Delta sDIC + \frac{\partial pH}{\partial TA}\Delta sTA + \frac{\partial pH}{\partial T}\Delta T + \Delta pH_{FW} + Res. \tag{6.2}$$

which can be more compactly written as:

$$\Delta pH = \Delta pH_{sDIC} + \Delta pH_{sTA} + \Delta pH_T + \Delta pH_{FW} + Res. \tag{6.3}$$

where $\Delta pH_{FW} = \frac{\partial pH}{\partial S}\Delta S + \frac{\partial pH}{\partial DIC}\Delta DICs + \frac{\partial pH}{\partial TA}\Delta TAs$

I calculate sDIC and sTA using the method of Friis et al. (2003). For sTA, we have:

$$sTA = \frac{TA_{S_{meas}} - TA_{S=0}}{S_{meas}}\, S_{ref} + TA_{S=0} \tag{6.4}$$

where $TA_{S_{meas}}$ and $TA_{S=0}$ refer to the TA values at the measured salinity and zero salinity, respectively. sTA is the TA at the reference salinity (S_{ref}). Climatological annual mean salinity for the time-series is used for the reference salinity and $TA_{S=0}$ taken to be the intercept of a linear fit of the TA values for the time-series against salinity.

$\Delta DICs$ and ΔTAs are computed as residuals:

$$\Delta DICs = \Delta DIC - \Delta sDIC \tag{6.5}$$

$$\Delta TAs = \Delta TA - \Delta sTA \tag{6.6}$$

Uncertainty on the seasonal cycle forcing components (e.g. ΔpH_{sDIC}) was estimated by Gaussian error propagation from uncertainties on $\Delta sDIC$, ΔsTA, ΔT and

ΔS, ignoring uncertainty in the partial derivatives. The anomaly uncertainties were computed by first assigning an uncertainty to each measured and computed value. Means for 1000 randomised versions of the group of observed and measured anomaly values for each month were then calculated and the standard deviation of these taken as the uncertainty on the corresponding monthly anomalies. This method explicitly accounts for contributions from measurement and computational uncertainties to the uncertainty on the monthly anomalies.

I also use the linear decomposition method to attribute long-term trends in pH and Ω_A to long-term trends in sDIC, sTA, temperature and salinity. To do so, we replace the anomalies on the RHS of (6.2) with the gradients of the long-term trends for the respective parameters. We then integrate each RHS term across the full record, calculating separate partial derivatives for each year so as to account for any changes in the buffering capacity of the seawater (e.g. due to DIC increase). A similar attribution analysis was previously conducted by Bates et al. (2012) for long-term trends in pCO_{2sw} at BATS.

To estimate whether the sDIC-driven components of the long-term pH and Ω_A trends are consistent with the local rise in atmospheric pCO_2 (assuming air-sea equilibrium), long-term atmospheric pCO_2 trends were determined for nearby GLOBALVIEW monitoring stations (Table 6.2). GLOBALVIEW-CO_2 data are available here. Trends were calculated using deseasonalised monthly means. Deseasonalisation was conducted using climatological monthly mean anomalies from GLOBALVIEW (no longer available online). From the long-term trends, annual mean pCO_{2sw} values were estimated for each year of the particular record and from this annual mean DIC values calculated using fixed climatological annual mean values for TA, SST, SSS, phosphate and silicate. A long-term DIC change was then calculated from the DIC annual means and the equivalent change in pH calculated using $\frac{\partial pH}{\partial DIC}$.

6.2 Time-series overview

6.2.1 BATS/Hydrostation S

The Bermuda Atlantic Time-series Study (BATS) and Hydrostation S (HS) sites are located in the western subtropical north Atlantic (Bates et al., 2012). DIC and TA data from HS for September 1983 to December 1987 were provided by the Bermuda Institute of Ocean Sciences upon request. HS temperature and salinity data covering

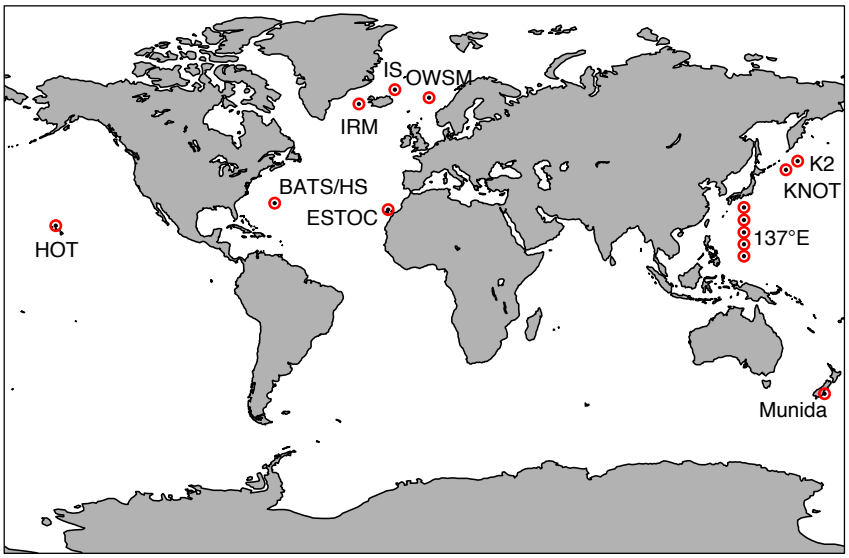

Figure 6.1: Locations of the time-series stations referred to in this chapter.

February 1955 to September 1988 were obtained from the BATS website (http://bats.bios.edu/bats_form_bottle.html) and matched to this DIC and TA data. BATS DIC and TA measurements from core, bloom and validation cruises (February 1989 to June 2011) were also obtained from the BATS website, and combined with measurements located within 21 km of BATS in CARINA and GLODAP. Core cruises sample the BATS site each month while bloom cruises are conducted during the spring bloom. An additional annual validation cruise covers a larger spatial domain around the BATS site. Only data located within 21 km of the nominal BATS and HS locations were used.

6.2.2 ESTOC

The European Station for Time Series in the Ocean at the Canary Islands (ESTOC, Santana-Casiano et al., 2007; González-Dávila and Santana-Casiano, 2009) is located around 100 km north of Gran Canaria within the southward-flowing Canary Current. Episodic dust depositions from the Sahara occur at ESTOC, while upwelling from the northwest African coast can also sometimes influence the site. ESTOC DIC, TA and pH measurements were obtained from the Carbon Dioxide Information Analysis Center or CDIAC (González-Dávila and Santana-Casiano, 2009). Sampling is typically monthly.

6.2.3 HOT

Station ALOHA (A Long-term Oligotrophic Habitat Assessment) of the Hawaiian Ocean Time-series (HOT) is located around 100 km north of Oahu, Hawaii in the north Pacific subtropical gyre (Dore et al., 2009). Here I simply refer to the time-series as HOT. Sampling at ALOHA is monthly and occurs within a circle of 10 km radius. ALOHA DIC, TA and pH observations were obtained from the HOT Data Organization and Graphical System (HOT-DOGS; http://hahana.soest.hawaii.edu/hot\/hot-dogs/bextraction.html). Spectrophotometric silicate was used where bottle silicate was missing.

6.2.4 IRM

The Irminger Sea time-series (IRM) is located to the south of Iceland in the north Atlantic subpolar gyre. As at IS, only DIC and pCO_{2sw} are measured at IRM. Pre-1991 DIC and pCO_{2sw} data were obtained from the IRM data file at CDIAC (Olafsson, 2007b). Post-1991 pCO_{2sw} data from this file were merged with post-1991 CARINA DIC data. Note that the what is usually referred to as the IRM time-series actually consists of observations from two separate locations 355 km apart (64.3°N, 28.0°W; 63.0°N, 21.5°W). Only observations from the station located at 28.0°W are used here. The best-observed months are February, May and August-November (Fig. 6.2d).

6.2.5 IS

The Iceland Sea time-series (IS) is located around 220 km northeast of Iceland in the Nordic Seas (Olafsson et al., 2009). Surface waters here are influenced by cold, fresh Arctic waters brought by the East Greenland Current and warmer, more saline Atlantic waters inflowing across the Greenland-Iceland-Faroes ridge. DIC and pCO_{2sw} are measured at IS. Pre-1991 DIC and pCO_{2sw} data were obtained from the IS data file at CDIAC (Olafsson, 2007a). DIC data from 1991 onwards were obtained from CARINA and merged with post-1991 pCO_{2sw} data from the CDIAC data file.

Note that what is usually referred to as the IS time-series actually consists of data from three separate locations (68.0°N, 18.8°W; 67.5°N, 13.3°W; 68.0°N and 12.7°W). Only observations from the station located at 12.7°W were used here. Sampling at IS is typically quarterly, with the best covered months being February, May, August and November (Fig. 6.2e).

6.2.6 KNOT/K2

Data from the Kyodo North Pacific Ocean Time-series (KNOT) and K2 were combined to form a single time-series. Kyodo means collaboration in Japanese. Both stations are located in the western subarctic Pacific gyre, KNOT around 400 km northeast of Hokkaido and K2 around 510 km north of KNOT. Technically the KNOT time-series only refers to sampling conducted at the KNOT site between June 1998 and October 2000, although the site has been periodically sampled since then. K2 is considered more representative of the western subarctic Pacific gyre than KNOT since subtropical and coastal waters sometimes intrude upon KNOT. The best-observed months for the combined time-series are May to October (Fig. 6.2f).

6.2.7 Station Munida

The Munida time-series transect is a 60 km-long transect extending offshore from the coastal waters of the southeast coast of the South Island of New Zealand, east-southeast out into the Southern Ocean (Currie et al., 2011; Brix et al., 2013). Only cruise-averaged data from 50-60 km offshore in subantarctic waters are used here, a location referred to as Station Munida. Sampling is bi-monthly.

6.2.8 OWSM

Ocean Weather Ship Station M (OWSM) is located in the eastern edge of the Norwegian Sea in the Norwegian Atlantic Current. The world's last weathership was stationed there until 2009. Here I analyse the same DIC and TA measurements as Skjelvan et al. (2008), obtained over 2001-2006. Additional temperature and salinity data for October 1948 to 2001 were obtained from OceanSITES (`ftp://ftp.ifremer.fr/ifremer\/oceansites/DATA/STATION-M`) for analysis of long-term trends.

6.2.9 Line 137°E

Line 137°E is a meridional transect along 137°E in the western north Pacific, extending from 3 to 34°N (Fig. 6.1). Here I analyse DIC, TA and spectrophotometric pH measurements from stations at 10, 15, 20, 25 and 30°N. pH has been measured spectrophotometrically along 137°E since 2003. The majority of the data are from PACIFICA and GLODAP, with additional measurements collated from 16 post-2008 cruises (cruise ids: KS0901, RF0901, KS0906, KS1001, RF1001, RF1002, RF1003,

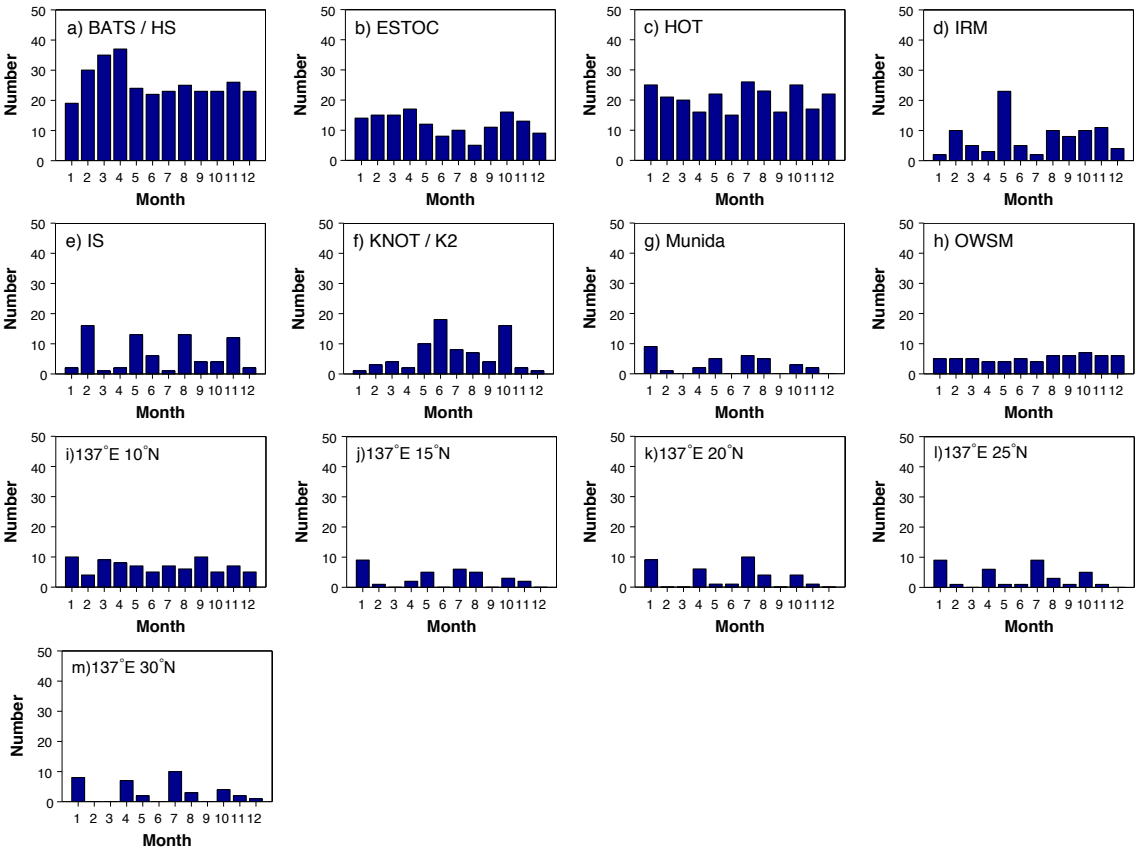

Figure 6.2: Number of observations by month for the time-series.

KS1004, KS1005, RF1005, KS1006, KS1102, KS1107, RF1107, RF1108, RF1111), obtained from the Japan Meteorological Agency (http://www.data.kishou.go.jp/db/vessel_obs/data-report/html/ship/ship_e.php). Temperature and salinity data from 1967 onwards not included in PACIFICA or GLODAP were also obtained for analysis of long-term trends. Observation times were converted from Japan Standard Time to Coordinated Universal Time (UTC). Bottle data flagged as anything other than 2 or 6 (meaning "Acceptable measurement" and "mean of replicate measurements') were excluded. Sampling has typically been quarterly, with January, April, July and October being amongst the best sampled months (Fig. 6.2 i-m).

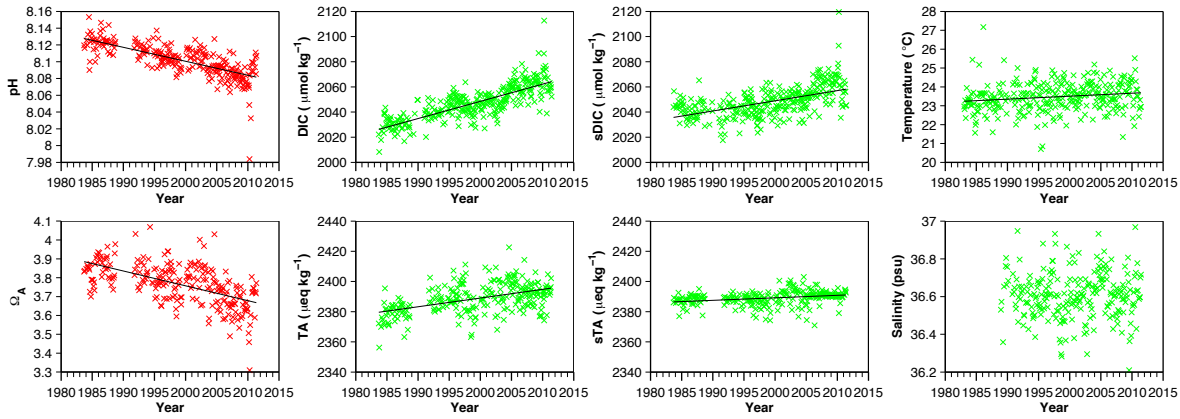

Figure 6.3: Long-term trend analysis for BATS/HS. Green and red crosses are observed and calculated values, respectively.

6.3 Results and discussion

6.3.1 Long-term trends

Long-term pH trends were analysed in detail for BATS, ESTOC, HOT, IRM and IS (Table 6.4). The total observed pH declines across the duration of these time-series are -0.047, -0.022, -0.038, -0.055 and -0.035 units (Figs. 6.3a, 6.4a, 6.5a, 6.6a and 6.7a). The average rates of decline range between from -0.0015 to -0.0024 yr^{-1}, with uncertainties around 0.0001-0.0002. Declining trends in Ω_A are also apparent at BATS, ESTOC and HOT, with total declines of -0.22 and -0.16, -0.17 and average decline rates of -0.008, -0.012 and -0.007 yr^{-1}. The uncertainties on the rates are relatively large at $\pm$0.002, 0.006 and 0.004, respectively. Long-term pH and Ω_A trends were not estimated for stations along Line 137°E due to limited pH, DIC and TA observations. Previously Midorikawa et al. (2010) calculated long-term pH trends for 137°E stations at 1° intervals between 3 and 33°N, with pH values for 1983-1993 being calculated from pCO_{2sw} and TA estimated from salinity. Their computed rates of pH decline range between 0.0015-0.0021 yr^{-1} for winter and 0.0008-0.0019 yr^{-1} for summer. They found that long-term trends in SST accounted for -25 to +44% of the long-term winter pH changes and -85 to +37% of the summer changes.

Linear decomposition of the pH and Ω_A trends into sDIC, sTA, SST and SSS-driven components reveals that uptake of anthropogenic CO_2 appears to be the principal cause of the long-term declines (Figs. 6.8 and 6.9). The ESTOC record provides

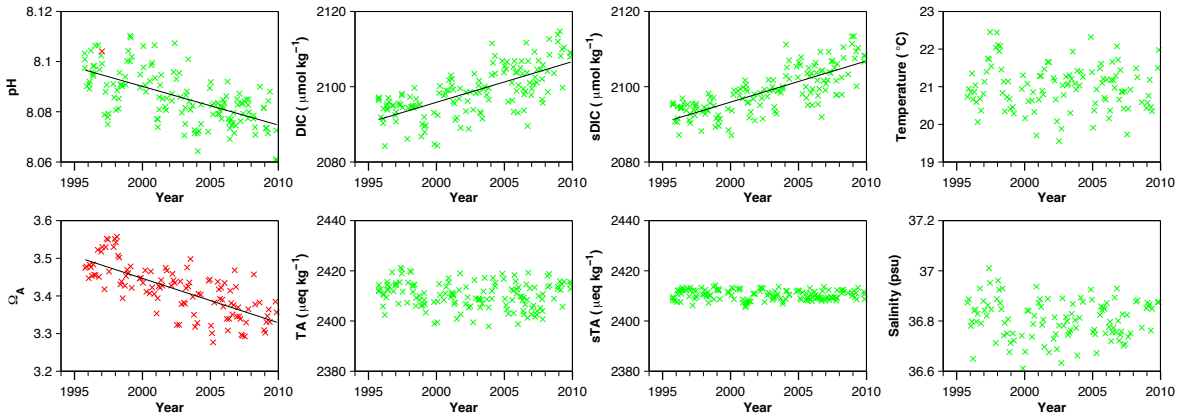

Figure 6.4: Long-term trend analysis for ESTOC, as for Fig. 6.3.

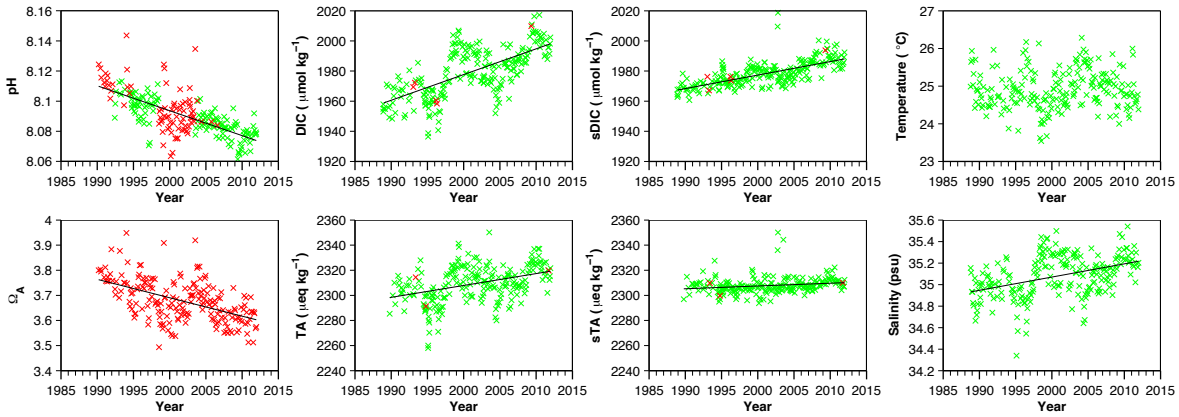

Figure 6.5: Long-term trend analysis for HOT, as for Fig. 6.3.

one of the clearest signals of anthropogenic acidification, exhibiting long-term pH and Ω_A declines that can be entirely explained by anthropogenic-driven increase in sDIC. Indeed, no long-term trends in sTA, SST or SSS are apparent for the station.

With the exception of IRM and ESTOC, the pH declines predicted from the increase in atmospheric CO_2 are greater than or equal to the actual sDIC-driven declines in pH and Ω_A. At BATS, HOT, IRM and IS, inter-decadal trends in sTA, SST and SSS have acted to enhance or counter the observed long-term sDIC-driven declines in pH and Ω_A. Long-term increases in sTA at BATS, HOT, IRM and IS have acted to counter the pH and Ω_A declines. Warming trends have acted to enhance acidification at BATS, IRM and IS, as have apparent salinification trends at BATS,

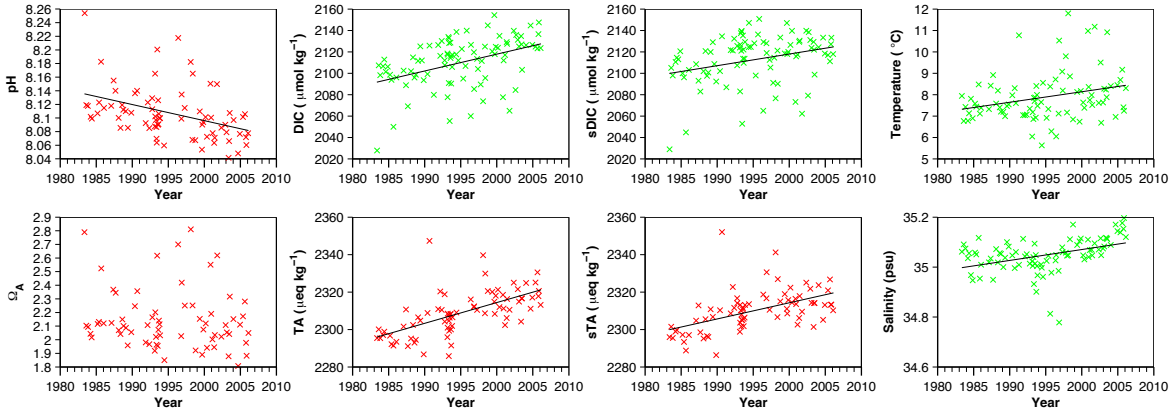

Figure 6.6: Long-term trend analysis for IRM, as for Fig. 6.3.

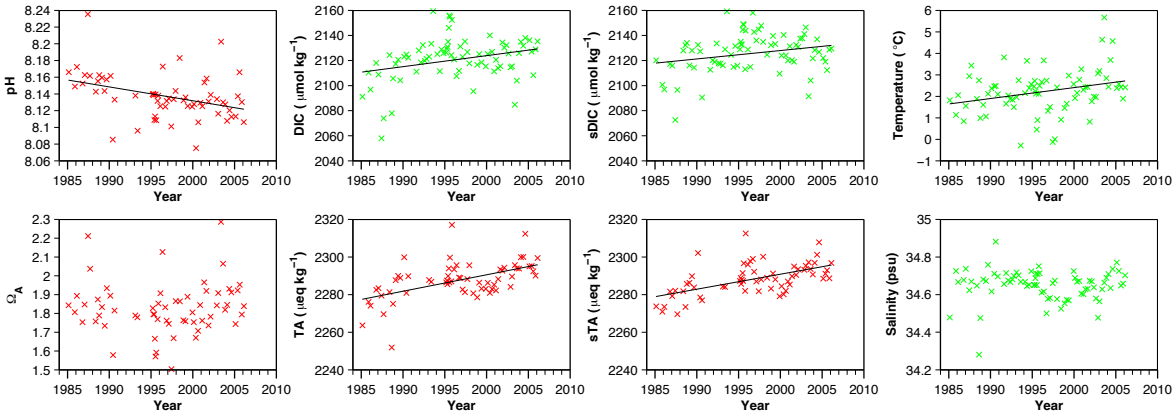

Figure 6.7: Long-term trend analysis for IS, as for Fig. 6.3.

HOT and IRM. Note that while no long-term salinity trend is found for BATS, a salinity-driven increase in pH is predicted since the trends in DICs and TAs (used to calculate the FW component) are statistically significant. Long-term salinity trends have acted to lower Ω_A at HOT and IRM, while temperature changes have been of minimal influence for Ω_A trends.

The pH trend attribution analysis for IS is sufficiently uncertain that it allows for the possibility of a positive, negative or zero trend in pH. This is also the case for Ω_A at IRM and IS. There is also large uncertainty on the FW forcing component of Ω_A at IRM and on the sDIC components for pH and Ω_A at IS.

The importance of distinguishing between long-term trends in DIC and TA from

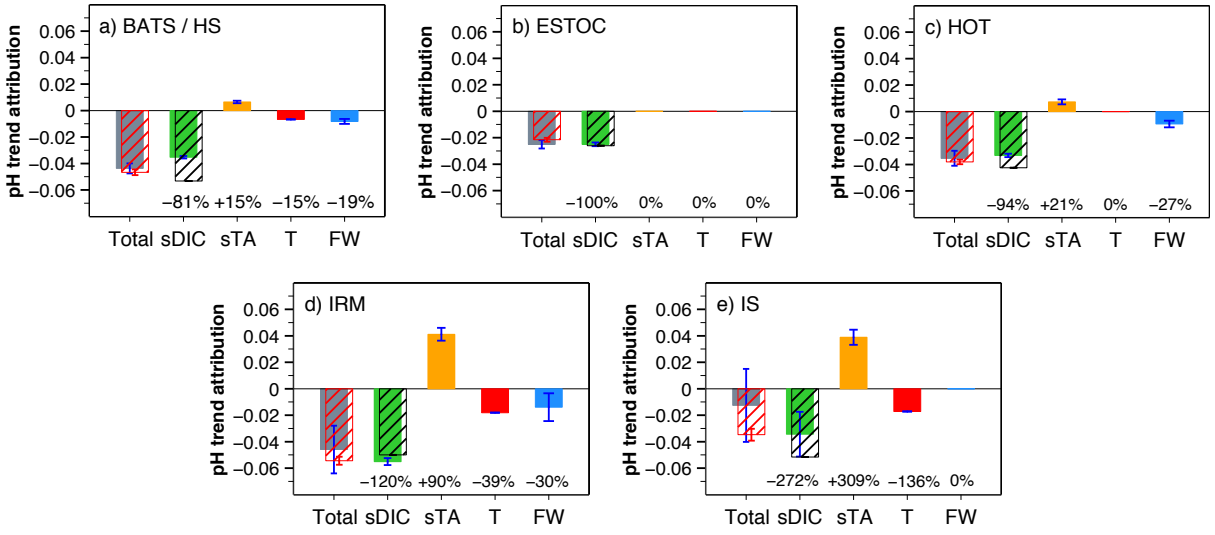

Figure 6.8: Decomposition analysis for long-term pH trends across five time-series. The grey solid bar for the total pH change over the time-series record is the sum of the four other solid bars. The red cross-hatched bar over the top is the total observed pH change based on the long-term pH trend. For accurate attribution, there needs to be overlap between the error bars for the aforementioned two bars. The black cross-hatched bar for sDIC represents the pH change that would be expected due to the increase in atmospheric pCO_2 at the paired GLOBALVIEW monitoring station. Bars are not shown where the corresponding long-term trends are not statistically significant. The freshwater (FW) bar is the contribution from salinity change.

those in sDIC and sTA is readily apparent for HOT, for which a salinification trend accounts for much of the long-term increase in DIC and TA (Fig. 6.5).

In addition, I have analysed long-term trends in SST and SSS for stations along Line 137°E. Long-term warming and freshening trends are apparent for the stations at 10, 15 and 20°N (Fig. 6.10). The trends range from 0.008 to 0.022°C yr^{-1} for temperature and -0.003 to -0.005 psu yr^{-1} for salinity.

6.3.2 Seasonal cycles

Subtropical waters

Seasonal cycles in pH are predominantly temperature-driven in the subtropics (Fig. 6.11). sDIC seasonality tends to be weak here as a consequence of fairly low, seasonally-invariant biological production under year-round nutrient limitation. Since pH is inversely related to temperature, the annual pH minimum tends to occur in summer

Table 6.1: General information about the time-series referred to in this chapter. The last six columns are climatological annual mean values. The 'Years' column indicates the years with carbonate chemistry observations.

Time-series station	**Location**	**Descriptive location**	**Years**	**DIC** μmol kg^{-1}	**TA** μeq kg^{-1}	**pH**	Ω_A	**SST** °C	**SSS** psu
Bermuda Atlantic Time Series (BATS) / Hydrostation S (HS)	32.00°N, 64.00°W/ 32.17°N 64.50°W	western north Atlantic subtropical gyre	1983-2011	2049.7	2389.3	8.10	3.7	23.5	36.60
European Station for Time Series in the Ocean, Canary Islands (ESTOC)	29.00°N, 15.50°W	eastern north Atlantic subtropical gyre	1995-2009	2096.6	2410.3	8.09	3.4	21.0	36.81
Hawaii Ocean Time-series (HOT)	22.75°N, 158.00°W	central north Pacific subtropical gyre	1988-2011	1978.1	2307.7	8.09	3.7	24.9	35.07
Iceland Sea time series station (IS)	68.00°N, 12.67°W	northern Iceland Sea	1985-2006	2125.8	2291.2	8.13	1.8	2.2	34.65
Irminger Sea time series station (IRM)	64.33°N, 28.00°W	northern Irminger Sea	1983-2006	2119.1	2314.5	8.09	2.1	8.1	35.07
Kyodo North Pacific Ocean Time-series (KNOT) / K2	44.00°N, 155.00°E / 47.00°N, 160.00°E	western subarctic Pacific gyre	1992-2008	2055.9	2225.1	8.09	1.9	7.2	32.90
Station Munida	45.50°S, 171.50°E	subantarctic southwest Pacific	1998-2011	2085.6	2285.0	8.09	2.2	10.3	34.30
Ocean Weather Station M (OWSM)	66.00°N, 2.00°E	eastern Norwegian Sea	1998-2006	2106.4	2303.3	8.08	2.1	8.9	35.10
137°E 10°N	10.00°N, 137.00°E	western tropical Pacific	1994-2012	1886.9	2231.0	8.07	3.8	29.1	34.00
137°E 15°N	15.00°N, 137.00°E	western tropical Pacific	1994-2012	1907.5	2254.9	8.07	3.9	28.9	34.38
137°E 20°N	20.00°N, 137.00°E	western tropical Pacific	1994-2012	1925.4	2266.9	8.07	3.8	28.0	34.60
137°E 25°N	25.00°N, 137.00°E	western subtropical Pacific	1994-2012	1944.2	2281.7	8.09	3.8	26.1	34.76
137°E 30°N	30.00°N, 137.00°E	western subtropical Pacific	1994-2012	1960.2	2273.5	8.10	3.5	23.5	34.62

Table 6.2: Pairings between the time-series and GLOBALVIEW atmospheric pCO_2 stations.

Time-series	**Station**	**Station code**
BATS/HS	Tudor Hill, Bermuda	BMW
ESTOC	Tenerife, Canary Islands	IZO
HOT	Mauna Loa, Hawaii	MLO
IS	Storhofdi, Vestmannaeyjar	ICE
IRM	Storhofdi, Vestmannaeyjar	ICE

Table 6.3: Climatological annual ranges for various time-series variables. Ranges for stations along Line 137°E were computed from seasonal means.

Time-series	**DIC**	**TA**	**sDIC**	**sTA**	**pH**	Ω_A	**SST**	**SSS**
	μmol kg^{-1}	μeq kg^{-1}	μmol kg^{-1}	μeq kg^{-1}			°C	psu
BATS/HS	40.6	19.1	19.6	1.9	0.09	0.4	8.4	0.32
ESTOC	14.2	8.8	14.7	1.9	0.05	0.3	5.2	0.13
HOT	13.5	10.5	12.2	3.1	0.03	0.2	3.1	0.17
IS	65.0	34.5	55.8	26.2	0.05	0.8	8.4	0.28
IRM	70.2	12.8	66.0	13.6	0.08	0.6	3.1	0.14
KNOT	134.2	30.6	98.7	16.3	0.09	1.2	12.8	0.55
Munida	35.6	8.5	35.8	9.3	0.02	0.4	4.2	0.11
OWSM	90.9	33.5	49.7	42.0	0.13	1.0	5.2	0.42
137°E 10°N	11.7	11.9	6.8	0.9	0.02	0.1	1.3	0.20
137°E 15°N	4.7	4.9	2.4	7.8	0.01	0.1	2.2	0.23
137°E 20°N	35.2	27.2	7.4	6.6	0.04	0.2	4.1	0.24
137°E 25°N	22.5	24.0	12.6	12.9	0.08	0.2	6.4	0.18
137°E 30°N	54.9	36.5	18.3	3.4	0.08	0.4	8.1	0.45

Table 6.4: Statistically significant ($p < 0.05$) long-term trends for the time-series. LT means long-term, in reference to the full record (years indicated in the last column), rather than the portion of the record with carbonate chemistry observations (other fields).

Time-series	**DIC** μmol kg^{-1} yr^{-1}	**TA** μeq kg^{-1} yr^{-1}	**sDIC** μmol kg^{-1} yr^{-1}	**sTA** μeq kg^{-1} yr^{-1}	**pH** yr^{-1}	Ω_A yr^{-1}	**SST** °C yr^{-1}	**SSS** psu yr^{-1}	**LT SST** °C yr^{-1}	**LT SSS** psu yr^{-1}	**Years for LT**
BATS/HS	1.37±0.02	0.58±0.02	0.81±0.02	0.16±0.02	-0.0017±0.0001	-0.008±0.002	0.016±0.000		0.013±0.000		1983-2011
ESTOC	1.08±0.07		1.09±0.06		-0.0015±0.0001	-0.012±0.006					1995-2009
HOT	1.71±0.03	0.95±0.04	0.90±0.03	0.22±0.05	-0.0017±0.0001	-0.007±0.004		0.012±0.000		0.012±0.000	1988-2011
IS	0.88±0.59	0.88±0.11	0.67±0.30	0.80±0.11	-0.0024±0.0001		0.051±0.000		0.051±0.000		1985-2006
IRM	1.57±0.05	1.11±0.10	1.09±0.05	0.86±0.10	-0.0017±0.0002		0.049±0.000	0.004±0.000	0.049±0.000	0.004±0.000	1983-2006
KNOT	2.29±0.00	1.65±0.26		1.14±0.25				0.018±0.004		0.018±0.005	1992-2008
Munida						-0.006±0.006	-0.037±0.000		-0.037±0.000		1998-2011
OWSM	2.08±0.00								0.008±0.000	-0.001±0.000	1998-2006
137°E 10°N	2.00±0.18								0.013±0.000	-0.005±0.001	1994-2012
137°E 15°N	1.39±0.41								0.022±0.000	-0.003±0.000	1994-2012
137°E 20°N			0.95±0.15						0.014±0.000	-0.004±0.000	1994-2012
137°E 25°N	1.42±0.83		1.12±0.28			-0.020±0.016					1994-2012
137°E 30°N		-2.15±1.39	1.52±0.13			-0.025±0.012	-0.083±0.000				1994-2012

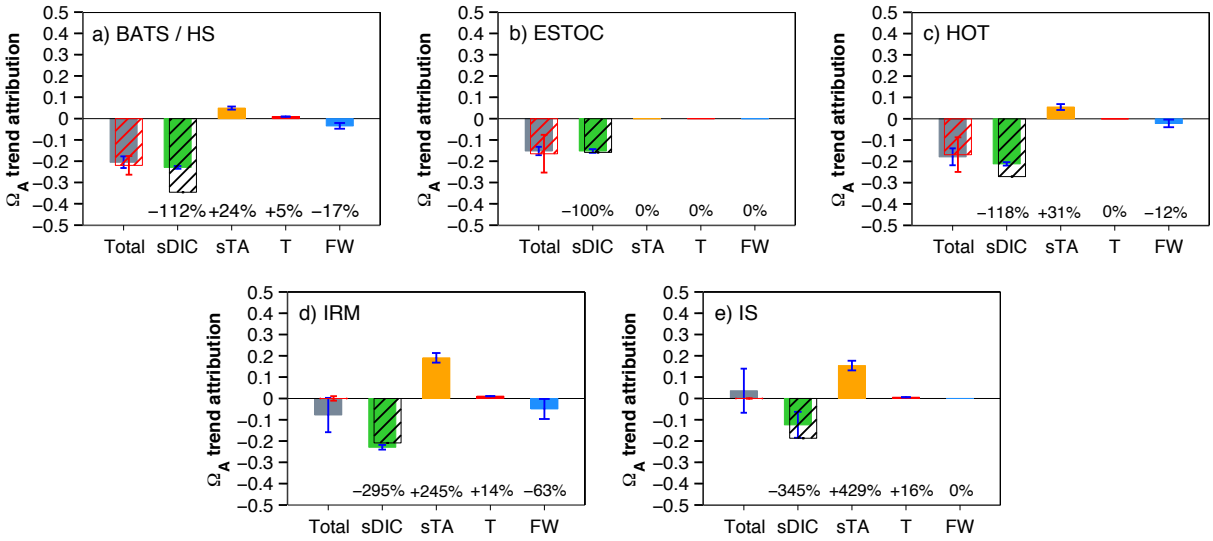

Figure 6.9: Decomposition analysis for long-term Ω_A trends, as for Fig. 6.8.

and the maximum in winter.

The amplitudes of the pH seasonal cycles for BATS, ESTOC and HOT vary in approximate proportion to the annual temperature range, with the latter being largest at BATS (8.4°C) and smallest at HOT (3.1°C). Similarly, the annual pH range increases from 15 to 25°N along Line 137°E (Fig. 6.13) as the annual temperature range increases (from 4.1°C at 15°N to 6.4°C at 25°N).

Ω_A seasonality is relatively weak (annual range $\leq$0.4) across the subtropical time-series (Fig. 6.12). Unlike the equivalent components for pH, the $\Delta\Omega_{A_{sDIC}}$ and $\Delta\Omega_{A_T}$ cycles tend to be in-phase since $\Delta sDIC$ and ΔSST cycle in anti-phase and $\frac{\partial\Omega_A}{\partial T}$ is positive and $\frac{\partial\Omega_A}{DIC}$ negative. Thus the seasonal cycles in $\Delta\Omega_{A_{sDIC}}$ and $\Delta\Omega_{A_T}$ cumulatively contribute to Ω_A seasonality, rather than destructively interfering as for pH. The annual range in $\Delta\Omega_{A_T}$ tends to be smaller than that for $\Delta\Omega_{A_{sDIC}}$, although they are of similar magnitude at BATS.

The largest Ω_A annual ranges across the subtropical time-series are for BATS and 137°E, 30°N. Winter mixing is stronger at BATS than at HOT or ESTOC (the winter mixed layer base is at ~250 m at BATS, compared to ~100 m at HOT and ~150-200 m at ESTOC), driving larger seasonal cycles in sDIC and SST. Ω_A seasonality increases along Line 137°E as the seasonal cycles of thermal and chemical forcing increase in amplitude (Fig. 6.13). sTA seasonality makes a negligible contribution to climatological pH and Ω_A seasonality at the subtropical time-series. Sporadic drawdowns

of sTA have, however, been noted to occur at BATS, attributed to coccolithophore blooms (Bates et al., 1996). The seasonal cycles of pH and Ω_A are in anti-phase at the subtropical stations (Fig. 6.14) since the cycles of the main driving components of each (ΔpH_T and $\Delta\Omega_{A_{sDIC}}$) are in anti-phase.

Subpolar waters

sDIC variation is the dominant driver of pH and Ω_A seasonality at the subpolar stations. sDIC seasonality is larger in subpolar waters than in the subtropics due to the greater seasonal variation in primary production and mixed layer depth. The climatological annual sDIC range varies from 22.1 to 98.7 μmol kg^{-1} across the subpolar stations compared to 2.4 to 18.3 μmol kg^{-1} across the subtropical time-series. Strong winds and convective overturn in fall and winter at mid to high latitudes drive entrainment of DIC-rich thermocline waters up into the mixed layer. A strong spring bloom in the subpolar and northern north Atlantic and western subarctic Pacific drives an sDIC drawdown at IRM, IS, OWSM and KNOT/K2 around May-July.

The largest seasonal cycles in pH are found at KNOT/K2, IRM and OWSM, with annual ranges of 0.09, 0.11 and 0.13, respectively. At KNOT and IRM, strong sDIC seasonality overwhelms the thermal forcing from large SST variation to exert the dominant influence on pH seasonality. It is hypothesised that the spring bloom at KNOT may be enhanced by iron input from Asian dust (Chierici et al., 2006). At OWSM, freshwater forcing, in addition to sDIC controls seasonal cycling of pH. Near-cancellation between the ΔpH_T and ΔpH_{sDIC} cycles occurs at Munida, resulting in a small seasonal cycle in pH (annual range of 0.02).

Ω_A seasonality tends to be larger at the subpolar stations than for the subtropical time-series due to the larger seasonal ranges in sDIC. Excluding Munida, the annual range in Ω_A varies from 0.6-1.2 across the subpolar time-series, compared to 0.1-0.4 across the subtropical stations. The seasonal range is largest at KNOT where the climatological annual range in sDIC is an impressive 98.7 μmol kg^{-1}

The seasonal cycles of pH and Ω_A are in-phase at the subpolar stations (Fig. 6.14) due to the seasonal cycles in ΔpH_{sDIC} and $\Delta\Omega_{A_{sDIC}}$ being in-phase.

6.3.3 Comparison with the pH/Ω_A and TA climatologies

The climatological seasonal cycles of TA and sTA for the time-series are compared to those for the respective grid cell from GCP TA in Figs. 6.15-6.22. Additional

comparison is made between the seasonal cycles for pH, Ω_A, DIC and sDIC and those from the primary pH/Ω_A climatology derived in the next chapter.

All the seasonal cycles are well captured by the climatologies for BATS/HS (Fig. 6.15), although with underestimation of the monthly sDIC anomalies for August-October. Note the fairly large uncertainties on the Ω_A anomalies from the climatology, these being larger than the standard deviations on the time-series anomalies. For ESTOC (Fig. 6.16), we find that the annual ranges for sDIC and DIC are overestimated and thus that the pH annual range is underestimated since this acts to counteract the predominantly thermally-driven seasonality. For the same reason, the climatology overestimates the Ω_A seasonal cycle. The sDIC and DIC seasonal cycles are also only loosely captured by the climatology for HOT (Fig. 6.17), again with resultant error in the pH and Ω_A cycles. Interannual variability in DIC and sDIC is however, large at HOT.

The general form of the seasonal cycle is fairly well captured by the climatology for IRM (Fig. 6.18) and IS (Fig. 6.19), although there is a lack of independence due to reliance on pCO_{2sw} observations for both the time-series' and climatology. There is apparent overestimation of the seasonal range for DIC and sDIC at KNOT (Fig. 6.20), although the time-series has relatively few observations. The same seasonal cycles also tend to be overestimated for Munida (Fig. 6.21). For OWSM (Fig. 6.22), the seasonal range for pH and Ω_A tends to be underestimated by the climatology, although again the time-series has relatively few observations.

6.3.4 Influence of buffer capacity on seasonality

Seawater buffer capacity has an important role in determining seasonal pH and Ω_A dynamics. The sensitivity of pH and Ω_A to sDIC and temperature varies between the better buffered (lower Revelle buffer factor) subtropical waters and more poorly buffered (higher Revelle buffer factor) subpolar waters. To demonstrate this, let us examine what happens when we have the same climatological seasonal cycles of sDIC, sTA, SST and SSS as for KNOT, but in seawater with the same annual mean conditions (and hence buffer capacity) as HOT. Fig. 6.23 reveals what the seasonal cycles in pH and Ω_A would look like. We find that the annual range for ΔpH_{sDIC} would be smaller since the seawater is better buffered ($\frac{\partial pH}{\partial DIC}$ is smaller), and thus that pH seasonality would be reduced. Ω_A seasonality would be enhanced since both $\frac{\partial \Omega_A}{\partial T}$ and $\frac{\partial \Omega_A}{\partial DIC}$ would be larger.

6.4 Changes in seasonal cycle amplitudes due to changes in buffer capacity

It has previously been noted that changes in seawater buffer capacity from anthropogenic CO_2 uptake can alter diel and seasonal cycles in pH, pCO_{2sw} and Ω_A (Riebesell et al., 2009; Egleston et al., 2010). Here I analyse the influence of changing buffer capacity on the pH and Ω_A seasonal cycles for a subtropical and a subpolar time-series (ESTOC and KNOT, respectively). I adopt a similar approach to Riebesell et al. (2009), who made projections for a pCO_{2sw} time-series in the central Labrador Sea. I make projections for the year 2100 assuming an atmospheric CO_2 level of 935.9 ppmv (taken from Representative Concentration Pathway 8.5). Assuming air-sea CO_2 equilibrium, we can calculate an annual mean DIC for 2100 using this and the climatological annual mean TA for the time-series (assuming this has not changed). Projected pH and Ω_A seasonal cycles for 2100 can then be calculated from sDIC, sTA, SST and SSS forcing components estimated for this year (the partial derivatives have changed). I perform two such calculations, one using the climatological annual mean SST and the other assuming this has increased by 4°C.

As can be seen from Figs. 6.24 and 6.25, the sensitivity of pH to DIC variation increases as the buffer capacity declines, while the sensitivity of Ω_A to DIC variation reduces. The sensitivity of both pH and Ω_A to temperature also declines. Large percentage changes are also apparent for some of the other partial derivatives, but their absolute magnitudes remain too small for them to be of much influence on pH and Ω_A.

For KNOT, we find that the annual range in pH is projected to be significantly enhanced by 2100 due to the larger sDIC forcing component (Fig. 6.26). At ESTOC, the sDIC forcing component is also enhanced (Fig. 6.27), which being in anti-phase with the dominant thermal forcing component, causes a reduction in the seasonal range for pH. For Ω_A, the seasonal range is reduced for both ESTOC and KNOT due to reduction in the sensitivity of Ω_A to temperature and DIC. The addition of a temperature change has minor influence on the projected seasonal cycles for KNOT and ESTOC.

6.5 Conclusions

Carbonate chemistry time-series provide conclusive evidence of ocean acidification driven by anthropogenic CO_2 emissions. They also reveal that trends in sTA, SST and SSS can modulate inter-decadal declining trends in pH and Ω_A. Warming and salinification act to enhance atmosphericCO_2-driven pH decline, while sTA increase acts to negate the effect. Salinification acts to enhance Ω_A decline while increases in sTA and SST act to raise Ω_A. ESTOC shows the clearest signal of CO_2-driven pH and Ω_A decline, with no long-term trends in SST, SSS or sTA being apparent for the time-series.

Seasonal cycles in pH are weak where both sDIC and SST seasonality are weak (e.g. HOT) or where sDIC and SST forcing are moderate but approximately cancel (e.g. Station Munida). Seasonal cycles of pH are larger where either sDIC dominates SST forcing (e.g. KNOT/K2) or SST forcing dominates sDIC forcing (e.g. BATS). In the subtropics the annual range in pH tends to vary in proportion to the amplitude of SST seasonal cycles. The largest seasonal ranges in pH (e.g. KNOT, OWSM) are of similar magnitude to the estimated decline in global-mean sea surface pH since the pre-industrial (0.1 units).

Seasonal cycles of Ω_A tend to be predominantly sDIC-driven, with a modest temperature-driven component. pH and Ω_A seasonal cycles are in-phase were sDIC forcing dominates pH seasonality at subpolar stations and in anti-phase at subtropical stations where SST dominates seasonal pH variation.

Buffer capacity can exert a strong influence on pH and Ω_A seasonal cycles. The seasonal pH and Ω_A ranges would be reduced and enhanced, respectively, at KNOT if this location had the same seasonal cycles of sDIC, sTA, SST and SSS, but the seawater had the same buffer capacity as at HOT. Simple calculations suggest that pH seasonality would increase at subpolar time-series and decline at subtropical time-series with ongoing acidification, in the absence of salinity or TA change. Ω_A seasonality would be expected to generally decline at both subpolar and subtropical time-series.

The primary pH/Ω_A climatology derived in the next chapter captures the general form of the climatological pH, Ω_A, sDIC and DIC seasonal cycles of the time-series. However, it has a tendency to overestimate the seasonal ranges in DIC and sDIC at ESTOC, KNOT and Munida, with consequent error in the estimated pH and Ω_A seasonal cycles.

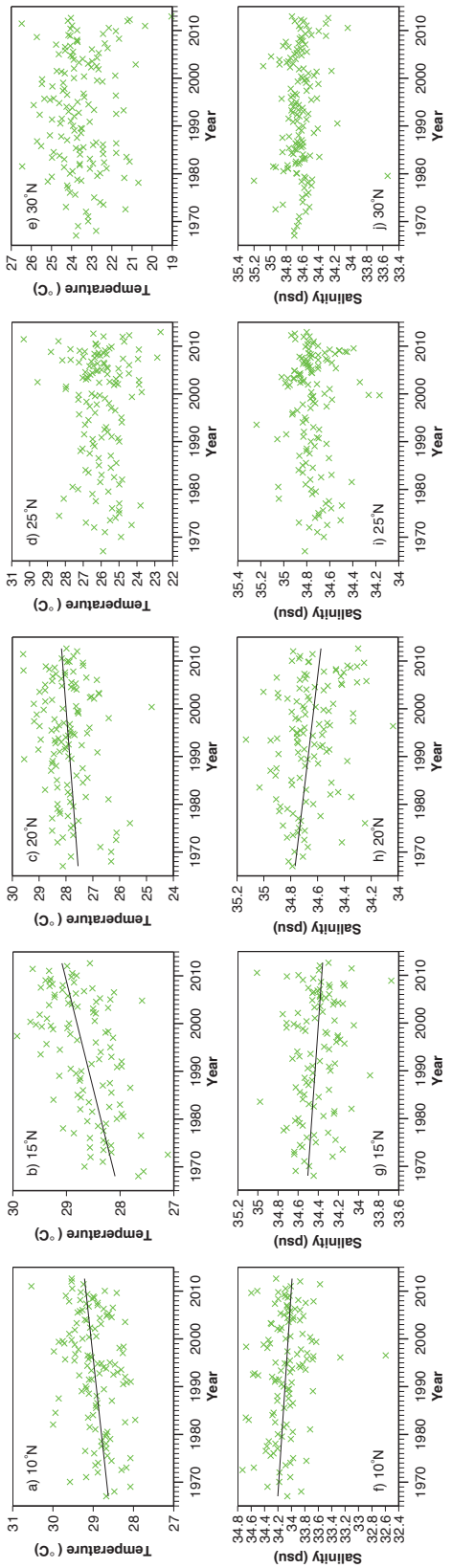

Figure 6.10: Long-term temperature and salinity trends for stations along Line 137°E.

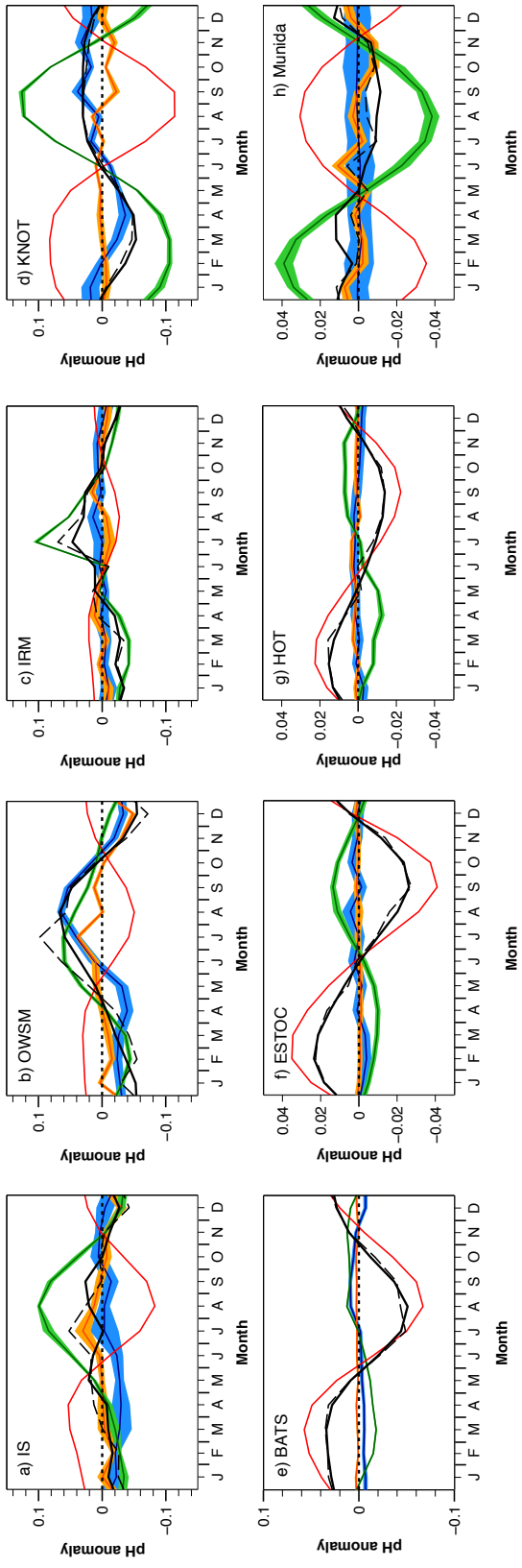

Figure 6.11: Analysis of drivers of climatological pH seasonality for various time-series. The dark red, green, blue and orange lines are the thermal, sDIC, FW and sTA forcing components, with the coloured bands around these indicating the respective uncertainties. The solid black line is the pH seasonal cycle, while the dashed black line is the sum of the four component lines and thus the pH seasonal cycle predicted from the linear decomposition analysis .The uncertainty band for the thermal forcing component is not shown as it is too small. Anomalies are from the annual mean, as is also the case for subsequent figures.

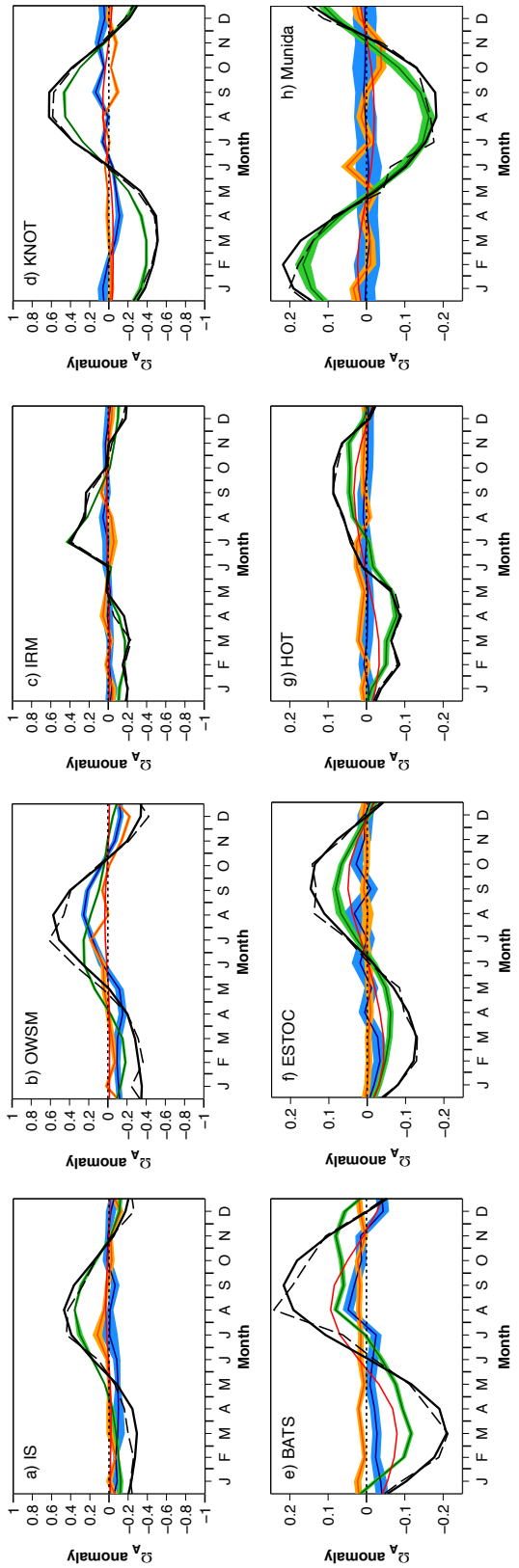

Figure 6.12: As for Fig. 6.11 but for Ω_A.

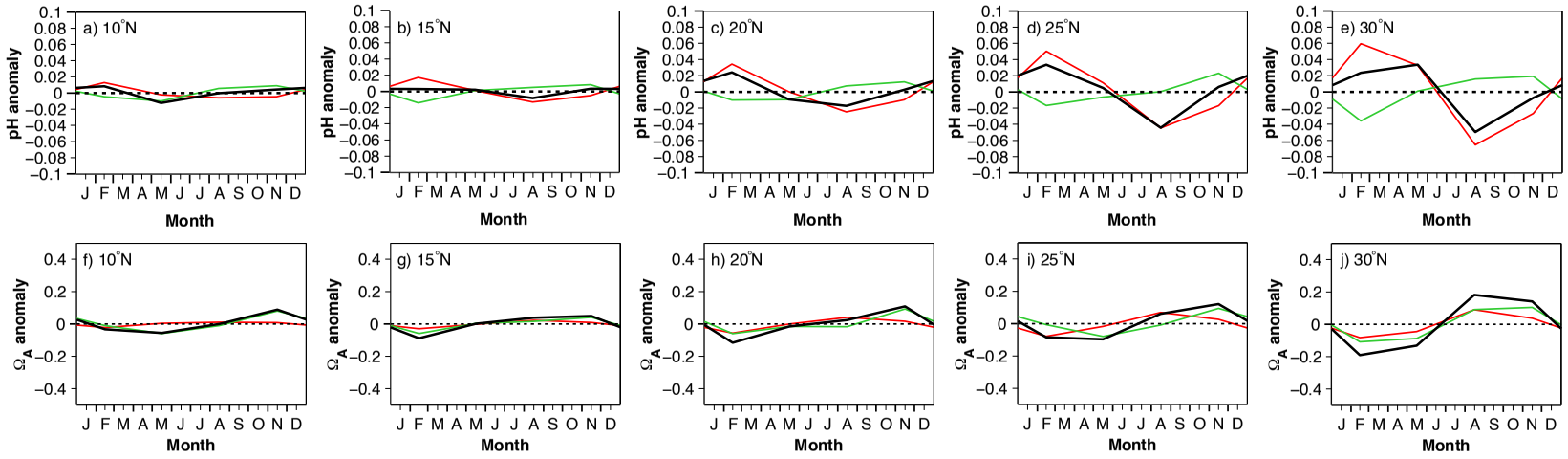

Figure 6.13: Simplified linear decomposition analysis for drivers of climatological pH and Ω_A seasonality (black lines) for stations along Line 137°E. Two forcing components are shown, thermal (red) and non-thermal (green). The non-thermal (chemical) forcing component is calculated as $\Delta Y_{chemical} = \Delta Y - \Delta Y_T$ where Y is pH or Ω_A.

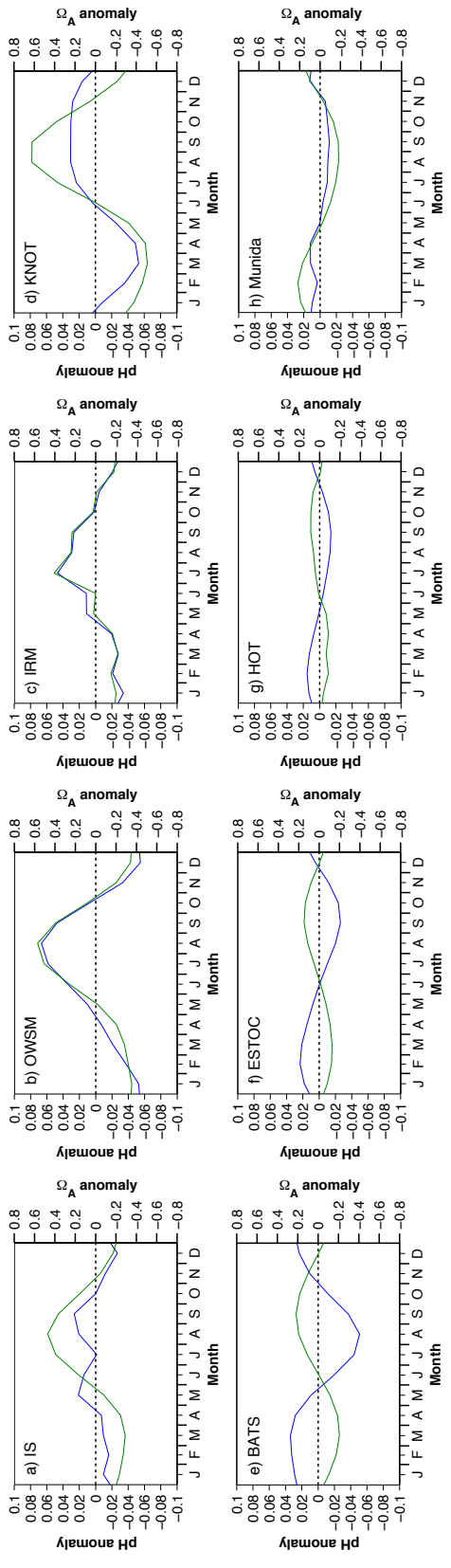

Figure 6.14: Comparison of climatological pH and Ω_A seasonal cycles at various time-series (blue and green lines, respectively). Subpolar time-series are on the top row.

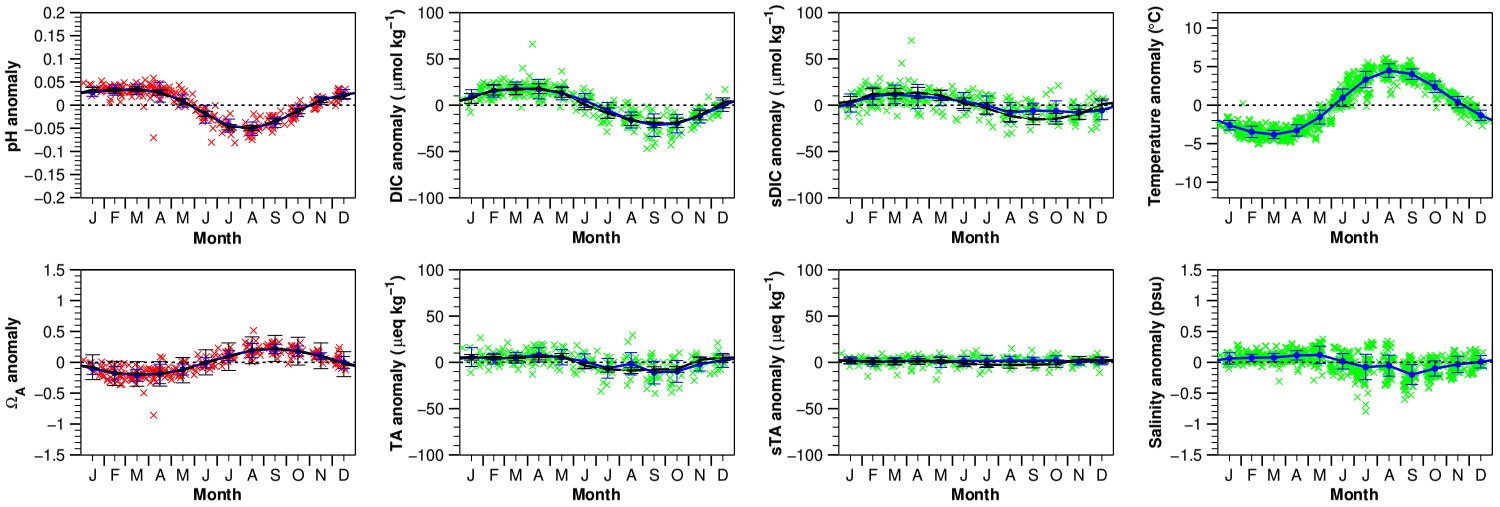

Figure 6.15: Climatological seasonal cycles for BATS/HS (blue lines). Also plotted on the pH, Ω_A, DIC and sDIC subplots are the seasonal cycles for the OISST/T09 version of the pH/Ω_A climatology derived in Chapter 7 (black dashed lines). The black lines atop the TA and sTA subplots are the respective grid cell seasonal cycles from the TA climatology derived in Chapter 5. The error bars on the blue lines show $\pm 1\sigma$, plotted for months with >3 observations. The error bars on the black dashed lines are the uncertainties on the climatological anomalies. Green and red crosses are measured and calculated values, respectively.

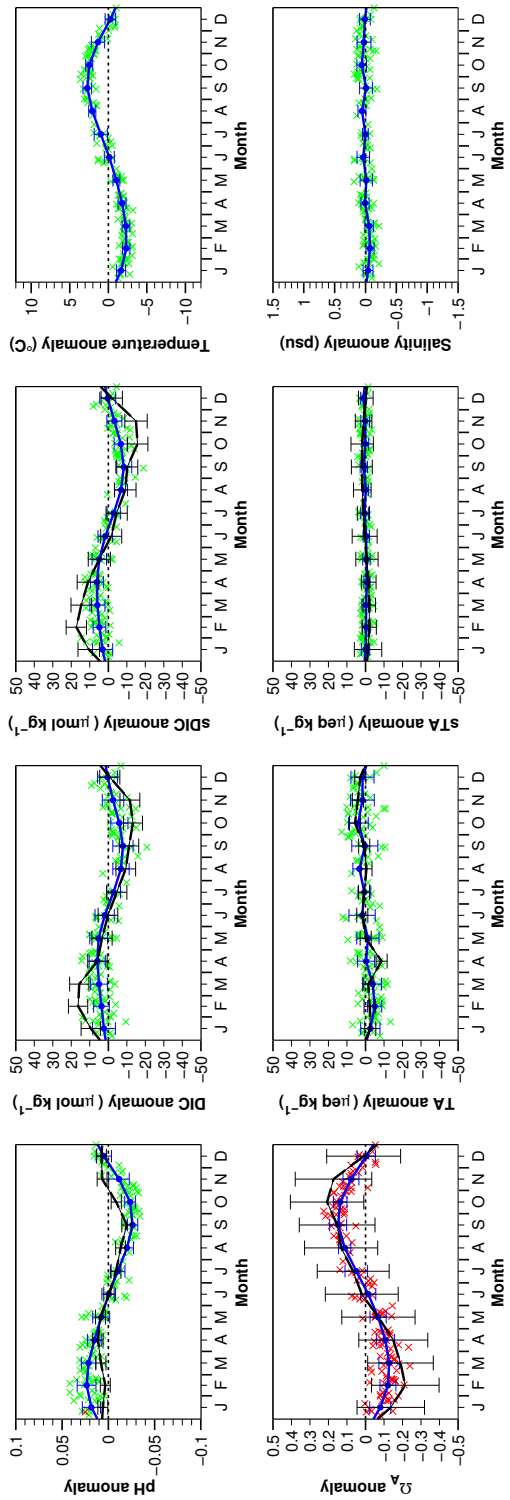

Figure 6.16: Climatological seasonal cycles for ESTOC, as for Fig. 6.15.

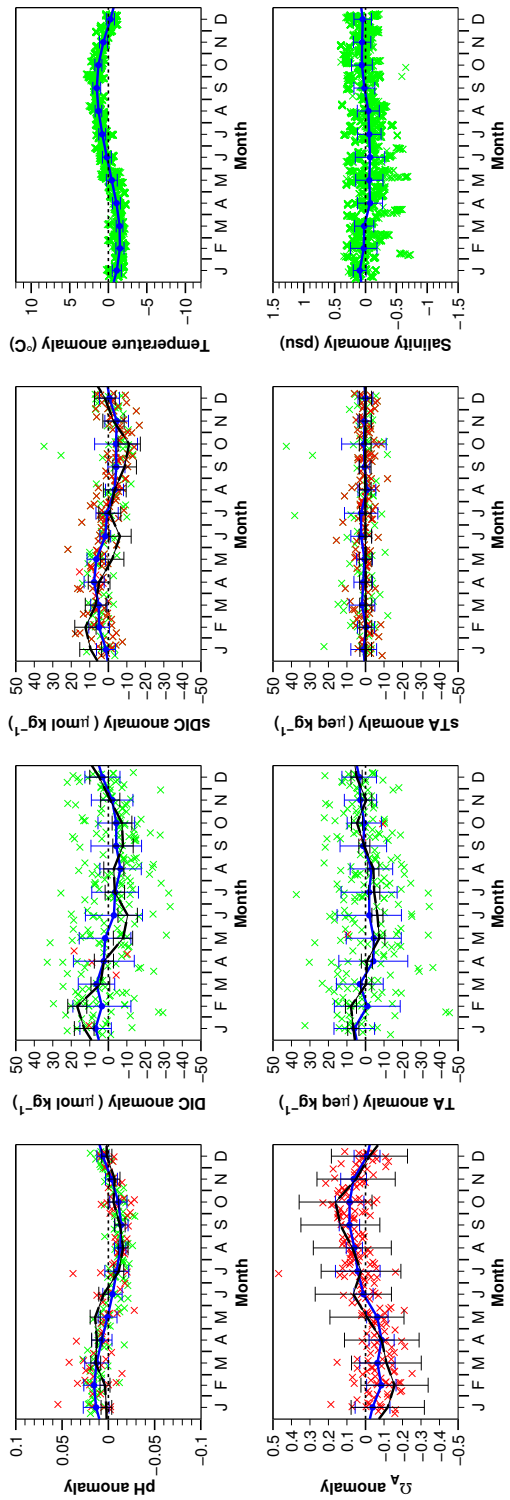

Figure 6.17: Climatological seasonal cycles for HOT, as for Fig. 6.15.

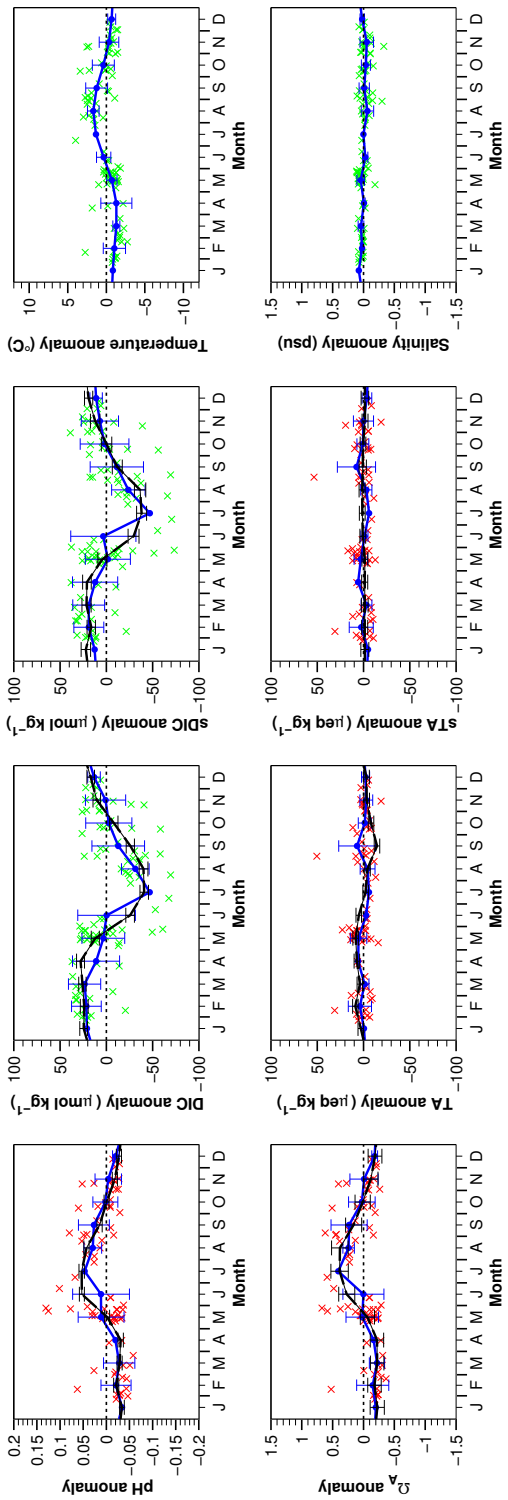

Figure 6.18: Climatological seasonal cycles for IRM, as for Fig. 6.15.

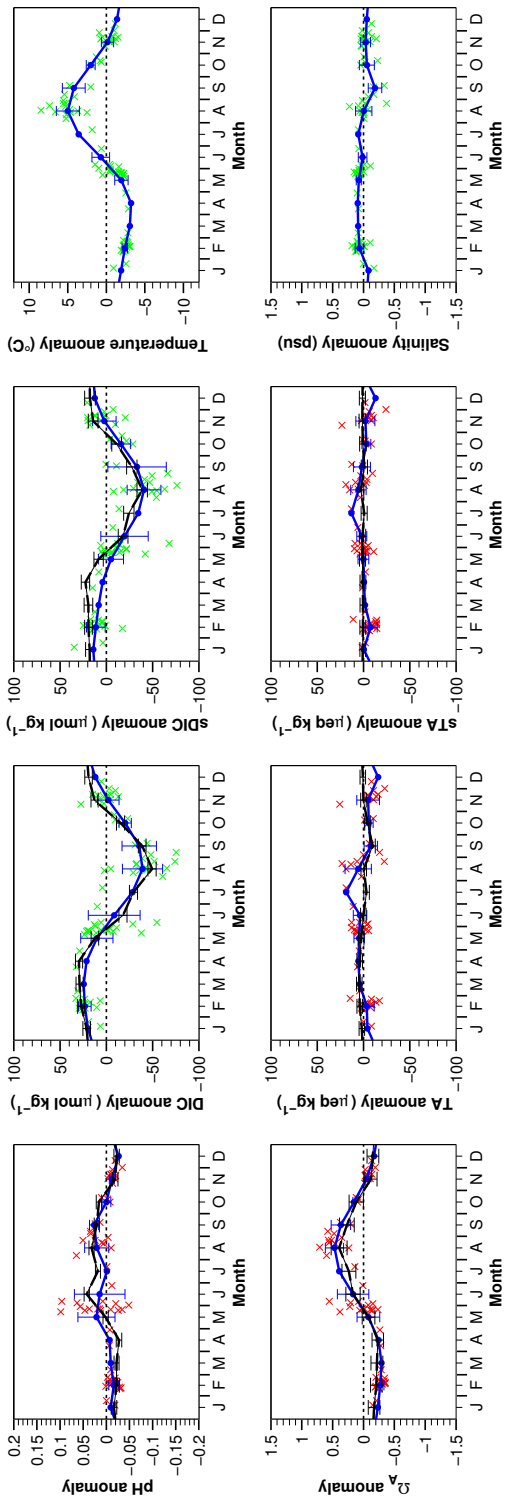

Figure 6.19: Climatological seasonal cycles for IS, as for Fig. 6.15.

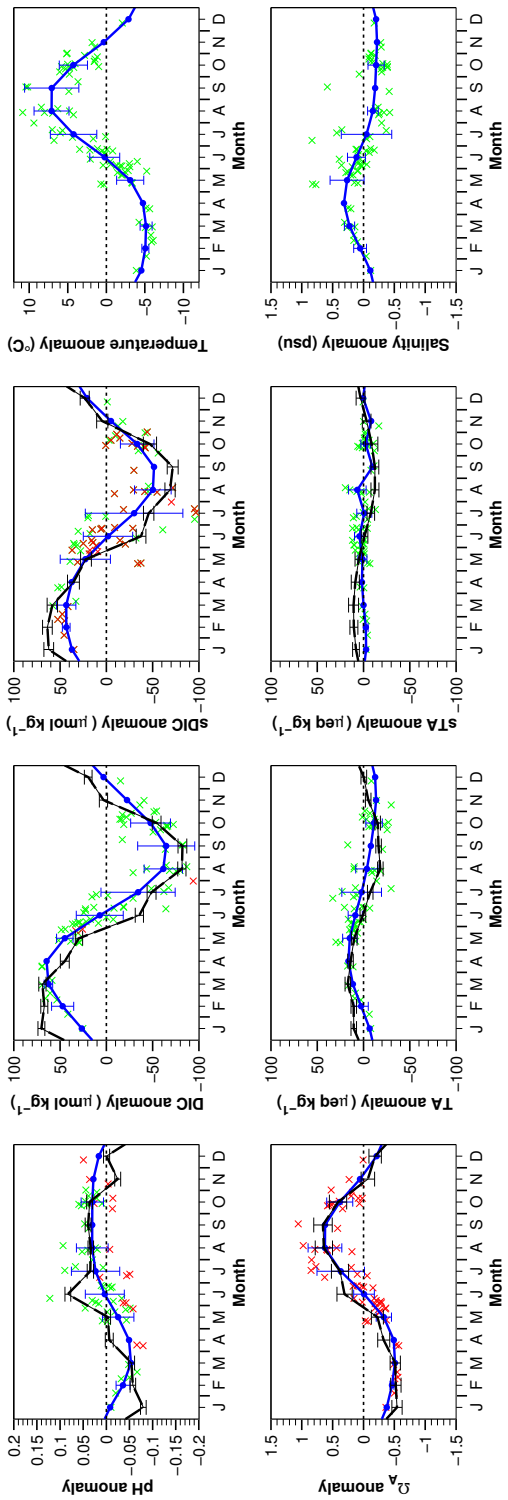

Figure 6.20: Climatological seasonal cycles for KNOT, as for Fig. 6.15.

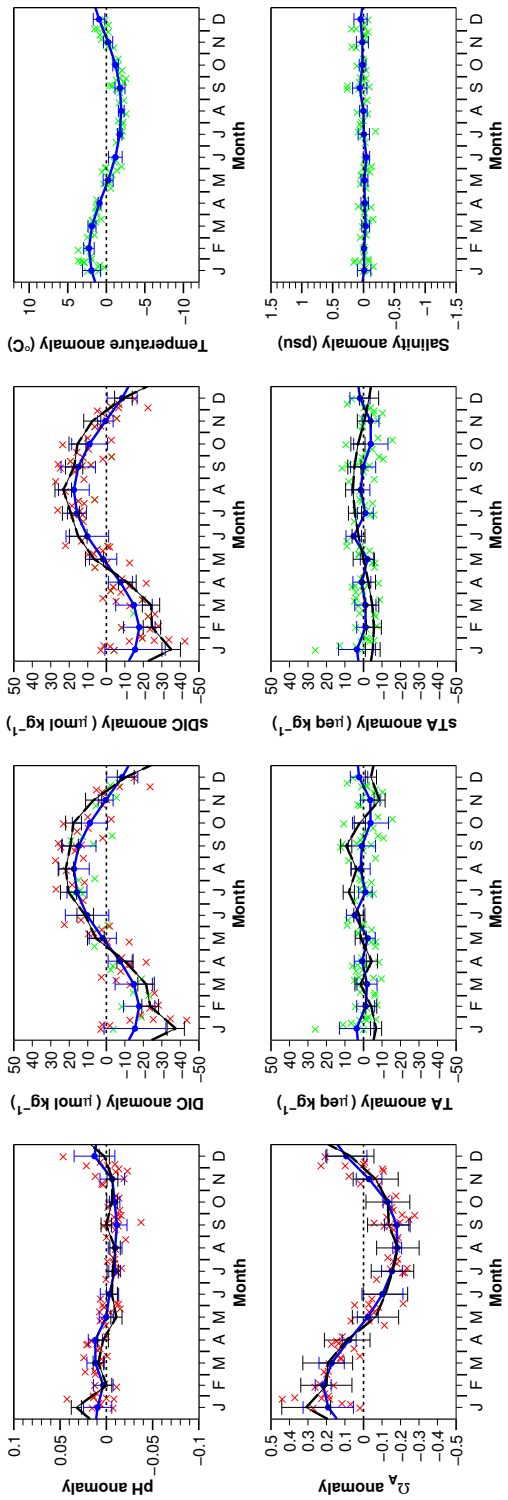

Figure 6.21: Climatological seasonal cycles for Station Munida, as for Fig. 6.15.

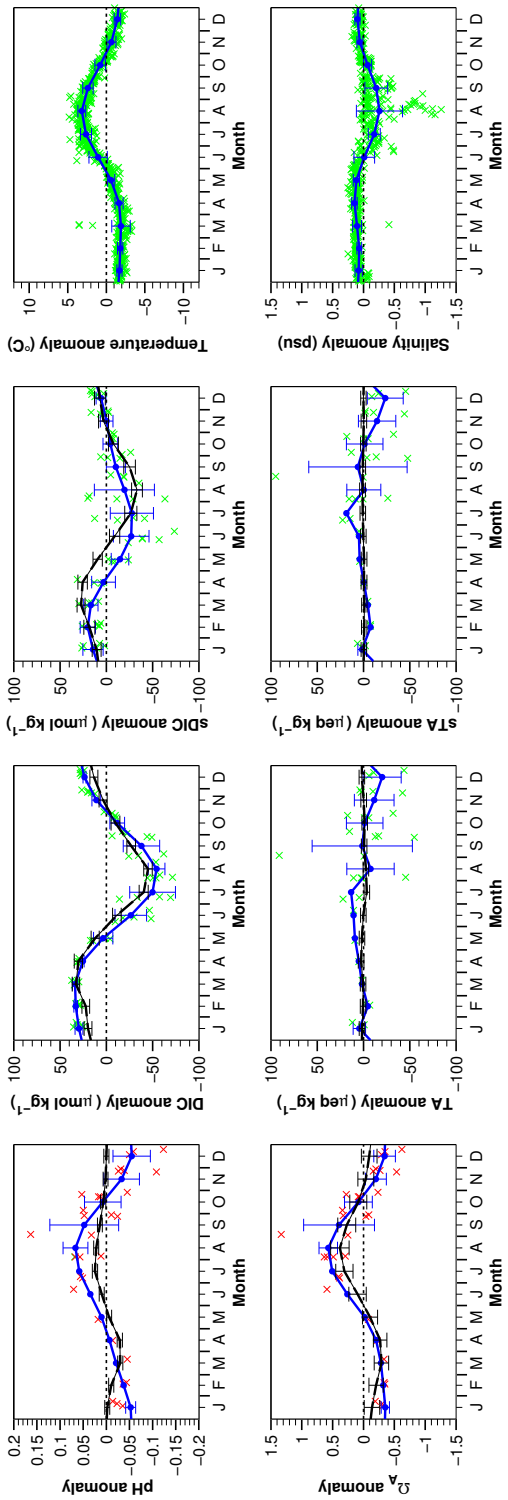

Figure 6.22: Climatological seasonal cycles for OWSM, as for Fig. 6.15.

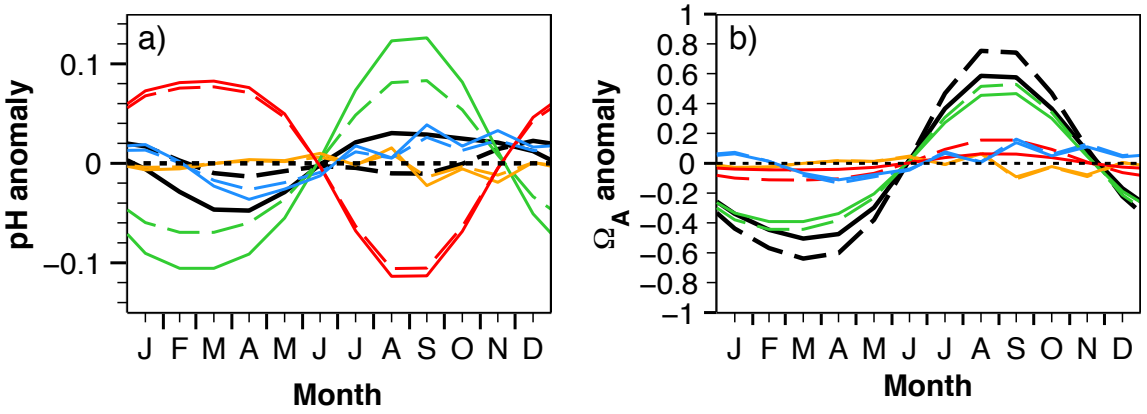

Figure 6.23: Climatological seasonal cycles for KNOT for a) pH and b) Ω_A (solid black lines) and the seasonal cycles as they would be if the seawater at KNOT had the same buffering capacity as at HOT (black dashed lines). The solid and dashed red, green, blue and orange lines are the corresponding thermal, sDIC, FW and sTA forcing components for these curves.

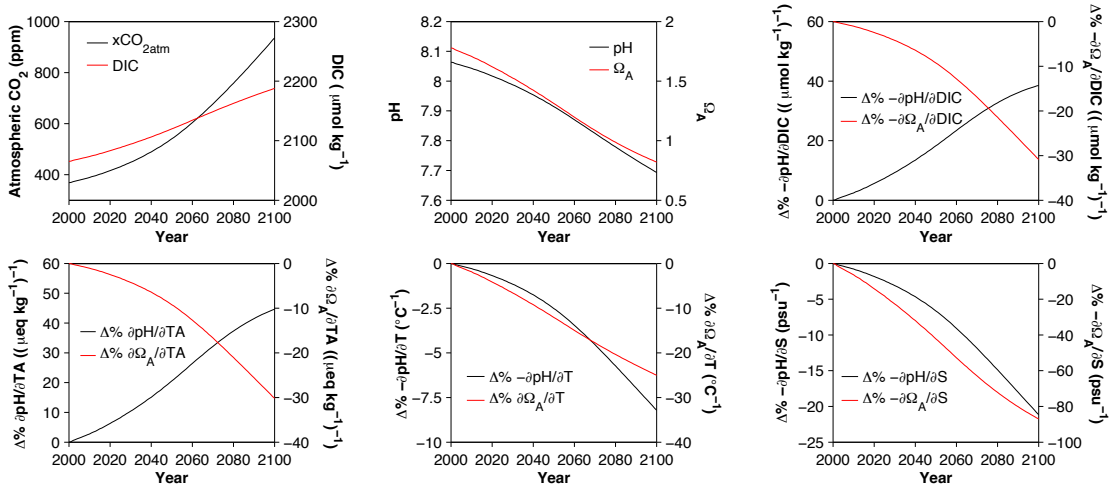

Figure 6.24: Projected changes in carbonate chemistry parameters and partial derivatives for KNOT under Representative Concentration Pathway 8.5 (no change in annual mean temperature). Percentage changes in the absolute magnitude of the partial derivatives are shown in the top right and bottom subplots.

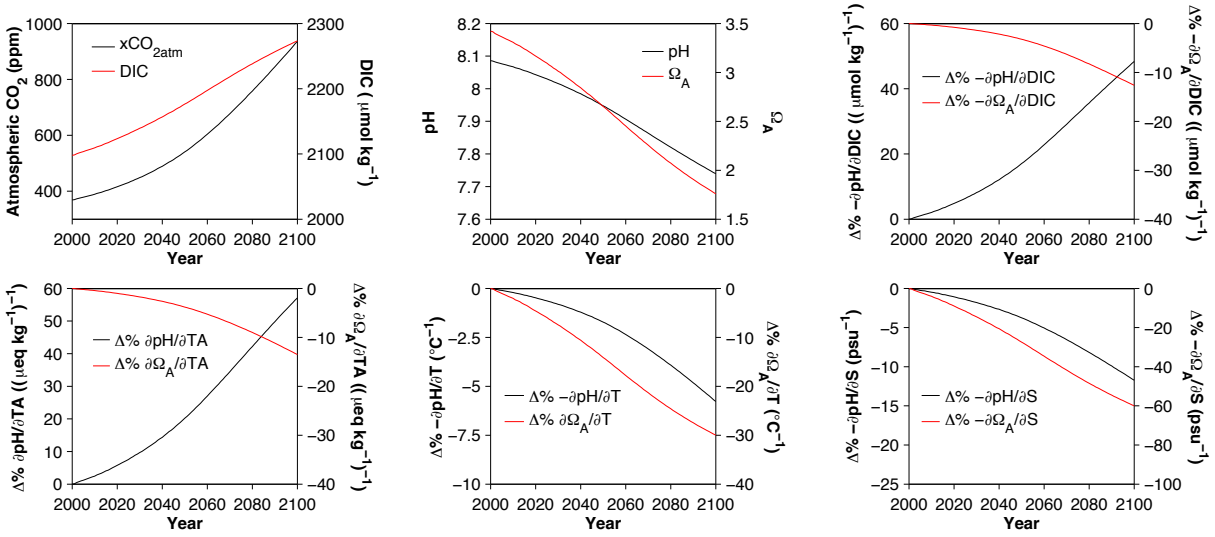

Figure 6.25: Projected changes in carbonate chemistry parameters and partial derivatives for ESTOC, as for Fig. 6.24.

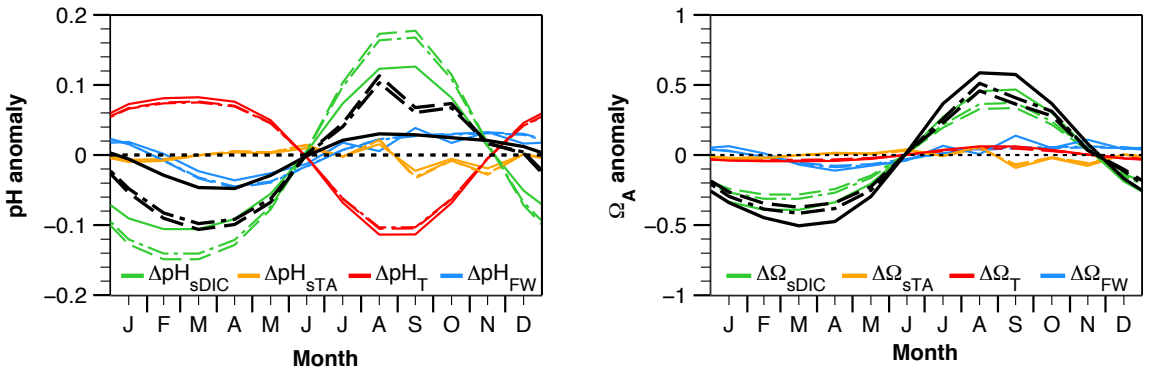

Figure 6.26: Climatological seasonal cycles and driving components for pH and Ω_A for the present-day (solid lines) and projected for 2100 for KNOT under Representative Concentration Pathway 8.5 with no SST change (dashed lines) and a 4°C increase in annual mean SST (dash-dot lines).

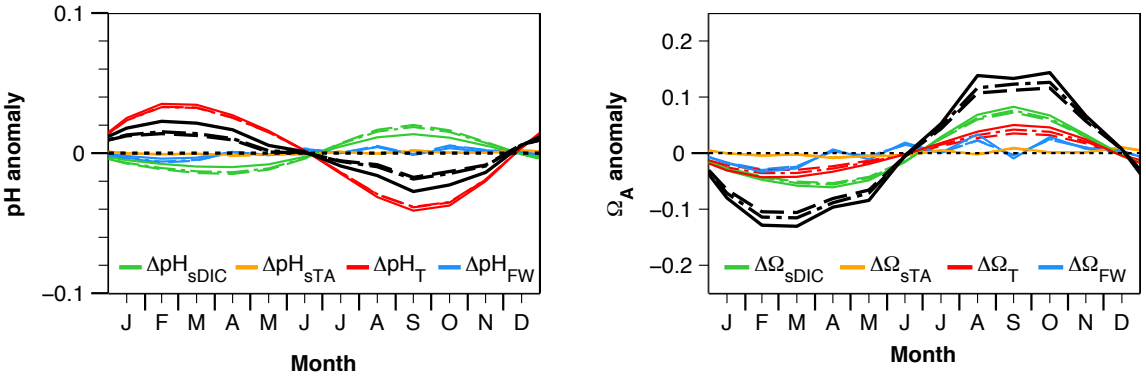

Figure 6.27: As for Fig. 6.26 but for ESTOC.

Chapter 7

Seasonal pH/Ω_A climatologies

pH is the one of the less frequently sampled observable carbonate chemistry parameters. In part due to data limitations, construction of a global-scale seasonal pH climatology directly from pH measurements has not yet been attempted. An additional difficulty with such an approach is that pH has been measured on different scales (e.g. total, seawater, NBS/NIST). Global annual mean sea surface pH fields have, however, been constructed by solving the carbonate chemistry system using DIC and TA from the GLODAP gridded product (e.g. Barry et al., 2010; Williams and Follows, 2011). Here I construct a new global-scale monthly fCO_{2sw} climatology and use it in combination with the SST and TA climatologies derived in Chapters 4 and 5 to solve the carbonate chemistry system and produce a monthly sea surface pH and Ω_A climatology on the Takahashi et al. (2009) (referred to as T09) 4°x5° grid. An additional pH/Ω_A climatology is constructed on the same grid using the T09 pCO_{2sw} climatology and an SST climatology derived from OISSTv2. This was previously referred to as the primary pH/Ω_A climatology.

7.1 Unionised CO_2 Climatologies

Two major efforts to synthesise unionised seawater CO_2 observations (i.e. xCO_{2sw}, pCO_{2sw}, fCO_{2sw}) have been undertaken in recent years, one by the Lamont-Doherty Earth Observatory (LDEO), led by Taro Takahashi and the other through the international project Surface Ocean CO_2 Atlas (SOCAT). Here I develop an original fCO_{2sw} climatology from the second version of the SOCAT database, SOCAT v2 (Bakker et al., 2013). SOCAT v2 updates the previous SOCAT database (v1.5) with

measurements from 2008-2011.

7.1.1 SOCAT v2 fCO_{2sw} climatology

The SOCAT fCO_{2sw} gridded climatology was developed from individual cruise files stored on the Publishing Network for Geoscientific and Environmental Data, known as PANGAEA (http://doi.pangaea.de/10.1594/PANGAEA.811776). Raw xCO_{2sw}, pCO_{2sw} and fCO_{2sw} observations were converted from equilibration temperature to the respective monthly temperature of the spatially corresponding grid cell of the USST climatology, following the method of T09. The aim of this method is to generate an fCO_2 climatology that is consistent with the SST climatology in terms of the temperature-driven component of the fCO_2 seasonal cycle. The method effectively removes fCO_2 variation due to diel or interannual variability in temperature. Residual seasonal variability can then be assumed due to non-thermal influences. Salinity adjustment was not attempted since the influence of salinity on pCO_2 is relatively weak ($\frac{\partial pCO_2}{\partial S} = 1\,\mu\text{atm}\,\text{psu}^{-1}$ compared to $\frac{\partial pCO_2}{\partial T} = 12\text{-}19\,\mu\text{atm}\,^{\circ}\text{C}^{-1}$). The SOCAT data processing routine 'SOCATcalcs' from SOCAT v1.5 was adapted to implement the temperature-adjustment procedure. This routine sets a preferential order for the type of unionised CO_2 input parameter (e.g. xCO_2 in dry air at equilibrium temperature) used to calculate fCO_2. Where conversion required salinity but salinity was missing, climatological values from WOA09 were used. Similarly, where equilibrator pressure was missing, measured atmospheric pressure or NCEP reanalysis pressure +3 hPa was used. Calculated pCO_{2sw} and fCO_{2sw} values were normalised to the year 2000 assuming a linear increase of $1.5\,\mu\text{atm}\,\text{yr}^{-1}$ everywhere, following T09.

Unionised CO_2 data flagged as other than WOCE flag 2 (i.e. "good") were excluded, as were coastal data from waters shallower than 200 m. Observations from El Niño months in the equatorial Pacific (10°N-10°S) were also removed for consistency with the Takahashi et al. (2009) pCO_{2sw} climatology. CO_2 outgassing is reduced during El Niño events in the equatorial Pacific. Observations from the same date and time were averaged over, except where there were >25 values or differences in distance >10 km, in which case the values were assumed suspect and discarded. These procedures left 6.2 million observations across 2196 cruises from which to generate the SOCAT fCO_{2sw} climatology. This compares with the 3 million open ocean unionised CO_2 measurements used by T09.

7.2 Method

Three pH/Ω_A climatologies were constructed by solving the carbonate chemistry system from pCO_{2sw}/fCO_{2sw}, GCP TA and WOA09 phosphate and silicate using CO2SYS (Lewis and Wallace, 1998). The primary version is derived from the T09 pCO_{2sw} climatology and OISSTv2 and is on the T09 4°x5° grid. A second version on the same grid was generated from USST and the SOCAT fCO_{2sw} climatology. A final additional climatology was generated that is the same as the primary climatology except that the input monthly T09 pCO_{2sw} values were normalised to the year 1995. This is compared against annual mean pH, Ω_A and DIC fields derived from GLODAP. A seasonally-averaged version of this climatology (with seasons JJA, SON, DJF, MAM) is compared against pH, Ω_A and DIC derived from the McNeil et al. (2007) DIC/TA Southern Ocean climatology.

Different formulations for the carbonic acid dissociation constants were used dependent on temperature to account for the variable valid temperature range of each. The carbonic acid dissociation constants of Mehrbach et al. (1973) as refit by Dickson and Millero (1987) were used for SST $\geq$2°C, Millero et al. (2006) for 0$\leq$ SST <2°C and Millero et al. (2002) for SST <0°C.

To estimate the uncertainty on each calculated monthly mean value, a Monte Carlo analysis was conducted in which 1000 Gaussian distributed randomised values were generated for each monthly mean value, with mean equal to the value and standard deviation equal to its estimated uncertainty. The uncertainty on the GCP TA monthly means was taken to be 3 μeq kg^{-1}. The monthly grid cell standard errors from SOCAT fCO_{2sw} and USST were used for the uncertainties on pCO_{2sw}/fCO_{2sw} and SST. Standard errors from WOA09 were used for the uncertainties on salinity, phosphate and silicate. Monthly latitudinal-average errors were used in place of missing values. Uncertainty in the carbonic acid dissociation constants and aragonite solubility product constant was taken into account using the same method, with generation of 1000 randomised values for each of K_0, $K_1^{'}$, $K_2^{'}$ and $K_{sp_A}^{'}$ for each set of inputs ($K_{sp_A}^{'}$ being the solubility product for aragonite). These were distributed with standard deviations equivalent to percentage uncertainties of 0.5, 1.3, 2.3 and 5%, respectively. The standard deviation of the randomised output values from CO2SYS was taken as the uncertainty on the respective monthly value. Uncertainties on the calculated monthly mean values range from 0.005-0.01 for pH, 0.05-0.2 for Ω_A and 3.5-9.5 for DIC.

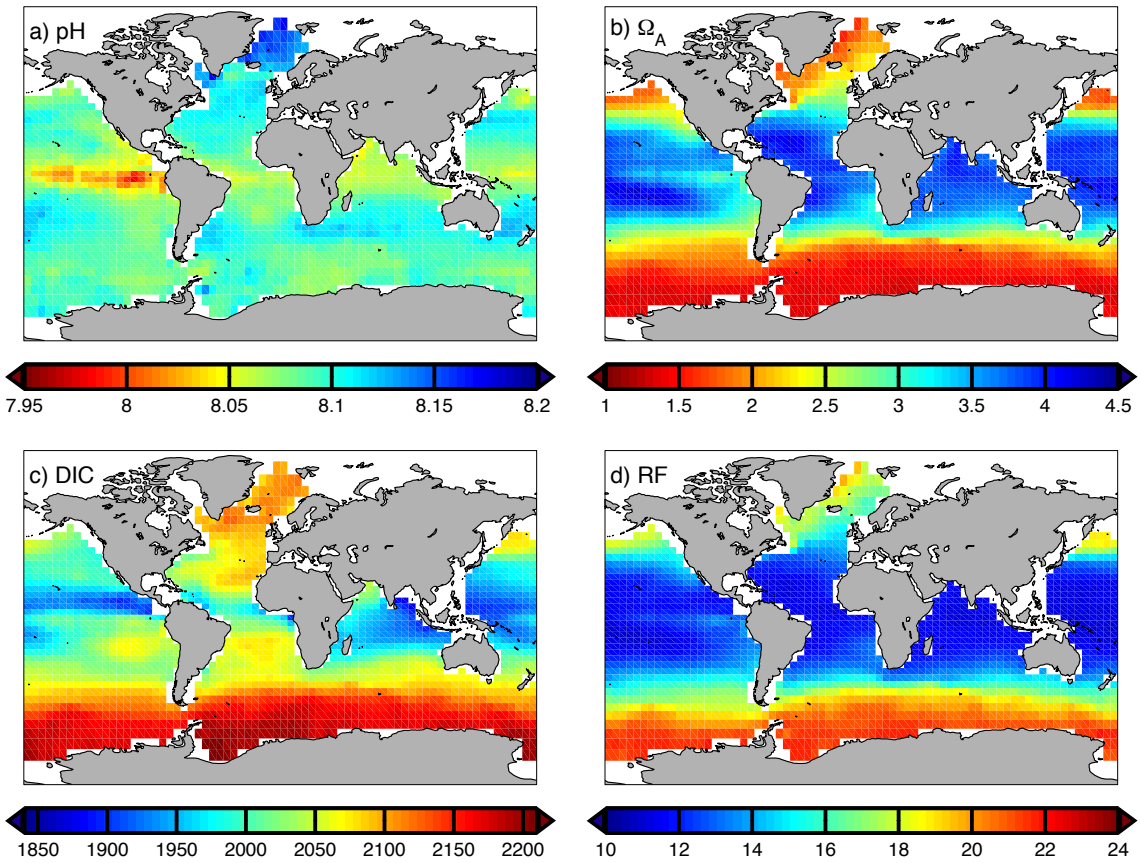

Figure 7.1: Annual mean fields for the primary version of the pH/Ω_A climatology. As for the other figures, DIC is in μmol kg^{-1}. The Revelle buffer factor (RF) is dimensionless.

Following the same method as for the time-series, a linear decomposition analysis was conducted to investigate the drivers of pH and Ω_A seasonality for the primary climatology. Uncertainties in the forcing components were estimated using Gaussian error propagation, randomising the monthly anomalies for sDIC, sTA, SST and SSS. Uncertainties on the partial derivatives were assumed negligible and thus neglected. Monthly ΔTAs and ΔsTA values were computed on the 1°x1° GCP TA grid as $\frac{\partial TA}{\partial S}\Delta S$ and $\Delta TA - \frac{\partial TA}{\partial S}\Delta S$, with $\frac{\partial TA}{\partial S}$ being computed directly from the GCP TA formulations. ΔsTA values were regridded from the 1°x1° WOA grid to the 4°x5° T09 grid by area-weighted averaging for the linear decomposition analysis.

7.3 Results and discussion

7.3.1 Annual mean

On an annual average pH tends to be lower in the tropics, particularly in the eastern equatorial Pacific upwelling region (Fig. 7.1a). Relatively high values (>8.12) are found in the northern north Atlantic. High values (>8.1) are also found at 20-45°S in the Indian Ocean and western Pacific and Atlantic, and subtropical/subpolar north Atlantic.

In comparison between pH from the pH/Ω_A climatology and that derived from GLODAP (Figs. 7.2c,d and 7.3b), we find that several maxima and minima are more pronounced for GLODAP. pH is lower in GLODAP in the Weddell Sea by 0-0.1 and higher to its north and in the northern Ross Sea by 0.05-0.15. pH is also higher in GLODAP in the Labrador current and Oyashio (by 0.05-0.2) and in a portion of the Indian ocean sector of the Southern Ocean (by 0.05-0.12). pH is lower adjacent to the northeast coast of Australia by 0.02-0.12. Similar spatial patterns in the differences are seen for DIC and Ω_A. The pH and Ω_A differences appear largely due to discrepancies between the DIC climatologies (Fig. 7.3a), with the spatial pattern of deviations being different for the comparison of GCP TA and GLODAP TA (Fig. 4.1d). Higher DIC values result in lower pH and Ω_A and vice versa, *ceteris paribus* (i.e. all other things being constant).

Annual mean Ω_A (Fig. 7.1b) shows a clear contrast between higher values (>3) in warm, tropical waters and lower values at mid to high latitudes. In the tropical Atlantic and Pacific, the values tend to be higher on the western side of the basins, away from the upwelling zones on the eastern boundaries. Values below 3 are found in the eastern equatorial Pacific upwelling, with these low saturation conditions suggested as a reason why the warm water coral reefs of the region tend to be poorly developed (Manzello et al., 2008). There is also an east-west divide in the subpolar and northern north Atlantic, with low saturation states in the Labrador, Irminger, Iceland and Greenland Seas and higher saturation states in the Gulf Stream and north Atlantic drift. This division is less pronounced in GLODAP Ω_A, although the distribution is otherwise similar (Figs. 7.2e,f and 7.3c).

Annual mean DIC is high in the Southern Ocean and subpolar north Atlantic and Nordic Seas and generally low in the tropical Indian Ocean, western tropical Pacific and eastern Pacific upwelling (Fig. 7.1c). DIC is found to be particularly high in the

Weddell Sea. GLODAP DIC shows a similar pattern (Fig. 7.2a,b) and suggests that DIC is fairly low (<2000 μmol kg^{-1}) in two regions not covered by the new pH/Ω_A climatologies; the Sea of Okhotsk and eastern Gulf of Alaska.

The Revelle buffer factor has a spatial distribution approximately opposite to that of Ω_A, being high in the Southern Ocean, subpolar north Atlantic and Pacific and Nordic Seas and low in the tropics and subtropics (Fig. 7.1d).

7.3.2 Comparison with McNeil et al. (2007)

Annual mean DIC from the 1995-normalised version of the pH/Ω_A climatology shows a similar distribution in the Southern Ocean to that from M07 (Figs. 7.4a,b and 7.7a). DIC tends to be high south of the Polar Front, particularly in the Weddell Sea. Overall, DIC tends to be higher in the pH/Ω_A climatology than in M07, with a mean difference$\pm\sigma M$ (standard error on the mean) of 5.6$\pm$0.29 μmol kg^{-1}. The spatial distributions of annual range are also similar (Figs. 7.4c,d and 7.8a), with ranges >45 μmol kg^{-1} found along the Antarctic continental shelf, in the northern Weddell Sea and east of southern Argentina. The mean difference$\pm\sigma M$ between the annual ranges is small at 1.8$\pm$0.5 μmol kg^{-1} (Fig. 7.8a).

Annual mean pH tends to be low south of the Polar Front (Fig. 7.5a,b). The differences between the climatologies are mostly small, with a mean difference$\pm\sigma M$ of -0.01$\pm$0.00 (Fig. 7.7b). However, the pH/Ω_A climatology does have lower pH by -0.02 to -0.035 in the subtropical southeast Pacific. The seasonal pH range is relatively small throughout the Southern Ocean (<0.05; Fig. 7.5c,d), except along the Antarctic continental shelf in the Pacific sector and northern Weddell Sea. There is essentially no mean difference between the climatological annual ranges (mean difference$\pm\sigma M$ of 0.00$\pm$0.00; Fig. 7.8b).

Like DIC, annual mean Ω_A shows a similar divide about the polar front (Fig. 7.6a,b), except with lower values to the south and higher to the north. The Ω_A values tend to be lower by 0.05 to 0.2 in the pH/Ω_A climatology north of the subantarctic front in the southeast Pacific, otherwise the differences between the climatologies are mostly small (within $\pm$0.1, Fig. 7.7c). The mean difference$\pm\sigma M$ is -0.04$\pm$0.00. The Ω_A seasonal range appears relatively small (<0.5) throughout most of the Southern Ocean (Fig. 7.6c,d), with the exception of a region to the east of southern Argentina. There is minimal mean difference between the climatological annual ranges (mean difference$\pm\sigma M$ of 0.02$\pm$0.04; Fig. 7.8c).

7.3.3 Seasonal range and drivers

pH seasonality is relatively small (annual range <0.05) in the tropics outside the eastern equatorial Pacific, and at 50-60°S in the Southern Ocean (Fig. 7.9a). Seasonal variation in temperature and sDIC tends to be small in the tropics. Moderate pH seasonality (annual range of 0.05-0.12) is found for the eastern equatorial Pacific, driven by sDIC (Fig. 7.11b). pH seasonality is moderate to large (annual range 0.05-0.1) in the subtropical north Atlantic and Pacific at 20-40°N, where it is predominantly thermally driven. pH being inversely related to temperature, the seasonal maxima in this region occur in boreal winter and the minima in boreal summer (Fig. 7.10 and 7.12). Small to moderate SST-driven seasonality (annual range of 0.03-0.1) also occurs at 20-40°S in the Atlantic and Indian oceans (Fig. 7.11a). The nature of pH seasonality and its drivers by latitude band are summarised in Figs. 7.12, 7.13 and 7.14.

pH seasonality is found to be large (annual range >0.05) in the Weddell, northern Ross, Irminger and Iceland seas, Oyashio current and western subarctic Pacific, driven by sDIC. Seasonal ranges are >0.1 in places. The seasonal maxima occur in the respective hemispheric summer and the minima in winter. The seasonal minima occur around March and September, respectively, at the high latitudes of the northern and southern hemispheres (Fig. 7.19). DIC and sDIC variation is generated by entrainment of DIC-rich waters into the mixed layer in winter and biological drawdown from phytoplankton blooms in spring and summer (Fig. 7.17). Seasonality is fairly small at 40-50°N in the subpolar north Atlantic (annual range <0.05) where sDIC and SST-driven variability partially cancel. Modest salinity-driven pH variation is found for the Labrador and Greenland Seas (Fig. 7.11d), where the climatological salinity range exceeds 1 psu. The contribution of sTA variation to pH seasonality is found to be small everywhere (Fig. 7.11c).

Ω_A seasonality is generally small in the tropics (Fig. 7.9b), outside the eastern equatorial Pacific and Atlantic upwelling regions, and everywhere driven by sDIC variation (Fig. 7.16b). The seasonal minima occur in the respective hemispheric winter (around March in the northern hemisphere and around September in the southern, Fig. 7.19) and the maxima in summer (Fig. 7.15 and 7.18). Temperature-driven variations slightly enhance seasonal ranges in the subtropics (Fig. 7.16a). Large seasonal ranges (>0.5) are found in the northern hemisphere mid-latitudes (30-60°N), Norwegian Sea and southern hemisphere subtropics. The largest seasonal ranges are

found in the Oyashio and western subarctic Pacific, where seasonal sDIC variation is large (Fig. 6.20). Ω_A seasonality is small in the Greenland Sea, despite sizeable salinity-driven variation (Fig. 7.16d). As for pH, sTA variation has minimal influence on Ω_A seasonality (Fig. 7.16c).

DIC seasonality is large (seasonal range $>50\,\mu\mathrm{mol\,kg^{-1}}$) in the Antarctic seasonal sea ice zone, eastern equatorial Pacific, western subarctic Pacific, the subtropical/subpolar north Atlantic and Nordic Seas (Fig. 7.9c). Annual ranges exceeding $125\,\mu\mathrm{mol\,kg^{-1}}$ are found for the Greenland and Iceland Seas and Oyashio.

As for the time-series, the seasonal pH and Ω_A cycles are found to be in-phase at subpolar latitudes, where sDIC variation exerts the dominant influence on pH seasonality (Fig. 7.18), and in anti-phase in the subtropics where pH seasonality is predominantly thermally-driven. The seasonal pH and Ω_A maxima and minima thus occur in different seasons in the subtropics (Fig. 7.19). Hence whether an organism is more sensitive to pH or CO_3^{2-} may be an important consideration for predicting the progression of the biological impacts of acidification here.

7.3.4 Comparison to SOCAT

The spatial distribution of grid cells with values in the uninterpolated SOCAT pH/Ω_A climatology reveals where there are sufficient unionised CO_2 observations to accurately constrain carbonate chemistry seasonality (Fig. 7.20). We find that coverage is poor in the southern hemisphere and good throughout most of the northern hemisphere, except in the Indian Ocean.

Some notable discrepancies are apparent between the seasonal ranges for the SOCAT version of the pH/Ω_A climatology and those of the primary version. For pH, we find that the minima in the subtropical/subpolar north Atlantic and subarctic Pacific found in the primary version are less apparent in the SOCAT version (7.9a, 7.20a, 7.21a). pH seasonality is also larger in the Norwegian Sea for the SOCAT version. The differences appear largely due to the use of different pCO_{2sw}/fCO_{2sw} climatologies rather than different SST climatologies. The seasonal pCO_{2sw} range is enhanced in the SOCAT climatology relative to T09 in the Labrador current, Norwegian Sea and central subarctic Pacific (Fig. 7.21d). Similar differences are apparent for DIC between the primary and SOCAT pH/Ω_A climatologies (Figs. 7.9c, 7.20c and 7.21c). Relative to T09, SOCAT improves coverage for 50-60°N in the subpolar north Atlantic and in the Nordic Seas.

Compared to pH, more of the seasonal ranges for Ω_A for the SOCAT version lie within the uncertainty range for the primary version, with the spatial pattern of the seasonal ranges being fairly similar (Fig. 7.20b). However, the annual ranges for the SOCAT version are still distinctly larger in the Norwegian Sea and Labrador current (Figs. 7.9b, 7.20b and 7.21b).

7.4 Conclusions

From the primary new pH/Ω_A climatology developed here I that find annual average pH tends to be low in the tropics, subarctic Pacific and Southern Ocean and particularly so in the eastern equatorial Pacific. In contrast, pH is relatively high in the Nordic Seas, subpolar north Atlantic and southern hemisphere subtropics. Annual mean Ω_A is high in the tropics outside the eastern equatorial Pacific and relatively low in the Southern Ocean, subarctic Pacific and Labrador, Irminger and Nordic Seas. The annual mean pH and Ω_A fields derived from the GLODAP product show similar spatial patterns to those from the primary climatology, although pH is higher by 0.05-0.2 in the former in the Labrador current and Oyashio. In the Southern Ocean, the annual means and ranges for pH and Ω_A are similar for both the primary pH/Ω_A climatology and that derived from the McNeil et al. (2007) DIC/TA climatology.

pH seasonality is relatively small in the tropics, outside the eastern equatorial Pacific, and moderate to large in the subtropics, where it is predominantly temperature driven. Large sDIC-driven seasonal cycles are found at high latitudes in the western subarctic Pacific and Ross, Weddell, Iceland and Irminger seas. sDIC variation tends to counteract the influence of SST on pH seasonality.

Ω_A seasonality is also small in the tropics, outside the eastern equatorial Pacific. Seasonality is moderate to large in the southern hemisphere subtropics and mid- to high latitude north Atlantic and Pacific. Ω_A seasonality is everywhere primarily driven by sDIC variation, although is modestly enhanced by SST seasonality in the subtropics.

Comparing the SOCAT pH/Ω_A climatology to the primary climatology we observe that the seasonal range minima in the subtropical/subpolar north Atlantic and subarctic Pacific found in the latter are less apparent in the former. This appears due to the use of a different unionised CO_2 climatology. The pH/Ω_A climatology appears insensitive to the depth range of the observations used to derive the SST climatology.

pH and Ω_A seasonal cycles are in-phase where sDIC exerts the dominant in-

fluence on seasonal pH variation and in anti-phase where pH seasonality is mainly temperature-driven. The maxima and minima of each occur in different seasons in the latter case, which may be of relevance to the biological impacts of acidification.

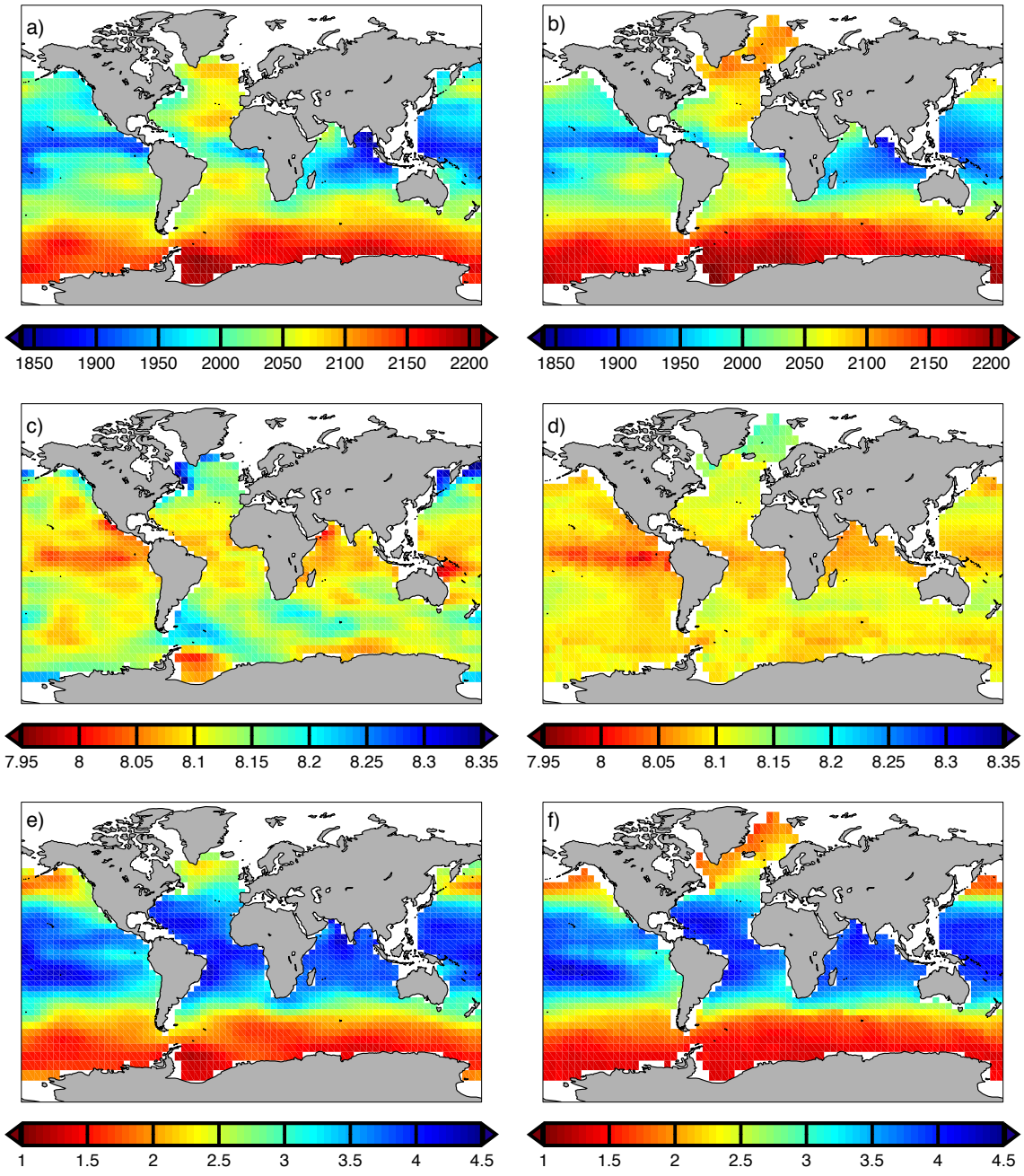

Figure 7.2: Annual mean sea surface a) DIC, c) pH and e) Ω_A derived from the GLODAP gridded product (regridded to the 4°x5° T09 grid) and b) DIC, d), pH and f) Ω_A from the 1995-normalised version of the primary (T09/OISST) pH/Ω_A climatology.

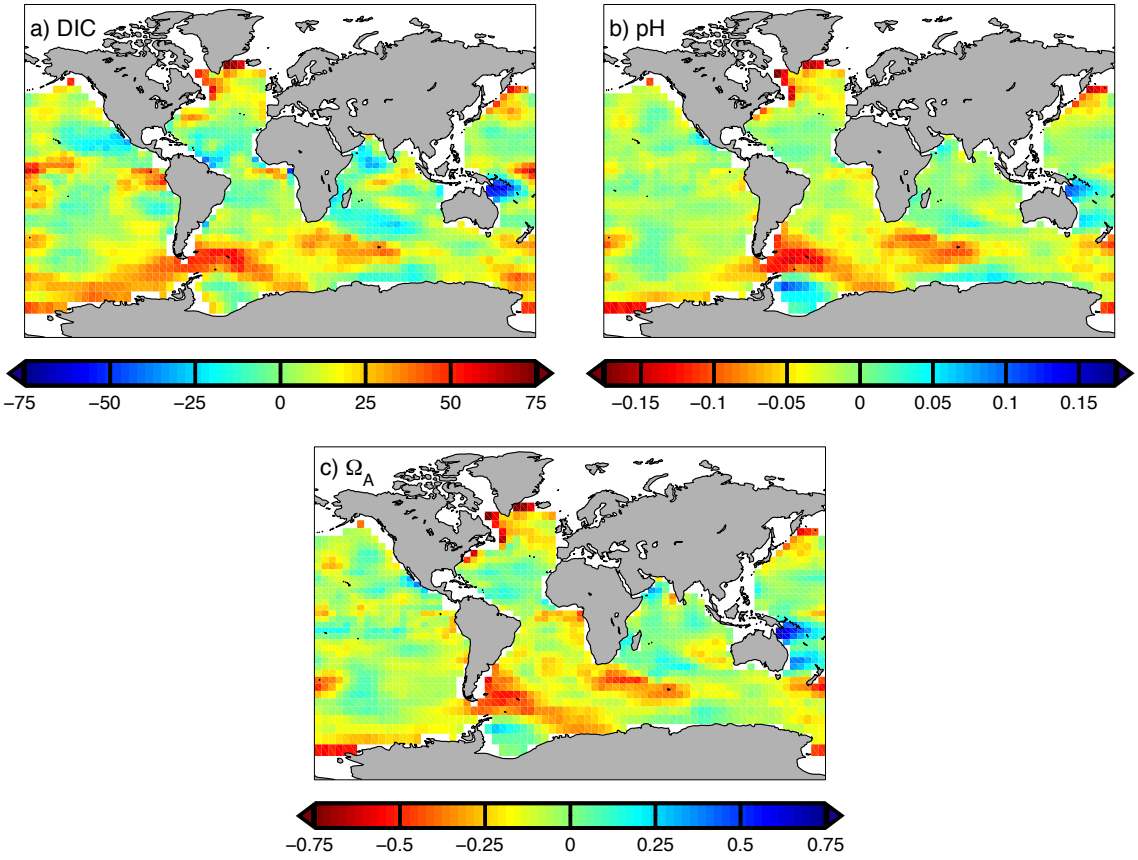

Figure 7.3: Difference between the annual mean fields in Fig. 7.2, i.e. those from the 1995-normalised version of the pH/Ω_A climatology minus those derived from GLODAP.

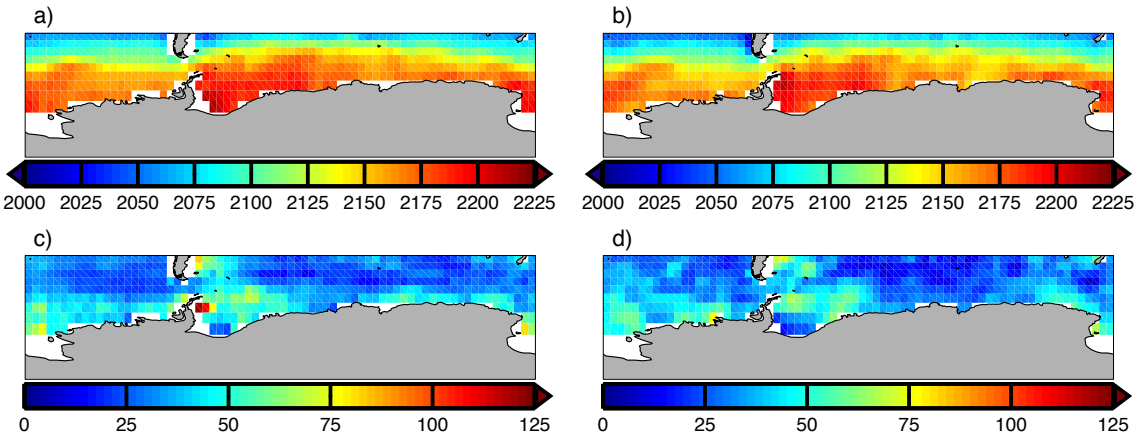

Figure 7.4: Annual means and ranges for DIC in the Southern Ocean from the 1995-normalised version of the pH/Ω_A climatology (a and c, respectively) and the McNeil et al. (2007) climatology (b and d, respectively; regridded to the 4°x5° T09 grid).

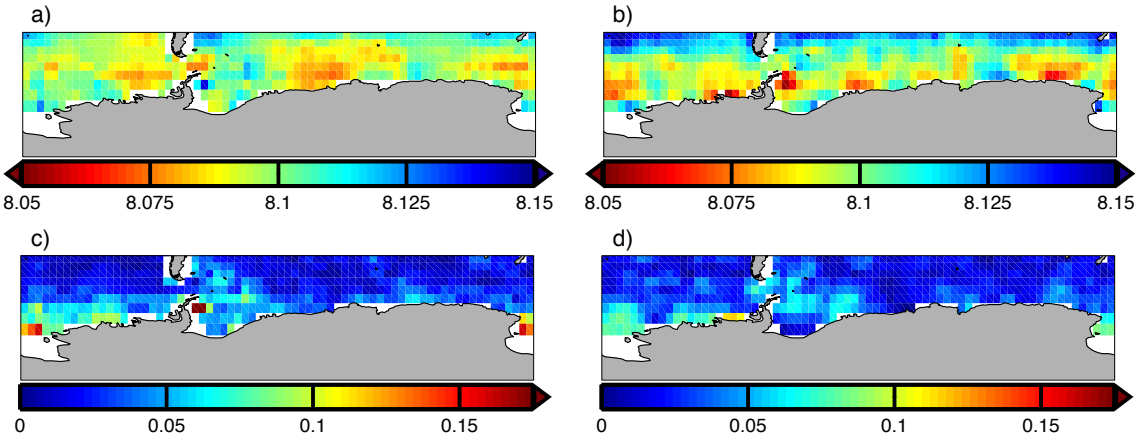

Figure 7.5: As for Fig. 7.4 but for pH.

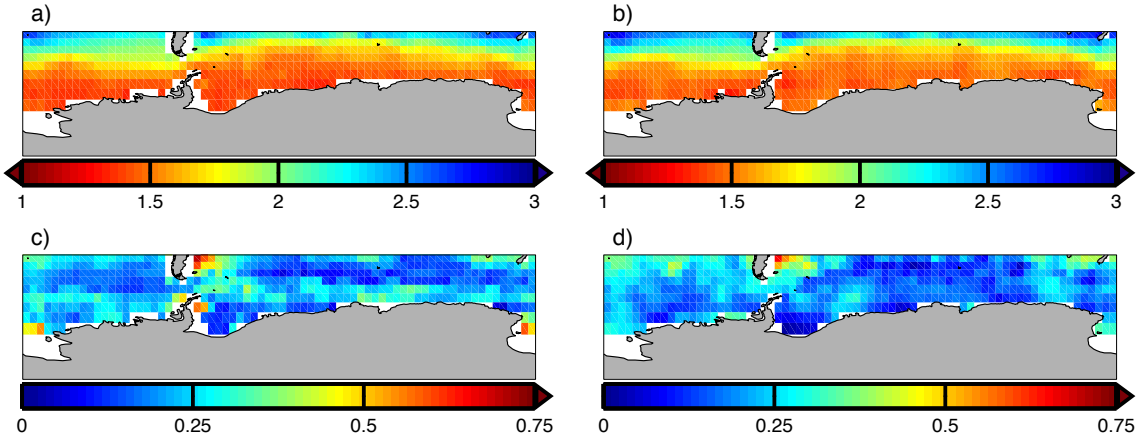

Figure 7.6: As for Fig. 7.4 but for Ω_A.

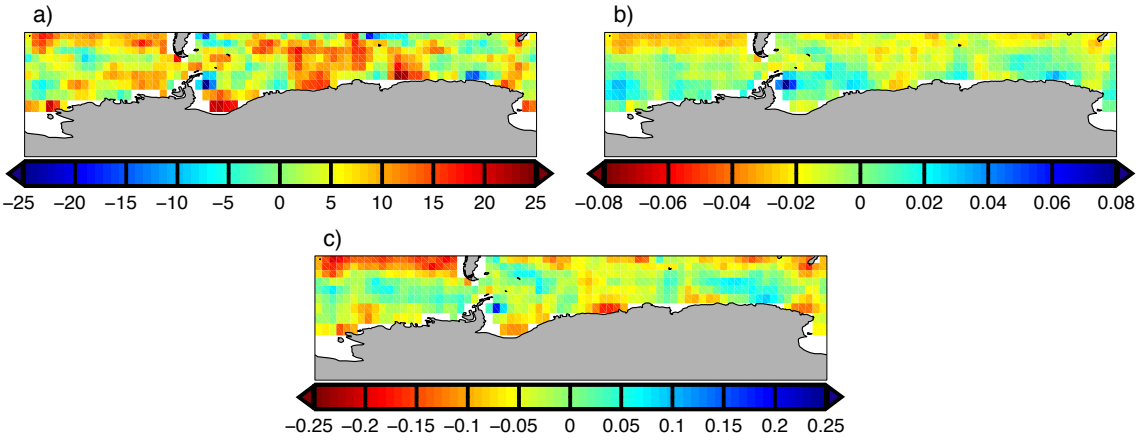

Figure 7.7: Difference between the 1995-normalised version of the pH/Ω_A climatology and fields derived from M07 for annual mean a) DIC, b) pH and c) Ω_A.

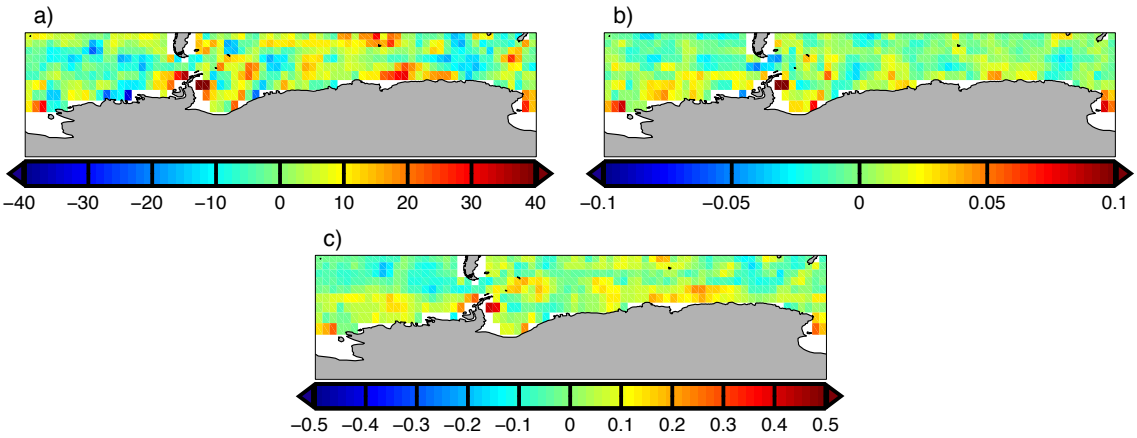

Figure 7.8: As Fig. 7.7 but for annual range.

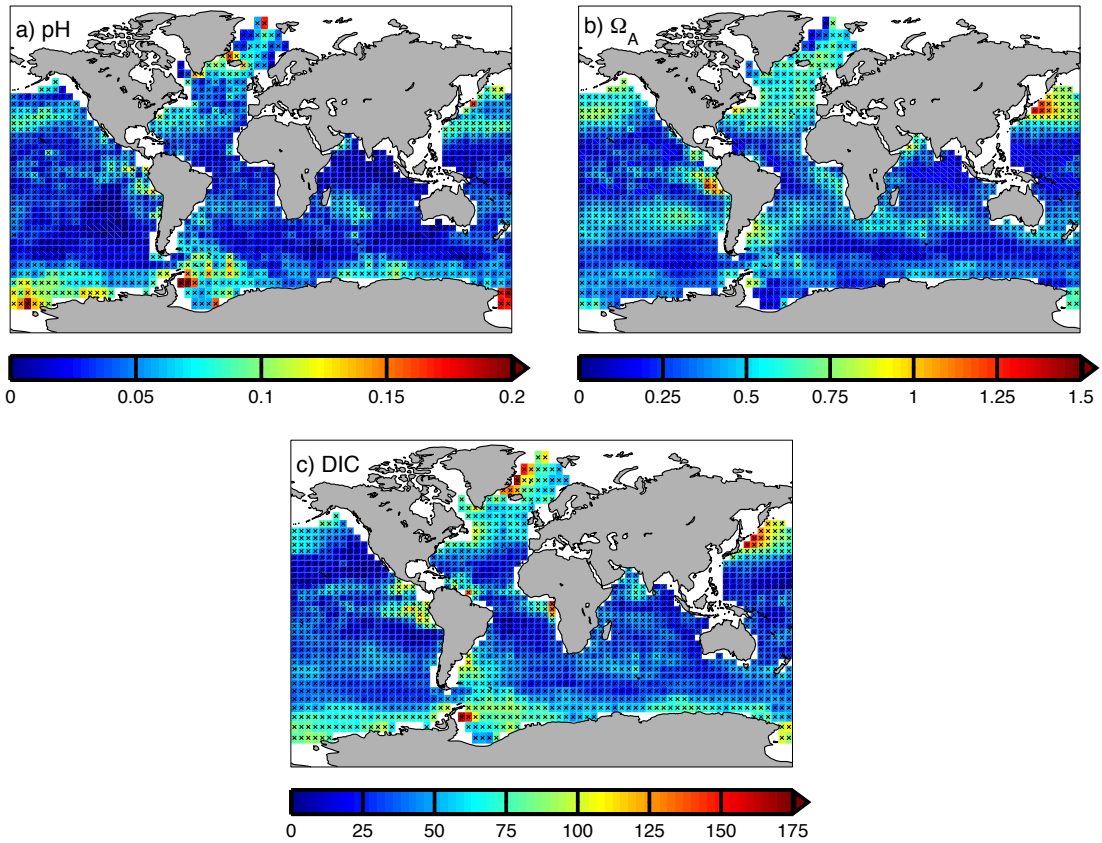

Figure 7.9: Annual range for a) pH, b) Ω_A and c) DIC from the primary pH/Ω_A climatology. The crosses indicate where the lower bound of the uncertainty interval on the annual range exceeds zero and thus where the annual range can be taken to be significant).

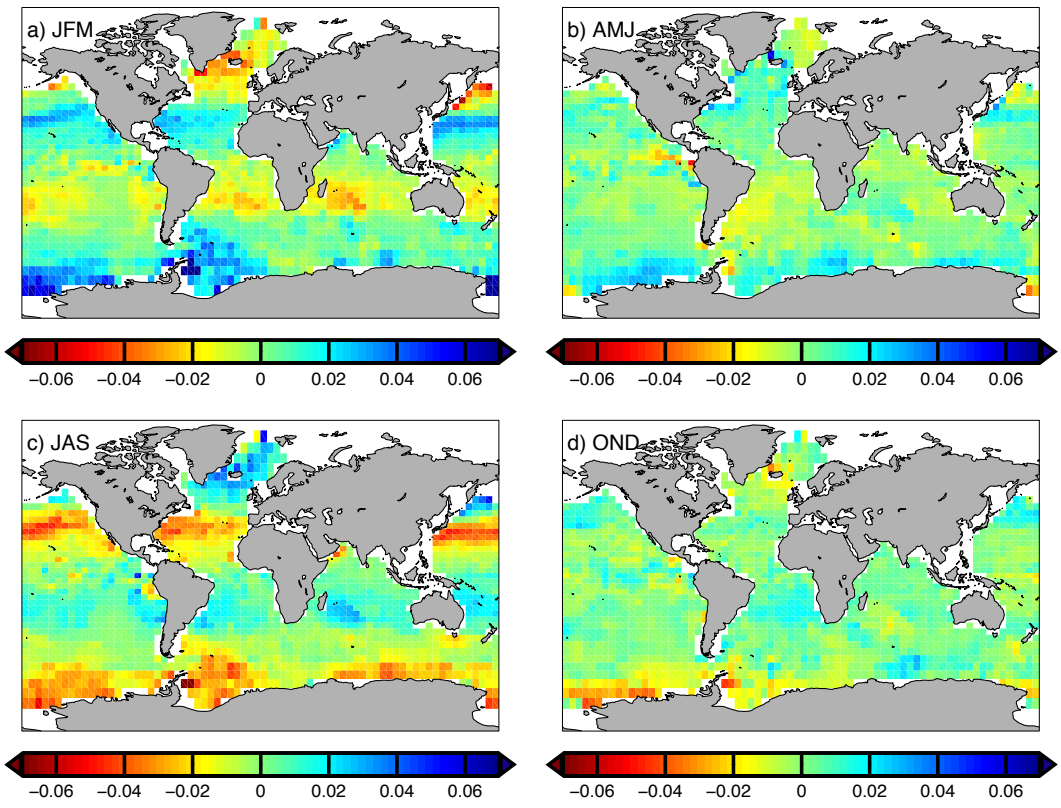

Figure 7.10: Seasonal-mean pH anomalies from the primary pH/Ω_A climatology.

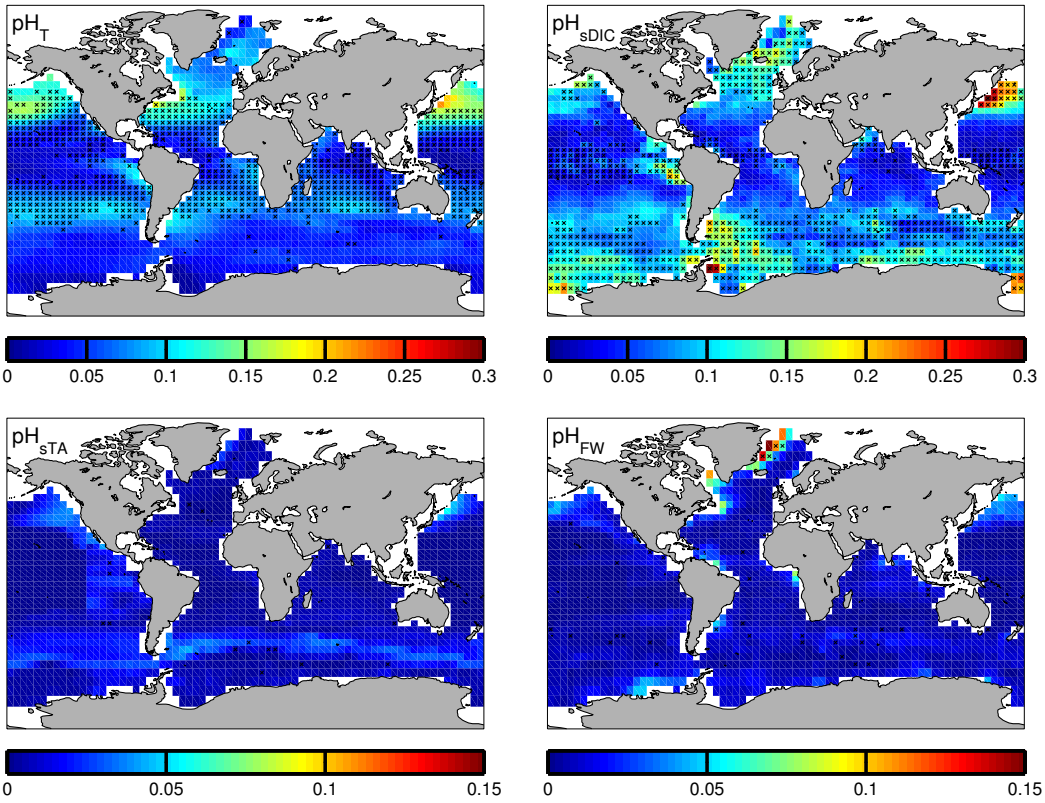

Figure 7.11: Annual range for the four driving components of pH seasonality. The crosses indicate where the seasonal range for the particular forcing component is the largest for that grid cell, and thus can be considered the main driver of pH seasonality.

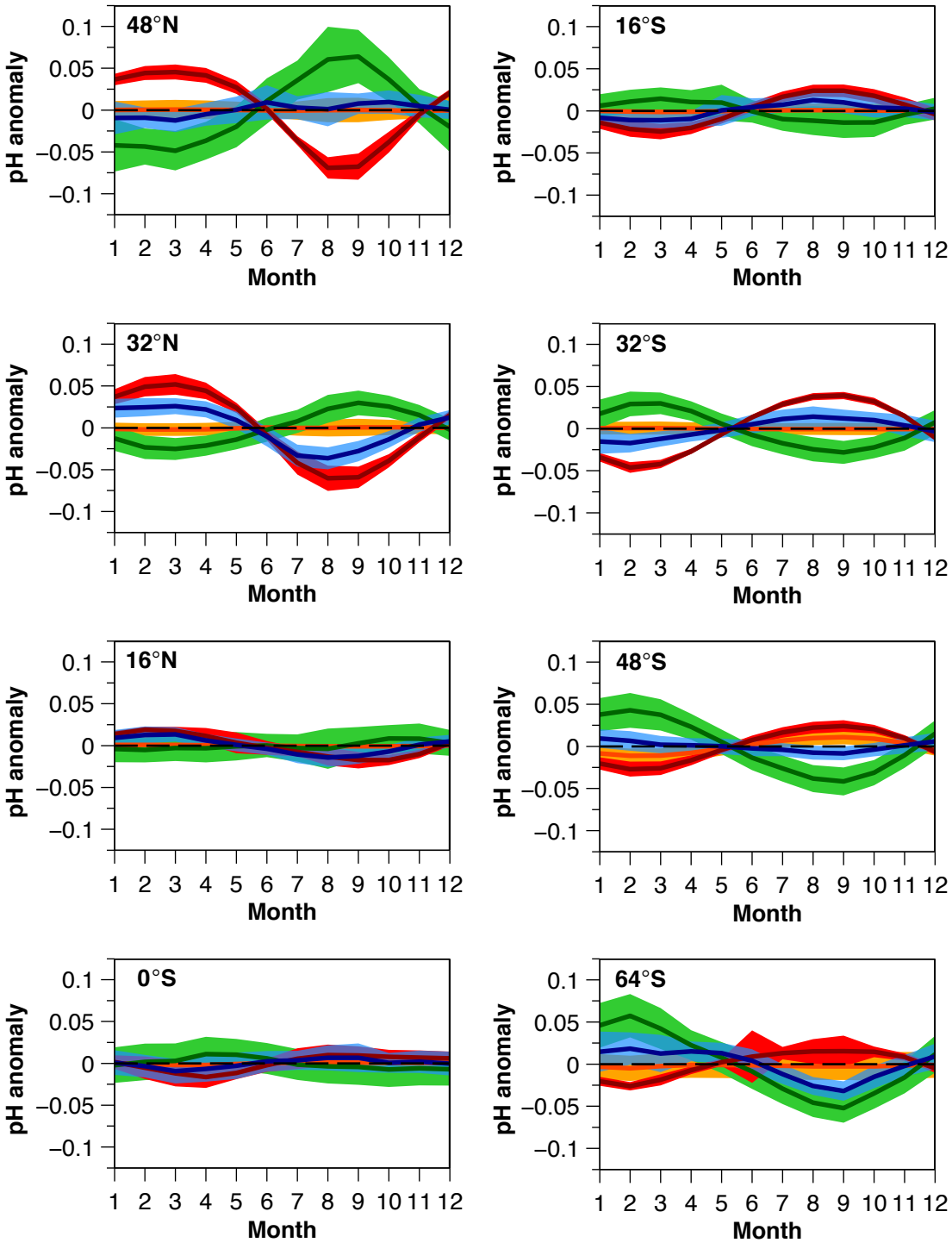

Figure 7.12: Latitudinal-average pH anomalies (blue lines) and the corresponding driving components (thermal in red, sDIC in green and sTA in orange). The freshwater driver is not plotted for simplicity. Its average is approximately seasonally-invariant at near-zero in all cases. The shaded bands around the lines are $\pm 1\sigma$, and incorporate the uncertainty on the individual monthly anomalies via Gaussian error propagation.

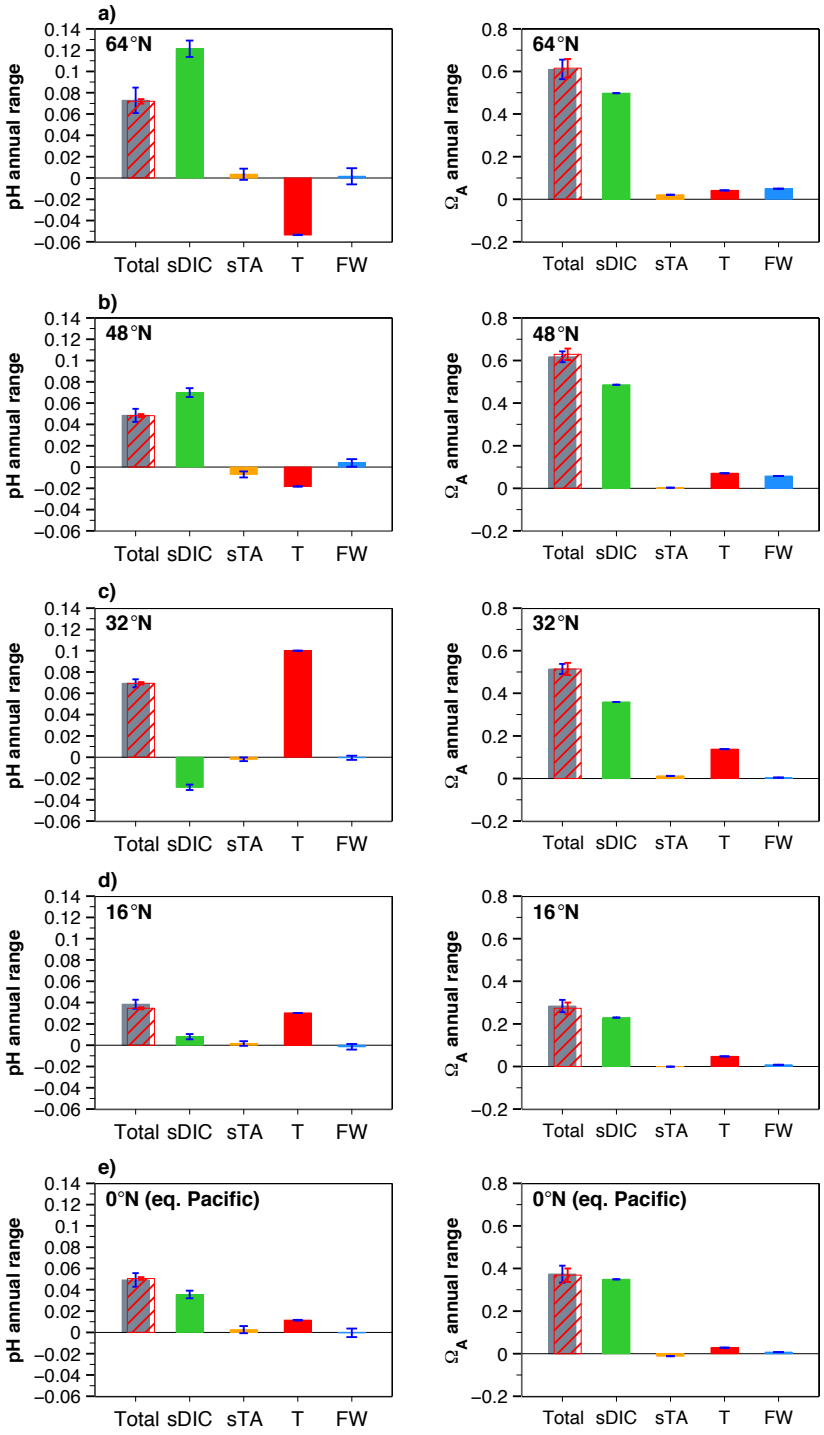

Figure 7.13: Analysis of the contribution of the sDIC, sTA, temperature (T) and freshwater (FW) components to the (total) annual range for pH and Ω_A averaged across various latitude bands. A negative value indicates that the component acts to reduce the pH or Ω_A annual range. The annual range predicted by summing the four components (calculated individually for each grid cell and then latitudinally-averaged) is shown by the grey bar. The red cross-hatched bar over the top gives the actual latitudinal-average annual range for pH or Ω_A. Subfigure (e) gives the averages for the equatorial Pacific at 0°N. Note that the four component bars will not necessarily sum to the grey bar.

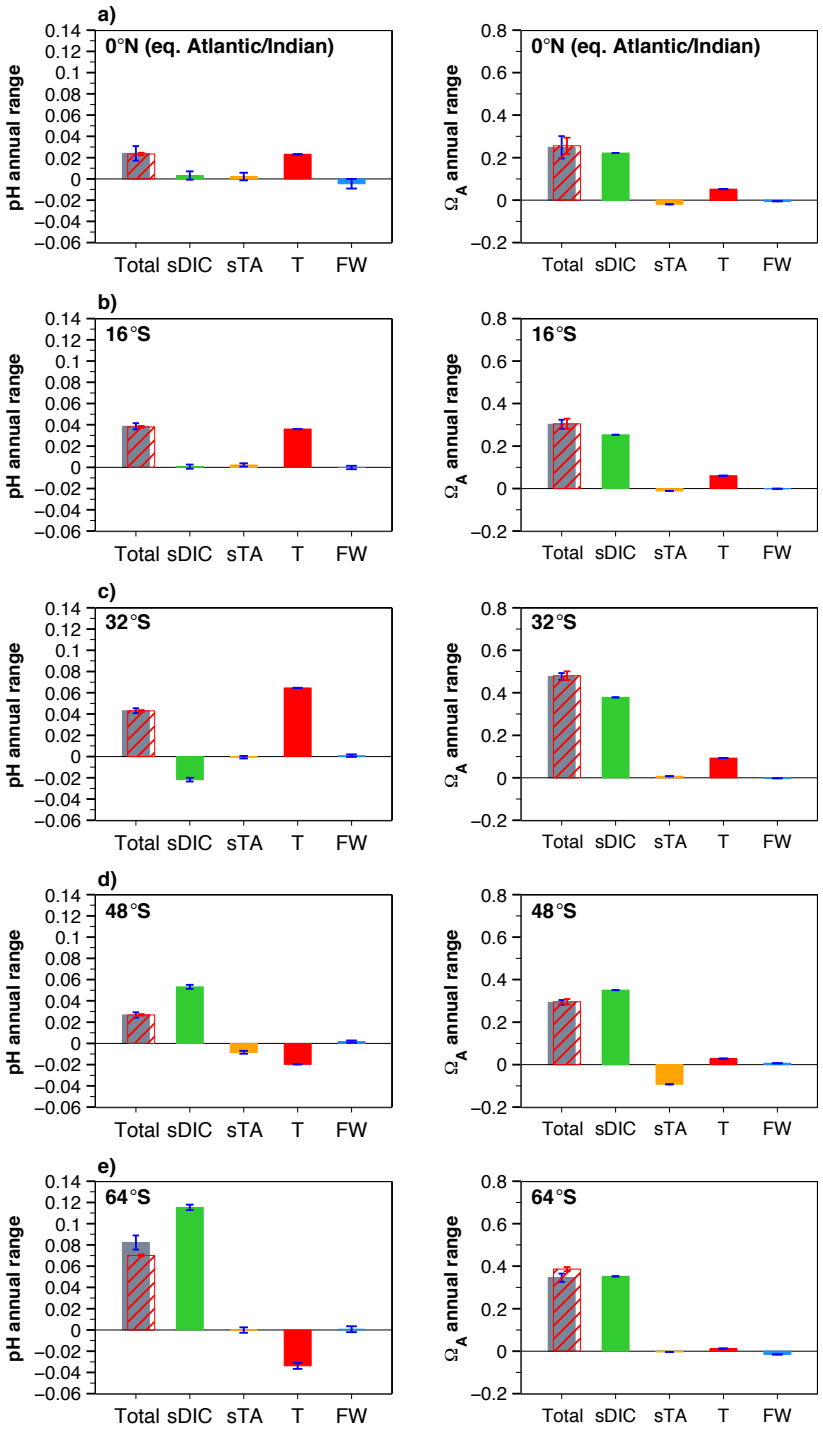

Figure 7.14: As for Fig. 7.13 but for different latitude bands. Subfigure (a) gives the averages for the combined equatorial Atlantic and Indian oceans along 0°N.

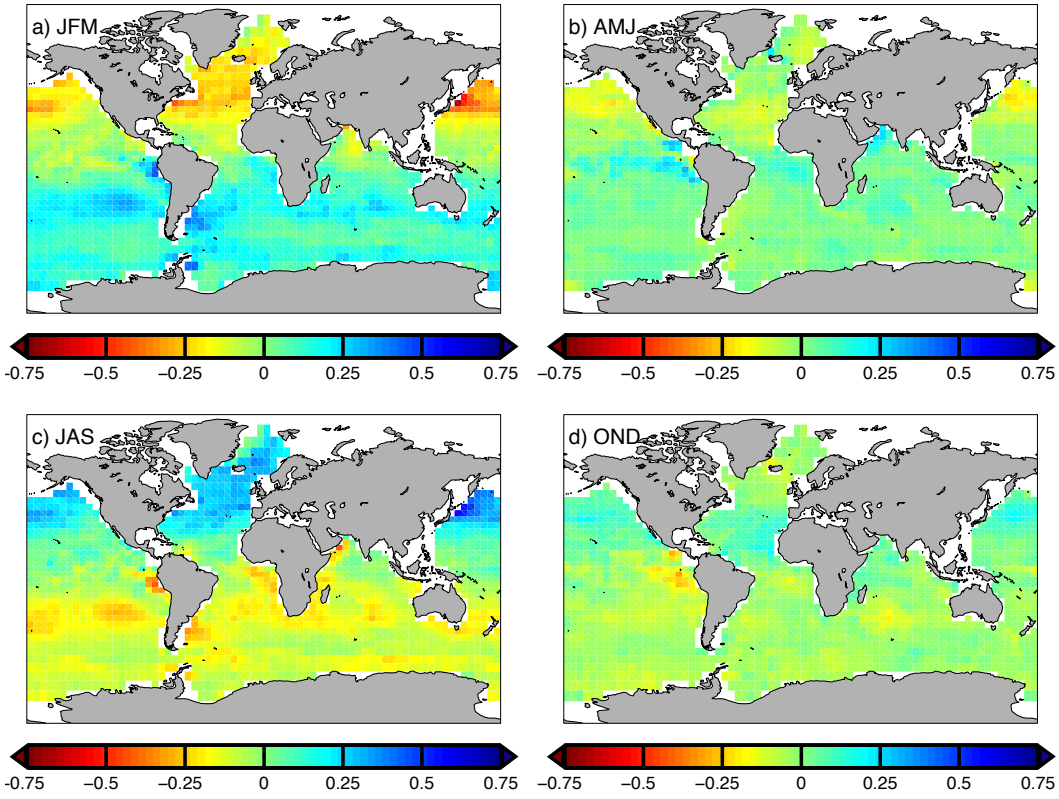

Figure 7.15: Seasonal-mean Ω_A anomalies from the primary pH/Ω_A climatology.

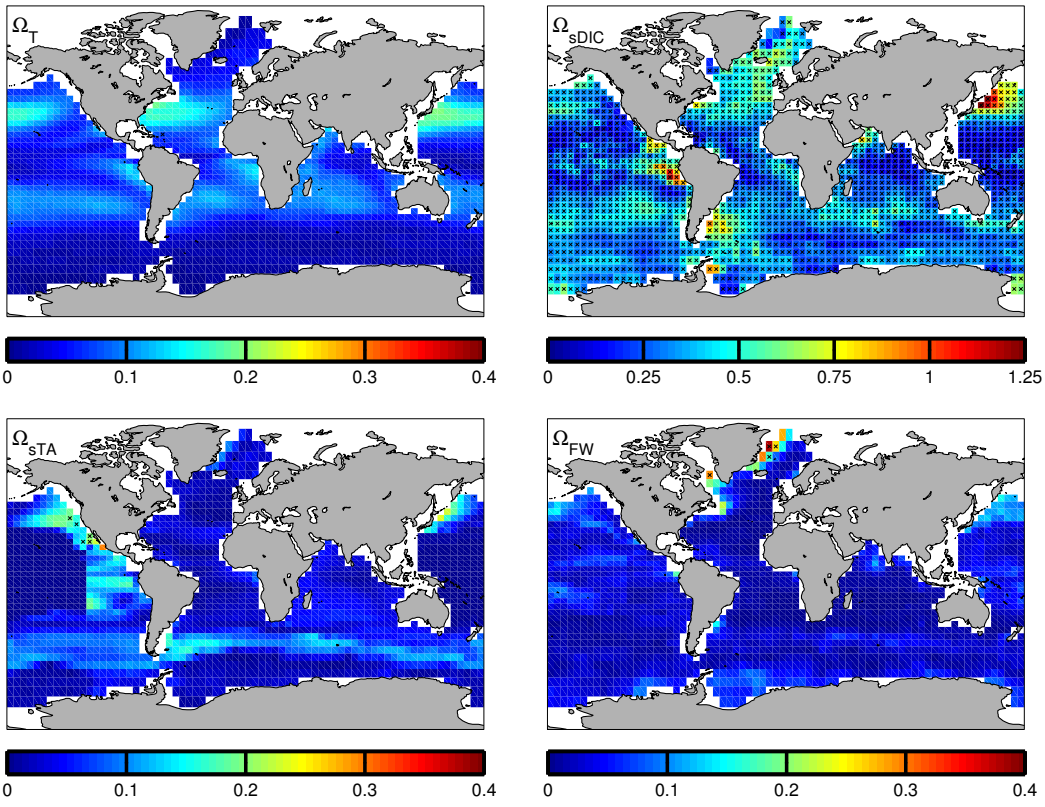

Figure 7.16: As Fig. 7.11 but for Ω_A.

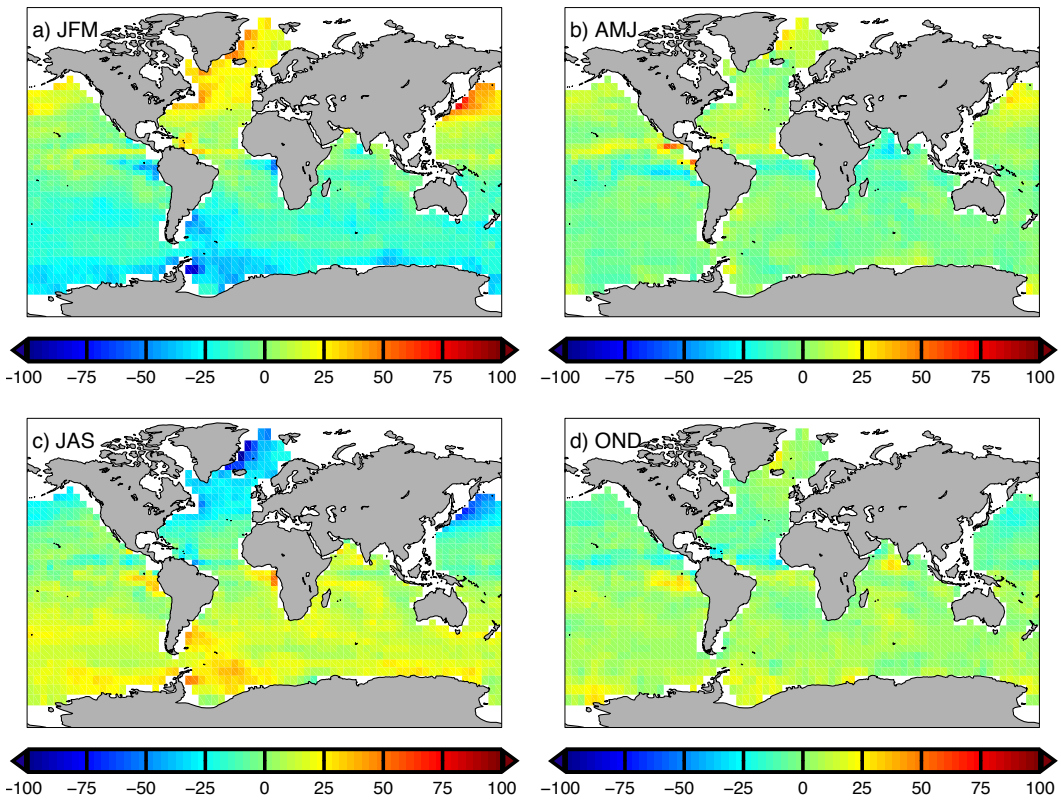

Figure 7.17: Seasonal-mean DIC anomalies from the primary pH/Ω_A climatology.

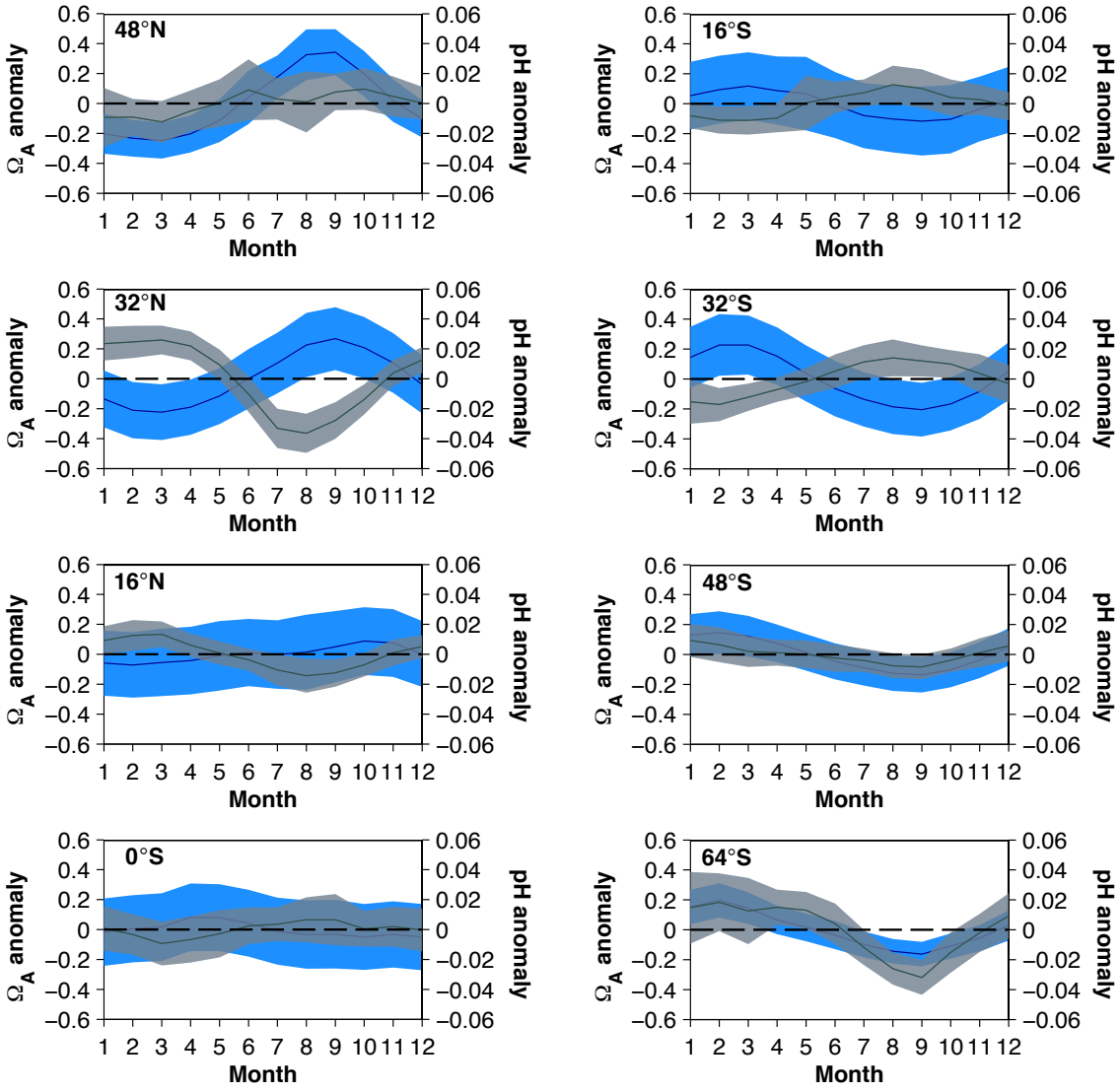

Figure 7.18: Latitudinal-average pH and Ω_A anomalies from the primary pH/Ω_A climatology. The grey and blue lines are for pH and Ω_A, respectively. The shaded bands around the lines are $\pm 1\sigma$ and incorporate the uncertainty on the individual monthly anomalies via Gaussian error propagation.

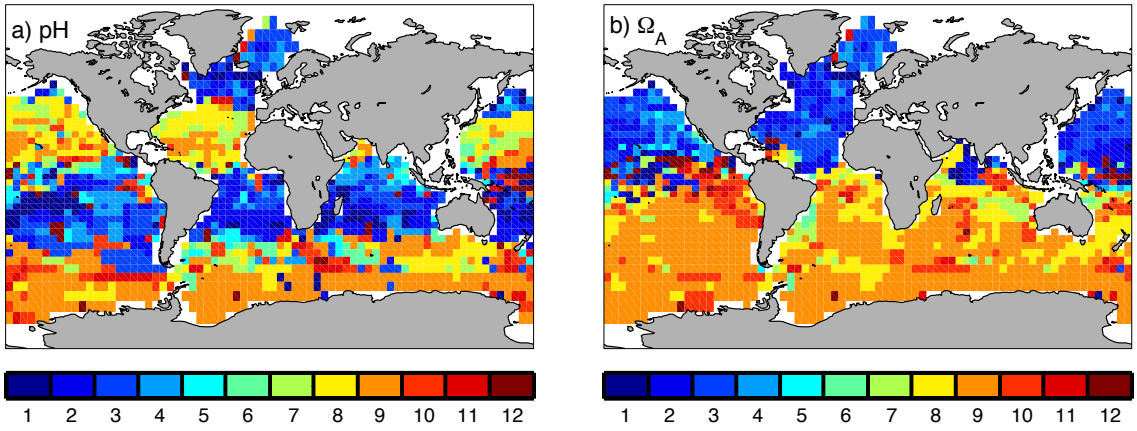

Figure 7.19: Month with the seasonal minimum value for a) pH and b) Ω_A from the primary pH/Ω_A climatology.

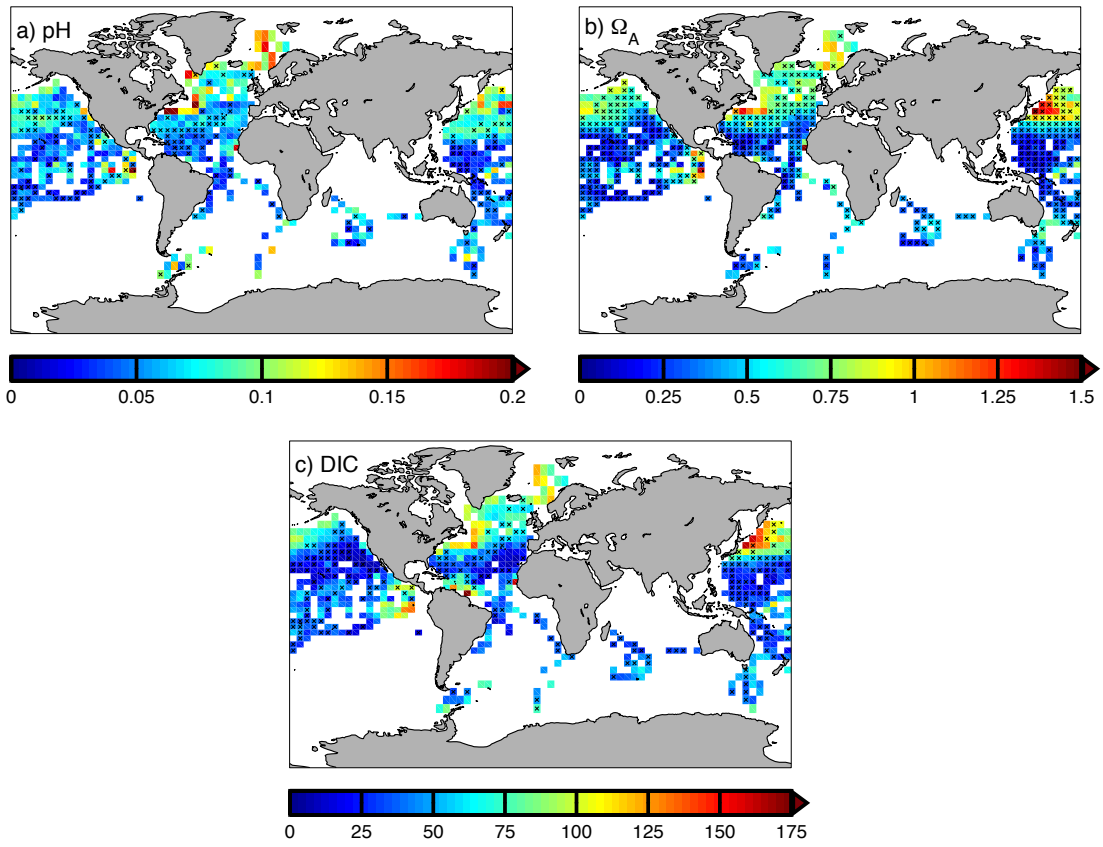

Figure 7.20: The annual range of pH, Ω_A and DIC for the SOCAT version of the pH/Ω_A climatology. The crosses indicate grid cells where the value of the annual range falls within the uncertainty range for the primary pH/Ω_A climatology.

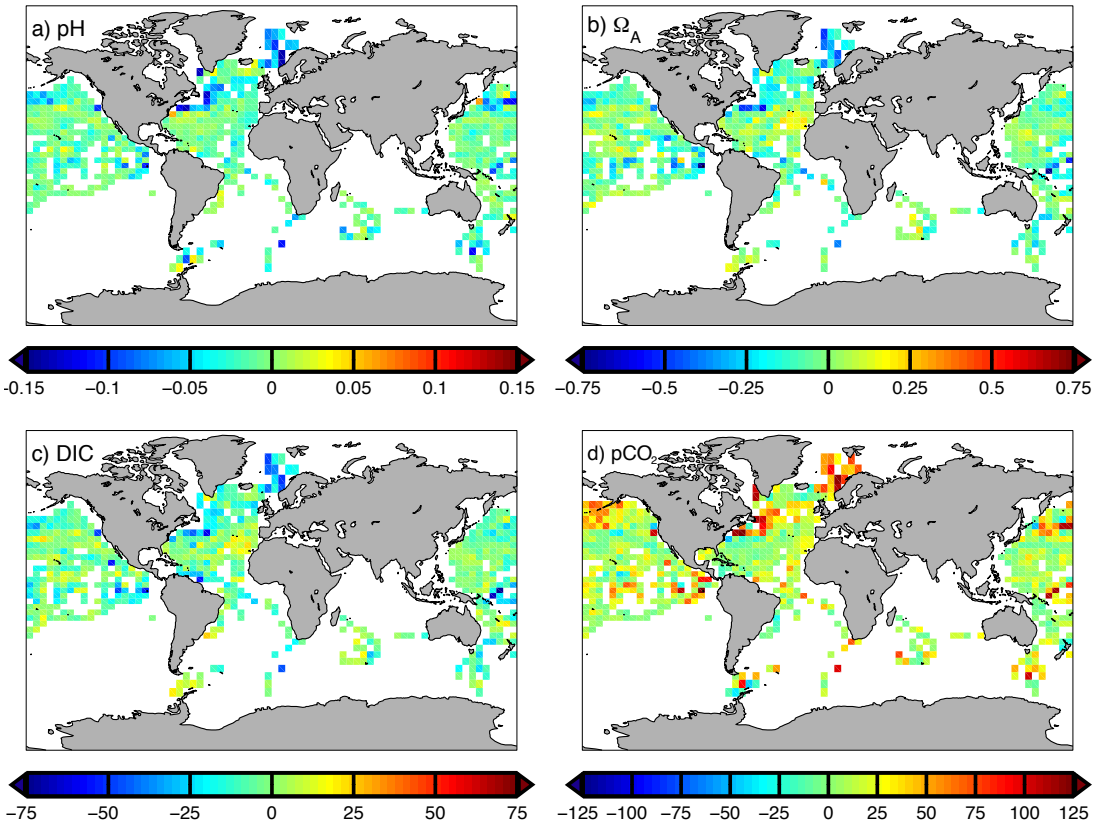

Figure 7.21: Differences between the annual ranges for the primary and SOCAT versions of the pH/Ω_A climatology. All differences are the primary climatology minus SOCAT, except for d) which is SOCAT minus T09 pCO_{2sw}.

Chapter 8

Synthesis and conclusions

Insufficient pH measurements exist to construct a global-scale seasonal sea surface pH climatology directly from observations. Such pH climatologies can, however, be derived by solving the carbonate chemistry system from more frequently-observed seawater CO_2 parameters. In this thesis I constructed pH/Ω_A climatologies by solving the ocean CO_2 system from pCO_{2sw}/fCO_{2sw} and total alkalinity. New fCO_{2sw}, TA and SST climatologies were developed for this purpose, utilising recent observational synthesis data products (SOCAT for fCO_{2sw} and CARINA and PACIFICA for TA).

Various SST climatologies were developed to test their sensitivity to the depth range of the input observations. The so-called upper SST (USST) climatology was constructed using only temperatures from the upper 2 m (USST), while the lower SST (LSST) climatology was constructed using deeper observations. New observations from the central tropical Pacific presented here reveal that temperature differences can be as large as 1°C across the upper 3 m. They also show the persistence of gradients exceeding $0.1°C\,m^{-1}$ in the upper few meters, day and night, even when 10 m wind speeds exceed $6\,m\,s^{-1}$. Climate models will require greater resolution at the near-surface to capture such hydrodynamics (their uppermost ocean layer can be 10 or more meters thick).

A seasonal cycle was found in the average monthly USST-LSST differences north of 30°N, with warmer temperatures in summer and cooler in winter. This may be due to seasonal variation in near-surface temperature gradients atop a background of year-round warm error in engine intake temperatures (a major component of LSST observations). The implication of the former is that sizeable near-surface temperature gradients are prevalent outside the tropics. Interestingly, physical modelling presented here suggests that intake warm errors are unlikely due to warming of in-

take seawater by hot engine room air. The cause of intake warm errors thus requires field assessment. USST was found to generally have larger seasonal ranges than LSST, perhaps indicative of stronger seasonality in the upper 2 m, although the differences are mostly small in percentage terms (within ±20%). Still, the combined evidence from the field research and new SST climatologies presented here suggests that use of the 'well-mixed near-surface' assumption in construction of SST datasets may lead to erroneous results.

The new TA climatology derived here suggests that TA seasonality is fairly small throughout the majority of the open ocean (annual range $<30\,\mu\mathrm{eq\,kg^{-1}}$). Seasonality is found to be largely salinity-driven, being large beneath the Intertropical Convergence Zone, in the Antarctic seasonal sea ice zone and in the Greenland Sea. It thus appears that calcification, being unrelated to salinity, has little or no role in climatological seasonal variation of TA. Compared to the Lee et al. (2006) TA climatology, the new climatology has markedly lower annual means and ranges in the north Pacific, a region with improved observational coverage courtesy of the PACIFICA database.

The primary new pH/Ω_A climatology developed here suggests that annual average pH is relatively low in the tropics, subarctic Pacific and Southern Ocean ($<$8.09), with a strong minimum in the eastern equatorial Pacific upwelling zone ($<$8.05). In contrast, pH is relatively high in the Nordic Seas ($>$8.12), subpolar north Atlantic ($>$8.1) and southern hemisphere subtropics ($>$8.09). Temperature, sDIC and in some locations, salinity, are found to be the main drivers of seasonal variation in pH. Seasonality is found to be relatively small in the tropics outside of the eastern equatorial Pacific (annual range $<$0.05), and moderate to large in the subtropics (annual range 0.05-0.1), where it is predominantly temperature-driven. Moderate to large sDIC-driven seasonal cycles (annual range $>$0.05) are also found at high latitudes in the western subarctic Pacific and Ross, Weddell, Iceland and Irminger seas.

Ω_A seasonality is found to be predominantly sDIC-driven everywhere, with a modest contribution from SST seasonality in the subtropics. Seasonality is found to be large (annual range $>$0.5) in the northern hemisphere mid-latitudes (30-60°N), Norwegian Sea and southern hemisphere subtropics, where sDIC seasonality is large.

Seasonal cycles of pH and Ω_A are found to be in anti-phase where thermal forcing is the dominant driver of pH seasonality, and in-phase where sDIC forcing predominates. The maxima and minima for the two parameters occur in different seasons in the former case, which may be of relevance to the biological impacts of acidification.

Compared with the primary pH/Ω_A climatology, the minima in seasonal pH range

in the subtropical/subpolar north Atlantic and subarctic Pacific are less apparent in the SOCAT version. This appears due to the use of a different unionised CO_2 climatology.

Various open ocean carbonate chemistry time-series were compared with the primary pH/Ω_A climatology. The climatology is found to capture the general form of the climatological pH, Ω_A, sDIC and DIC seasonal cycles from the time-series, although it overestimates the DIC and sDIC seasonal cycles for certain stations. An unusually detailed attribution analysis for long-term pH and Ω_A trends was also conducted for select time-series. Long-term pH declines for BATS, ESTOC, HOT and IRM were mainly attributable to uptake of anthropogenic CO_2. These acidification trends were found to be modulated by long-term trends in SST, SSS and/or sTA at several time-series. Investigation was also conducted into how changes in seawater buffer capacity due to acidification might alter pH and Ω_A seasonality at a subtropical and subpolar time-series. pH seasonality was found to increase in amplitude at the subpolar time-series and decline at the subtropical time-series, while Ω_A seasonality was found to decline at both. A larger amplitude cycle in pH implies that lower pH values will be encountered sooner under acidification than if the amplitude did not change.

The carbonate chemistry research presented here should be of use for adaptation to ocean acidification, both in terms of deriving projections for future ocean chemical conditions and for developing adaptation strategies. For instance, the months in which the seasonal minima in sea surface pH and Ω_A occur in different ocean regions have been identified, the times of year when we might expect the biological impacts of acidification to be most readily apparent. Further, the spatial patterns of where the annual ranges for pH and Ω_A are relatively large and relatively small have been identified. This knowledge can be used to assess the extent to which species that experience larger natural variability in carbonate chemistry in the open ocean are less vulnerable to acidification. It can also (hopefully) be used to improve the accuracy of climate model projections of acidification through identifying deficiencies in their simulation of present-day seasonal cycles of pH and Ω_A. My analysis of the drivers of inter-decadal pH and Ω_A trends for ocean time-series suggests that models will also need to be able to accurately capture recent trends in annual-mean sDIC, sTA, temperature and salinity to give dependable short-term projections. Note that there is the potential for complex feedbacks between marine biology, and seasonal cycles and long-term trends in seawater pH, Ω_A and temperature.

Appendix A

The history of sea surface temperature measurement

This Appendix and Appendix B are published as part of Matthews (2013).

International recommendations for SST measurement were first established at the Brussels Maritime Conference of 1853. The conference report proposed that the temperature of surface seawater be measured using wooden buckets (Woodruff et al., 2008). Folland and Parker (1995) (referred to as FP95) describe a 19^{th} century ship's wooden bucket of 12 L capacity. It has been suggested that the buckets used transitioned from predominantly wooden to predominantly canvas between the 1850s and 1920s. As discussed by (Jones and Bradley, 1992), that such a widespread changeover actually occurred is highly uncertain, with canvas buckets known to have been used since at least the 1840s (Parker, 1993). Regardless, I suggest from practical experience that sampling with general-purpose ships' wooden buckets would have been impractical and dangerous on the steamships that gradually replaced slower sailing vessels of lower freeboard in the late 19^{th} century. Such buckets bounce along the sea surface when suspended from ships travelling in excess of $\sim$7 kt ($\sim$3.5 m s^{-1}) and considerable drag is generated once they dip beneath the surface. Canvas buckets do not bounce along the surface and those used aboard steamships appear to have been of fairly small volume (2–4 L, Brooks, 1928; referred to as B28) and often weighted to help them sink (e.g. with a wood base). A photograph featuring such a bucket is presented in Brooks (1932). Retrieval of buckets can be challenging, particularly from the bridge of large modern merchant vessels at 30 m up and underway at speeds of 20 kt ($\sim$10 m s^{-1}) or more. Hénin and Grelet (1996) note that such hauls "can be

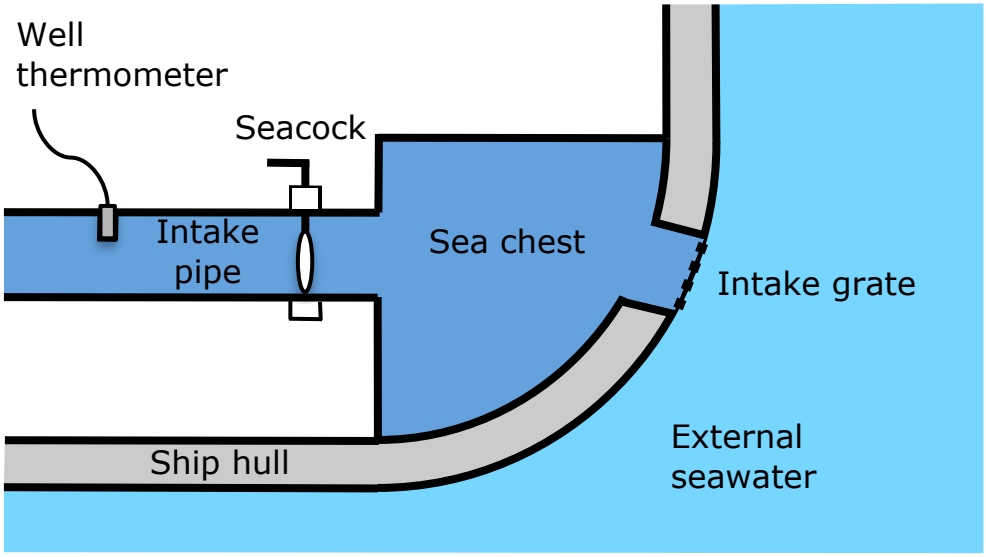

Figure A.1: Schematic of a typical engine cooling water intake system on a modern merchant vessel.

an arduous and acrobatic process". Indeed, HMSO (1956) recommends that ships travelling faster than 15 kt should obtain intake readings in preference to bucket temperatures for safety reasons.

Intake depths reported in the early literature are presented in Table A.1. Brooks (1928) reports an intake depth of ∼7 m on a Canadian Pacific steamship in the 1920s. James and Shank (1964) estimate intake depths of ∼3–10 m for various US merchant, Navy and Coast Guard observing ships reporting in 1962 and 1963. They defined relations between intake depth and full-load draft for different hull types and categorised observing ships by hull type to estimate their intake depth. More contemporary intake depths averaged by type of VOS ship reporting this between 1995 and 2004 are presented in Table 5 of Kent et al. (2007). Container ships and tankers were found to have intakes at ∼7–9 m depth while intakes on bulk and livestock carriers were found to often exceed 10 m. Kent and Taylor (2006) report that the average intake depth for VOS reporting this in 1997 was 8.4±4.1 m, with the deepest inlet being at 26 m. Oceanographic research vessels often have dedicated seawater intakes for underway scientific measurements, typically sampling at ∼2–4 m depth. These scientific intakes are distinct from engine intakes in that the pipes tend to be of much smaller diameter, a few centimetres (e.g. Kirk and Gordon, 1952)

With EIT readings traditionally being obtained by ships' engineers for engine

monitoring purposes, procedures and instruments have varied from ship to ship and remain unstandardised and poorly documented today. As reported in Appendix B, intake thermometers are generally mounted within 15 m inboard of the inlet and beyond a seacock (Fig. A.1). On modern vessels seawater is often piped aboard through a sea chest, a sealed metal box built into the hull with an external grate. Intake thermometers are sometimes mounted into the sea chest itself Tabata (1978c), reportedly a favoured position for distant-reading thermometers (WMO, 2008). In addition to one or more main engine intake lines (e.g. with multiple engines), ships can have multiple ancillary lines, and temperature be measured on several (B28; Saur, 1963). Two main types of EIT method can be distinguished: well and faucet. In the well method, a temperature probe or thermometer bulb is mounted inside a well sunk into the intake pipe to around a third its inside diameter (e.g. Kirk and Gordon, 1952; Piip, 1974) sometimes referred to as thermometer pockets or thermowells. Rapid conduction across the well casing allows intake temperature to be measured while at the same time enabling the probe or bulb to be readily removed for maintenance. The sensing element can also be directly inserted into the pipe (e.g. Stupart et al., 1929). Both well and direct insertion temperatures are sometimes referred to as injection temperatures. In the faucet method, seawater is sampled from the intake through an attached pipe fitted with a tap and its temperature measured externally (e.g. B26; HMSO, 1956; Piip, 1974).

Manually-read mercury-in-glass thermometers have been used for both bucket (B28; Tauber, 1969; Collins et al., 1975; Tabata, 1978c) and intake (B28; Saur, 1963; Tauber, 1969) measurements. Intake temperatures have also been taken using mercury-in-steel HMSO (1956); Piip (1974); Collins et al. (1975) and electrical resistance thermometers (B26; Tabata, 1978b), and thermistors Tabata (1978a). Hagart-Alexander (2010) provide a review of thermometer types and a description of thermowells. EIT has sometimes been continuously recorded using a thermograph (e.g. B26; Collins et al., 1975; Piip, 1974). Brooks (1932) presents a photograph of an early version of such a setup. On modern vessels, a distant-reading display may be available in the engine room or on the bridge WMO (2008).

The prevalence of EIT readings in the decades prior to World War II (WWII) is poorly known but assumed small. In the primary compilation of historical SST measurements, the International Comprehensive Ocean-Atmosphere Data Set (ICOADS, Woodruff et al., 2011), observations from this period largely originate from British, Dutch and German vessels, for which the bucket method was recommended. EIT are

thought to dominate SST measurements from 1942–1945 when there was an increase in the proportion of observations coming from US ships, on which the intake method is thought to have prevailed (Thompson et al., 2008). Furthermore, nighttime bucket deployments were likely avoided during WWII since they would have required use of a light on deck (FP95). Kent et al. (2010) present measurement method attribution plots for ICOADS SST data.

Table A.1: Intake depths reported for observing ships of various type in pre-1980 literature. All are from ships contemporary to the publication year except Collins et al. (1975), which are from vessels operating during 1927 to 1933. CSIRO is the Commonwealth Scientific and Industrial Research Organisation of Australia.

Reference	**Intake depth(s)**	**Ship type(s)**
Brooks (1926)	22–24 ft (∼7 m)	Canadian Pacific steamship (RMS *Empress of Britain*)
	15 ft (∼4.5 m)	2 US Coast Guard Ice Patrol vessels (*Tampa* and *Modoc*)
Lumby (1927)	30 ft (∼9 m)	Ocean liner (RMS *Majestic*)
Roll (1951b)	4.5 m	German Fishery Patrol Vessel (*Meerkatze*)
Kirk and Gordon (1952)	9 ft (∼3 m)	British ocean weather ships
Saur (1963)	10–22 ft (∼3–7 m)	3 US Military Sea Transport Service ships, 9 US Navy Radar Picket ships
James and Shank (1964)	10–32 ft (∼3–10 m) (average of 21ft)	US merchant, Navy and Coast Guard vessels
James and Fox (1972)	0–9 m	WMO voluntary observing ships
Piip (1974)	2–6 m	Merchant vessels traversing 0–50°S, 135–180°E and reporting to CSIRO
Collins et al. (1975)	5 m	Canadian Pacific steamships
Tabata (1978b)	3 m	Canadian ocean weather ships

Appendix B

Review of bucket-intake field comparisons

B.1 Field and lab evaluations of shipboard methods

B.1.1 Bucket-intake temperature comparisons

Field evaluations of SST measurement methods have largely focused on average differences between bucket and engine intake temperatures. Brooks (1926) compared tin bucket and engine intake temperatures collected aboard the Canadian Pacific steamship RMS *Empress of Britain* on a cruise between New York and the West Indies in February and March 1924. Faucet and injection temperatures were found to respectively average 0.1°F (∼0.06°C) and 0.5°F (∼0.3°C) warmer than near-simultaneous tin bucket temperatures. The injection temperatures were obtained from thermometers mounted on the condenser intake pumps, noted as difficult to read to better than 1°F (∼0.6°C). Brooks suggests the injection temperatures in error due to parallax in reading and warming of intake seawater about the pumps. A fast-response cylindrical bulb thermometer was used to obtain both the tin bucket and faucet temperatures and appears to have been readable to 0.1°F. This was not the thermometer in standard use for bucket measurements aboard the *Empress of Britain*; rather, a longer-response spherical bulb thermometer read to 0.5 or 1°F was used. Brooks suggests the tin bucket samples cooled slightly pre-measurement, at most by 0.2°F (∼0.1°C). Finding the maximum difference between the faucet and tin bucket tem-

peratures to be only 0.25°F (∼0.15°C), he concluded that the upper ocean had been well-mixed to at least the intake depth (∼7 m). He does note, however, that sizeable positive average bucket-intake differences had previously been found in spring and summer in the Grand Banks aboard the *Tampa*. Reported average differences across the upper 5 m were 0.6°F (∼0.3°C) in daytime and 0.3°F (∼0.2°C) at night for April to July 1925. Note that 0.6°F was added to the intake readings for supposed parallax error so the unadjusted differences were in fact larger. Similar gradients were found for the western North Atlantic in summertime by James and Shank (1964) using bathythermographs. They found the temperature contrast between 10 and 30 ft (∼3–9 m) exceeded 0.6°F (∼0.3°C, ∼0.05°C m^{-1}) over 15% of the time in June, July and August but was ≤0.2°F (∼0.1°C, ∼0.02°C m^{-1}) over 85% of the time from September to March. Isothermal conditions were observed at least 55% of the time during the latter period.

Brooks conducted an additional shipboard comparison aboard the ocean liner SS *Finland* on a cruise between San Francisco and New York in May 1928 (B28).Temperatures from the main engine intake were found to average 0.8°C warmer than those obtained by fast measurement with a rubber-covered tin bucket of small volume (1.7 L). Those from the refrigerator intake in the refrigerator room averaged 0.2°C warmer. Respectively, the engine intake and refrigerator intake readings were found to average 0.7 and 0.3°C warmer than those from a specially-fitted intake thermograph. While details of the engine intake thermometer were not reported, the refrigeration intake thermometer was graduated in intervals of 2°F (∼1.1°C). Temperature change of the tin bucket sample pre-measurement was assumed small, although cooling of 0.1 °C was noted in one minute following collection under a wind speed of 9 m s^{-1} and SST-wet bulb temperature contrast of 6°C.

Roll (1951b) compared bucket and intake temperatures obtained in the North Sea and Norwegian Sea from June to October 1950 by the German Fishery Patrol Vessel *Meerkatze*. A pipe was specially fitted to the engine intake to divert seawater, in a system designed to obtain accurate EIT readings. Bucket temperatures were obtained using a rubber-insulated water scoop of very small volume (0.6 L). An average bucket-intake difference of −0.07°C was found from 410 comparisons. Small positive average differences of 0.1°C and below were generally found at low wind speeds (up to Beaufort force 4) and attributed to near-surface temperature gradients. Increasingly negative average differences were found at higher wind speeds and attributed to enhanced cooling of bucket samples, changing from −0.1°C at Beaufort force 5 to

nearly −0.25°C at force 6.

Kirk and Gordon (1952) compared bucket and intake temperatures obtained aboard Dutch merchant vessels in the eastern North Atlantic south of the British Isles. Intake temperatures tended to be ∼1°F (∼0.6°C) warmer than bucket readings. Considerable scatter was found in the individual bucket-intake differences, with standard deviations ranging from around 0.7 to 0.9°F (∼0.4–0.5°C) across the Marsden squares analysed, increasing towards higher latitudes. They also compared bucket (UK Met Office Mk III) and intake thermograph measurements obtained by British ocean weather ships in the eastern subpolar North Atlantic between March and November 1949. The Mk III is a canvas bucket with an internal double-walled copper vessel and spring lid. The average across various cruise-mean intake-bucket differences for three weather ships was 0.4°F (∼0.2°C) on-station and 0.2°F (∼0.1°C) underway. The larger difference on-station was suggested due to enhanced engine room warming of intake seawater from a reduced volume flow through the intake. The cruise averages varied between −0.6 and +0.3°C for both on-station and underway measurements.

Tauber (1969) evaluated EITs collected by three Soviet research vessels in the Pacific and Indian Oceans and by trawlers in the Black Sea and Sea of Asov between April 1967 and February 1968. Virtually all EITs (98%) obtained by one research vessel were found to be overly-warm by >0.5°C (compared against accurate measurements) while on the other vessels they were 1.2–2.3°C too warm in 83% of cases. Tauber thus concluded EIT measurements were unreliable.

Saur (1963) analysed 6826 pairs of bucket and engine intake temperatures obtained aboard 12 US military vessels between May 1959 and January 1962. Three of the vessels were traversing the North Pacific while the remainder were usually stationed ∼300 miles off the US west coast. The fleet average intake-bucket difference derived from average differences for the individual vessels was 1.2±0.6°F (∼0.7±0.3°C). There was significant variation in the latter differences, ranging between −0.5 and +3°F (around −0.3 and +1.7°C), and between cruise averages for individual vessels, in one case varying between 0.3 and 1.8°F (around 0.2 and 1°C). Specially-designed buckets and thermometers accurate to at least 0.15°F (∼0.1°C) were used for the bucket measurements. Thus the non-zero average differences likely primarily reflect errors in the intake temperatures, although with near-surface temperature gradients playing some role. Intake temperatures were only reported in whole °F, being read from thermometers graduated in intervals of 2 or sometimes 5°F (around 1.1 and

2.8°C). Saur notes that a comparison between intake thermometers used aboard five US Coast Guard weather ships and an accurate thermometer had found systematic errors between −2 and +3.9°F (around −1.1 and +2.2°C).

One of the most observation-rich bucket-intake comparisons ever conducted was that of James and Fox (1972). They analysed 13 876 pairs of near-simultaneous bucket and intake temperatures obtained aboard VOS ships between 1968 and 1970. Although of global distribution, reports were mainly from the North Atlantic and North Pacific shipping lanes. From a compilation of all observations, intake temperatures averaged 0.3°C warmer than bucket readings. Considerable spread was found in the individual differences with 68% falling within ±0.9°C and the largest differences exceeding ±2.5°C. This noise is not surprising given the temporal and spatial coverage of the collated observations and the heterogeneity of the bucket and intake methods (e.g. variable thermometer quality and observer care). They found that intake temperatures from mercury thermometers yielded a larger average intake-bucket difference (0.3°C) than those from precision thermometers or thermistors (both 0.09 °C).

On the whole, these studies suggest a tendency for intakes to read warmer than buckets, in opposition to what we would expect from typical near-surface temperature gradients (cooler with depth). The precise cause of reported average bucket-intake differences is not always clear, potentially being due to both bucket and intake errors where neither has been shown to be accurate. Confusing matters, buckets and intakes cannot be assumed to sample seawater of the same temperature in the presence of near-surface temperature gradients. This leads us to a discussion of terminology. The term "bias" is sometimes applied to average bucket-intake differences (e.g. Kennedy et al., 2011a) yet seems inappropriate given that both bucket and intake temperatures may show average deviations from the actual SST. By the latter I mean the actual temperature in the upper few centimetres. Similarly, use of the term "correction" to describe adjustment of bucket temperatures to be more consistent with EIT and vice versa is also unsuitable.

Identification of individual errors in bucket and intake temperatures in field comparisons requires supplementary accurate in situ temperature measurements. Studies by Susumu Tabata published in the late 1970s are amongst the most comprehensive in this regard. Tabata (1978b) analyses upper ocean temperatures collected over 1956–1976 by Canadian weather ships at Station P and traversing Line P in the northeast Pacific, a ∼1425 km-long transect extending from the coastal waters of southwestern Vancouver Island, British Columbia, to Station P in the mid-Gulf of

Alaska (Crawford et al., 2007). The mean difference between temperatures from a specially-designed meteorological bucket and an accurate reversing thermometer in the upper 1m was 0.04±0.13°C over 1969–1976, with bucket temperatures thus concluded accurate to ±0.1°C. Like Saur (1963), average bucket-intake differences were found to vary widely between ships and between cruises on the same ship, although the individual cruise standard deviations were generally smaller and more consistent at around 0.05–0.25°C (compared to around 0.3-0.8°C for Saur). The latter likely reflects reduced noise in the intake temperatures from the weather ships due to better observing practices (they were collected by meteorological observers) and use of higher precision instruments (precision of ±0.2°C). Mean cruise intake-bucket differences were −0.02 and +0.18 on two weather ships over 1962–1967 (*St. Catherines* and *Stonetown*), and −0.05 and −0.02°C for two other weather ships over 1967–1976 (*Vancouver* and *Quadra*). Except for the *St. Catherines* there was considerable variation in the average differences for individual cruises on these ships, for example, mostly varying within ±0.3°C for the *Quadra*.

Tabata (1978c,d) conducted a similar analysis using measurements collected by a Canadian oceanographic research vessel in the northeast Pacific in August and September 1975. Only observations coincident with wind speeds exceeding $\sim$6 m s^{-1} were analysed, conditions under which the upper 10m was considered isothermal. EIT (inlet at 4 m) averaged 0.3±1.2°C warmer than accurate temperatures from a salinity-temperature-depth (STD) meter. Tabata attributed the large standard deviation to reading error of the intake thermometer by the engine room crew, with the largest differences exceeding ±2°C.

More recently, Hénin and Grelet (1996) compared meteorological bucket temperatures to conductivity-temperature-depth (CTD) temperatures at 1–2 m depth obtained by research vessels in the western equatorial Pacific. Bucket temperatures were found to average 0.13±0.34°C and 0.16±0.22°C warmer than CTD temperatures on two cruises and 0.60±0.48°C cooler on another cruise. The warm average differences may have been attributable to temperature gradients over the upper few metres. The cause of the cool average difference is unclear but apparently due to the bucket measurements since the corresponding average CTD-thermosalinograph difference was similar to those for the other cruises.

B.1.2 Canvas bucket experiments by the Sea Education Association

The accuracy of canvas bucket temperatures was tested by field experiments in the early 1990s aboard the Sea Education Association (SEA) sailing vessel *Corwith Cramer*. The *Cramer* is the Atlantic sister ship of the *Robert C. Seamans* described in Chapter 3, the *Seamans* operating in the Pacific. The experiments, undertaken for the late Reginald Newell of the Massachusetts Institute of Technology, were conducted over several cruises across the western North Atlantic and Caribbean. They are described in a series of student project reports in the SEA archives in Falmouth, MA, USA. FP95 compared observations from one cruise to results from their canvas bucket model (described in Sect. 4). Underway at around 15 to 25 locations on each cruise, a replica Mk II canvas bucket was filled with surface seawater and hung on deck for 10 min in a wind-exposed, sun-shaded location. During this 10 min period, the sample temperature was measured each minute and the bucket agitated every half minute to mix the sample. The Mk II was in use aboard British ships (likely mostly motor vessels) from the 1930s until at least the 1950s (FP95; HMSO, 1956). Cooling over 5 or 10 min equating to average rates of $\sim$0.05–0.10°C min^{-1} was generally reported. Cooling rates in the first minute (mostly unreported) were likely faster due to non-linearity, with cooling of 0.2–0.3°C or more found in one minute in some cases.

One peculiarity in the experimental method is that the replica canvas bucket itself appears often not to have been used for seawater collection, apparently due to concerns this valuable bucket would be damaged. Instead, a plastic bucket was used for sampling and the Mk II then filled with seawater from this. In one report it is noted that the the canvas bucket was dipped into the plastic bucket for filling so that its walls were made wet, although the extent to which this was the case for other cruises is unclear. Results for both wet and dry walls are reported for some cruises. Regardless, the experiments suggest that samples in small-volume canvas buckets can cool rapidly.

B.1.3 Field comparisons of different bucket types

Few shipboard comparisons between different bucket types have ever been conducted. James and Fox (1972) report average bucket-intake differences for various bucket types but no direct differences between bucket types.

B26 compared temperatures from canvas and tin buckets (4 L and, 2 or 4 L, respectively) obtained aboard the *Empress of Britain*. When dropped from the bridge, the canvas bucket measured an average of 0.5°F (∼0.3°C) cooler than a tin bucket launched from a lower deck in 10 comparisons, increasing to 1°F (∼0.6°C) when the quartermasters took the canvas bucket measurements rather than Brooks himself ($n = 79$). The bulk of the latter comparisons ($n = 65$) were conducted south of 35°N (and above 9°N), for which the average difference was smaller at 0.3°C. The extent to which the larger difference found for the quartermasters' measurements is due to additional sample cooling rather than thermometric error is unclear. The quartermasters were using the ship's slow-response (and perhaps poorly-calibrated) thermometer while Brooks was using a calibrated fast-response thermometer. Recall also that the quartermasters were only measuring to a half or whole °F. Brooks attributes the difference to several sources, including cooling by or of the thermometer.

Brooks conducted a similar comparison aboard the *Finland* in May 1928 (B28). Canvas bucket temperatures (4 L bucket, double-walled) obtained by the crew averaged 0.4°C lower than tin bucket temperatures obtained by Brooks with a calibrated thermometer, both buckets being deployed from a similar low deck level. Although attributed to cooling of the canvas bucket samples, the main thermometer used by the crew (a galley thermometer) exhibited variable error between −0.5 and +0.75°F (−0.3 and +0.4°C) dependent upon temperature. However, the cool error of the canvas bucket temperatures was found to increase with larger depressions of the wet bulb temperature below the SST, as would be expected for sample cooling. It was also found to be substantially larger at nighttime than daytime, averaging 1.1 and 0.4 °C, respectively. The larger nighttime error was attributed to the observers removing the reservoir thermometer from the bucket to hold under a light for reading..

B.1.4 Wind tunnel experiments

Ashford (1949) measured the temperature change of water samples in several types of bucket when suspended in a wind tunnel. The buckets were first dipped in a water bath, the temperature of which was varied to yield a range of air–water temperature contrasts. Wind speed was held fixed at 20 mph (∼9 m s^{-1}) while air temperature and relative humidity varied from 15.6–18.3°C and 50–60%, respectively. Note that the latter is fairly low compared to typical open ocean values. The rate of sample temperature change was found to increase with greater contrast between the wet bulb

and water temperature, with warming observed for positive differences and cooling for negative. Measured cooling rates with an Mk II bucket were intermediate between those for a rubber-walled German scoop thermometer and a German rubber pail. With a 3°C water-wet bulb contrast, the scoop thermometer cooled at $\sim$0.2°C min^{-1} and the Mk II by $\sim$0.1°C min^{-1}, while the sample in the rubber pail did not change temperature perceptively. These contrasting cooling rates may partly reflect the different volumetric capacities of the buckets (0.6 L for the scoop thermometer, 4 L for the Mk II and unknown volume for the rubber pail). Cooling rates were found to be independent of whether the external surface of the bucket was wet or dry.

Roll (1951a) conducted wind tunnel experiments with the same model of scoop thermometer as used by Ashford (1949). This was again immersed in a tank of water at a desired temperature and then suspended. Wind speed was varied between 2 and 19 m s^{-1} and air–water temperature contrast was varied between +5 and −10°C. With a −2.5°C air–water temperature contrast, the sample cooled, respectively, by 0.1 and 0.25°C in the first minute at wind speeds of 8 and 10 m s^{-1}, with cooling not detected at lower wind speeds. No cooling was detected in the first minute for wind speeds of 6 m s^{-1} and below. The rate of temperature change was found to decline over the 10 min measurement period as the temperature contrast was diminished by heat exchange. Roll (1951b) stresses the difficulty of using results from wind tunnels to correct bucket temperatures given that the wind conditions experienced by buckets during the exposure period aboard ships cannot be reliably estimated.

B.2 Bucket and engine intake temperature adjustments

FP95 developed physical models for temperature change of seawater samples in wood and canvas buckets. Modelled temperature change is dependent on air–sea temperature difference, relative humidity and apparent wind speed. Different versions of the models were developed by altering parameters such as ship speed and bucket exposure to solar radiation. Two canvas buckets of different dimension were modelled, one the size of the Mk II and the other half its diameter at 8 cm. Adjustments were derived for both “fast” and “slow” ships to represent motor and sailing vessels, with ship speed set to 7 and 4 m s^{-1}, respectively.

The FP95 bucket models are particularly sensitive to the choice of exposure time.

For canvas bucket adjustments in non-equatorial regions with appreciable seasonal SST cycles and sufficient data, exposure time was determined using the finding that seasonal cycle amplitudes were generally larger in pre-1942 years (Folland, 2005). FP95 assumed the larger amplitudes were due to environmental cooling of wood and canvas buckets, the strength of which varies seasonally in their adjustments. Exposure time was altered in 10° latitude bands to find adjustments that would minimise the variance of three pre-1942 30-year average seasonal cycles relative to the total variance of their complete record. The longest exposure times so derived exceeded 5 min and the shortest were under 2 min. An "optimum integration time" (not reported) was calculated for each model version by averaging over derived times for all 30-year averages across all latitude bands. The exposure time for wooden bucket adjustments was set to 4 min everywhere, partitioned into a 1 min hauling period and a 3 min on-deck phase.

To generate final pre-1942 "corrections", the adjustments from different model versions were combined to fit a time-variant ratio of the number of wood to canvas bucket observations and an assumed linear increase in ship speed from 4 to 7 $\mathrm{m\,s^{-1}}$ between 1870 and 1940. The former was set so that the resulting adjustments would minimise the difference between night marine air temperature (NMAT) and SST anomalies in the tropical Pacific and southern tropical Indian Ocean between 1856 and 1920. FP95 found pre-1942 annual mean northern- and southern-hemispheric NMAT anomalies were up to 0.5°C larger than the corresponding SST anomalies and attributed this to bucket cooling. It is commonly assumed that NMAT and SST anomalies should be similar on seasonal and longer timescales.

The FP95 adjustments have been applied with some modifications to pre-1942 bucket temperatures in the UK Met Office Hadley Centre Sea Ice and SST dataset, HadISST (Rayner et al., 2003), and the second and third versions of the Hadley Centre SST dataset, HadSST2 (Rayner et al., 2006) and HadSST3 (Kennedy et al., 2011b,a). Independent bucket adjustments have been applied to the US National Oceanic and Atmospheric Administration's Extended Reconstruction SST version 3, ERSSTv3 (Smith et al., 2008), derived by (Smith and Reynolds, 2002) using the assumption of similarity between NMAT and SST anomalies. Kent et al. (2010) compare bucket adjustments applied to HadSST2 and ERSSTv3. Both generally increase on a global annual average from the mid-19^{th} century to around 1920 and then plateau to the late 1930s. In HadSST2, the global-mean of the adjustments increases from ∼0.2°C in 1880 to ∼0.4°C in 1920. This is due to the specification of increases in the proportion

of canvas to wooden bucket measurements and "fast" to "slow" ships over this period.

As of 2008, in situ observations in historical SST datasets had not been adjusted post-1941. (Thompson et al., 2008) suggested a need to apply adjustments to more recent observations, arguing an abrupt 1945 drop of ∼0.3°C in global-mean SST from HadSST2 was the result of uncorrected method changeover. In HadSST3, adjustments have been applied to measurements from buckets, buoys and engine intakes over the duration of the record (1850–2006). The FP95 "fast ship" adjustments are used post-1941, with their wooden bucket adjustments applied to temperatures from modern "insulated" buckets. A linear switchover from canvas buckets to the latter is specified over the 1950s and 1960s. As for HadSST2, different realisations of the FP95 adjustments were derived by varying bucket model parameters within their supposed uncertainty ranges.

Multiple realisations of EIT adjustments were also developed for HadSST3. For measurements obtained in the North Atlantic between 1970 and 1994, adjustments were generated from the EIT errors of (Kent and Kaplan, 2006). Adjustments for other regions and years were derived by taking the best estimate for the average EIT error from the literature to be 0.2°C too warm. Note that "strictly speaking" adjustments are intended to be relative to the mix of observations in the respective dataset reference period (in this case 1961–1990) rather than corrections back towards "true" values.

HadSST3 has been combined with the fourth version of the Climatic Research Unit (CRU) near-surface land air temperature dataset, CRUTEM4 (Jones et al., 2012), to produce a new global instrumental surface temperature record, HadCRUT4 (Morice et al., 2012).

B.3 Exposure time

The magnitude of the temperature change simulated by the FP95 bucket models critically depends on the specified exposure time. This can be partitioned into a hauling phase and an on-deck period. Here an attempt is made to constrain the historical durations of these periods using information in the literature.

The length of the hauling period depends on the height of the observer above the waterline and the quickness of the haul. (Lumby, 1928) notes that buckets could be drawn upward a distance of 30–60 ft (∼9–18 m) or more. (Brooks, 1926) reported that quick hauls with a 4 L tin bucket from 10 to 20 ft (∼3–6 m) up on the leeward

stern of the *Empress of Britain* took him 20 to 30 s, equating to hauling speeds of $\sim$0.2 m s^{-1}. The hauling period would undoubtedly have been longer for the canvas bucket measurements conducted by the crew from the bridge, but no estimates are given. (Lumby, 1928) estimates the exposure time for these measurements to have been no longer than 2 min based on his own experimental sample cooling rates (0.11–0.12°C min^{-1}) and the portion of the canvas bucket error attributed to sample cooling by Brooks ($\sim$0.25°C), both of which are rather uncertain. On the *Finland*, the typical hauling period for the mariners' canvas bucket deployments from a low deck (likely $\sim$9 m up) was apparently 2 min, equating to a very slow hauling speed of 0.08 m s^{-1}. Brooks suggested this could have been reduced to 1 min by faster handwork. For comparison, the hauling period for Brooks' tin bucket measurements from a similar deck level (9 m up) appears to have been $\sim$20–30 s (his exposure time was $\sim$30–40 s and his fast-response thermometer stabilised in $\sim$10 s), equating to hauling speeds $\sim$0.3–0.45 m s^{-1}. Note that all these values are for bucket deployments conducted on large ocean liners. It is unclear whether deployments were generally conducted from the bridge or from a lower deck on such vessels. More generally, the extent to which deployments are and were conducted from heights exceeding 10 m is unknown, with deployments becoming increasingly difficult at greater heights and vessel speeds.

With regards to the on-deck period, this can generally be assumed to be largely comprised of the waiting period for thermometer stabilisation following insertion, at least for those buckets without built-in thermometers. Bucket temperature readings conducted aboard the *Finland* by the ships' crew took $\sim$45–60 s, suggesting that the thermometers used stabilised within a similar period. This would be consistent with (Lumby, 1928) who notes that a thermometer will indicate the water temperature in one minute with reasonably active stirring. On-deck periods for pre-WWII bucket measurements are generally assumed to have been much longer than this based on recommended waiting periods for thermometer equilibration of 2–3 min or more (FP95). However, written instructions do not necessarily equate to the actual practices of mariners. (Schott, 1893) suggests that periods of 3–4 min noted in some books are much too long for most instruments in use given the potential for bucket cooling. He reports waiting an average of 1 min before obtaining a reading. A post-WWII source, (HMSO, 1956), states that thermometers attain a steady reading after about 30 s with vigourous stirring, with (Stubbs, 1965) noting that this was the waiting period respected on a British ocean weather ship. The response time of liquid-in-glass thermometers is almost entirely dependent on bulb diameter (Nicholas and White, 2001),

being longer for larger diameter bulbs. Placing greater weight on actual reports of the duration of thermometer stabilisation periods over recommendations from observing instructions, I suggest that the on-deck period would generally have been around 1 min.

B.4 Synthesis and conclusions

Various techniques have been used to measure sea surface temperature since the mid-19^{th} century. Methods differ in terms of platform, measurement depth and extent of automation (e.g. manual observation and recording). Shipboard methods include temperature measurement of bucket samples and of engine cooling water intakes. Methodological details are generally poorly documented for both methods, but particularly so for intakes. The latter not being a dedicated scientific method, instruments and procedures have likely varied widely between ships. Many details of shipboard methods show general changes over time. Indeed ships themselves have clearly altered dramatically since the 1850s, with a general increase in average speed, freeboard and the deepest drafts. Intake depths on modern voluntary observing ships appear typically around 7–10 m, although can exceed 15 m.

Accurate temperatures can be obtained with either the bucket or intake method. However, measurements cannot be expected to be of high accuracy or precision when obtained by untrained sailors using poorly calibrated, low resolution thermometers. This is not of major concern with regards the accuracy of large-scale area-average SST records since random and systematic errors associated with individual observations and instruments tend to cancel out across large numbers of observations. The literature suggests a tendency for the lowest resolution liquid-in-glass thermometers in use to have generally been poorer for intake readings than for bucket measurements. There are reports of intake thermometers graduated in intervals of only 2 or 5 °F (B28; Saur, 1963), consistent with the idea that EIT readings would only have been needed to accuracy of 1–2°C in their traditional engine monitoring role. However, whether intake thermometers were generally of poorer accuracy and precision than those used for bucket measurements is unclear. Saur (1963) describes a study in which several were found to read in systematic error by between −1 and +2°C, while B28 notes that a galley thermometer used for bucket measurements aboard the *Finland* read in variable error between −0.3 and +0.4°C.

Bucket temperatures have generally been found to average a few tenths of °C cooler

than simultaneous intake temperatures in field studies, although with considerable scatter amongst the individual bucket-intake differences (e.g. James and Fox, 1972). Such variability is likely, at least in part, due to poor observation and recording with thermometers of variable accuracy and resolution. Such noise does not necessarily negate the accuracy of average differences, however. Average bucket-intake differences are found to vary widely, both between ships and between cruises on the same ship (Saur, 1963; Tabata, 1978b). Crucially though, individual errors in bucket and intake temperatures cannot be directly distinguished from relative bucket-intake differences. To do so requires supplementary accurate in situ temperatures and these have rarely been obtained in field comparisons. In their absence it is difficult to distinguish, for instance, between contributions from thermometric errors, temperature change of bucket samples and near-surface temperature gradients in non-zero average differences found for individual ships and cruises.

The magnitude of bucket cooling depends on the cooling rate and the time elapsed between sampling and thermometer reading (the exposure time). Field and lab experiments suggest samples in small-volume canvas buckets can cool at rates of 0.05–0.10°C min^{-1} or more (e.g. 0.2°C min^{-1}). Wind tunnel experiments (Ashford, 1949; Roll, 1951a) have shown cooling to be faster under larger sea–air temperature contrasts and at higher wind speeds. From physical principles we would expect cooling rates to vary with bucket type and construction (e.g. material, presence of a lid) and sample volume. Different buckets can have quite different volumes, so the influence of each of these factors is often unclear in field and lab experiments. Canvas buckets of volumetric capacity between 2 and 12 L are known to have been used (B28; Schott, 1893; Uwai and Komura, 1992).

Systematic warm error in intake temperatures is also a plausible explanation for negative average bucket-intake differences. For instance, Tabata (1978c,d) found EIT to average 0.3±1.2°C warmer than accurate in situ temperatures on a research vessel, while Brooks (1928) found EIT to be overly-warm by 0.7°C on average on an ocean liner. Given the large magnitude of these errors, it is possible that the principal cause of the 0.3°C average intake-bucket difference found by James and Fox (1972) is EIT error rather than bucket cooling. Note that the general origin of systematic warm errors in EIT is poorly known, with it being demonstrated in Appendix C that warming of intake seawater by hot engine room air is an unlikely explanation.

Bucket adjustments have been applied to historical SST datasets in an attempt to reduce supposed bucket cooling error. In the case of the Hadley Centre SST datasets

(e.g. HadSST3), these were derived using variants of the FP95 bucket models. These models are particularly sensitive to the choice of exposure time, an interval comprised of a hauling period and an on-deck phase. Based on the literature, there is scope for both of these periods to have ranged between tens of seconds and a few minutes. For their wooden bucket adjustments, FP95 assume a 1 min hauling phase and a 3 min on-deck period, giving a total exposure time of 4 min. They support their use of on-deck periods of several minutes by citing instructions recommending waiting periods for thermometer equilibration of 2–3 min or more. However, the few reports we have detailing actual durations of thermometer reading periods suggest they could typically have been only around a minute in duration (Schott, 1893; B28). Since this is uncertain, I suggest that the range of possible average exposure times used to derive bucket adjustments be widened to allow for periods of 1–2 min.

Bucket-intake field comparisons are of variable relevance to the bulk of the historical SST data in ICOADS. Studies vary greatly in terms of the type(s) of vessel used (e.g. scientific or merchant; sail or motor), the methods assessed and the spatial and temporal coverage of measurements (e.g. region(s), season(s) and number of observations). Further, a minor variant of a historical method may have been tested (e.g. a particular type of bucket) that was not in widespread use. This in itself is difficult to assess given the lack of metadata accompanying historical SST measurements. In terms of deducing the extent to which bucket and intake errors are due to actual change in sample temperature, the utility of several field studies is reduced by poor measurement quality (e.g. the use of an inaccurate ships' thermometer in the B28 study). Accurate measurement of sample temperature change requires use of well-calibrated, high precision, fast-response thermometers. Such limitations of previous studies can be addressed through additional field experiments of the type presented in Chapter 3.

Appendix C

Engine intake warming model

I developed the following model for heating of seawater flowing through a pipe to test whether engine room warming of intake seawater is physically plausible. This Appendix is published as part of Matthews and Matthews (2013).

Fixed-value model parameters are given in Table C.3 together with their symbols, units and prescribed value(s) used to generate Figs. C.3 and C.4. Computed model variables and their symbols, units and range of values calculated in generation of Fig. C.3 are given in Table C.4. Illustrative schematics highlighting some of the basic model parameters and variables are provided in Figs. C.1 and C.2.

Volumetric flow rate through a pipe is given by

$$\dot{v} = \frac{1}{\rho}\frac{\mathrm{d}m}{\mathrm{d}t} = \frac{1}{\rho}\dot{m}, \tag{C.1}$$

where ρ is density, m is mass, t is time and $\dot{m}$ the mass flow rate.

Flow velocity is given by

$$u = \frac{\dot{v}}{A_\mathrm{c}}, \tag{C.2}$$

where A_c is the inside cross-sectional area of the pipe.

For a cylindrical pipe of inside diameter D_i, $A_\mathrm{c} = \frac{\pi D_i^2}{4}$. Outside diameter D_o is related to inside diameter through wall thickness, Δx, by $D_\mathrm{o} = D_i + 2\Delta x$.

For a pipe of length L, the surface area of the inside wall is given by

$$A_\mathrm{i} = \pi D_\mathrm{i} L\,. \tag{C.3}$$

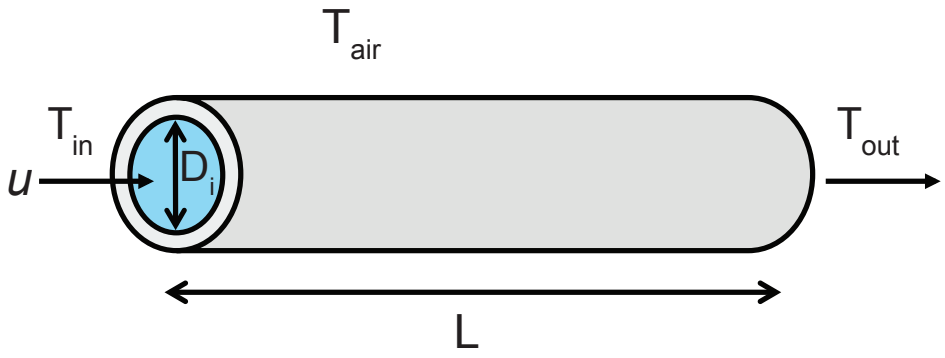

Figure C.1: Schematic of the model for warming of intake seawater by engine room air at temperature T_{air}. The seawater is flowing at velocity u in a pipe of inside diameter D_{i}. The initial seawater temperature is T_{in} and the temperature after pipe length L is T_{out}. I do not explicitly model a sea chest, rather I assume the temperature of the seawater in a sea chest is the same as that of the external seawater beyond the inlet (i.e. T_{in}). The model can thus be considered to represent a length of pipe inboard of a sea chest.

Similarly the surface area of the outside wall, $A_{\text{o}} = \pi D_{\text{o}} L$.

A single heat transfer process is assumed to occur in each medium; free (natural) convection in the engine room air, conduction across the pipe wall and forced convection in the intake seawater. Radiative transfer is neglected.

From Fourier's Law of Conduction, the rate of conductive heat transfer in one dimension is given by

$$q_{\text{cond}} = kA\frac{\Delta T}{\Delta x}, \tag{C.4}$$

where ΔT is a positive temperature difference across a material of thermal conductivity k, surface area A and thickness Δx.

From Newton's Law of Cooling, the rate of convective heat transfer is given by

$$q_{\text{conv}} = hA\Delta T, \tag{C.5}$$

where h is the convective heat transfer coefficient. Since the surface area of a cylindrical pipe is different for the inside and outside walls, we replace A in (C.5) with a log-mean cross-sectional area, $A_{\text{lm}} = \frac{\pi(D_{\text{o}} - D_i)}{\ln(\frac{D_{\text{o}}}{D_i})} L$.

Thin boundary layers or films exist along the inside and outside walls of intake

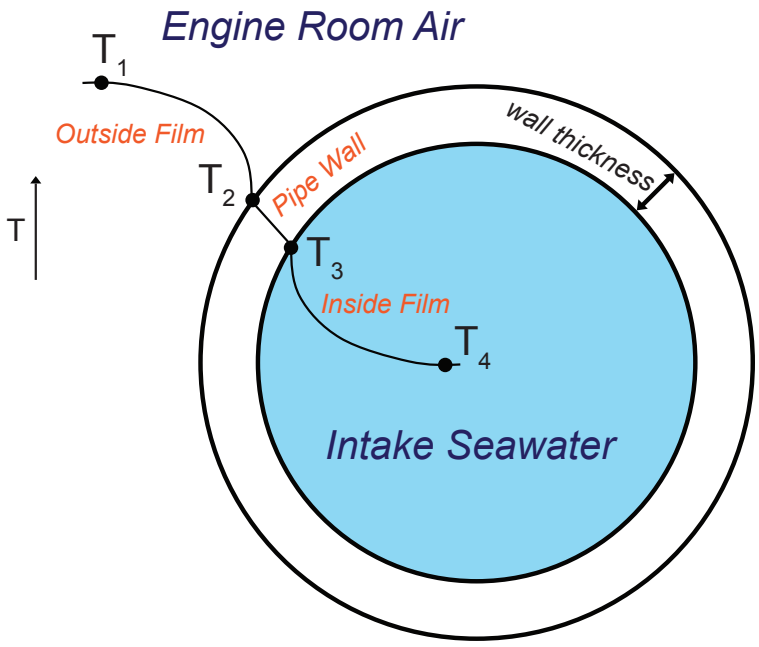

Figure C.2: Cross-section through the modelled intake pipe. An illustrative temperature profile is shown by the solid black lines connecting temperatures T_1, T_2, T_3 and T_4, with engine room air temperature, T_1, being the warmest.

pipes, with flow velocity reduced towards the wall and strong temperature gradients present (Fig. C.2). I define convective heat transfer coefficients for the inside and outside films, h_{if} and h_{of}, respectively.

Equating convective heat flow across the outside and inside films with conductive heat flow across the pipe wall we have

$$q = h_{\mathrm{of}} A_{\mathrm{o}} (T_1 - T_2) = k_{\mathrm{w}} A_{\mathrm{lm}} \frac{T_2 - T_3}{\Delta x_{\mathrm{w}}} = h_{\mathrm{if}} A_{\mathrm{i}} (T_3 - T_4), \tag{C.6}$$

where T_{1-4} are defined as in Fig. C.2, k_{w} is the thermal conductivity of the wall and Δx_{w} the wall thickness. I model an unlagged steel pipe.

Rearranging for the temperature contrasts driving the convective and conductive

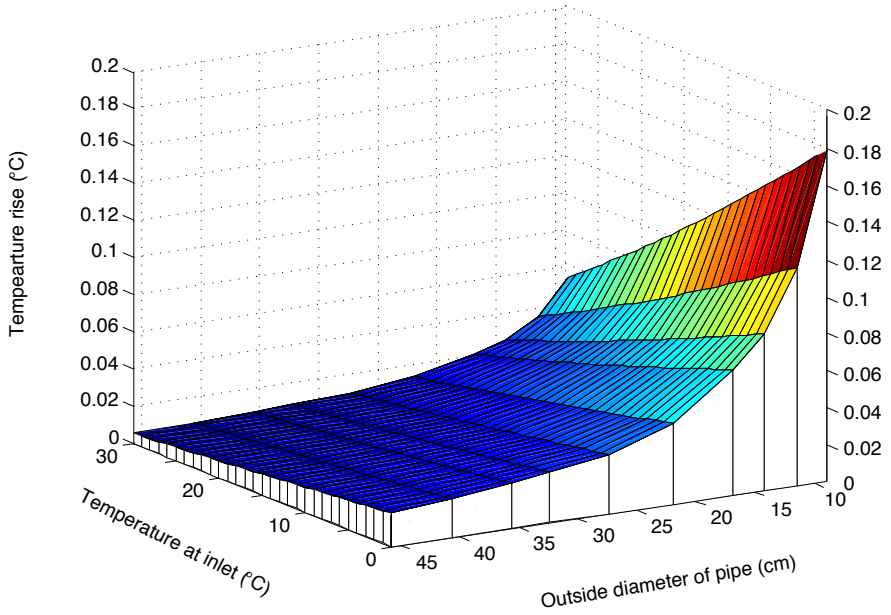

Figure C.3: Calculated warming of seawater along an intake pipe of length 20 m for variable outside diameter and inlet temperature. Engine room air temperature was set to 50°C and flow velocity to $1\,\mathrm{m\,s^{-1}}$.

heat flow

$$T_1 - T_2 = \frac{q}{h_{\mathrm{of}} A_{\mathrm{o}}} \tag{C.7}$$

$$T_2 - T_3 = \frac{q \Delta x_{\mathrm{w}}}{k_{\mathrm{w}} A_{\mathrm{lm}}} \tag{C.8}$$

$$T_3 - T_4 = \frac{q}{h_{\mathrm{if}} A_{\mathrm{i}}}. \tag{C.9}$$

Combining (C.7), (C.8) and (C.9) we can solve for the outside and inside wall temperatures, T_2 and T_3 as

$$T_2 = T_4 + \frac{\frac{\Delta x_{\mathrm{w}}}{k_{\mathrm{w}} A_{\mathrm{lm}}} + \frac{1}{h_{\mathrm{if}} A_{\mathrm{i}}}}{\frac{1}{h_{\mathrm{of}} A_{\mathrm{o}}} + \frac{\Delta x_{\mathrm{w}}}{k_{\mathrm{w}} A_{\mathrm{lm}}} + \frac{1}{h_{\mathrm{if}} A_{\mathrm{i}}}} (T_1 - T_4) \tag{C.10}$$

$$T_3 = T_1 - \frac{\frac{\Delta x_{\mathrm{w}}}{k_{\mathrm{w}} A_{\mathrm{lm}}} + \frac{1}{h_{\mathrm{of}} A_{\mathrm{o}}}}{\frac{1}{h_{\mathrm{of}} A_{\mathrm{o}}} + \frac{\Delta x_{\mathrm{w}}}{k_{\mathrm{w}} A_{\mathrm{lm}}} + \frac{1}{h_{\mathrm{if}} A_{\mathrm{i}}}} (T_1 - T_4). \tag{C.11}$$

Given that seawater temperature varies along the pipe, we replace T_4 with an average seawater temperature, $T_{\mathrm{ave}} = \frac{T_{in} + T_{\mathrm{out}}}{2}$ and $T_1 - T_4$ with a log-mean temperature

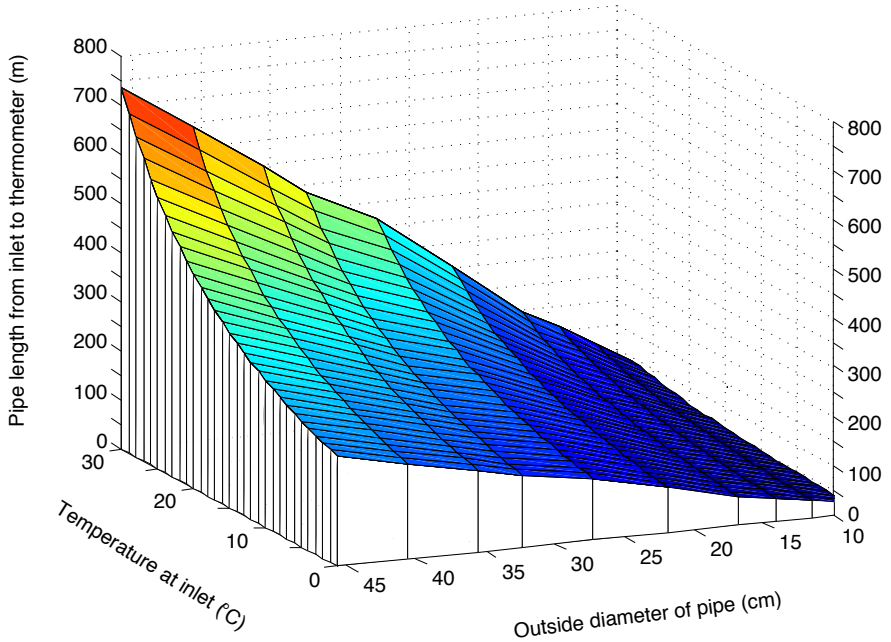

Figure C.4: Pipe length required for intake seawater to warm by 0.2°C given an engine room air temperature of 50°C and flow velocity of $1\,\mathrm{m\,s^{-1}}$.

difference, $\Delta T_{\mathrm{lm}} = \frac{(T_1 - T_{\mathrm{in}}) - (T_1 - T_{\mathrm{out}})}{\ln(\frac{T_1 - T_{\mathrm{in}}}{T_1 - T_{\mathrm{out}}})}$. T_{in} and T_{out} are the seawater temperatures at the inlet and after pipe length L, respectively.

We can now define an overall inside heat transfer coefficient, U_{i} such that

$$q = U_{\mathrm{i}} A_{\mathrm{i}} \Delta T_{\mathrm{lm}}. \tag{C.12}$$

Summing (C.7), (C.8) and (C.9) and taking $T_1 - T_4 = \Delta T_{\mathrm{lm}}$ then

$$\Delta T_{\mathrm{lm}} = q\left(\frac{1}{h_{\mathrm{of}} A_{\mathrm{o}}} + \frac{\Delta x_{\mathrm{w}}}{k_{\mathrm{w}} A_{\mathrm{lm}}} + \frac{1}{h_{\mathrm{if}} A_{\mathrm{i}}}\right). \tag{C.13}$$

We can now solve for U_i using (C.12):

$$U_{\mathrm{i}} = \frac{1}{\frac{A_{\mathrm{i}}}{h_{\mathrm{of}} A_{\mathrm{o}}} + \frac{A_{\mathrm{i}} \Delta x_{\mathrm{w}}}{k_{\mathrm{w}} A_{\mathrm{lm}}} + \frac{1}{h_{\mathrm{if}}}}. \tag{C.14}$$

The specific heat capacity of the intake seawater, c_p is related to its warming by

$$q = \dot{m} c_{\mathrm{p}} (T_{\mathrm{out}} - T_{\mathrm{in}}). \tag{C.15}$$

Equating (C.12) and (C.15) and substituting in (C.3):

$$\dot{m}c_{\mathrm{p}}(T_{\mathrm{out}} - T_{\mathrm{in}}) = U_{\mathrm{i}}(\pi D_{\mathrm{i}} L)\Delta T_{\mathrm{lm}}. \tag{C.16}$$

Rearranging for the temperature change after pipe length L:

$$T_{\mathrm{out}} - T_{\mathrm{in}} = \frac{U_{\mathrm{i}}(\pi D_{\mathrm{i}} L)\Delta T_{\mathrm{lm}}}{\dot{m}c_{\mathrm{p}}}. \tag{C.17}$$

For the range of inside diameters adopted (Table C.1) and the specified flow velocity of $1\,\mathrm{m\,s^{-1}}$, pipe flow is turbulent with Reynolds number, Re, exceeding 10 000. Note Reynolds number is calculated as $Re = \frac{4\dot{m}}{\pi D_i \mu}$ with μ the dynamic viscosity.

We model convective heat transfer about the inside film (if) as for fully developed turbulent flow, using the empirical correlation of Gnielinski (1976) for a smooth tube:

$$Nu = \frac{\frac{f}{8}(Re - 1000)Pr}{1 + 12.7(\frac{f}{8})^{\frac{1}{2}}(Pr^{\frac{2}{3}} - 1)}, \tag{C.18}$$

where Nu is the Nusselt number, f the friction factor and Pr the Prandtl number given by $Pr = \frac{c_p \mu}{k}$.

Equation (C.18) is valid for $0.5 < \mathrm{Pr} < 2000$ and $3000 < \mathrm{Re} < 5 \times 10^6$. I compute the friction factor using the explicit relation of Petukhov (1970): $f = (0.79\ln(Re) - 1.64)^{-2}$.

The convective heat transfer coefficient for the inside film is calculated using the thermal conductivity of the inside film, k_{if} as

$$h_{\mathrm{if}} = \frac{Nu_{\mathrm{if}}\, k_{\mathrm{if}}}{D_{\mathrm{i}}}. \tag{C.19}$$

For convection about the outside film (of) I use the Nusselt number formulation of Tahavvor and Yaghoubi (2008) for natural convection around a cold horizontal cylinder:

$$Nu_{\mathrm{of}} = 0.3607 R_{\mathrm{aD}}^{0.2802}, \tag{C.20}$$

where R_{aD} is the Rayleigh number based on D_{o} as the characteristic length and given by $R_{aD} = \frac{g\beta_{\mathrm{of}}}{\alpha_{\mathrm{of}}\nu_{\mathrm{of}}}(T_1 - T_2)D_{\mathrm{o}}^3$ (Homayoni and Yaghoubi, 2008). β_{of} is the thermal expansion coefficient, α_{of} thermal diffusivity, ν_{of} kinematic viscosity and g acceleration

due to gravity.

We use (C.20) up to $R_{aD} = 4.44 \times 10^8$, above the specified R_{aD} upper limit of 10^8. This is acceptable given that only relations for warm cylinders (i.e. those with outside wall temperature warmer than the adjacent air) are otherwise available and use of these yields similar values for h_{of}. For instance, use of relation (16b) in Tahavvor and Yaghoubi (2008), valid for warm cylinders and $R_{aD} > 10^8$, yields h_{of} values ranging from 3.9–5.4 $W\,m^{-2}\,K^{-1}$ for Fig. C.3 compared to 4.1–7.1 $W\,m^{-2}\,K^{-1}$ using (C.20). Differences between computed $T_{out} - T_{in}$ values were all <0.01°C.

Similar to (C.19):

$$h_{of} = \frac{Nu_{of} k_{of}}{D_o}. \tag{C.21}$$

Dimensionless parameters and other variables computed to find h_{if} and h_{of} are calculated respectively at the inside and outside film temperatures (T_{if} and T_{of}), taken to be

$$T_{if} = \frac{T_3 + T_{ave}}{2} \tag{C.22}$$

$$T_{of} = \frac{T_1 + T_2}{2}. \tag{C.23}$$

The intake warming model is solved iteratively from initial guesses for T_{out}, h_{if} and h_{of} with T_{out} updated each iteration as follows: $T_{out_{n+2}} = \frac{T_{out_n} + T_{out_{n+1}}}{2}$ where n is iteration number.

We adopt an upper limit for engine room air temperature of 50°C and vary inlet temperature in 1°C intervals between 0 and 30°C. Pipe inside diameter is varied from around 6 to 37 cm corresponding to a range of standard outside diameters with wall thicknesses of common upper limit (Table C.1).

Pipe inside diameters are dependent on engine horsepower and type and determined from volume flux requirements for engine cooling. Kirk and Gordon (1952) report intake pipes of 14 inch (∼35 cm) inside diameter on British Ocean Weather Ships while Saur (1963) notes pipe diameters varied between 4 and 20 inches (around 10 to 50 cm) across 12 US military vessels. Piip (1974) describes well thermometers inserted into engine intakes to at least 25 cm depth, so inside diameters were perhaps double this. Tabata (1978c) reports an engine intake pipe of 20 cm diameter on a Canadian research vessel. A typical inside diameter on a modern 100 000 tonne diesel tanker would be ∼25 cm. Intakes on steamships could have been larger still given

Table C.1: Intake pipe specifications used to generate Figs. C3 and C4.

Outside diameter (cm)	Wall thickness (cm)	Schedule	Inside diameter (cm)	Nominal bore (inches)
8.89	1.52	XXS	5.85	3
11.43	1.71	XXS	8.01	4
14.13	1.90	XXS	10.33	5
16.83	2.20	XXS	12.43	6
21.91	2.30	160	17.31	8
27.30	2.54	XXS	22.22	10
32.39	3.33	160	25.73	12
35.56	3.57	160	28.42	14
40.64	4.05	160	32.54	16
45.72	4.52	160	36.68	18

Table C.2: Inlet-thermometer pipe lengths reported in the literature.

Reference	Pipe length from inlet to thermometer
Saur (1963)	Few feet to 25 feet
James and Fox (1972)	0–9 m
Piip (1974)	3–15 m
Tabata (1978c)	∼1 m

that steam engines are closed cycle and so do not expel some of their waste heat through gaseous exhaust like diesel engines. To derive Fig. C.3 I adopted a fixed pipe length of 20 m, above the upper end of inlet-thermometer distances reported in the literature (Table C.2). Seawater-specific heat capacity, thermal conductivity and dynamic viscosity were calculated using the Massachusetts Institute of Technology Thermophysical Properties of Seawater toolbox (`http://web.mit.edu/seawater/`), using a salinity of 35 psu.

Table C.3: Fixed parameters of the engine intake warming model including their value(s) for Figs. C3 and C4.

Model parameter	Symbol	Value(s)	Unit
Pipe inside diameter	D_i	0.0585–0.3668	m
Pipe outside diameter	D_o	0.0889–0.4572	m
Pipe wall thickness	Δx_w	0.0152–0.0452	m
Surface area of inside wall	A_i	3.7–23.0	m^2
Surface area of outside wall	A_o	5.6–28.7	m^2
Log-mean wall surface area	A_lm	4.6–25.8	m^2
Inside cross-sectional area	A_c	2.688×10^{-3}–1.057×10^{-1}	m^2
Thermal conductivity of pipe wall (unlagged steel)	k_w	45	$\mathrm{W\,m^{-1}\,K^{-1}}$
Flow velocity	u	1	$\mathrm{m\,s^{-1}}$
Volumetric flow rate	$\dot{v}$	2.688×10^{-3}–1.057×10^{-1} (2.7–$105.7\,\mathrm{L\,s^{-1}}$)	$\mathrm{m^3\,s^{-1}}$
Engine room air temperature	T_1	50	°C
Seawater temperature at inlet	T_in	0–30	°C
Seawater salinity	S	35	psu
Acceleration due to gravity	g	9.81	$\mathrm{m\,s^{-2}}$

Table C.4: Variables computed by the engine intake warming model including their calculated range in Fig. C3.

Model variable	Symbol	Computed range	Unit
Outside wall temperature	T_2	0.35–30.13	°C
Inside wall temperature	T_3	0.16–30.07	°C
Inside film temperature	T_{if}	0.08–30.05	°C
Outside film temperature	T_{of}	25.18–40.06	°C
Seawater temperature after pipe length L	T_{out}	0.02–30.05	°C
Bulk seawater temperature	T_{ave}	0.01–30.03	°C
Log-mean temperature difference across the pipe wall	ΔT_{lm}	19.97–49.99	°C
Seawater temperature difference between inlet and thermometer	ΔT	0.01–0.18	°C
Overall inside heat transfer coefficient	U_{i}	5.1–10.7	$\mathrm{W\,m^{-2}\,K^{-1}}$
Heat transfer rate	q	596.6–7779.1	W
Seawater specific heat capacity	c_{p}	3991.1–4003.1	$\mathrm{J\,kg^{-1}\,K^{-1}}$
Seawater density	ρ	1021.7–1028.1	$\mathrm{kg\,m^{-3}}$
Mass flow rate	$\dot{m}$	2.7–108.6	$\mathrm{kg\,s^{-1}}$
Seawater thermal conductivity (inside film)	k_{if}	0.57–0.62	$\mathrm{W\,m^{-1}\,K^{-1}}$
Air thermal conductivity (outside film)	k_{of}	0.03	$\mathrm{W\,m^{-1}\,K^{-1}}$
Reynolds number (inside film)	Re_{if}	3.18×10^4–4.36×10^5	dimensionless
Prandtl number (inside film)	$\mathrm{Pr}_{\mathrm{if}}$	5.59–13.31	dimensionless
Seawater dynamic viscosity (inside film)	μ_{if}	8.60×10^{-4}–1.90×10^{-3}	$\mathrm{kg\,m^{-1}\,s^{-1}}$
Friction factor	f	1.35×10^{-2}–2.33×10^{-2}	dimensionless
Air thermal diffusivity (outside film)	α_{of}	2.23×10^{-5}–2.45×10^{-5}	$\mathrm{m^2\,s^{-1}}$
Air thermal expansion coefficient (outside film)	β_{of}	3.19×10^{-3}–3.35×10^{-3}	$\mathrm{K^{-1}}$
Air kinematic viscosity (outside film)	ν_{of}	1.57×10^{-5}–1.72×10^{-5}	$\mathrm{m^2\,s^{-1}}$
Rayleigh number for characteristic length D_{o}	R_{aD}	1.04×10^6–4.44×10^8	dimensionless
Nusselt number (inside film)	Nu_{if}	286.1–1929.7	dimensionless
Nusselt number (outside film)	Nu_{of}	17.5–95.5	dimensionless
Convective heat transfer coefficient (inside film)	h_{if}	2221.6–4178.6	$\mathrm{W\,m^{-2}\,K^{-1}}$
Convective heat transfer coefficient (outside film)	h_{of}	4.1–7.1	$\mathrm{W\,m^{-2}\,K^{-1}}$

Appendix D

El Niño periods

El Niño months in the equatorial Pacific (10°N-10°S) were taken to be those months for which the Niño 3.4 index has a value of $\geq$+0.5. The Niño 3.4 index dataset available here was used and the following months found to be El Niño months based on the aforementioned criterion:

July 1951 - January 1952
January 1953 - February 1954
April 1957 - June 1958
November 1958 - February 1959
July 1963 - February 1964
May 1965 - April 1966
July 1968 - January 1970
May 1972 - March 1973
October 1976 - January 1977
September 1977 - January 1978
May 1982 - June 1983
September 1986 - January 1988
June 1991 - June 1992
October 1994 - March 1995
May 1997 - May 1998
May 2002 - March 2003
July 2004 - January 2005
September 2006 - January 2007
July 2009 - April 2010

Appendix E

Relationships between carbonate chemistry parameters

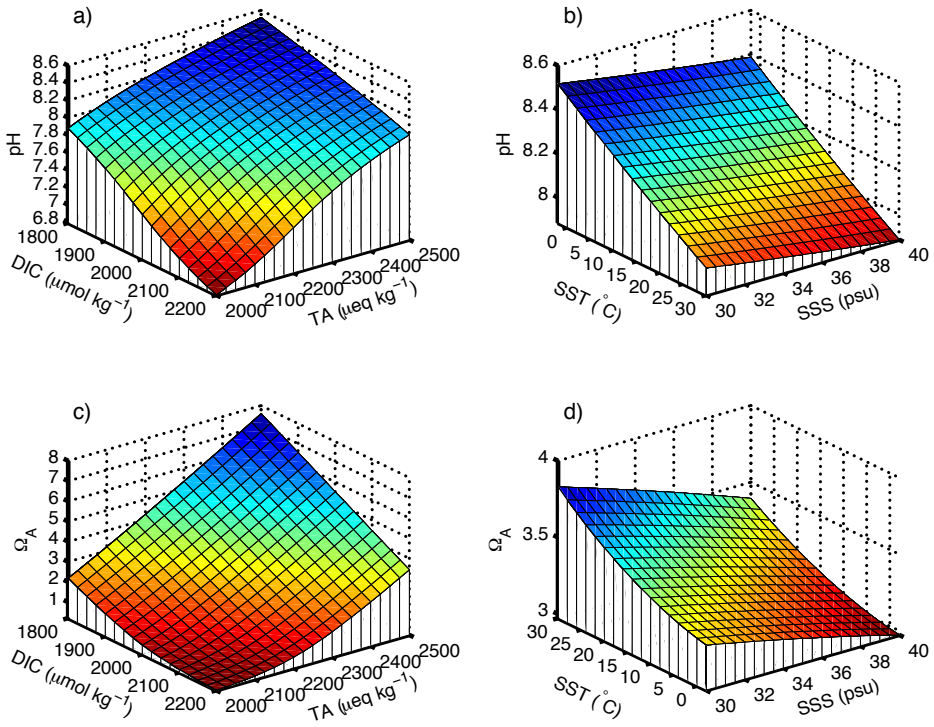

Figure E.1: The relationship between a), pH and c) Ω_A and DIC and TA, and b) pH and d) Ω_A and SST and SSS. The values for pH and Ω_A were calculated in CO2SYS, with phosphate and silicate both set to 0 μmol kg^{-1}.

Appendix F

Uncertainty in solution of the carbonate chemistry system

From Dickson (2010) we can calculate the combined standard uncertainty (u_c) on a dependent variable y given uncertainties on the independent variables $x_1, x_2, .., x_n$ of $u(x_i)$ as:

$$u_c(y(x_1, ..., x_n)) = \sqrt{\sum_{i=1,n} \left(\frac{\partial y}{\partial x_i}\right)^2 u(x_i)^2} \tag{F.1}$$

For pH we have:

$$\mathrm{u_c}\left(pH(DIC, TA, K_0, K_1', K_2')\right) = \sqrt{\left(\tfrac{\partial pH}{\partial DIC}\right)^2 {u_{DIC}}^2 + \left(\tfrac{\partial pH}{\partial TA}\right)^2 {u_{TA}}^2 + \left(\tfrac{\partial pH}{\partial K_0}\right)^2 {u_{K_0}}^2 + \left(\tfrac{\partial pH}{\partial K_1'}\right)^2 {u_{K_1'}}^2 + \left(\tfrac{\partial pH}{\partial K_2'}\right)^2 {u_{K_2'}}^2} \tag{F.2}$$

For CO_3^{2-} we have:

$$\mathrm{u_c}\left(CO_3^{2-}(DIC, TA, K_0, K_1', K_2')\right) = \sqrt{\left(\tfrac{\partial CO_3^{2-}}{\partial DIC}\right)^2 {u_{DIC}}^2 + \left(\tfrac{\partial CO_3^{2-}}{\partial TA}\right)^2 {u_{TA}}^2 + \left(\tfrac{\partial CO_3^{2-}}{\partial K_0}\right)^2 {u_{K_0}}^2 + \left(\tfrac{\partial CO_3^{2-}}{\partial K_1'}\right)^2 {u_{K_1'}}^2 + \left(\tfrac{\partial CO_3^{2-}}{\partial K_2'}\right)^2 {u_{K_2'}}^2} \tag{F.3}$$

I assume $u_{DIC} = 3\,\mu\mathrm{mol\,kg^{-1}}$ and $u_{TA} = 3\,\mu\mathrm{eq\,kg^{-1}}$, and take the uncertainties on K_0, K_1' and K_2' to be 0.5, 1.3 and 2.3%, respectively. Calculating the partial derivatives in CO2SYS (Lewis and Wallace, 1998) using annual mean conditions for HOT, this method yields uncertainties on individual calculated values of pH and CO_3^{2-} of 0.009 and $3.2\,\mu\mathrm{mol\,kg^{-1}}$ when computed from DIC and TA. When calculated from pCO_{2sw} and TA (taking u_{pCO_2}=3 μatm), the uncertainties are 0.007 and $4.4\,\mu\mathrm{mol\,kg^{-1}}$, respectively. on K_{sp_A}' to be 5%, the uncertainty on Ω_A is 0.09 for both combinations of input parameters.

Let us compare these uncertainties with those calculated using the Gaussian error propagation method described in Chapter 6. Using the same uncertainties on DIC,

TA, pCO_{2sw}, K_0, $K_1^{'}$ and $K_2^{'}$, and additional uncertainties on phosphate and silicate of 4% and 3%, respectively, we find that u_{pH} is 0.012 from DIC and TA and 0.007 from pCO_{2sw} and TA. u_{Ω_A} is 0.1 for both parameter combinations.

Bibliography

Alenius, B. and Munguia, P. (2012). Effects of pH variability on the intertidal isopod, Paradella dianae. *Marine and Freshwater Behaviour and Physiology*, 45(4):245–259, doi:10.1080/10236244.2012.727235.

Ashford, O. M. (1949). A new bucket for measurement of sea surface temperature. *Marine Observer*, 19:107–112. Available from: www.metoffice.gov.uk/hadobs/hadsst3/references/Ashford_1949.pdf.

Bakker et al. (2013). An update to the Surface Ocean CO_2 Atlas (SOCAT version 2). *Earth System Science Data Discussions*, 6(2):465–512, doi:10.5194/essdd-6-465-2013.

Barry, J. P., Tyrrell, T., Hansson, L., Plattner, G. K., and Gattuso, J.-P. (2010). Atmospheric CO_2 targets for ocean acidification perturbation experiments, Guide to best practices for ocean acidification research and data reporting. Technical report, Publications Office of the European Union, Luxembourg. Available from: http://www.epoca-project.eu/index.php/guide-to-best-practices-for-ocean-acidification-research-and-data-reporting.html.

Bates, N. R., Best, M. H. P., Neely, K., Garley, R., Dickson, A. G., and Johnson, R. J. (2012). Detecting anthropogenic carbon dioxide uptake and ocean acidification in the North Atlantic Ocean. *Biogeosciences*, 9(7):2509–2522, doi:10.5194/bg-9-2509-2012.

Beggs, H. M., Verein, R., Paltoglou, G., Kippo, H., and Underwood, M. (2012). Enhancing ship of opportunity sea surface temperature observations in the Australian region. *Journal of Operational Oceanography*, 5(1):59–73.

Available from: http://www.ingentaconnect.com/content/imarest/joo/2012/00000005/00000001/art00006.

Bopp, L., Resplandy, L., Orr, J. C., Doney, S. C., Dunne, J. P., Gehlen, M., Halloran, P., Heinze, C., Ilyina, T., Séférian, R., Tjiputra, J., and Vichi, M. (2013). Multiple stressors of ocean ecosystems in the 21st century: projections with CMIP5 models. *Biogeosciences Discussions*, 10(2):3627–3676, doi:10.5194/bgd-10-3627-2013.

Brix, H., Currie, K. I., and Mikaloff Fletcher, S. E. (2013). Seasonal variability of the carbon cycle in subantarctic surface water in the South West Pacific. *Global Biogeochemical Cycles*, 27(1):200–211, doi:10.1002/gbc.20023.

Brooks, C. F. (1926). Observing Water-surface Temperatures at Sea. *Monthly Weather Review*, 54(6):241–253. Available from: http://journals.ametsoc.org/doi/abs/10.1175/1520-0493(1926)54%3C241%3AOWTAS%3E2.0.CO%3B2.

Brooks, C. F. (1928). Reliability of different methods of taking sea-surface temperatures. *Journal of the Washington Academy of Sciences*, 18:525–545. Available from: http://www.metoffice.gov.uk/hadobs/hadsst3/references/Brooks_1928.pdf.

Brooks, C. F. (1932). Oceanography and Meteorology. In *Physics of the Earth - V: Oceanography, Bulletin of the National Research Council, 85*, chapter 14, pages 457–519. The National Research Council of the Academy of Sciences, Washington, DC, USA. Available from: http://books.google.com.mx/books?id=ECMrAAAAYAAJ.

Caldeira, K. and Wickett, M. E. (2003). Oceanography: Anthropogenic carbon and ocean pH. *Nature*, 425(6956):365–365, doi:10.1038/425365a.

Cao, L. and Caldeira, K. (2008). Atmospheric CO_2 stabilization and ocean acidification. *Geophysical Research Letters*, 35(19):L19609, doi:10.1029/2008GL035072.

Chierici, M., Fransson, A., and Nojiri, Y. (2006). Biogeochemical processes as drivers of surface fCO_2 in contrasting provinces in the subarctic North Pacific Ocean. *Global Biogeochemical Cycles*, 20(1):1–16, doi:10.1029/2004GB002356.

Collins, C. A., Giovando, L. F., and Abbott-Smith, K. B. (1975). Comparison of Canadian and Japanese Merchant-Ship Observations of Sea-Surface Temperature

in the Vicinity of Present Ocean Weather Station"P," 1927-1933. *Journal of the Fisheries Research Board of Canada*, 32(2):253–258, doi:10.1139/f75-023.

Cooley, S. R., Kite-Powell, H. L., and Doney, S. C. (2009). Ocean acidification's potential to alter global marine ecosystem services. *Oceanography*, 22(4):172–181, doi:10.5670/oceanog.2009.106.

Cooley, S. R., Lucey, N., Kite-Powell, H., and Doney, S. C. (2012). Nutrition and income from molluscs today imply vulnerability to ocean acidification tomorrow. *Fish and Fisheries*, 13(2):182–215, doi:10.1111/j.1467-2979.2011.00424.x.

Crawford, W., Galbraith, J., and Bolingbroke, N. (2007). Line P ocean temperature and salinity, 1956-2005. *Progress in Oceanography*, 75(2):161–178, doi:10.1016/j.pocean.2007.08.017.

Currie, K. I., Reid, M. R., and Hunter, K. A. (2011). Interannual variability of carbon dioxide drawdown by subantarctic surface water near New Zealand. *Biogeochemistry*, 104(1-3):23–34, doi:10.1007/s10533-009-9355-3.

Dickson, A. G. (1981). An exact definition of total alkalinity and a procedure for the estimation of alkalinity and total inorganic carbon from titration data. *Deep Sea Research Part A.Oceanographic Research Papers*, 28(6):609–623, doi:10.1016/0198-0149(81)90121-7.

Dickson, A. G. (2010). The carbon dioxide system in seawater: equilibrium chemistry and measurements, Guide to best practices for ocean acidification research and data reporting. Technical report, Publications Office of the European Union, Luxembourg. Available from: `http://www.epoca-project.eu/index.php/guide-to-best-practices-for-ocean-acidification-research-and-data-reporting.html`.

Dickson, A. G. and Millero, F. J. (1987). A comparison of the equilibrium constants for the dissociation of carbonic acid in seawater media. *Deep Sea Research Part A.Oceanographic Research Papers*, 34(10):1733–1743, doi:10.1016/0198-0149(87)90021-5.

Dickson, A. G. and Riley, J. P. (1978). The effect of analytical error on the evaluation of the components of the aquatic carbon-dioxide system. *Marine Chemistry*, 6(1):77–85, doi:10.1016/0304-4203(78)90008-7.

Dieckmann, G. S., Nehrke, G., Papadimitriou, S., Göttlicher, Steininger, R., Kennedy, H., Wolf-Gladrow, D., and Thomas, D. N. (2008). Calcium carbonate as ikaite crystals in Antarctic sea ice. *Geophysical Research Letters*, 35(8):1–3, doi:10.1029/2008GL033540.

Doney, S. C., Fabry, V. J., Feely, R. A., and Kleypas, J. A. (2009). Ocean Acidification: The Other CO_2 Problem. *Annual Review of Marine Science*, 1(1):169–192, doi:10.1146/annurev.marine.010908.163834.

Doney, S. C., Mahowald, N., Lima, I., Feely, R. A., Mackenzie, F. T., Lamarque, J.-F., and Rasch, P. J. (2007). Impact of anthropogenic atmospheric nitrogen and sulfur deposition on ocean acidification and the inorganic carbon system. *Proceedings of the National Academy of Sciences*, 104(37):14580–14585, doi:10.1073/pnas.0702218104.

Donlon, C. J., Martin, M., Stark, J., Roberts-Jones, J., Fiedler, E., and Wimmer, W. (2012). The Operational Sea Surface Temperature and Sea Ice Analysis (OSTIA) system. *Remote Sensing of Environment*, 116(0):140–158, doi:10.1016/j.rse.2010.10.017.

Donlon, C. J., Minnett, P. J., Gentemann, C., Nightingale, T. J., Barton, I. J., Ward, B., and Murray, M. J. (2002). Toward Improved Validation of Satellite Sea Surface Skin Temperature Measurements for Climate Research. *Journal of Climate*, 15(4):353–369.

Dore, J. E., Lukas, R., Sadler, D. W., Church, M. J., and Karl, D. M. (2009). Physical and biogeochemical modulation of ocean acidification in the central North Pacific. *Proceedings of the National Academy of Sciences*, 106(30):12235–12240, doi:10.1073/pnas.0906044106.

Ecology and Environment Inc. (2007). Final Environmental Impact Statement/Environmental Impact Report for the Cabrillo Port Liquefied Natural Gas Deepwater Port License Application: Volume III: Appendix D5. Technical report, California State Lands Commission, Sacramento, CA, USA. Available from: http://www.slc.ca.gov/division_pages/DEPM/DEPM_Programs_and_Reports/BHP_Deep_Water_Port/FinalEIR/Volume%20III/Appendix%20D5/Appendix%20D5.pdf.

Egleston, E. S., Sabine, C. L., and Morel, F. M. M. (2010). Revelle revisited: Buffer factors that quantify the response of ocean chemistry to changes in DIC and alkalinity. *Global Biogeochemical Cycles*, 24(1):GB1002, doi:10.1029/2008GB003407.

Emerson, S., Sabine, C., Cronin, M. F., Feely, R., Cullison Gray, S. E., and DeGrandpre, M. (2011). Quantifying the flux of $CaCO_3$ and organic carbon from the surface ocean using in situ measurements of O_2, N_2, pCO_2, and pH. *Global Biogeochemical Cycles*, 25(3):GB3008, doi:10.1029/2010GB003924.

Emery, W. J., Castro, S., Wick, G. A., Schluessel, P., and Donlon, C. (2001). Estimating Sea Surface Temperature from Infrared Satellite and In Situ Temperature Data. *Bulletin of the American Meteorological Society*, 82(12):2773–2785. Available from: http://journals.ametsoc.org/doi/abs/10.1175/1520-0477(2001)082%3C2773%3AESSTFI%3E2.3.CO%3B2.

Folland, C. (2005). Assessing Bias Corrections in Historical Sea Surface Temperature using a Climate Model. *International Journal of Climatology*, 25(7):895–911, doi:10.1002/joc.1171.

Folland, C. K. (1991). Climate Research Technical Note, CRTN 14, Sea temperature bucket models used to correct historical SST data in the Meteorological Office. Technical report, Hadley Centre for Climate Prediction and Research, Bracknell, UK.

Folland, C. K. and Parker, D. E. (1995). Correction of instrumental biases in historical sea surface temperature data. *Quarterly Journal of the Royal Meteorological Society*, 121(522):319–367, doi:10.1002/qj.49712152206.

Friedrich, T., Timmermann, A., Abe-Ouchi, A., Bates, N. R., Chikamoto, M. O., Church, M. J., Dore, J. E., Gledhill, D. K., González-Dávila, M., Heinemann, M., Ilyina, T., Jungclaus, J. H., McLeod, E., Mouchet, A., and Santana-Casiano, J. M. (2012). Detecting regional anthropogenic trends in ocean acidification against natural variability. *Nature Climate Change*, 2(3):167–171, doi:10.1038/nclimate1372.

Friis, K., Körtzinger, A., and Wallace, D. W. R. (2003). The salinity normalization of marine inorganic carbon chemistry data. *Geophysical Research Letters*, 30(2):1–4, doi:10.1029/2002GL015898.

Gnielinski, V. (1976). New equations for heat and mass transfer in turbulent pipe and channel flow. *International Journal of Chemical Engineering*, 16:359–368.

González-Dávila, M. and Santana-Casiano, J. M. (2009). Sea Surface and Atmospheric fCO_2 data measured during the ESTOC Time Series cruises from 1995-2009. Technical report, Carbon Dioxide Information Analysis Center, Oak Ridge National Laboratory, US Department of Energy, Oak Ridge, TN, USA. doi:10.3334/CDIAC/otg.TSM_ESTOC.

Gouretski, V., Kennedy, J., Boyer, T., and Köhl, A. (2012). Consistent near-surface ocean warming since 1900 in two largely independent observing networks. *Geophysical Research Letters*, 39(19):L19606, doi:10.1029/2012GL052975.

Guinotte, J. M., Buddemeier, R. W., and Kleypas, J. A. (2003). Future coral reef habitat marginality: temporal and spatial effects of climate change in the Pacific basin. *Coral Reefs*, 22(4):551–558, doi:10.1007/s00338-003-0331-4.

Hagart-Alexander, C. (2010). Temperature Measurement. In Boyes, W., editor, *Instrumentation Reference Book (4th Edition)*, chapter 21, pages 269–326. Butterworth-Heinemann, Burlington, MA, USA. Available from: http://www.sciencedirect.com/science/book/9780750683081.

Hauri, C., Gruber, N., Vogt, M., Doney, S. C., Feely, R. A., Lachkar, Z., Leinweber, A., McDonnell, A. M. P., Munnich, M., and Plattner, G. K. (2013). Spatiotemporal variability and long-term trends of ocean acidification in the California Current System. *Biogeosciences*, 10(1):193–216, doi:10.5194/bg-10-193-2013.

Hénin, C. and Grelet, J. (1996). A merchant ship thermo-salinograph network in the Pacific Ocean. *Deep Sea Research Part I: Oceanographic Research Papers*, 43(11-12):1833–1855, doi:10.1016/S0967-0637(96)00084-2.

Hinga, K. R. (2002). Effects of pH on coastal marine phytoplankton. *Marine Ecology Progress Series*, 238:281–300, doi:10.3354/meps238281.

HMSO (1956). *Handbook of meteorological instruments Part 1*, pages 400–409. HMSO. Available from: http://www.metoffice.gov.uk/hadobs/hadsst3/references/Handbook_of_met_instruments_1956.pdf.

Hofmann, G. E., Smith, J. E., Johnson, K. S., Send, U., Levin, L. A., Micheli, F., Paytan, A., Price, N. N., Peterson, B., Takeshita, Y., Matson, P. G., Crook, E. D., Kroeker, K. J., Gambi, M. C., Rivest, E. B., Frieder, C. A., Yu, P. C., and Martz, T. R. (2011). High-Frequency Dynamics of Ocean pH: A Multi-Ecosystem Comparison. *PLoS ONE*, 6(12):28983, doi:10.1371l.pone.0028983.

Homayoni, H. and Yaghoubi, M. (2008). Investigation of aiding flow for natural convection around a horizontal isothermal circular cylinder by finite volume. In *Proceedings of the 1st WSEAS International Conference on Finite differences - Finite Elements - Finite Volumes - Boundary Elements (F-and-B'08)*, pages 79–83. Available from: `http://www.wseas.us/e-library/conferences/2008/malta/fb-mn/fb11.pdf`.

Hönisch, B., Ridgwell, A., Schmidt, D. N., Thomas, E., Gibbs, S. J., Sluijs, A., Zeebe, R., Kump, L., Martindale, R. C., Greene, S. E., Kiessling, W., Ries, J., Zachos, J. C., Royer, D. L., Barker, S., Marchitto, T. M., Moyer, R., Pelejero, C., Ziveri, P., Foster, G. L., and Williams, B. (2012). The Geological Record of Ocean Acidification. *Science*, 335(6072):1058–1063, doi:10.1126/science.1208277.

Hunter, K. A. (1998). The temperature dependence of pH in surface seawater. *Deep Sea Research Part I: Oceanographic Research Papers*, 45(11):1919–1930, doi:10.1016/S0967-0637(98)00047-8.

Iglesias-Rodriguez, M. D., Anthony, K. R. N., Bijma, J., Dickson, A. G., Doney, S. C., Fabry, V. J., Feely, R. A., Gattuso, J.-P., Lee, K., Riebesell, U., Saino, T., and Turley, C. (2010). Developing a Global Ocean Acidification Observation Network. In Hall, J., Harrison, D. E., and Stammer, D., editors, *Proceedings of OceanObs09: Sustained Ocean Observations and Information for Society (Vol. 1), Venice, Italy, 21-25 September 2009*. ESA Publication WPP-306. doi:10.5270/OceanObs09.pp.24.

James, R. W. and Fox, P. T. (1972). Comparative Sea-Surface Temperature Measurements. Technical report, WMO, Geneva, Switzerland.

James, R. W. and Shank, M. K. (1964). Effect of Variation of Intake Depths on Water Injection Temperatures. Technical report, Marine Sciences Department, US Naval Oceanographic Office, Washington, DC, USA.

Johnson, D. R., Boyer, T. P., Garcia, H. E., Locarnini, R. A., Baranova, O. K., and Zweng, M. M. (2009). World Ocean Database 2009 Documentation. NODC

internal Report 20. Technical report, NOAA Printing Office, Silver Spring, MD, USA. Available from: http://rda.ucar.edu/datasets/ds285.0/docs/wod09/wod09readme.pdf.

Jones, P. D. and Bradley, R. S. (1992). Climatic variations in the longest instrumental records. In Bradley, R. S. and Jones, P. D., editors, *Climate since A.D. 1500*, chapter 13, pages 246–268. Routledge, London, UK.

Jones, P. D., Lister, D. H., Osborn, T. J., Harpham, C., Salmon, M., and Morice, C. P. (2012). Hemispheric and large-scale land-surface air temperature variations: An extensive revision and an update to 2010. *Journal of Geophysical Research*, 117:D05127, doi:10.1029/2011JD017139.

Juranek, L. W., Feely, R. A., Gilbert, D., Freeland, H., and Miller, L. A. (2011). Real-time estimation of pH and aragonite saturation state from Argo profiling floats: Prospects for an autonomous carbon observing strategy. *Geophysical Research Letters*, 38(17):L17603, doi:10.1029/2011GL048580.

Kennedy, J. J., Brohan, P., and Tett, S. F. B. (2007). A global climatology of the diurnal variations in sea-surface temperature and implications for MSU temperature trends. *Geophysical Research Letters*, 34:L05712, doi:10.1029/2006GL028920.

Kennedy, J. J., Rayner, N. A., Smith, R. O., Parker, D. E., and Saunby, M. (2011a). Reassessing biases and other uncertainties in sea surface temperature observations measured in situ since 1850: 2. Biases and homogenization. *Journal of Geophysical Research*, 116:D14104, doi:10.1029/2010JD015220.

Kennedy, J. J., Rayner, N. A., Smith, R. O., Parker, D. E., and Saunby, M. (2011b). Reassessing biases and other uncertainties in sea surface temperature observations measured in situ since 1850: 1. Measurement and sampling uncertainties. *Journal of Geophysical Research*, 116:D14103, doi:10.1029/2010JD015218.

Kent, E. C. and Challenor, P. G. (2006). Toward Estimating Climatic Trends in SST. Part II: Random Errors. *Journal of Atmospheric and Oceanic Technology*, 23(3):476–486, doi:10.1175/JTECH1844.1.

Kent, E. C. and Kaplan, A. (2006). Toward Estimating Climatic Trends in SST. Part III: Systematic Biases. *Journal of Atmospheric and Oceanic Technology*, 23(3):487–500, doi:10.1175/JTECH1845.1.

Kent, E. C., Kennedy, J. J., Berry, D. I., and Smith, R. O. (2010). Effects of instrumentation changes on sea surface temperature measured in situ. *Wiley Interdisciplinary Reviews: Climate Change*, 1(5):718–728, doi:10.1002/wcc.55.

Kent, E. C. and Taylor, P. K. (2006). Toward Estimating Climatic Trends in SST. Part I: Methods of Measurement. *Journal of Atmospheric and Oceanic Technology*, 23(3):464–475, doi:10.1175/JTECH1843.1.

Kent, E. C., Woodruff, S. D., and Berry, D. I. (2007). Metadata from WMO Publication No. 47 and an Assessment of Voluntary Observing Ship Observation Heights in ICOADS. *Journal of Atmospheric and Oceanic Technology*, 24(2):214–234, doi:10.1175/JTECH1949.1.

Key, R. M., Kozyr, A., Sabine, C. L., Lee, K., Wanninkhof, R., Bullister, J. L., Feely, R. A., Millero, F. J., Mordy, C., and Peng, T.-H. (2004). A global ocean carbon climatology: Results from Global Data Analysis Project (GLODAP). *Global Biogeochemical Cycles*, 18(4):GB4031, doi:10.1029/2004GB002247.

Key, R. M., Tanhua, T., Olsen, A., Hoppema, M., Jutterström, S., Schirnick, C., van Heuven, S., Kozyr, A., Lin, X., Velo, A., Wallace, D. W. R., and Mintrop, L. (2010). The CARINA data synthesis project: introduction and overview. *Earth System Science Data*, 2(1):105–121, doi:10.5194/essd-2-105-2010.

Khatiwala, S., Tanhua, T., Mikaloff Fletcher, S., Gerber, M., Doney, S. C., Graven, H. D., Gruber, N., McKinley, G. A., Murata, A., Ríos, A. F., and Sabine, C. L. (2013). Global ocean storage of anthropogenic carbon. *Biogeosciences*, 10(4):2169–2191. Available from: http://www.biogeosciences.net/10/2169/2013/.

Kirk, T. H. and Gordon, A. H. (1952). Comparison of intake and bucket methods for measuring sea temperature. *Marine Observer*, 22:33–39. Available from: http://www.metoffice.gov.uk/hadobs/hadsst3/references/Kirk_and_Gordon_1952.pdf.

Kleypas, J. A., Buddemeier, R. W., Archer, D., Gattuso, J.-P., Langdon, C., and Opdyke, B. N. (1999). Geochemical Consequences of Increased Atmospheric Carbon Dioxide on Coral Reefs. *Science*, 284(5411):118–120, doi:10.1126/science.284.5411.118.

Krishna Rao, P., Smith, W. L., and Koffler, R. (1972). Global Sea-Surface Temperature Distribution Determined From an Environmental Satellite. *Monthly Weather Review*, 100(1):10–14.

Langdon, C., Broecker, W. S., Hammond, D. E., Glenn, E., Fitzsimmons, K., Nelson, S. G., Peng, T.-H., Hajdas, I., and Bonani, G. (2003). Effect of elevated CO_2 on the community metabolism of an experimental coral reef. *Global Biogeochemical Cycles*, 17(1):1011, doi:10.1029/2002GB001941.

Le Quéré, C., Andres, R. J., Boden, T., Conway, T., Houghton, R. A., House, J. I., Marland, G., Peters, G. P., van der Werf, G. R., Ahlström, A., Andrew, R. M., Bopp, L., Canadell, J. G., Ciais, P., Doney, S. C., Enright, C., Friedlingstein, P., Huntingford, C., Jain, A. K., Jourdain, C., Kato, E., Keeling, R. F., Klein Goldewijk, K., Levis, S., Levy, P., Lomas, M., Poulter, B., Raupach, M. R., Schwinger, J., Sitch, S., Stocker, B. D., Viovy, N., Zaehle, S., and Zeng, N. (2013). The global carbon budget 1959-2011. *Earth System Science Data*, 5(2):165–185, doi:10.5194/essdd-5-1107-2012.

Lee, K., Tong, L. T., Millero, F. J., Sabine, C. L., Dickson, A. G., Goyet, C., Park, G.-H., Wanninkhof, R., Feely, R. A., and Key, R. M. (2006). Global relationships of total alkalinity with salinity and temperature in surface waters of the world's oceans. *Geophysical Research Letters*, 33(19):L19605, doi:10.1029/2006GL027207.

Lewis, E. and Wallace, D. (1998). CO2SYS - Program Developed for CO_2 System Calculations. Technical report, Carbon Dioxide Information Analysis Center; Report ORNL/CDIAC-105. Available from: `http://cdiac.ornl.gov/oceans/co2rprt.html`.

Locarnini, R. A., Mishonov, A. V., Antonov, J. I., Boyer, T. P., Garcia, H. E., Baranova, O. K., Zweng, M. M., and Johnson, D. R. (2010). *World Ocean Atlas 2009, Volume 1: Temperature, NOAA Atlas NESDIS 68*. U.S. Government Printing Office, Washington, D.C., USA. Available from: `ftp://ftp.nodc.noaa.gov/pub/WOA09/DOC/woa09_vol1_text_figures.pdf`.

Lüger, H., Wallace, D. W. R., Körtzinger, A., and Nojiri, Y. (2004). The pCO_2 variability in the midlatitude North Atlantic Ocean during a full annual cycle. *Global Biogeochemical Cycles*, 18(3), doi:10.1029/2003GB002200.

Lumby, J. R. (1927). The surface sampler, an apparatus for the collection of samples from the sea surface from ships in motion, with a note on surface temperature observations. *Journal du Conseil Permanennt International pour l'Exploration de la Mer*, 2:332–342. Available from: www.metoffice.gov.uk/hadobs/hadsst3/references/Lumby_1927.pdf.

Lumby, J. R. (1928). Modification of the Surface Sampler with a view to the Improvement of Temperature Observation. *Journal du Conseil Permanennt International pour l'Exploration de la Mer*, 3:340–350. Available from: www.metoffice.gov.uk/hadobs/hadsst3/references/Lumby_1928.pdf.

Manzello, D. P., Kleypas, J. A., Budd, D. A., Eakin, C. M., Glynn, P. W., and Langdon, C. (2008). Poorly cemented coral reefs of the eastern tropical Pacific: Possible insights into reef development in a high-CO_2 world. *Proceedings of the National Academy of Sciences*, 105(30):10450–10455, doi:10.1073/pnas.0712167105.

Matthews, J. B. R. (2009). Comparing Historical and Modern Sea Surface Temperature measurement methods in the Tropical Pacific, B.Sc. Dissertation, University of East Anglia.

Matthews, J. B. R. (2013). Comparing historical and modern methods of sea surface temperature measurement - Part 1: Review of methods, field comparisons and dataset adjustments. *Ocean Science*, 9(4):683–694, doi:10.5194/os-9-683-2013.

Matthews, J. B. R. and Matthews, J. B. (2013). Comparing historical and modern methods of sea surface temperature measurement - Part 2: Field comparison in the central tropical Pacific. *Ocean Science*, 9(4):695–711, doi:10.5194/os-9-695-2013.

McCabe, W. L., Smith, J. C., and Harriott, P. (2001). *Unit Operations of Chemical Engineering (6th Edition)*. McGraw-Hill, New York, NY, USA.

McElhany, P. and Busch, D. S. (2013). Appropriate pCO_2 treatments in ocean acidification experiments. *Marine Biology*, 160(8):1807–1812, doi:10.1007/s00227-012-2052-0.

McNeil, B. I. and Matear, R. J. (2008). Southern Ocean acidification: A tipping point at 450-ppm atmospheric CO_2. *Proceedings of the National Academy of Sciences*, 105(48):18860–18864, doi:10.1073/pnas.0806318105.

McNeil, B. I., Metzl, N., Key, R. M., Matear, R. J., and Corbiere, A. (2007). An empirical estimate of the Southern Ocean air-sea CO_2 flux. *Global Biogeochemical Cycles*, 21(3):GB3011, doi:10.1029/2007GB002991.

Mehrbach, C., Culberson, C. H., Hawley, J. E., and Pytkowicz, R. M. (1973). Measurement of the Apparent Dissociation Constants of Carbonic Acid in Seawater at Atmospheric Pressure. *Limnology and Oceanography*, 18(6):897–907. Available from: `http://aslo.org/lo/toc/vol_18/issue_6/0897.pdf`.

Merchant, C. J., Llewellyn-Jones, D., Saunders, R. W., Rayner, N. A., Kent, E. C., Old, C. P., Berry, D., Birks, A. R., Blackmore, T., Corlett, G. K., Embury, O., Jay, V. L., Kennedy, J., Mutlow, C. T., Nightingale, T. J., O'Carroll, A. G., Pritchard, M. J., Remedios, J. J., and Tett, S. (2008). Deriving a sea surface temperature record suitable for climate change research from the along-track scanning radiometers. *Advances in Space Research*, 41(1):1–11, doi:10.1016/j.asr.2007.07.041.

Midorikawa, T., Ishii, M., Saito, S., Sasano, D., Kosugi, N., Motoi, T., Kamiya, H., Nakadate, A., Nemoto, K., and Inoue, H. Y. (2010). Decreasing pH trend estimated from 25-yr time series of carbonate parameters in the western North Pacific. *Tellus B*, 62(5):649–659, doi:10.1111/j.1600-0889.2010.00474.x.

Millero, F. J., Graham, T. B., Huang, F., Bustos-Serrano, H., and Pierrot, D. (2006). Dissociation constants of carbonic acid in seawater as a function of salinity and temperature. *Marine Chemistry*, 100(1-2):80, doi:10.1016/j.marchem.2005.12.001.

Millero, F. J., Lee, K., and Roche, M. (1998). Distribution of alkalinity in the surface waters of the major oceans. *Marine Chemistry*, 60(1-2):111–130, doi:10.1016/S0304-4203(97)00084-4.

Millero, F. J., Pierrot, D., Lee, K., Wanninkhof, R., Feely, R., Sabine, C. L., Key, R. M., and Takahashi, T. (2002). Dissociation constants for carbonic acid determined from field measurements. *Deep Sea Research Part I: Oceanographic Research Papers*, 49(10):1705–1723, doi:10.1016/S0967-0637(02)00093-6.

Morice, C. P., Kennedy, J. J., Rayner, N. A., and Jones, P. D. (2012). Quantifying uncertainties in global and regional temperature change using an ensemble of observational estimates: The HadCRUT4 dataset. *Journal of Geophysical Research*, 117:D08101, doi:10.1029/2011JD017187.

Murray, J. W. (2004). Ocean Carbonate Chemistry, The Aquatic Chemistry Fundamentals. In Follows, M. and Oguz, T., editors, *The Ocean Carbon Cycle and Climate*, NATO Science Series, Vol. 40, chapter 1, pages 1–29. Kluwer Academic Publishers, Dordrecht, The Netherlands.

Nicholas, J. V. and White, D. R. (2001). *Traceable Temperatures: An Introduction to Temperature Measurement and Calibration (Second Edition)*. Wiley, Chichester, UK.

Olafsson, J. (2007a). Iceland Sea cruise data from 1991-2006 cruises, CARINA Data Set. Technical report, Carbon Dioxide Information Analysis Center, Oak Ridge National Laboratory, US Department of Energy, Oak Ridge, TN, USA. doi:10.3334/CDIAC/otg.CARINA_IcelandSea.

Olafsson, J. (2007b). Irminger Sea cruise data from the 1991-2006 cruises, CARINA Data Set. Technical report, Carbon Dioxide Information Analysis Center, Oak Ridge National Laboratory, US Department of Energy, Oak Ridge, TN, USA. doi:10.3334/CDIAC/otg.CARINA_IrmingerSea.

Olafsson, J., Olafsdottir, S. R., Benoit-Cattin, A., Danielsen, M., Arnarson, T. S., and Takahashi, T. (2009). Rate of Iceland Sea acidification from time series measurements. *Biogeosciences*, 6(11):2661–2668, doi:10.5194/bg-6-2661-2009.

Parker, D. E. (1993). Hadley Centre Internal Note 34: Summary of information on sampling apparatus for sea surface temperature measurement. Technical report, Meteorological Office, Bracknell, UK.

Petukhov, B. S. (1970). Heat Transfer and Friction in Turbulent Pipe Flow with Variable Physical Properties. *Advances in Heat Transfer*, 6:503–564, doi:10.1016/S0065-2717(08)70153-9.

Piip, A. (1974). A Critical Description of the CSIRO Sea Surface Temperature and Salinity Sampling Program from Merchant Ships. Technical Report 57, Marine Laboratory, Cronulla, Sydney, NSW, Australia.

Price, N. N., Martz, T. R., Brainard, R. E., and Smith, J. E. (2012). Diel Variability in Seawater pH Relates to Calcification and Benthic Community Structure on Coral Reefs. *PLoS ONE*, 7(8):43843, doi:10.1371l.pone.0043843.

Raven, J. A. (2013). Half a Century of Pursuing the Pervasive Proton. *Progress in Botany*, 74:3–34, doi:10.1007/978-3-642-30967-0_1.

Rayner, N. A., Brohan, P., Parker, D. E., Folland, C. K., Kennedy, J. J., Vanicek, M., Ansell, T. J., and Tett, S. F. B. (2006). Improved Analyses of Changes and Uncertainties in Sea Surface Temperature Measured In Situ since the Mid-Nineteenth Century: The HadSST2 Dataset. *Journal of Climate*, 19(3):446–469, doi:10.1175/JCLI3637.1.

Rayner, N. A., Parker, D. E., Horton, E. B., Folland, C. K., Alexander, L. V., Rowell, D. P., Kent, E. C., and Kaplan, A. (2003). Global analyses of sea surface temperature, sea ice, and night marine air temperature since the late nineteenth century. *Journal of Geophysical Research*, 108:4407, doi:10.1029/2002JD002670.

Revelle, R. and Suess, H. E. (1957). Carbon Dioxide Exchange Between Atmosphere and Ocean and the Question of an Increase of Atmospheric CO_2 during the Past Decades. *Tellus*, 9(1):18–27, doi:10.1111/j.2153-3490.1957.tb01849.x.

Reynolds, R. W., Rayner, N. A., Smith, T. M., Stokes, D. C., and Wang, W. (2002). An Improved In Situ and Satellite SST Analysis for Climate. *Journal of Climate*, 15(13):1609–1625.

Riebesell, U., Körtzinger, A., and Oschlies, A. (2009). Sensitivities of marine carbon fluxes to ocean change. *Proceedings of the National Academy of Sciences*, 106(49):20602–20609, doi:10.1073/pnas.0813291106.

Ries, J. B., Cohen, A. L., and McCorkle, D. C. (2009). Marine calcifiers exhibit mixed responses to CO_2-induced ocean acidification. *Geology*, 37(12):1131–1134, doi:10.1130/G30210A.1.

Roll, H. U. (1951a). The accuracy of measuring water temperature with the water scoop thermometer (Marinepütz - German scoop thermometer). *Annalen der Meteorologie*, 10-12:480–482. Available from: `www.metoffice.gov.uk/hadobs/hadsst3/references/Roll_1951.pdf`.

Roll, H. U. (1951b). Water temperature measurements on deck and in the engine room. *Annalen der Meteorolgie*, 4:439–443.

Royal Society (2005). Ocean acidification due to increasing atmospheric carbon dioxide. Policy document 12/05. Technical report, The Royal Society, London, UK. Available from: http://royalsociety.org/uploadedFiles/Royal_Society_Content/policy/publications/2005/9634.pdf.

Sabine, C. L., Feely, R. A., Gruber, N., Key, R. M., Lee, K., Bullister, J. L., Wanninkhof, R., Wong, C. S., Wallace, D. W. R., Tilbrook, B., Millero, F. J., Peng, T.-H., Kozyr, A., Ono, T., and Rios, A. F. (2004). The Oceanic Sink for Anthropogenic CO_2. *Science*, 305(5682):367–371, doi:10.1126/science.1097403.

Santana-Casiano, J. M., González-Dávila, M., Rueda, M.-J., Llinás, O., and González-Dávila, E.-F. (2007). The interannual variability of oceanic CO_2 parameters in the northeast Atlantic subtropical gyre at the ESTOC site. *Global Biogeochemical Cycles*, 21(1):GB1015, doi:10.1029/2006GB002788.

Sarmiento, J. L. and Gruber, N. (2006). *Carbon Cycle*, chapter 8, pages 318–358. Ocean Biogeochemical Dynamics. Princeton University Press, Princeton, NJ, USA.

Saur, J. F. T. (1963). A Study of the Quality of Sea Water Temperatures Reported in Logs of Ships' Weather Observations. *Journal of Applied Meteorology*, 2(3):417–425.

Schott, G. (1893). Scientific results of a research voyage at sea carried out in the years 1891 and 1892. Technical report, Justus Perthes, Gotha, Germany.

Shaw, E. C., McNeil, B. I., and Tilbrook, B. (2012). Impacts of ocean acidification in naturally variable coral reef flat ecosystems. *Journal of Geophysical Research: Oceans*, 117:C03038, doi:10.1029/2011JC007655.

Siuda, A. N. S. (2008). Final report for S.E.A. Cruise S217. Technical report, Sea Education Association, Woods Hole, MA, USA. Available from: http://hdl.handle.net/1912/4476.

Skjelvan, I., Falck, E., Rey, F., and Kringstad, S. B. (2008). Inorganic carbon time series at Ocean Weather Station M in the Norwegian Sea. *Biogeosciences*, 5(2):549–560, doi:10.5194/bg-5-549-2008.

Smith, T. M. and Reynolds, R. W. (2002). Bias Corrections for Historical Sea Surface Temperatures Based on Marine Air Temperatures. *Journal of Climate*, 15(1):73–87. Available from: 10.1175/1520-0442(2002)015<0073:BCFHSS>2.0.CO;2.

Smith, T. M., Reynolds, R. W., Peterson, T. C., and Lawrimore, J. (2008). Improvements to NOAA's Historical Merged Land-Ocean Surface Temperature Analysis (1880-2006). *Journal of Climate*, 21(10):2283–2296, doi:10.1175/2007JCLI2100.1.

Soloviev, A. and Klinger, B. (2008). Open Ocean Convection. In Steele, J. H., Turekian, K. K., and Thorpe, S. A., editors, *Encyclopedia of Ocean Sciences (Second Edition)*, pages 218–225. Elsevier. Available from: http://www.sciencedirect.com/science/article/pii/B9780123744739001181.

Soloviev, A. and Lukas, R. (2006). *The Near-Surface Layer of the Ocean: Structure, Dynamics and Applications*. Springer, Dordrecht, The Netherlands.

Stubbs, M. W. (1965). The standard error of a sea surface temperature as measured using a canvas bucket. *Meteorological Magazine*, 94:66–69. Available from: www.metoffice.gov.uk/hadobs/hadsst3/references/Stubbs_1965.pdf.

Stupart, F., Patterson, J., and Smith, H. G. (1929). Ocean surface-water temperatures - methods of measuring and preliminary results. *Bulletin of the National Research Council, 68*.

Suzuki, T., Ishii, M., Aoyama, M., Christian, J. R., Enyo, K., Kawano, T., Key, R. M., Kosugi, N., Kozyr, A., Miller, L. A., Murata, A., Nakano, T., Ono, T., Saino, T., Sasaki, K., Sasano, D., Takatani, Y., Wakita, M., and Sabine, C. (2013). PACIFICA Data Synthesis Project. ORNL/CDIAC-159, NDP-092. Technical report, Carbon Dioxide Information Analysis Center, Oak Ridge National Laboratory, U.S. Department of Energy, Oak Ridge, TN, USA. doi:10.3334/CDIAC/OTG.PACIFICA_NDP092.

Tabata, S. (1978a). Comparison of Observations of Sea Surface Temperatures at Ocean Station P and NOAA Buoy Stations and Those Made by Merchant Ships Traveling in Their Vicinities, in the Northeast Pacific Ocean. *Journal of Applied Meteorology*, 17(3):374–385.

Tabata, S. (1978b). An Evaluation of the Quality of Sea Surface Temperatures and Salinities Measured at Station P and Line P in the Northeast Pacific Ocean. *Journal of Physical Oceanography*, 8(6):970–986.

Tabata, S. (1978c). An examination of the quality of sea-surface temperatures and salinities observed recently in the northeast Pacific Ocean. Technical report, Pacific

Marine Science Report 78-3, Institute of Ocean Sciences, Sidney, BC, Canada. Available from: www.dfo-mpo.gc.ca/Library/54883.pdf.

Tabata, S. (1978d). On the accuracy of sea surface temperatures and salinities observed in the northeast pacific ocean. *Atmosphere-Ocean*, 16(3):237–247, doi:10.1080/07055900.1978.9649032.

Tahavvor, A. R. and Yaghoubi, M. (2008). Natural cooling of horizontal cylinder using Artificial Neural Network (ANN). *International Communications in Heat and Mass Transfer*, 35(9):1196–1203, doi:10.1016/j.icheatmasstransfer.2008.05.009.

Takahashi, T., Sutherland, S. C., Sweeney, C., Poisson, A., Metzl, N., Tilbrook, B., Bates, N., Wanninkhof, R., Feely, R. A., Sabine, C., Olafsson, J., and Nojiri, Y. (2002). Global sea-air CO_2 flux based on climatological surface ocean pCO_2, and seasonal biological and temperature effects. *Deep Sea Research Part II: Topical Studies in Oceanography*, 49(9-10):1601–1622, doi:10.1016/S0967-0645(02)00003-6.

Takahashi, T., Sutherland, S. C., Wanninkhof, R., Sweeney, C., Feely, R. A., Chipman, D. W., Hales, B., Friederich, G., Chavez, F., Sabine, C., Watson, A., Bakker, D. C. E., Schuster, U., Metzl, N., Yoshikawa-Inoue, H., Ishii, M., Midorikawa, T., Nojiri, Y., Körtzinger, A., Steinhoff, T., Hoppema, M., Olafsson, J., Arnarson, T. S., Tilbrook, B., Johannessen, T., Olsen, A., Bellerby, R., Wong, C. S., Delille, B., Bates, N. R., and de Baar, H. J. W. (2009). Climatological mean and decadal change in surface ocean pCO_2, and net sea-air CO_2 flux over the global oceans. *Deep Sea Research Part II: Topical Studies in Oceanography*, 56(8-10):554–577, doi:10.1016/j.dsr2.2008.12.009.

Tauber, G. M. (1969). The comparative measurements of sea-surface temperature in the USSR. Technical report, WMO, Geneva, Switzerland.

Thomas, B. R., Kent, E. C., and Swail, V. R. (2005). Methods to Homogenize Wind Speeds from Ships and Buoys. *International Journal of Climatology*, 25(7):979–995, doi:10.1002/joc.1176.

Thompson, D. W. J., Kennedy, J. J., Wallace, J. M., and Jones, P. D. (2008). A large discontinuity in the mid-twentieth century in observed global-mean surface temperature. *Nature*, 453(7195):646–649, doi:10.1038/nature06982.

Uwai, T. and Komura, K. (1992). The Collection of Historical Ships' Data in Kobe Marine Observatory. In *Proceedings of the International COADS Workshop, Boulder, Colorado, 13-15 January 1992*. NOAA Environmental Research Laboratories, Climate Research Division, Boulder, CO, USA. Available from: http://icoads.noaa.gov/Boulder/Boulder.Uwai.pdf.

Velo, A., Pérez, F. F., Tanhua, T., Gilcoto, M., Ríos, A. F., and Key, R. M. (2013). Total alkalinity estimation using MLR and neural network techniques. *Journal of Marine Systems*, 111-112(0):11–18, doi:10.1016/j.jmarsys.2012.09.002.

Wallace, D. W. R. (1995). Monitoring Global Ocean Carbon Inventories, Ocean Observing System Development Panel Background Report Number 5. Technical report, Texas A&M University, College Station, TX, USA. Available from: http://ioc-goos-oopc.org/documents/oosdp/oosdp_br5.pdf.

Webster, P. J., Clayson, C. A., and Curry, J. A. (1996). Clouds, Radiation, and the Diurnal Cycle of Sea Surface Temperature in the Tropical Western Pacific. *Journal of Climate*, 9(8):1712–1730.

Wentz, F. J., Gentemann, C., Smith, D., and Chelton, D. (2000). Satellite Measurements of Sea Surface Temperature Through Clouds. *Science*, 288(5467):847–850, doi:10.1126/science.288.5467.847.

Wilkinson, C., Woodruff, S. D., Brohan, P., Claesson, S., Freeman, E., Koek, F., Lubker, S. J., Marzin, C., and Wheeler, D. (2011). Recovery of logbooks and international marine data: the RECLAIM project. *International Journal of Climatology*, 31(7):968–979, doi:10.1002/joc.2102.

Williams, R. G. and Follows, M. J. (2011). *Carbonate chemistry fundamentals*, chapter 6, pages 125–155. Ocean Dynamics and the Carbon Cycle. Cambridge University Press, Cambridge, UK.

WMO (2008). Guide to Meteorological Instruments and Methods of Observation (WMO-No. 8): Part II - Observing Systems, Chapter 4 - Marine Observations. Technical report, WMO, Geneva, Switzerland. Available from: ftp://ftp.wmo.int/Documents/MediaPublic/Publications/WMO8_CIMOguide/Part-II/WMO8_Ed2008_PartII_Ch4_Up2010_en.pdf.

Wolf-Gladrow, D. A., Zeebe, R. E., Klaas, C., Körtzinger, A., and Dickson, A. G. (2007). Total alkalinity: The explicit conservative expression and its application to biogeochemical processes. *Marine Chemistry; Special issue: Dedicated to the memory of Professor Roland Wollast*, 106(1-2):287–300, doi:10.1016/j.marchem.2007.01.006.

Woodruff, S. D., Diaz, H. F., Kent, E. C., Reynolds, R. W., and Worley, S. J. (2008). The Evolving SST Record from ICOADS. In Brönnimann, S., Luterbacher, J., Ewen, T., Diaz, H. F., Stolarski, R. S., and Neu, U., editors, *Climate Variability and Extremes during the Past 100 Years*, Advances in Global Change Research, Vol. 33, chapter 4, pages 65–83. Springer, USA. Available from: http://link.springer.com/chapter/10.1007%2F978-1-4020-6766-2_4.

Woodruff, S. D., Worley, S. J., Lubker, S. J., Ji, Z., Freeman, J. E., Berry, D. I., Brohan, P., Kent, E. C., Reynolds, R. W., Smith, S. R., and Wilkinson, C. (2011). ICOADS Release 2.5: extensions and enhancements to the surface marine meteorological archive. *International Journal of Climatology*, 31(7):951–967, doi:10.1002/joc.2103.

Zeebe, R. E. and Wolf-Gladrow, D. (2001). *CO_2 in Seawater: Equilibrium, Kinetics, Isotopes*. Elsevier Science B.V., Amsterdam, The Netherlands.